AN INVESTIGATION INTO THE EFFECTS OF COMPLEX TOPOGRAPHY ON PARTICLE DRY DEPOSITION

by

SIMON TOBY PARKER

A thesis submitted to
The University of Birmingham
for the degree of
DOCTOR OF PHILOSOPHY

Volume Two: Figures, Tables and Appendices

Division of Environmental Health and Risk Management
School of Geography, Earth and Environmental Sciences
The University of Birmingham
February 2004

FIGURES

Figure 1.1

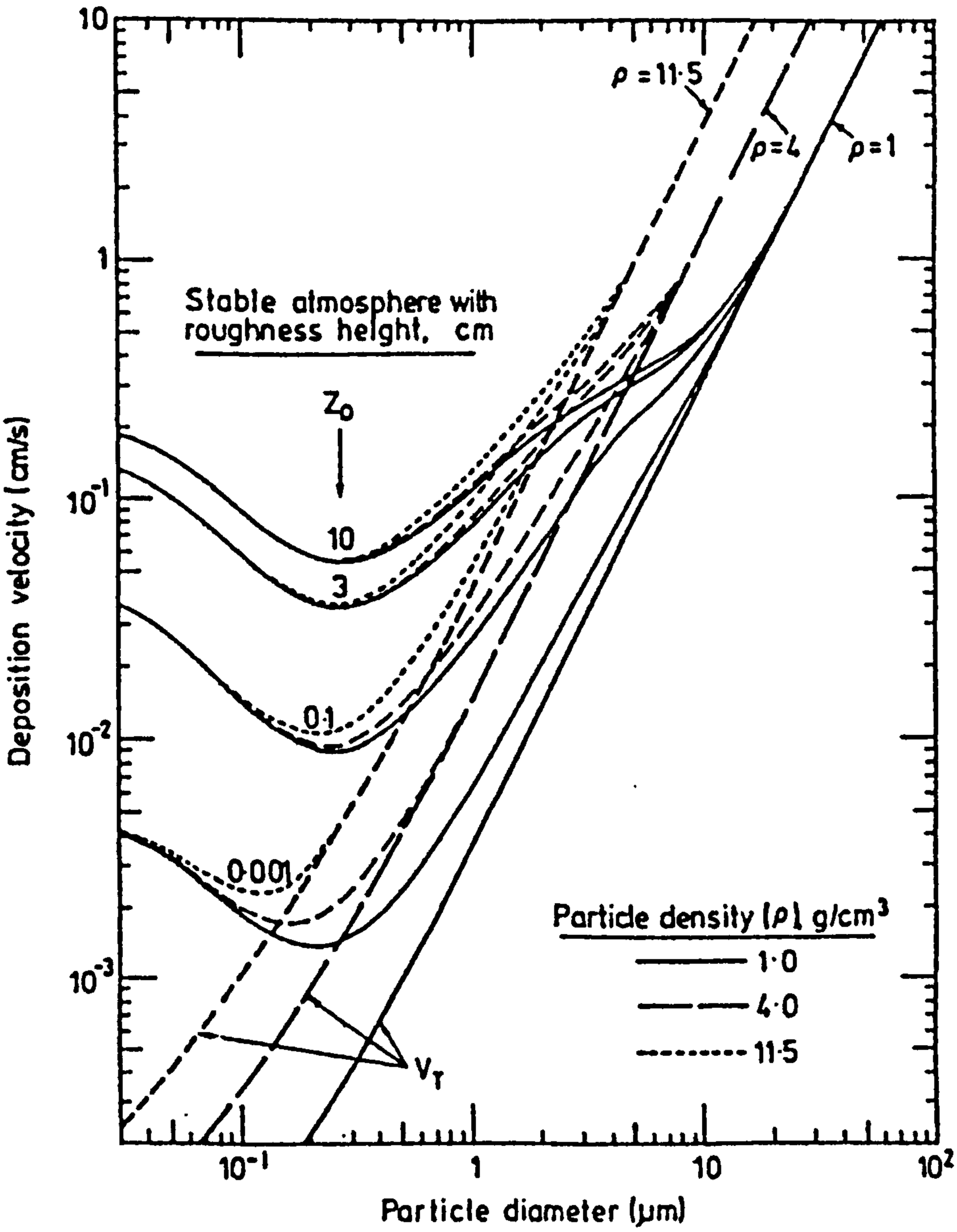

Particle deposition velocities for a range of diameters, densities and roughness heights, reproduced from Nicholson (1988), after Sehmel (1980). Illustrating the wide range of values and sensitivity to particle diameter. Data are extrapolated from wind tunnel measurements.

Figure 2.1

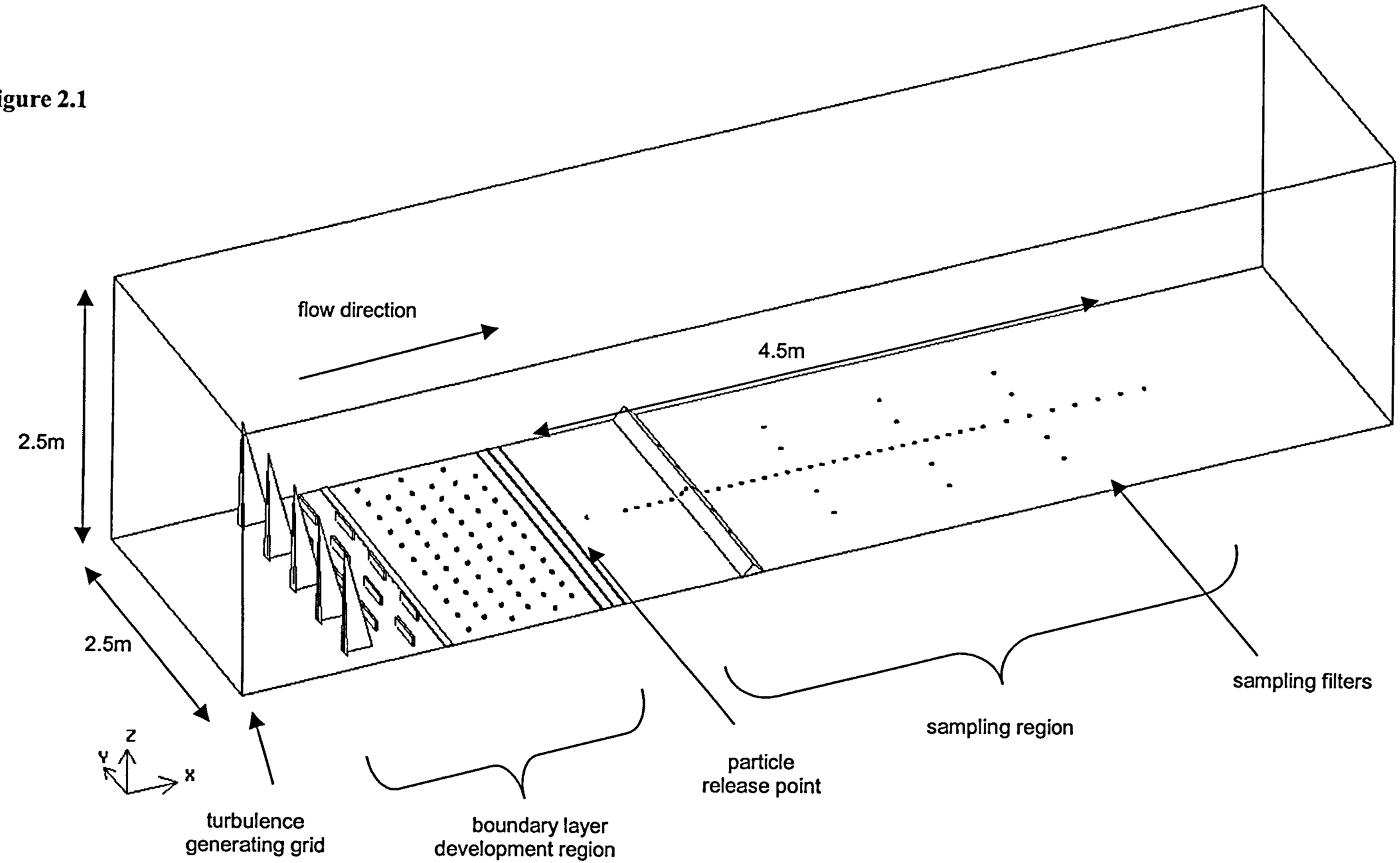

Diagram of experimental wind tunnel arrangement, shown with ridge of 1 in 1 slope installed.

Figure 2.2

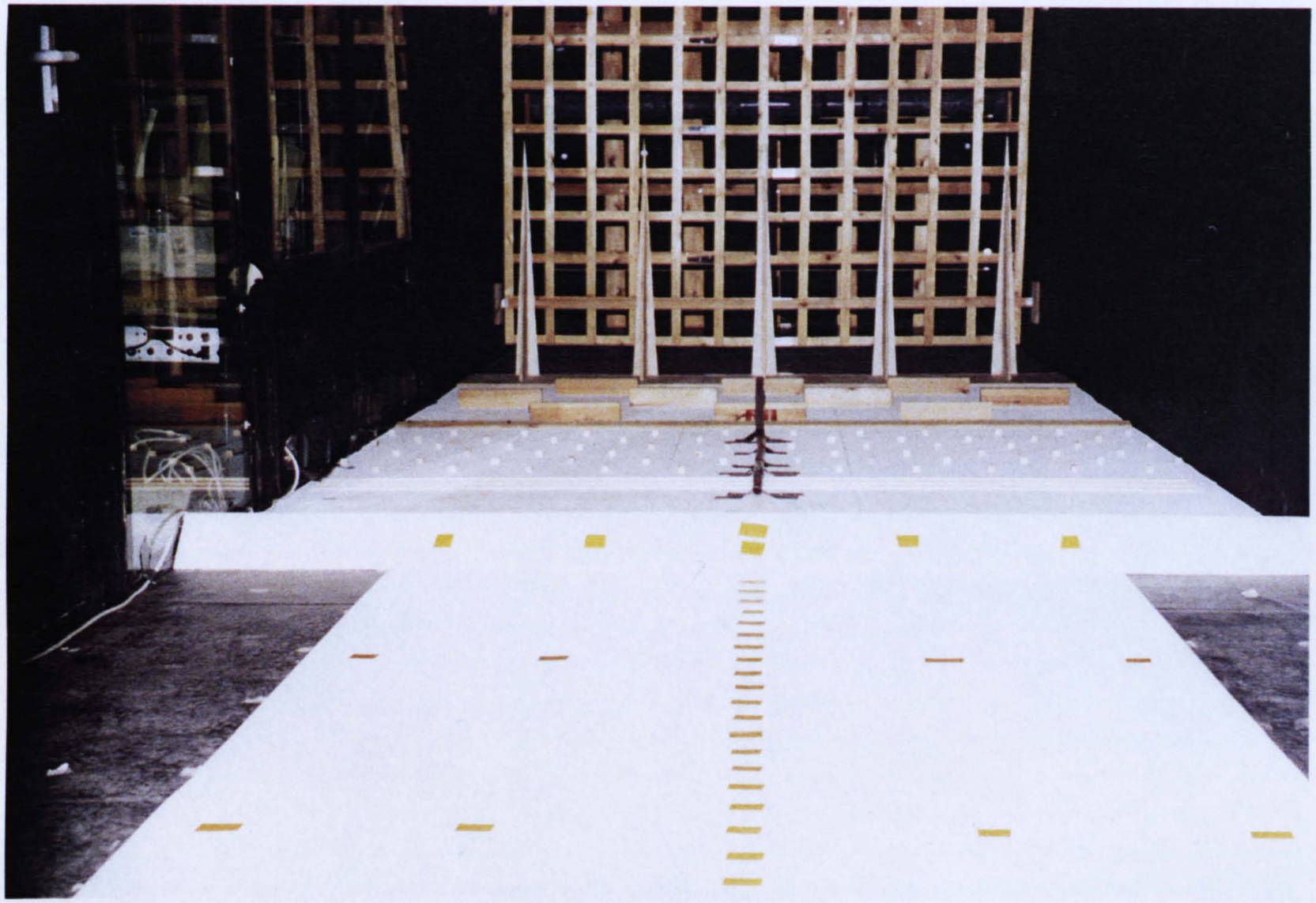

Photograph of experimental wind tunnel arrangement, shown with ridge of 1 in 1 slope installed. L:ooking upwind towards the boundary-layer generation region.

Figure 2.3

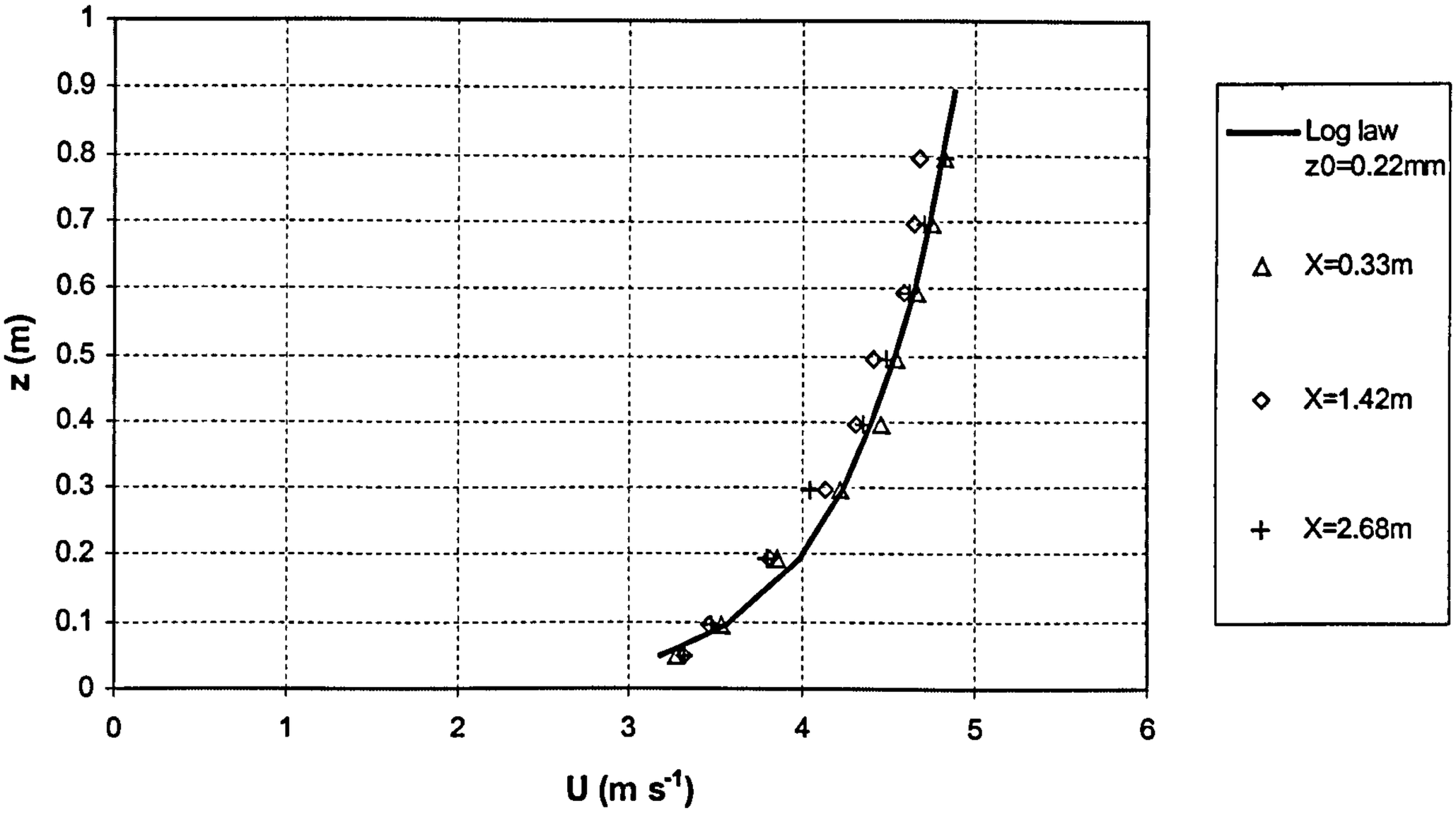

Vertical (Z) profile of experimental streamwise velocity at 3 different positions, and log-law velocity. X is distance downstream from particle release point. All measurements along centreline of wind tunnel (Y=0m).

Figure 2.4

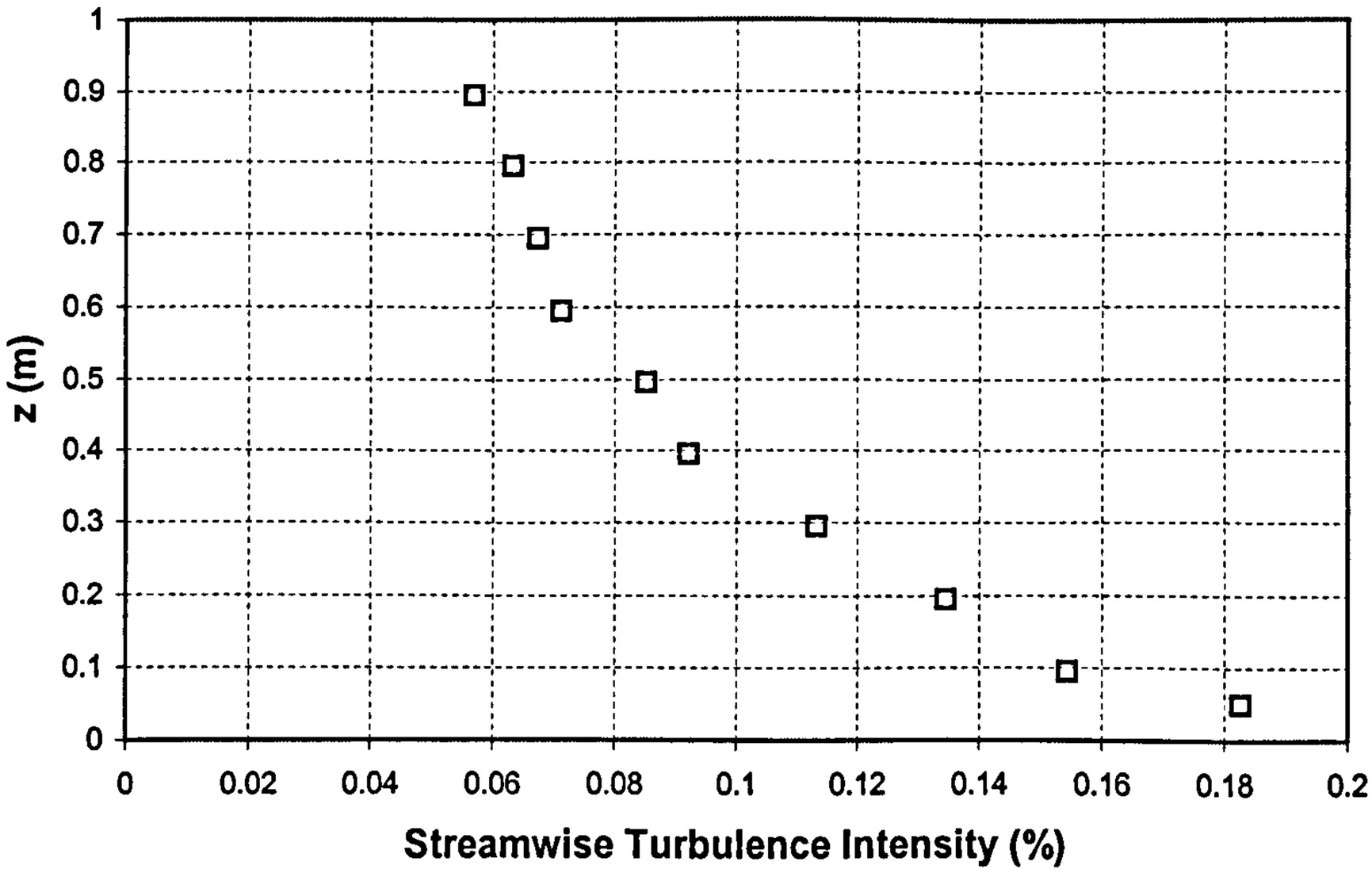

Streamwise turbulence intensity. Vertical profile, measured at distance 0.33m downstream from particle release point, wind tunnel centreline (Y=0m).

Figure 2.5

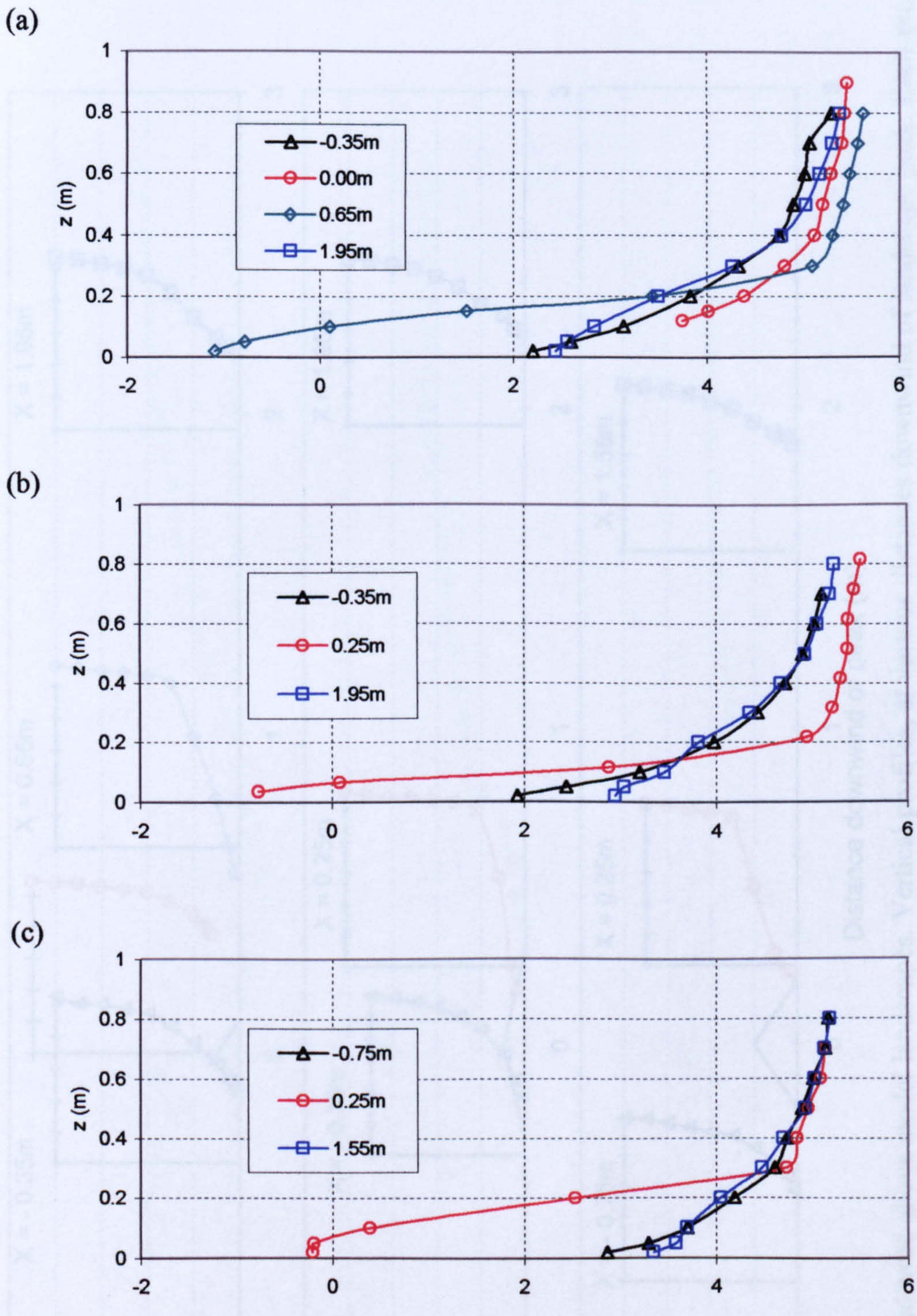

Streamwise velocity measured above model landscapes. Vertical profiles, at various distances downwind of landscape peak. Each profile measured along wind tunnel centreline (Y=0m). Note, Z is height above flat plane, not hill surface. Negative distances indicate location upwind of peak. (a) 1 in 1 ridge, (b) 1 in 3 ridge and (c) 1 in 1 cone.

Figure 2.6

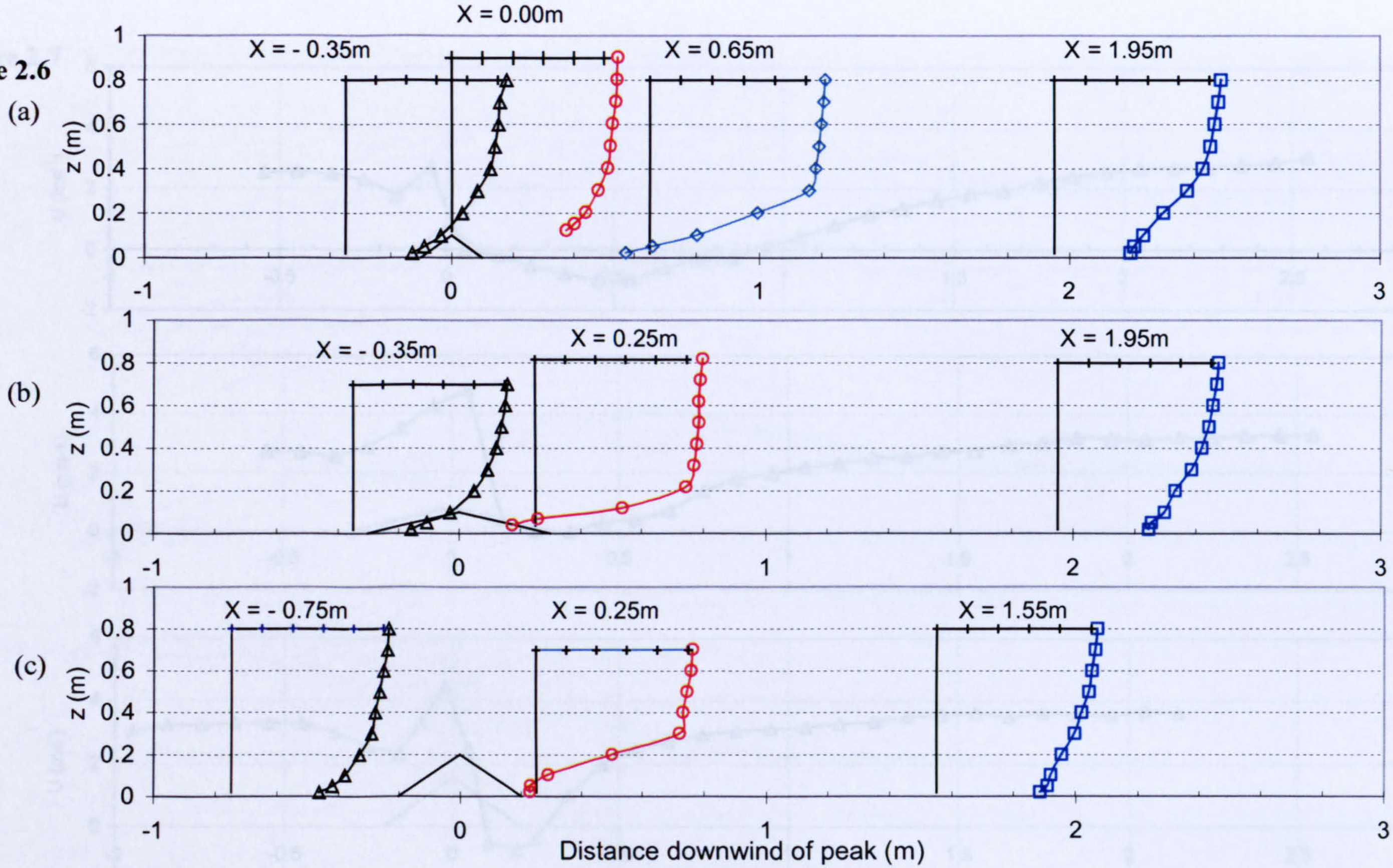

Streamwise velocity measured above model landscapes. Vertical profiles, at various distances downwind of landscape peak. Each profile measured along wind tunnel centreline (Y=0m). Normalised to freestream velocity and indicating landscape cross sections (a) 1 in 1 ridge, (b) 1 in 3 ridge and (c) 1 in 1 cone.

Figure 2.7

(a)

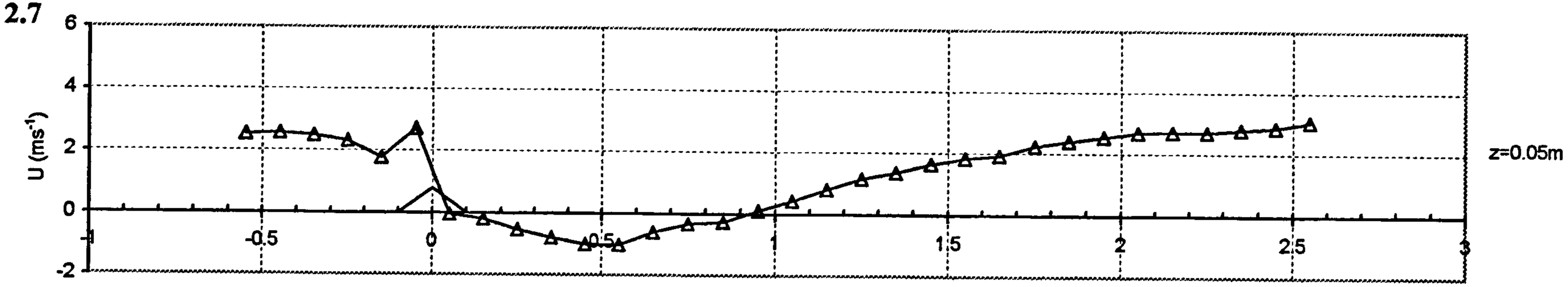

(b)

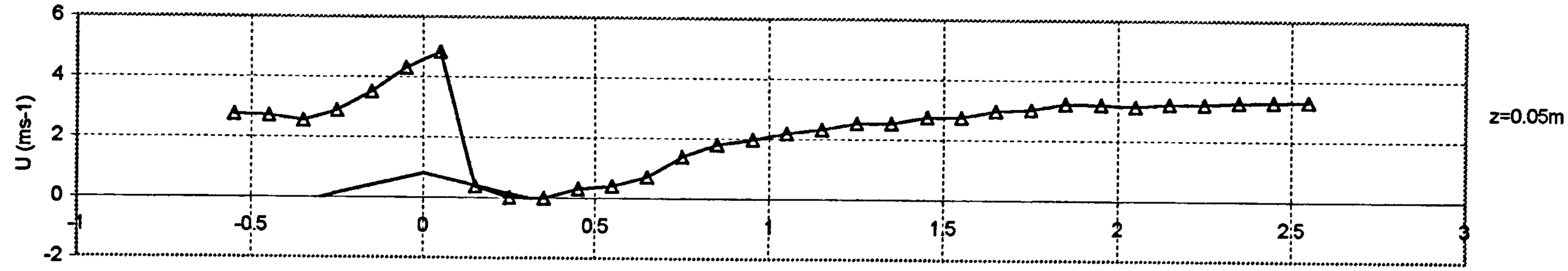

(c)

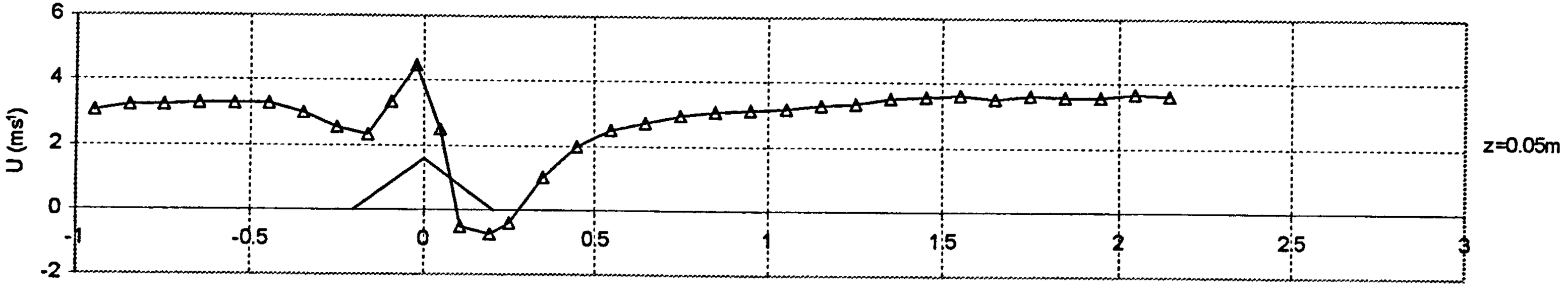

Streamwise velocity measured above model landscapes. Longitudinal profiles, measured at 0.05m above the surface along wind tunnel centreline (Y=0m), plotted against distance downwind from landscape peak (a) 1 in 1 ridge, (b) 1 in 3 ridge and (c) 1 in 1 cone.

Figure 2.8

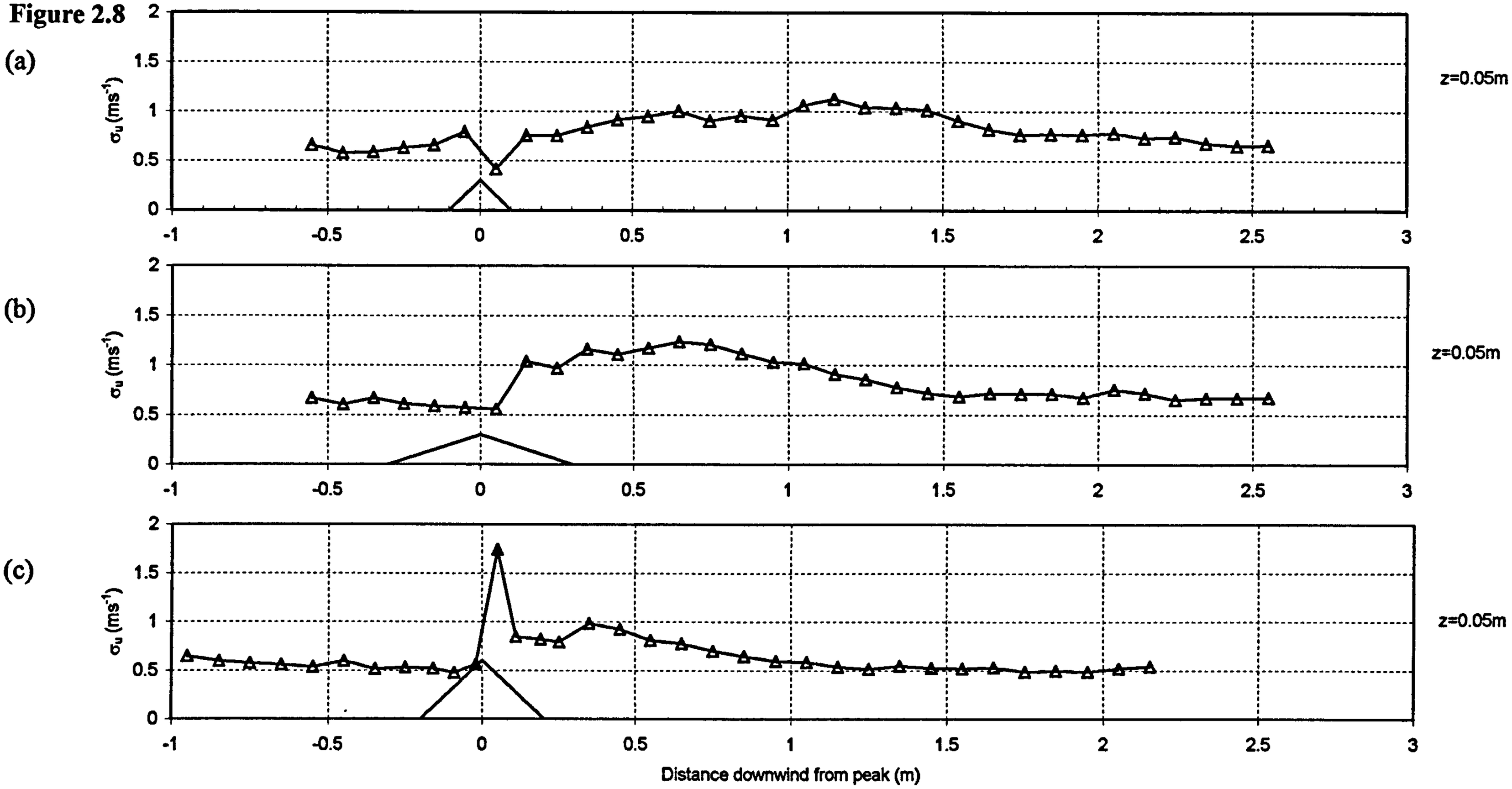

Streamwise turbulent velocity measured above model landscapes. Longitudinal profiles, measured at 0.05m above the surface along wind tunnel centreline (Y=0m), plotted against distance downwind from landscape peak (a) 1 in 1 ridge, (b) 1 in 3 ridge and (c) 1 in 1 cone

Figure 2.9

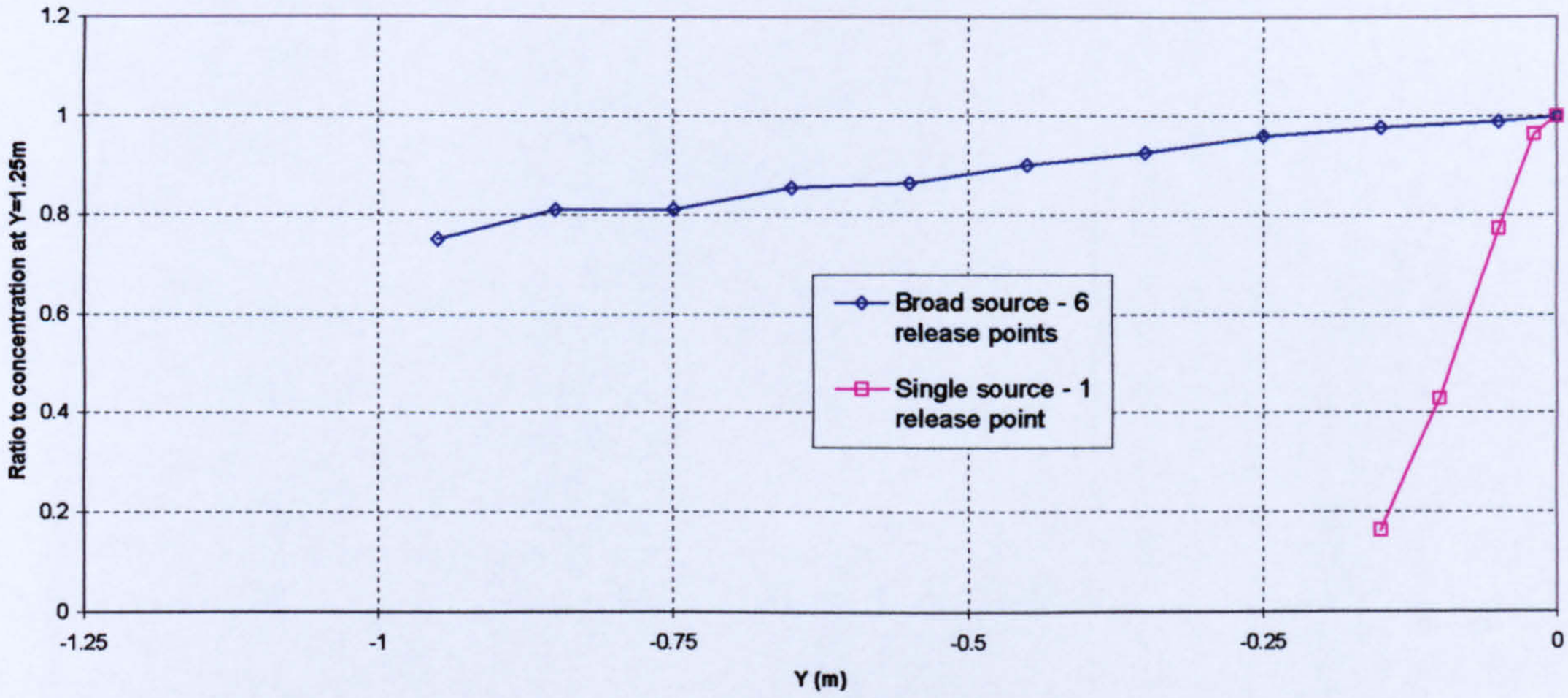

Lateral profile of particle concentration for point source and broad source. Size range 0.75-2.0μm. Measured at distance 0.05m downwind of roughness elements.

Figure 2.10

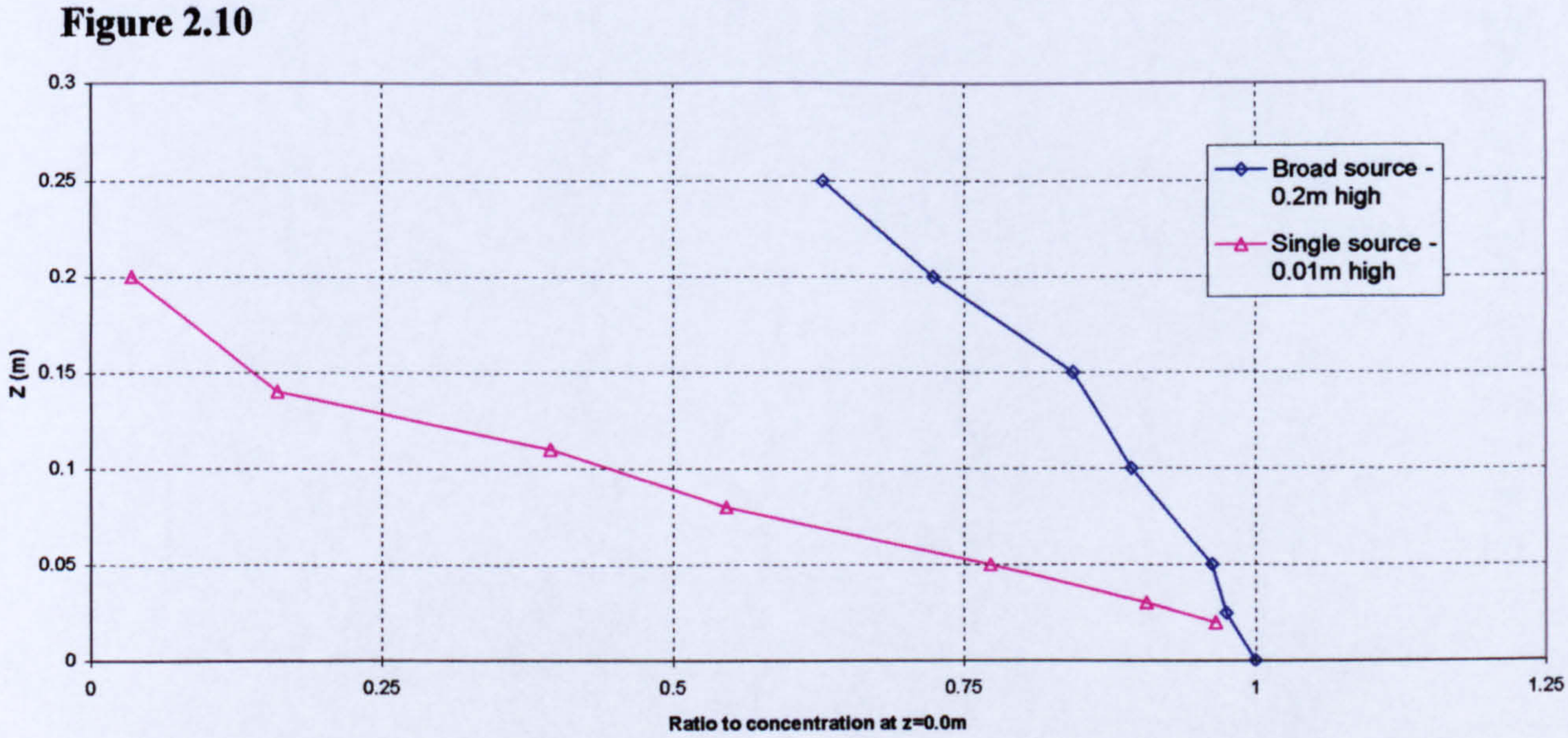

Vertical profile of particle concentration for point source and broad source. Size range 0.75-2.0μm. Measured at distance 0.05m downwind of roughness elements.

Figure 2.11

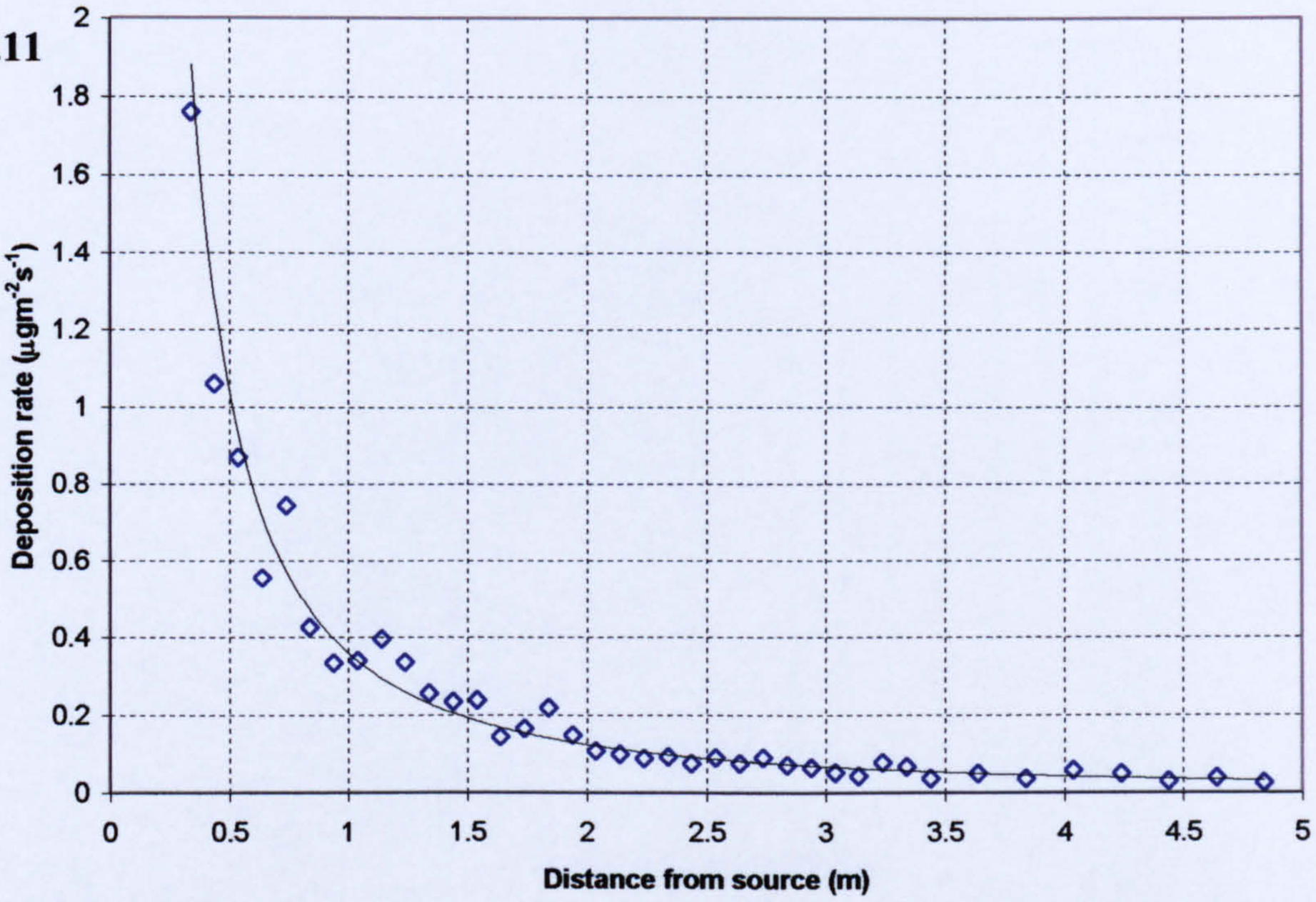

Particle deposition rate with downwind distance for flat case. Measured on wind tunnel centreline (Y=0m). Distance is from particle source. Averaged over 30 minute period. Fitted line is curve: $Y = 0.3593\ X^{-1.5352}$.

Figure 2.12

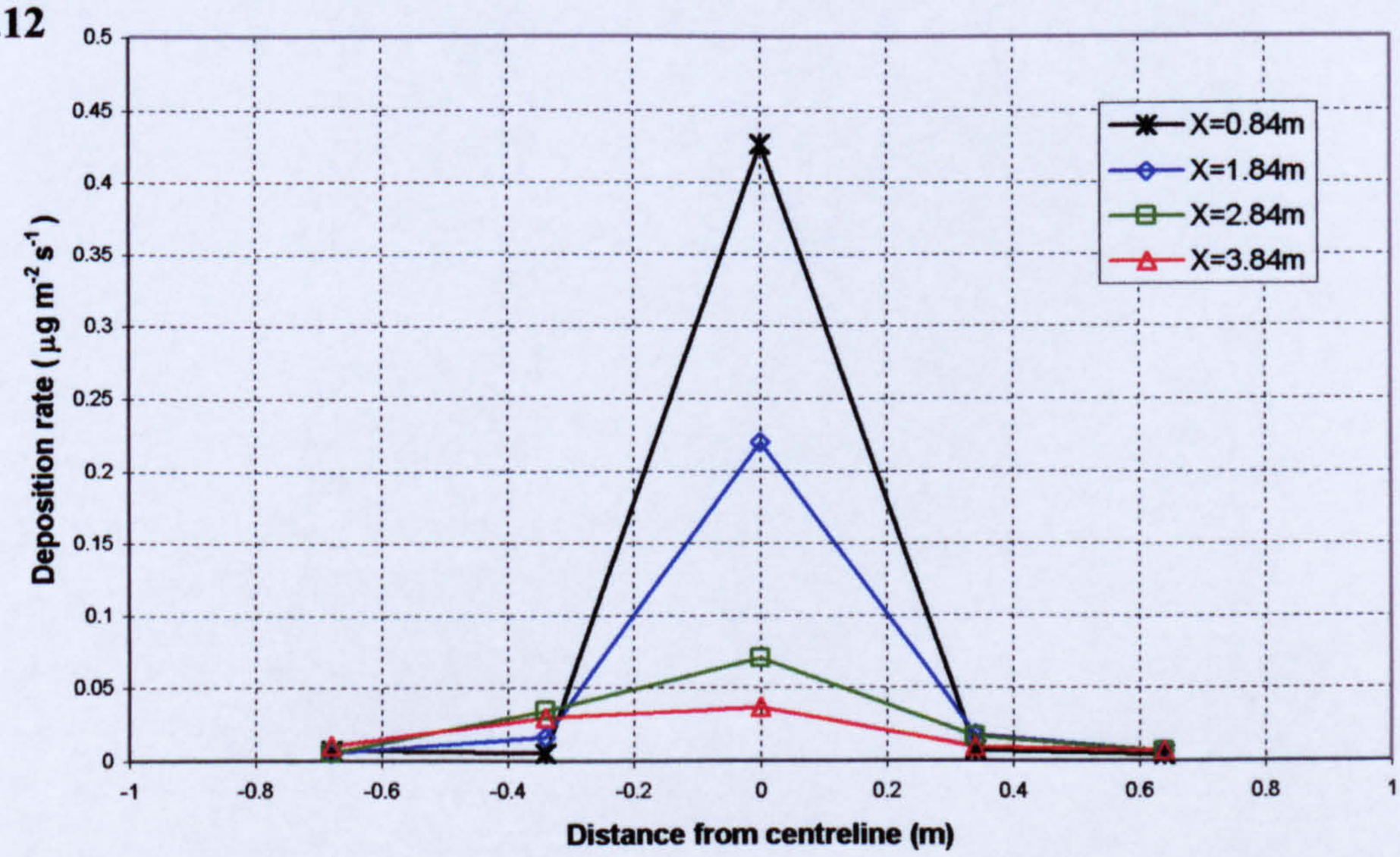

Lateral variation in particle deposition rate at 4 downwind distances. Distance is from wind tunnel centreline (Y=0m) and downwind distance is from particle source. Averaged over 30 minute period.

Figure 2.13

(a)

(b)

(c)

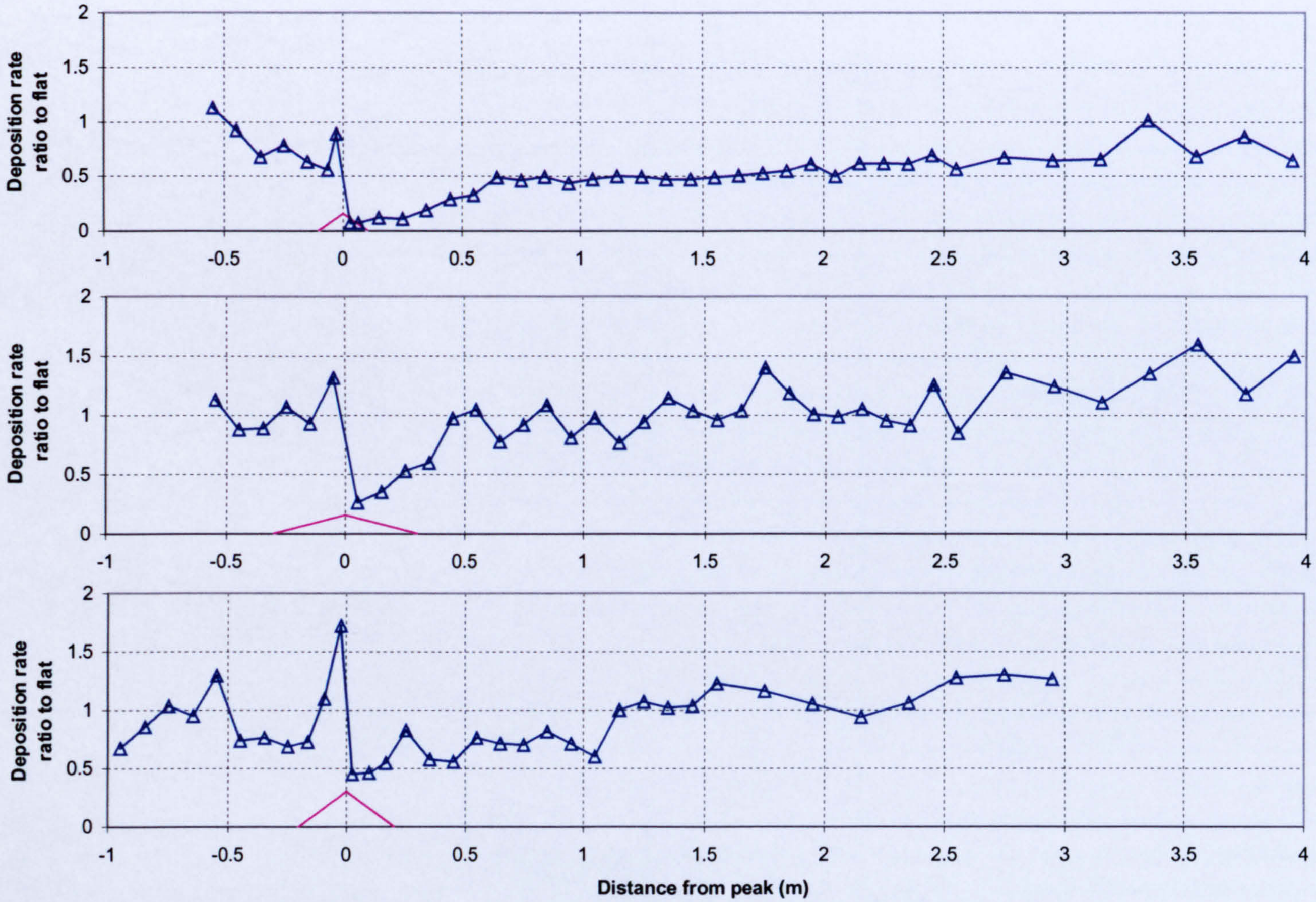

Ratio of deposition rate for three landscape models to the flat case. Distance is distance downwind of landscape peak. All data measured along centreline of wind tunnel (Y=0m), (a) 1 in 1 ridge, (b) 1 in 3 ridge and (c) 1 in 1 cone.

Figure 2.14

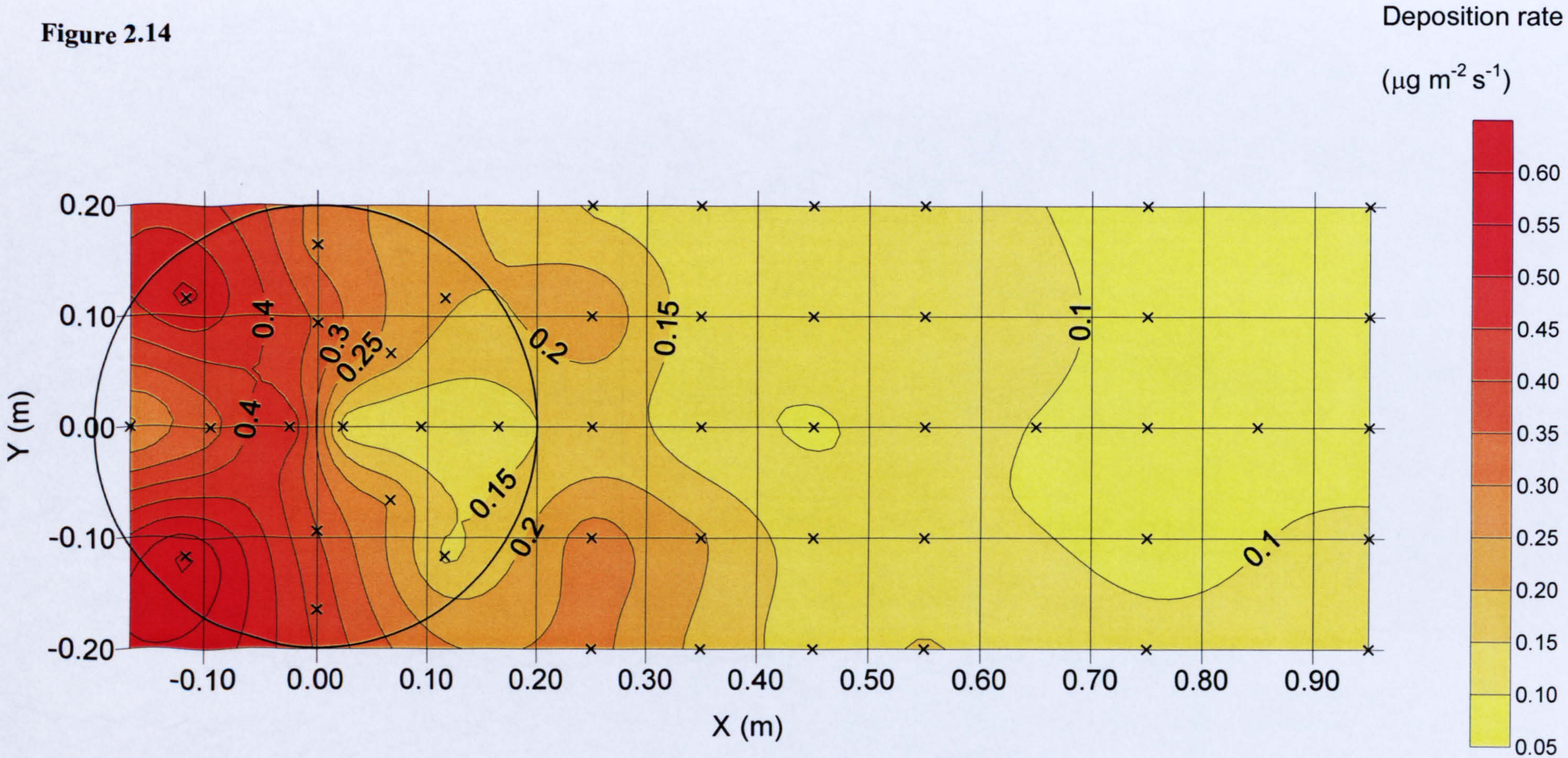

Particle deposition rate to 1 in 1 cone and wake. Crosses mark the sampling locations, coloured contours are interpolated from the values at these points, using a Kriging algorithm. X is downwind distance from peak of cone and Y is lateral distance from centreline. Circle marks the base of the cone.

Figure 2.15

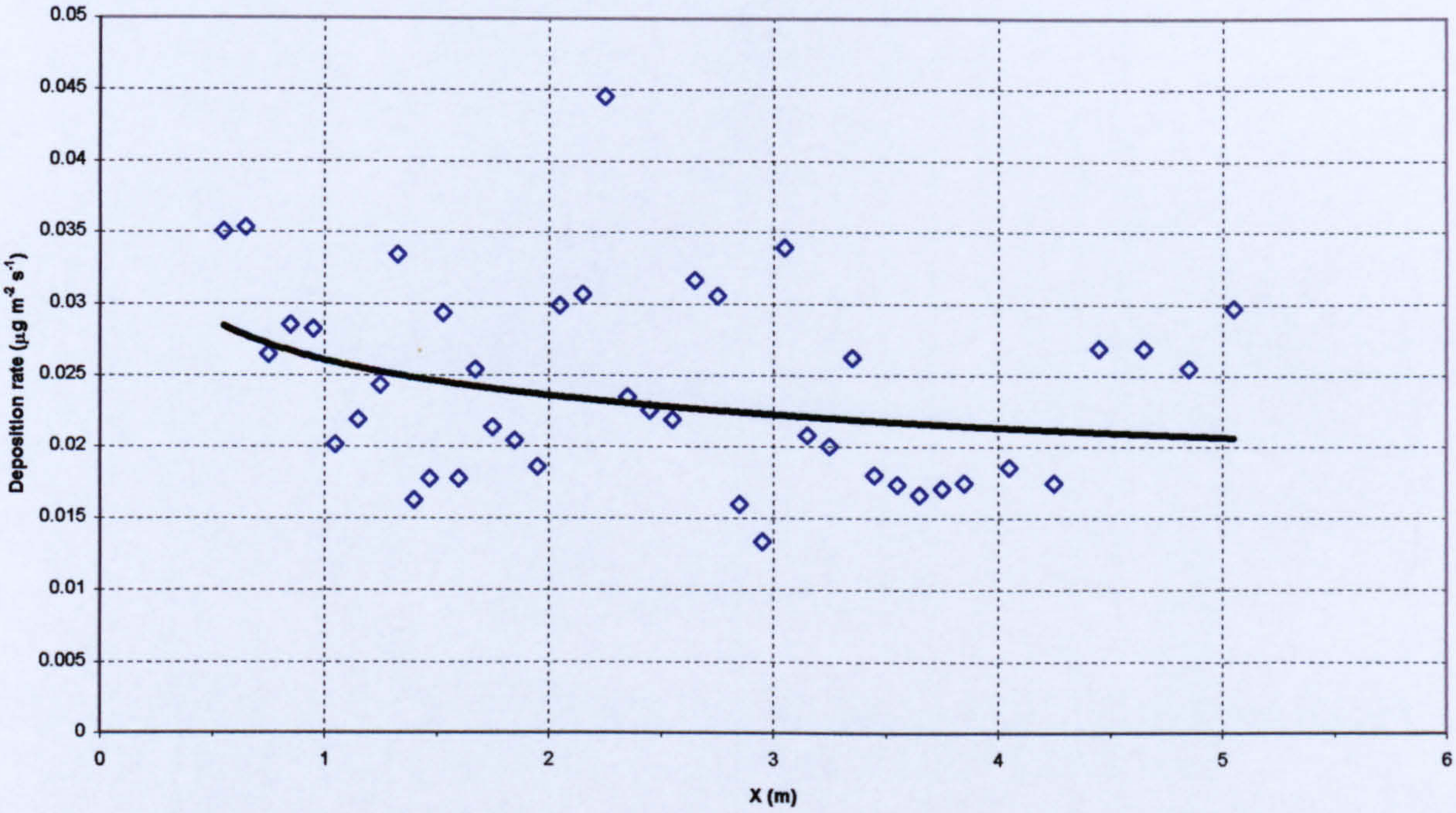

Particle deposition rate for broader source, flat case. Measured along wind tunnel centreline (Y=0m). Fitted line is a power curve, with equation $Y = 0.0261\ X^{-0.145}$. X is distance downwind from end of roughness elements.

Figure 2.16

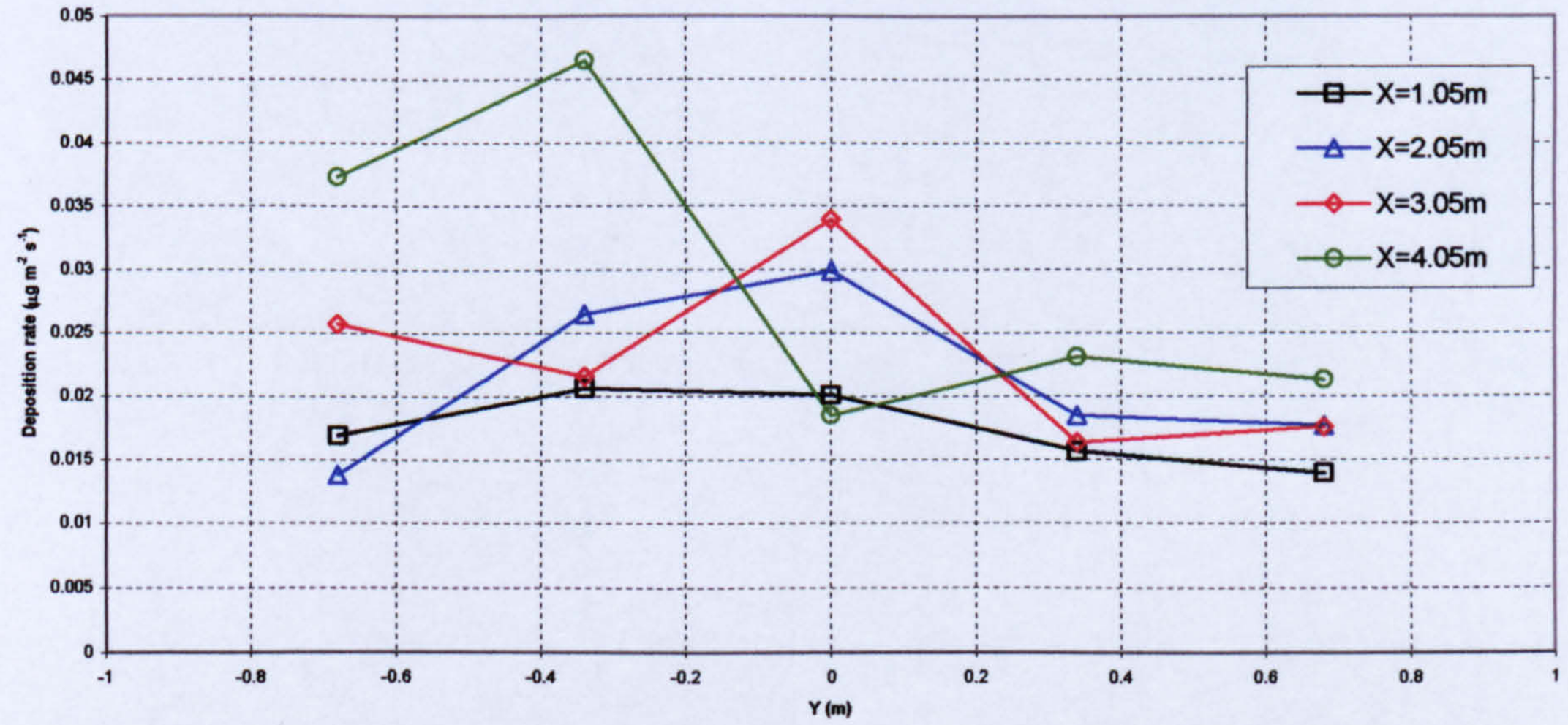

Lateral variation in particle deposition rate at 4 downwind distances. Distance is from wind tunnel centreline and downwind distance is from end of roughness elements. Averaged over a 90 minute period.

Figure 2.17

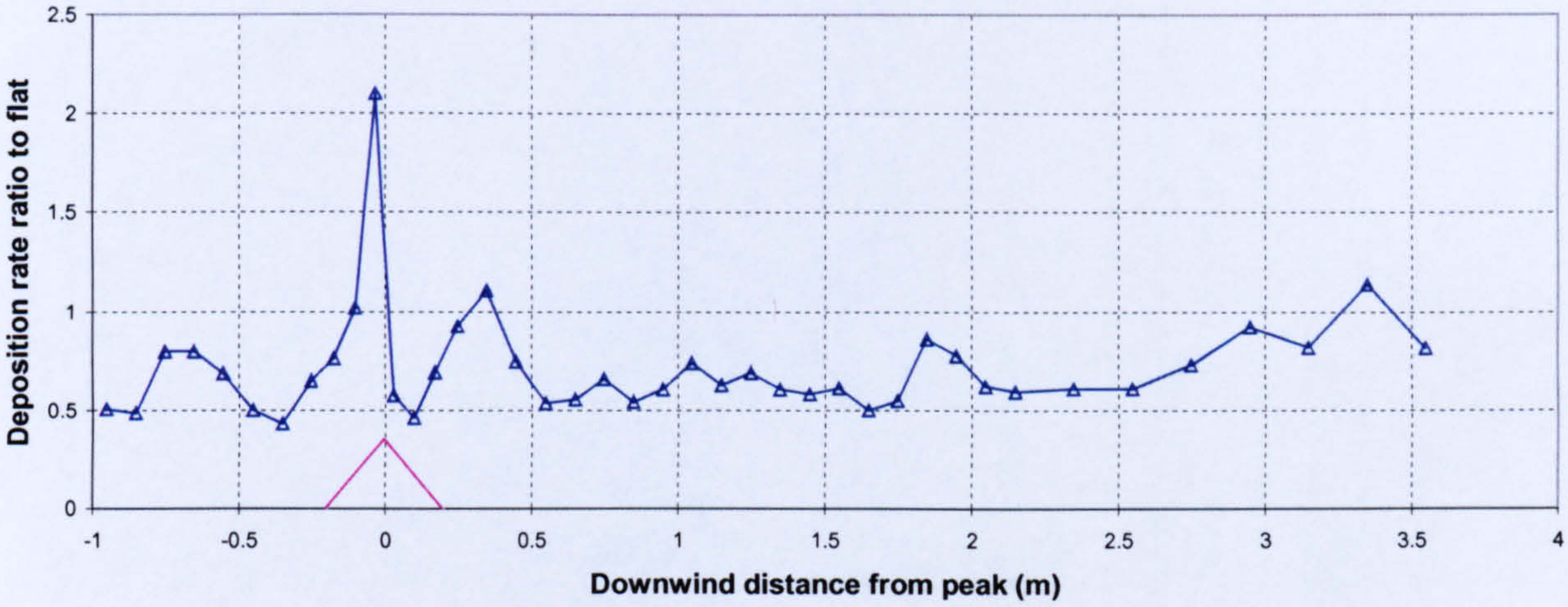

Particle deposition ratio of cone to flat case for a broad particle source. Distance is distance downwind of cone peak. All data is along centreline of wind tunnel (Y=0m).

Figure 2.18

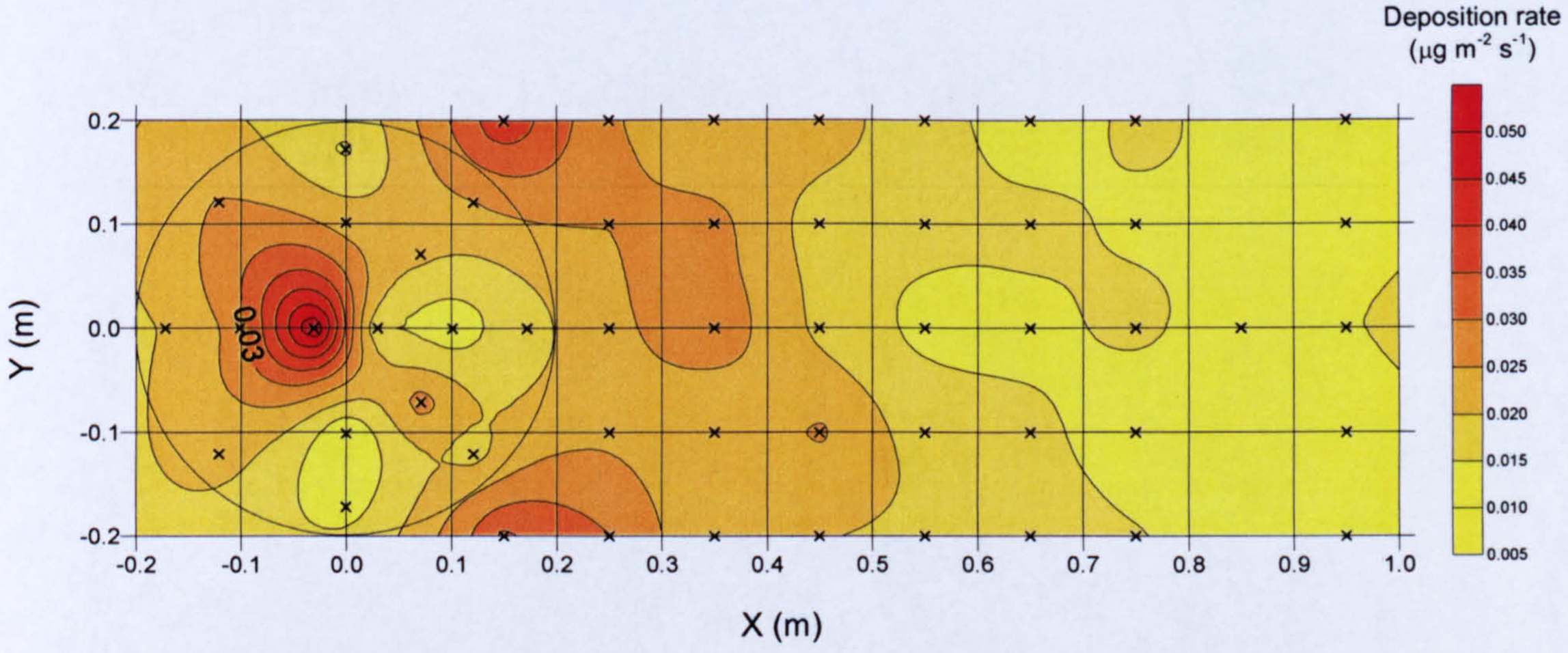

Particle deposition rate for the 1 in 1 cone case with a broad particle source, for the area over the cone and in the immediate wake. Crosses mark the sampling locations, coloured contours are interpolated from the values at these points. X is downwind distance from peak of cone and Y is lateral distance from centreline. Circle marks the base of the cone.

Figure 2.19

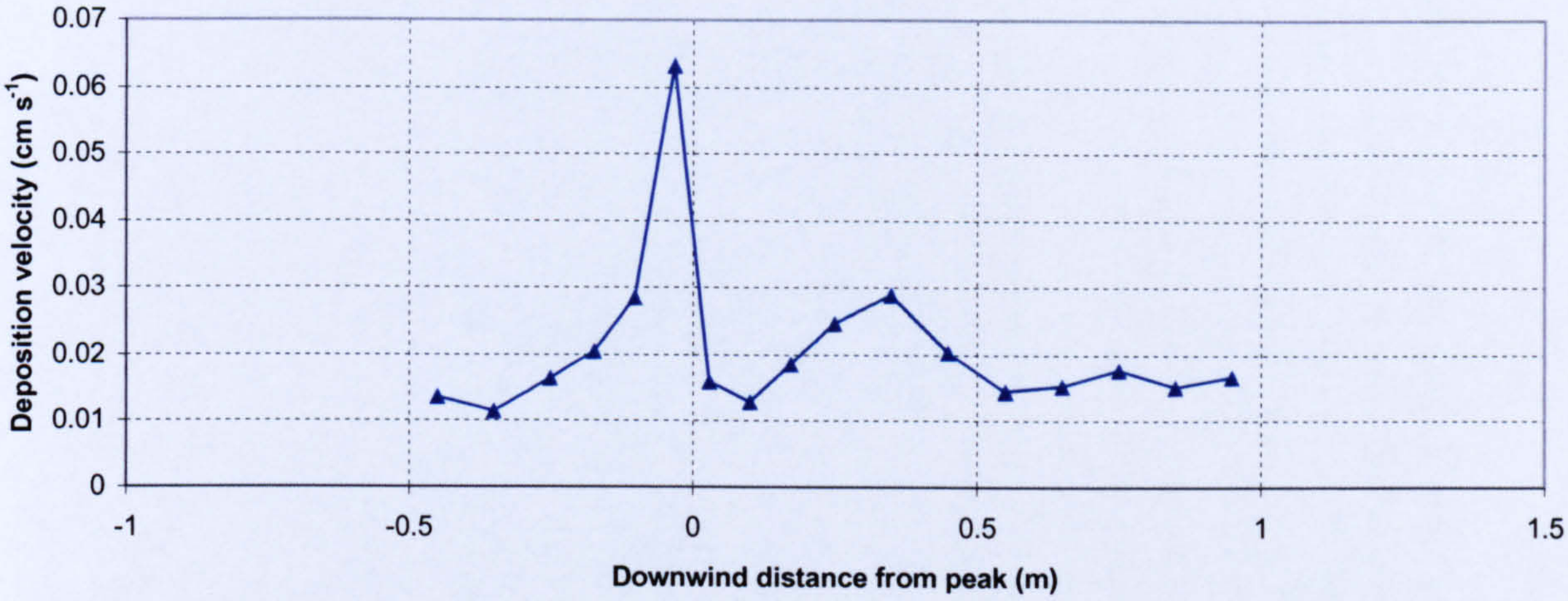

Longitudinal profile of deposition velocity measured for cone and broad source. Measured along centreline of wind tunnel (Y=0m). Downwind distance is from peak of cone.

Figure 2.20

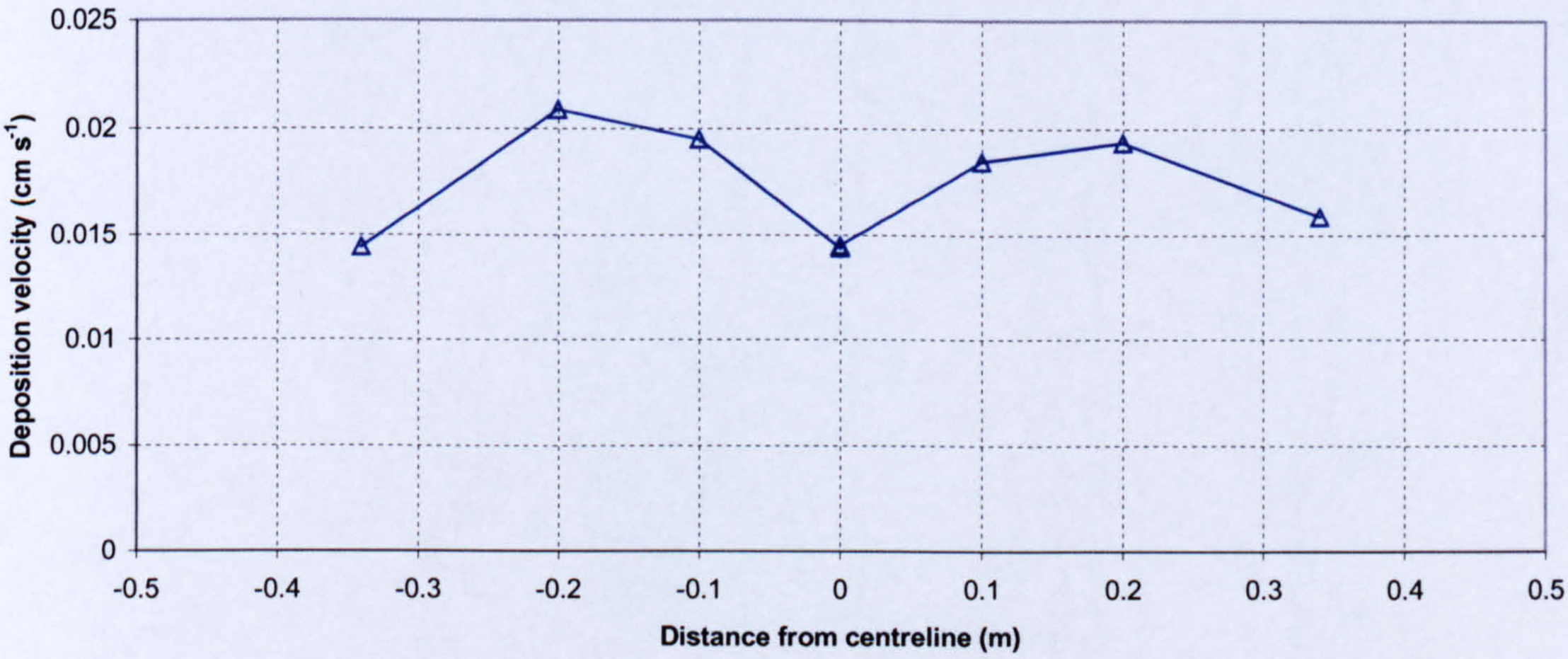

Lateral profile of deposition velocity measured for cone and broad source. Measured at distance 0.55m downwind from peak of cone. Distance plotted is distance from centreline of wind tunnel (Y=0m).

Figure 3.1

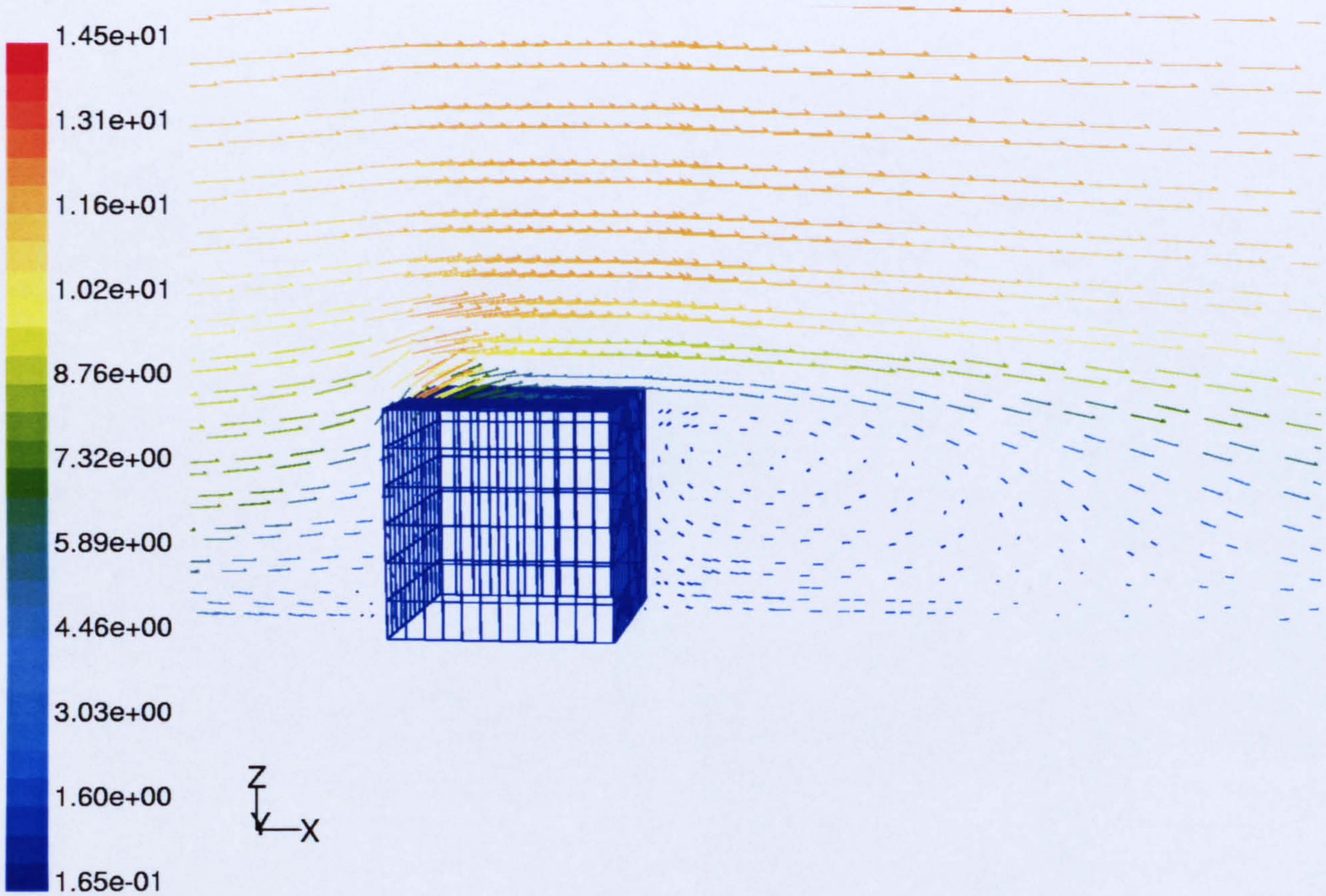

Velocity vectors in vertical plane normal to the ground, parallel to the mean wind direction and passing through the centre of the cube.

Figure 3.2

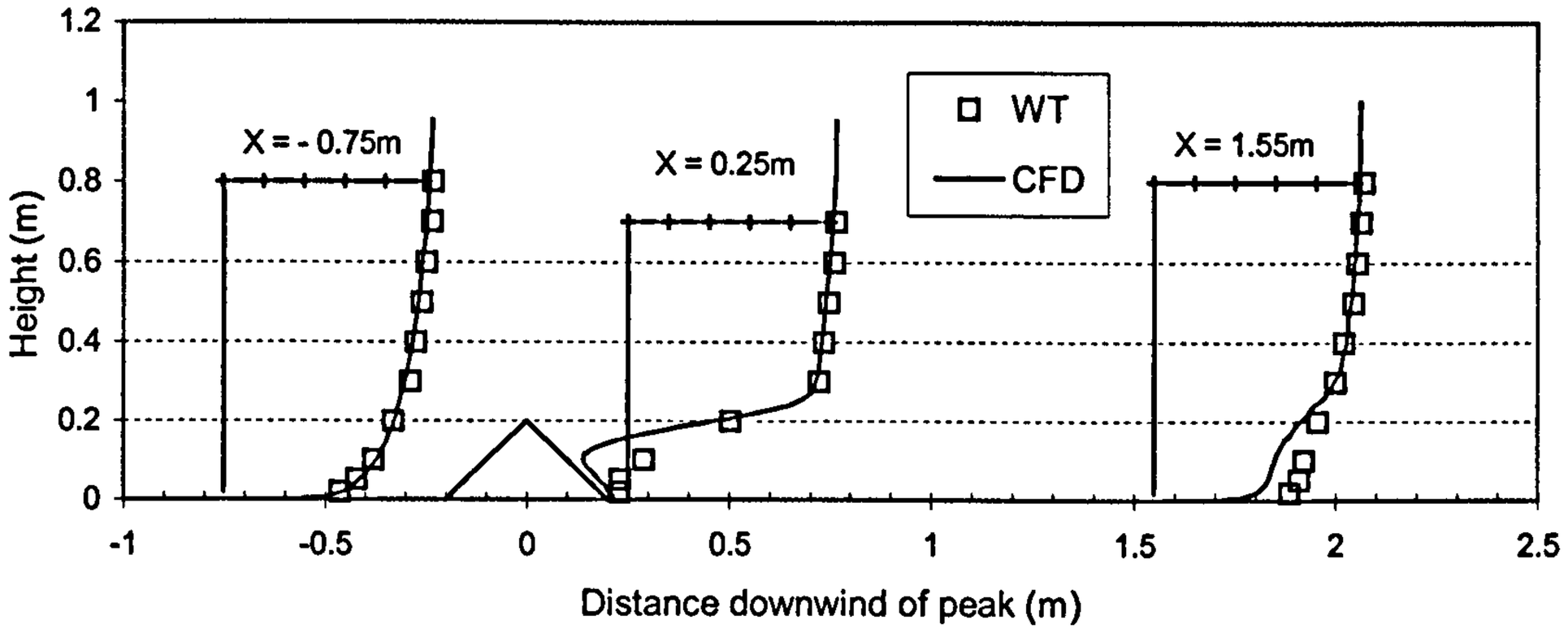

Comparison of experimental (wind tunnel) and CFD vertical profiles of streamwise velocity for 1 in 1 cone. Measured at three downwind locations above wind tunnel centreline (Y=0m).

Figure 3.3

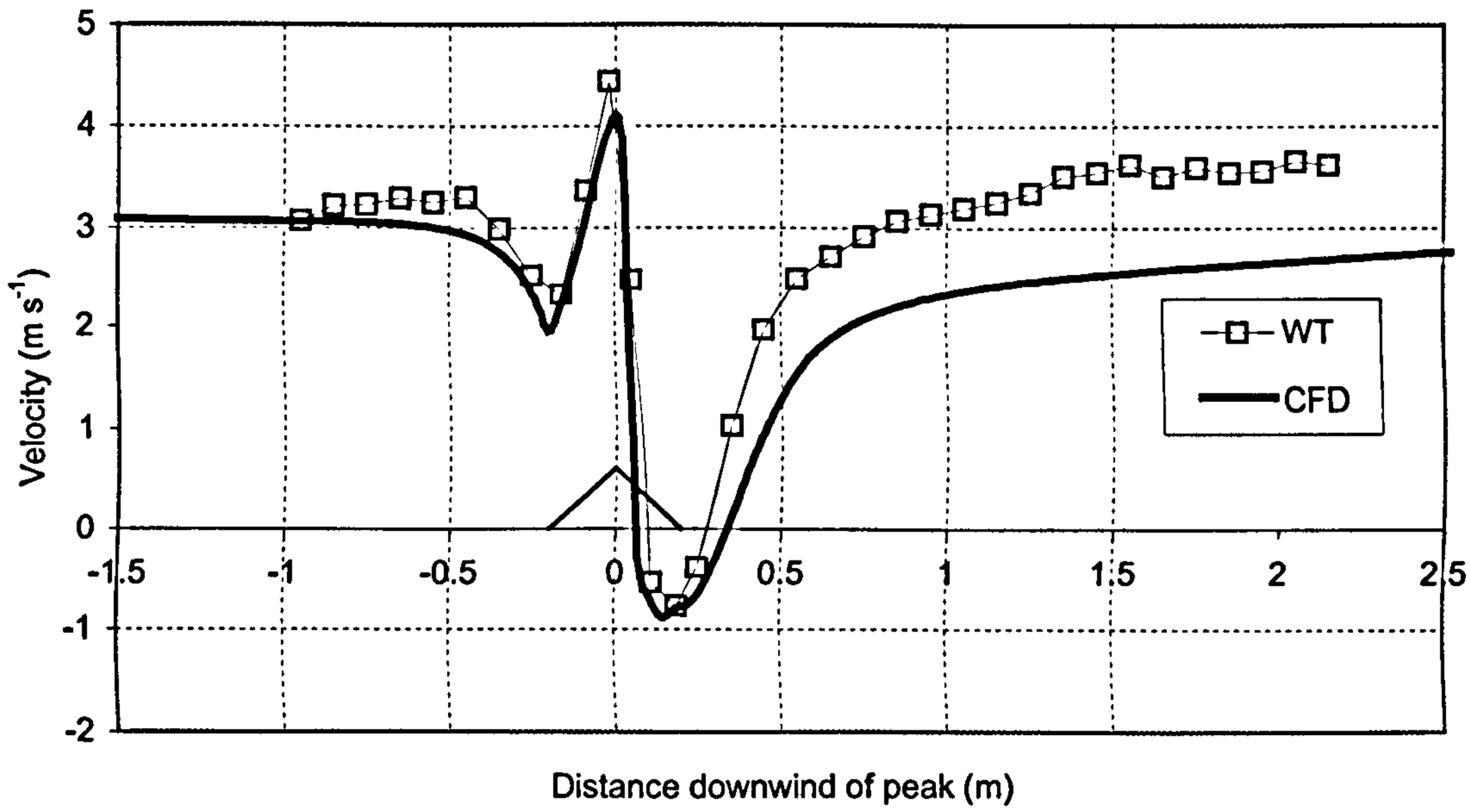

Comparison of longitudinal profile of streamwise velocity for CFD and wind tunnel, for cone of slope 1 in 1. Measured at a height z = 0.05m, model scale above the surface, along wind tunnel centreline (Y=0m).

Figure 3.4

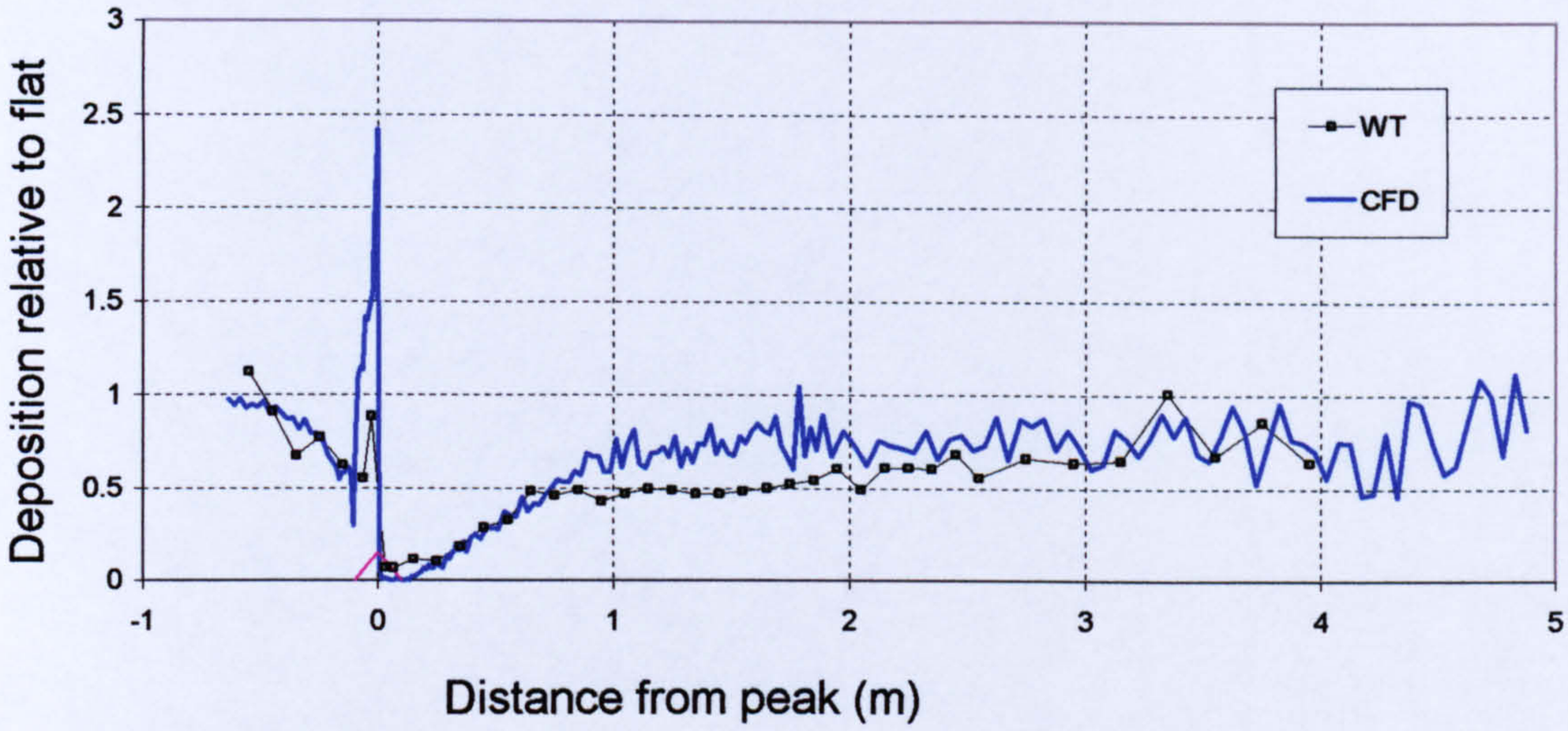

Comparison of relative deposition rate to 1 in 1 sloped ridge for wind tunnel and CFD, plotted along wind tunnel centreline (Y=0m).

Figure 3.5

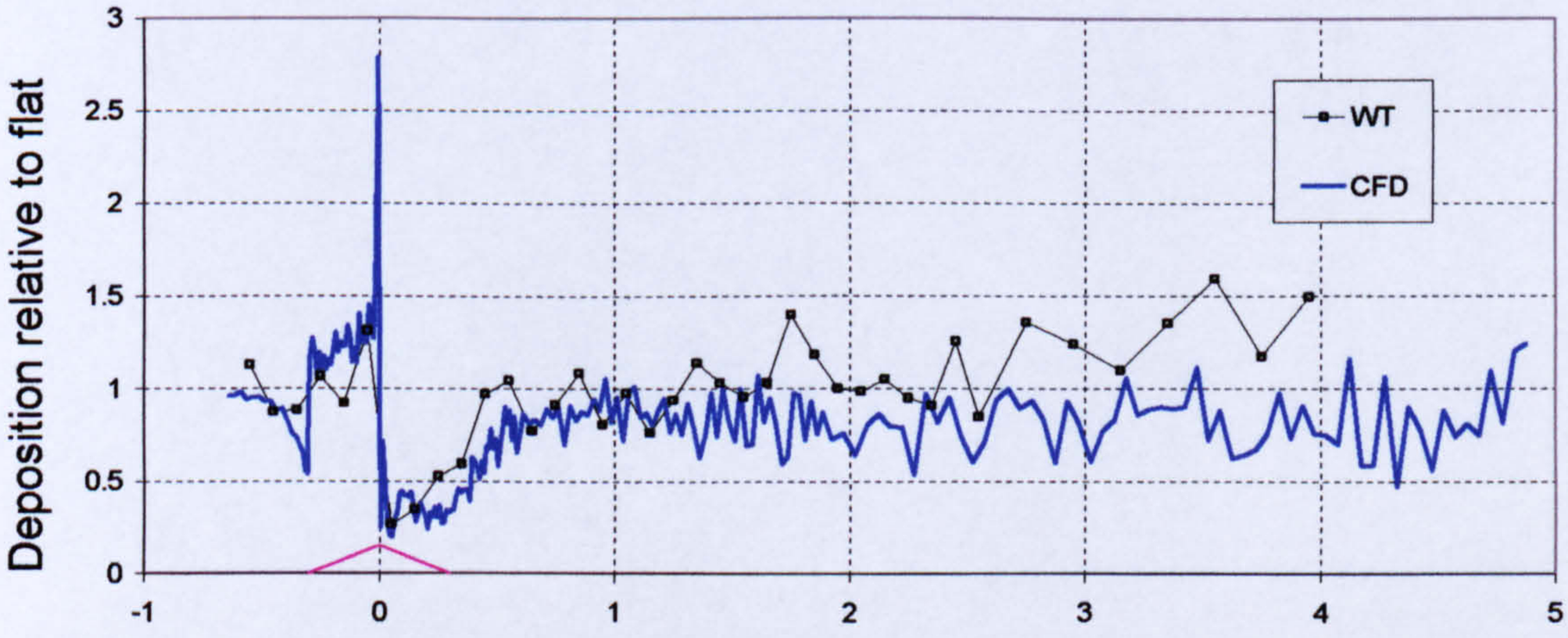

Comparison of relative deposition rate to 1 in 3 sloped ridge for wind tunnel and CFD, plotted along wind tunnel centreline (Y=0m).

Figure 3.6

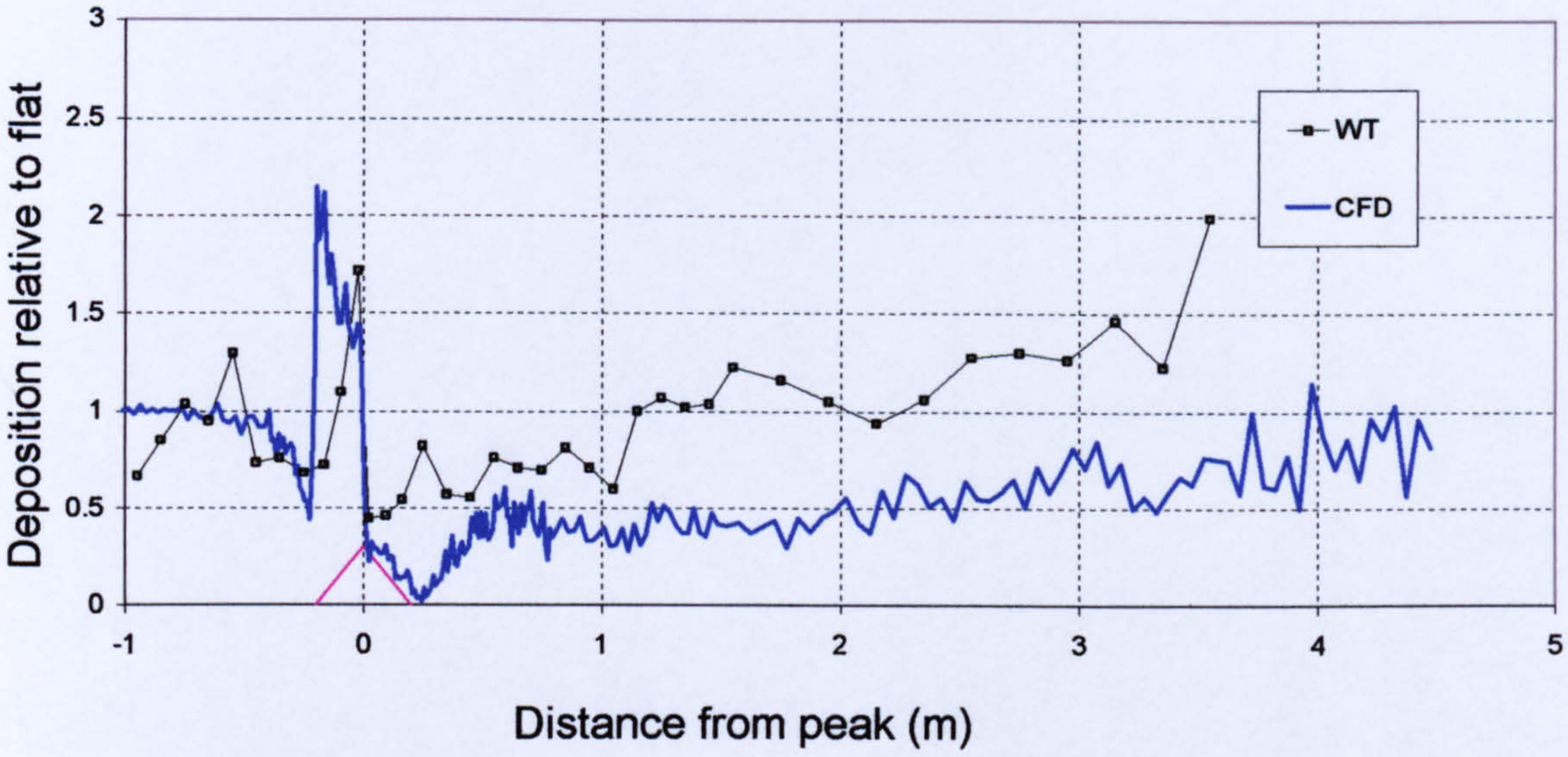

Comparison of relative deposition rate to 1 in 1 sloped cone for wind tunnel and CFD, point source. Plotted along wind tunnel centreline (Y=0m).

Figure 3.7

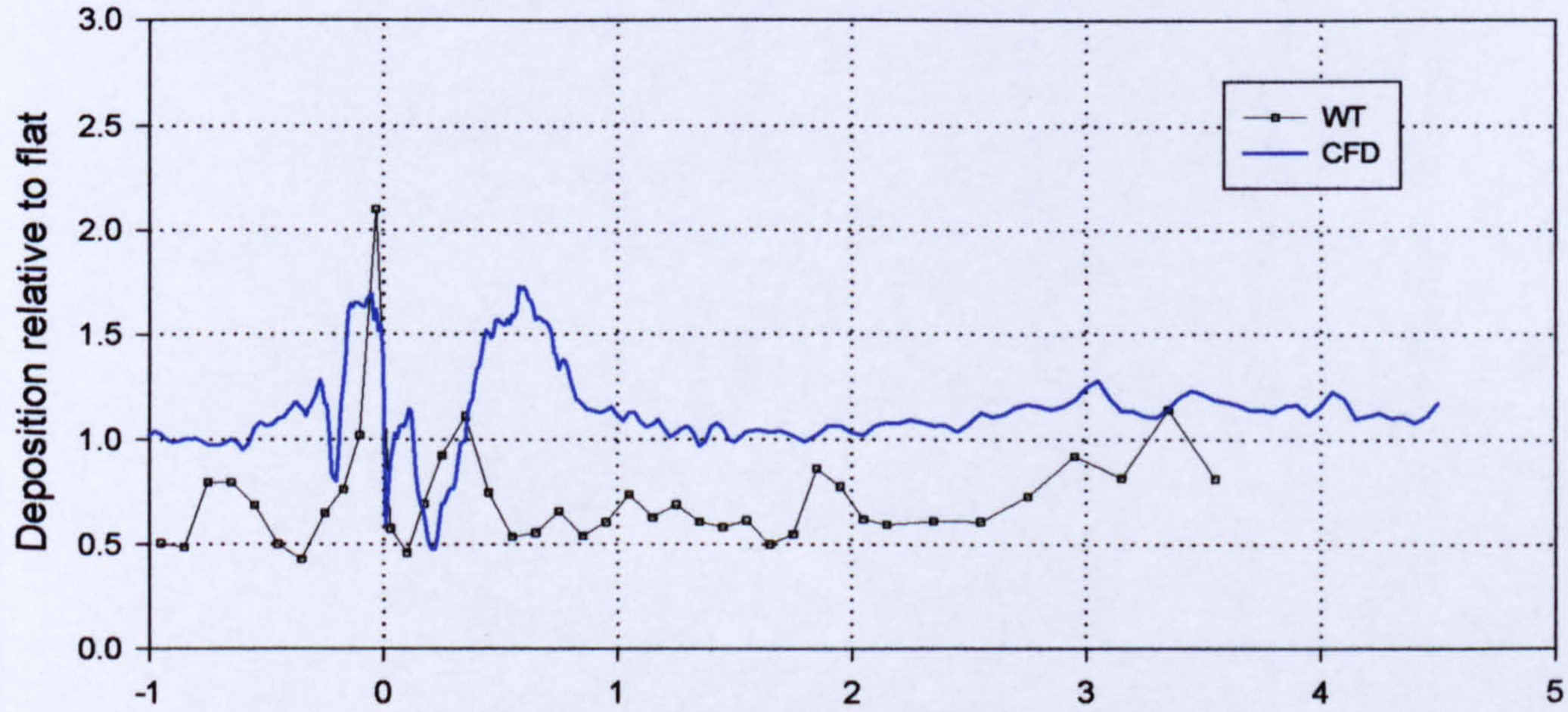

Comparison of relative deposition rate to 1 in 1 sloped cone for wind tunnel and CFD, broad source. Plotted along wind tunnel centreline (Y=0m).

Figure 3.8

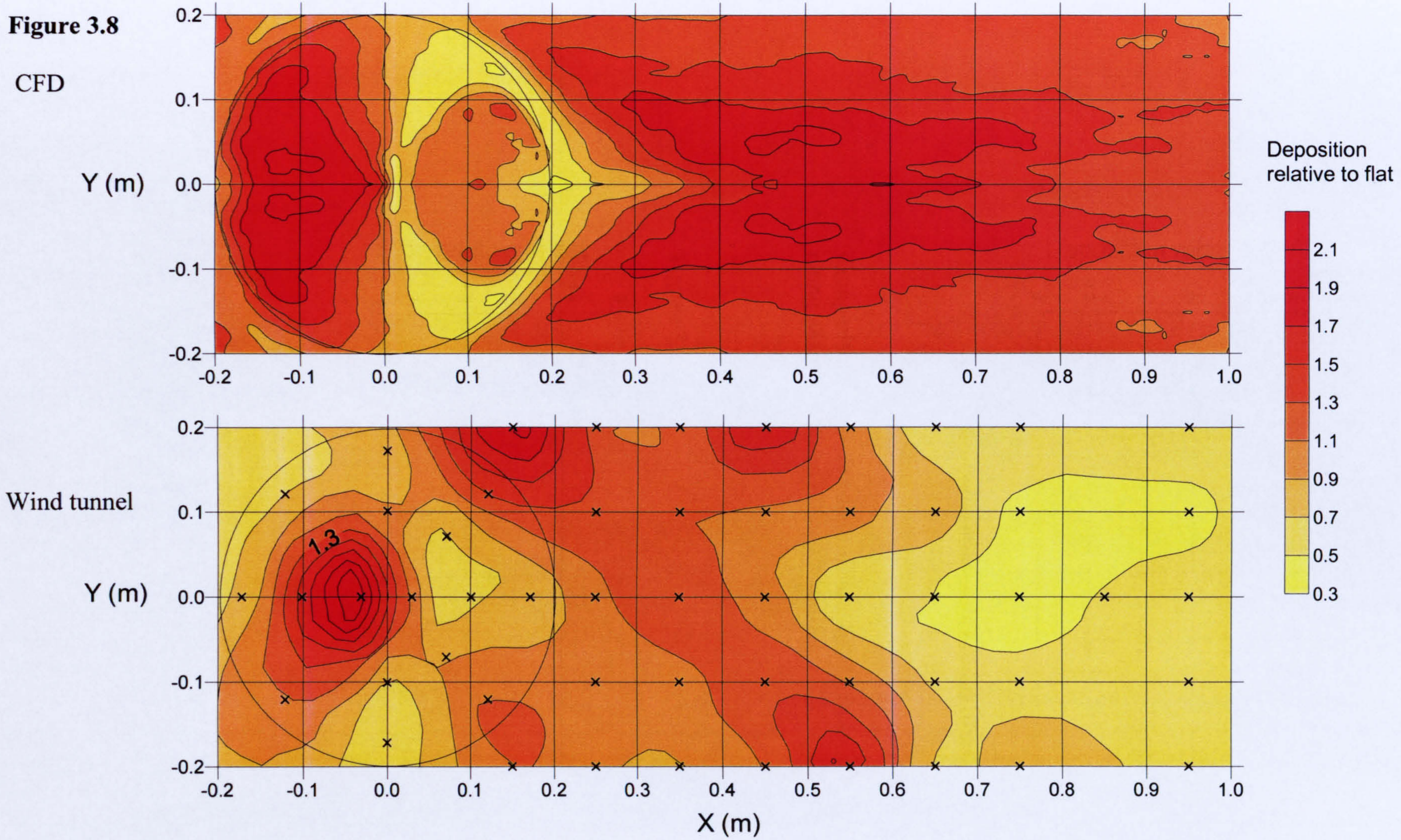

Deposition ratio to flat case for cone geometry exposed to a broad source of particle. CFD (above) and wind tunnel (below). (x) marks sample locations for wind tunnel data. X is downwind distance.

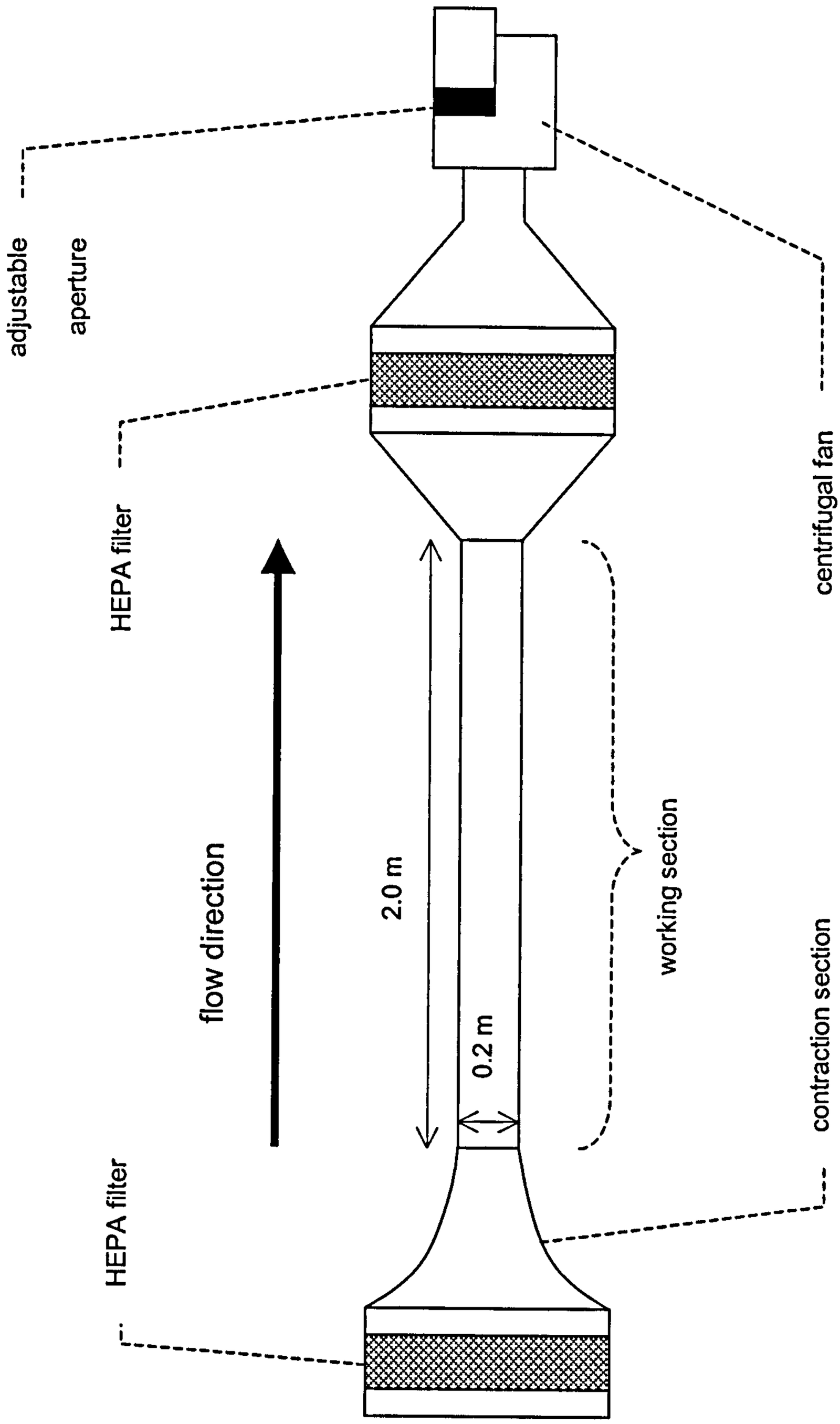

Figure 4.1 Wind tunnel diagram, side view.

Figure 4.2

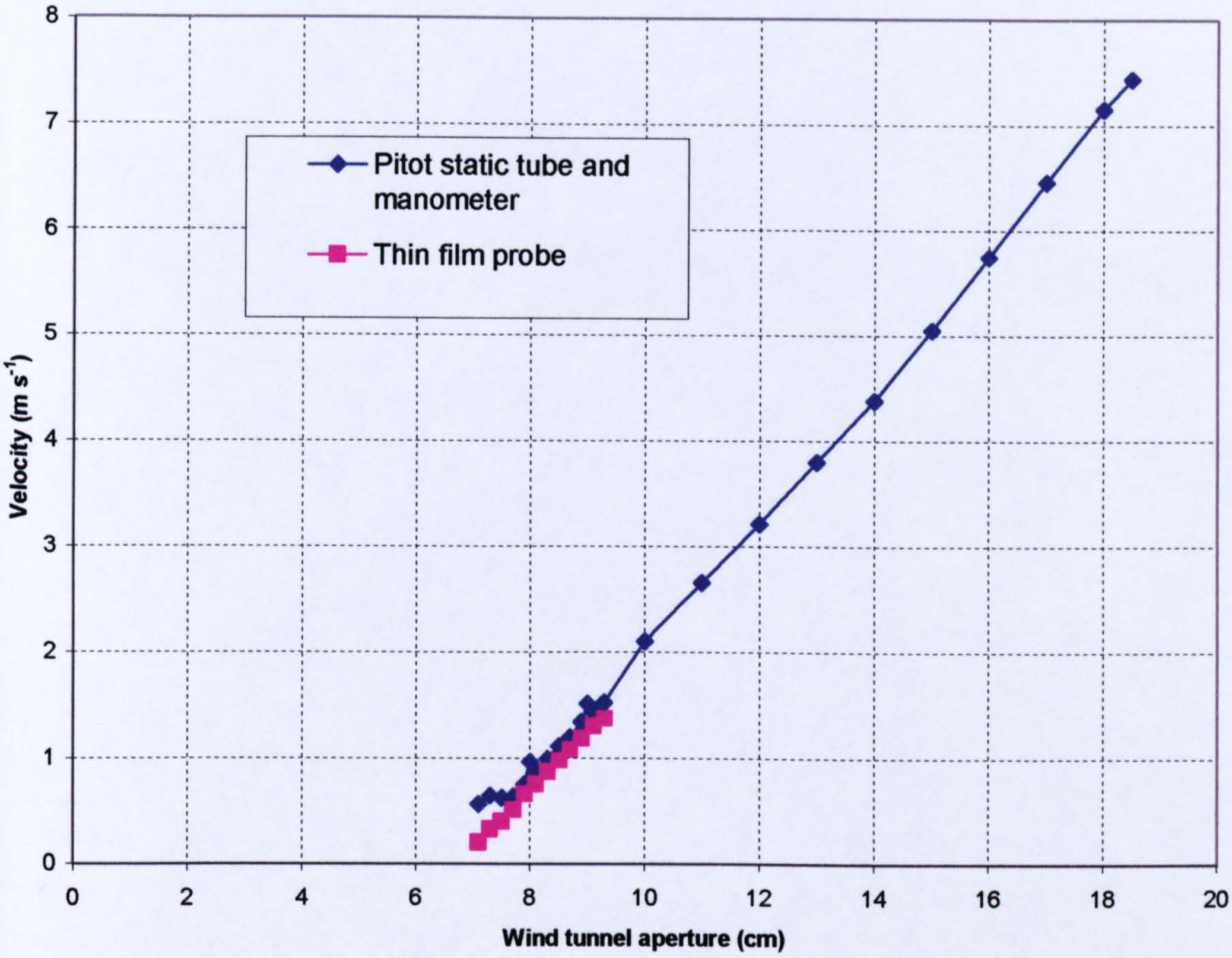

Wind tunnel mean streamwise velocity, plotted against variation in control aperture.

Figure 4.3

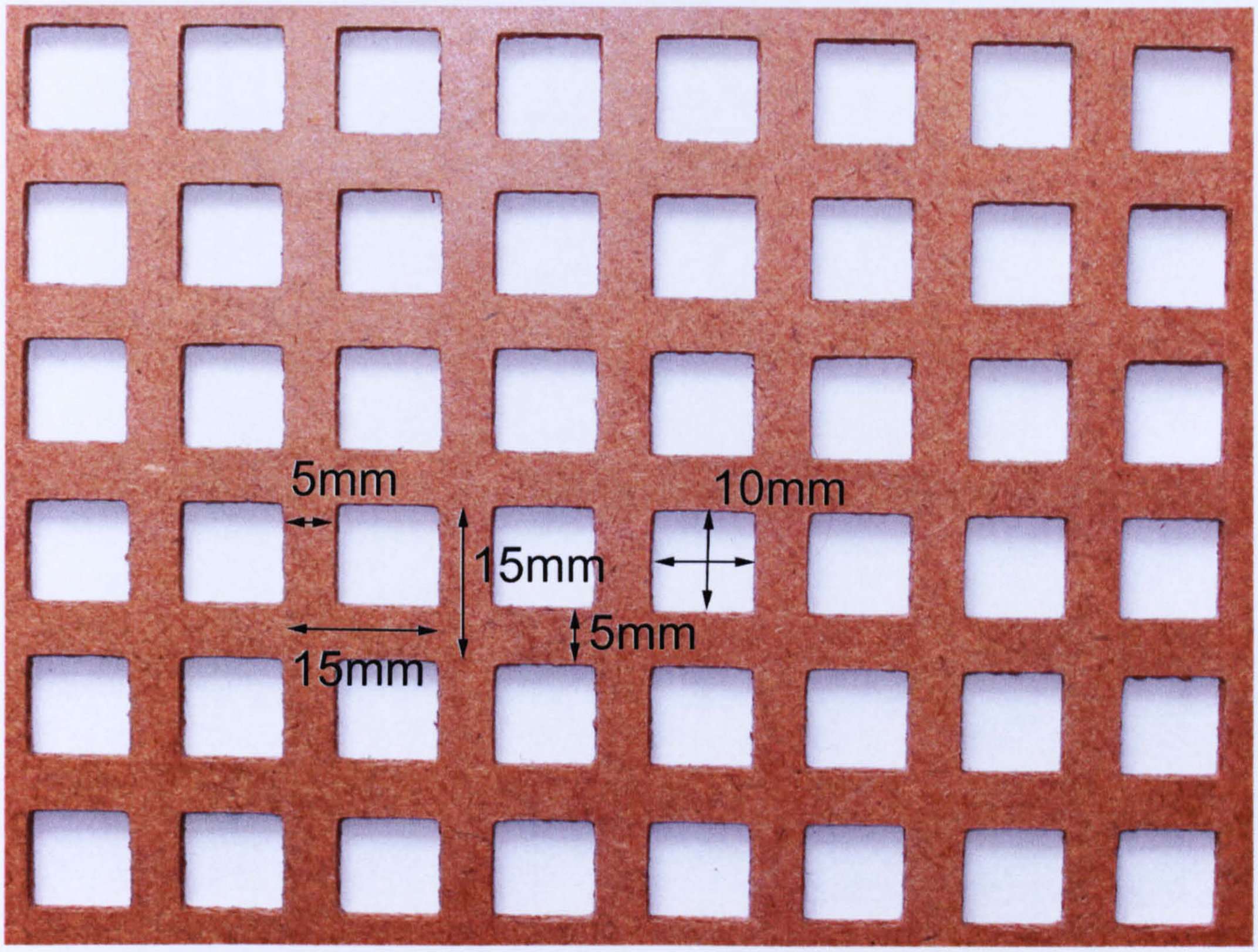

Photograph of grid section showing spacing of apertures and dimensions. Grid spacing (M) = 0.015m.

Figure 4.4

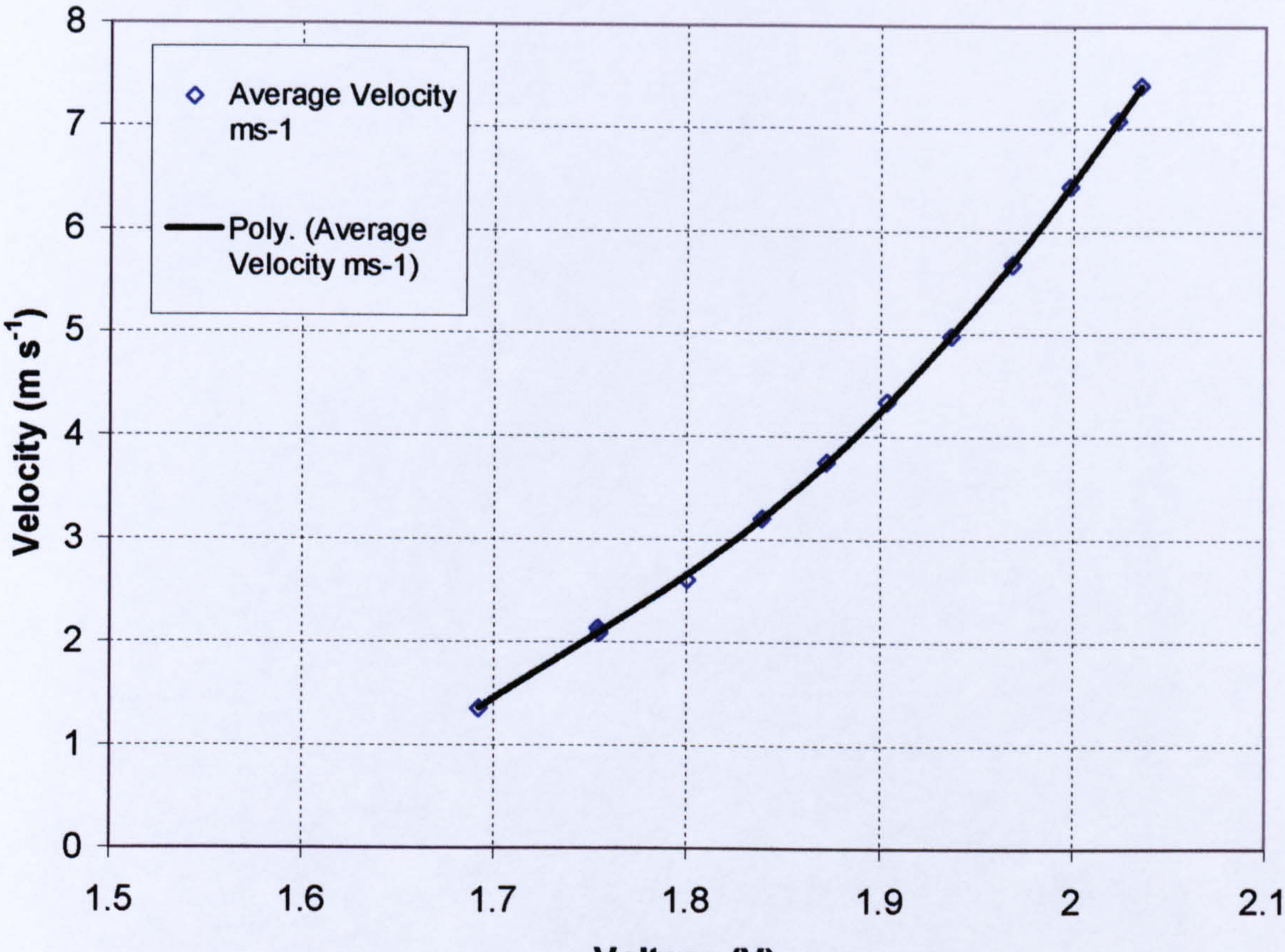

$y = -1.62754E+02x^4 + 1.24897E+03x^3 - 3.55952E+03x^2 + 4.48421E+03x - 2.11150E+03$

$R^2 = 9.99882E-01$

Example calibration graph for hotwire anemometer. Note 6 significant figures are required to ensure accuracy in polynomial.

Figure 4.5

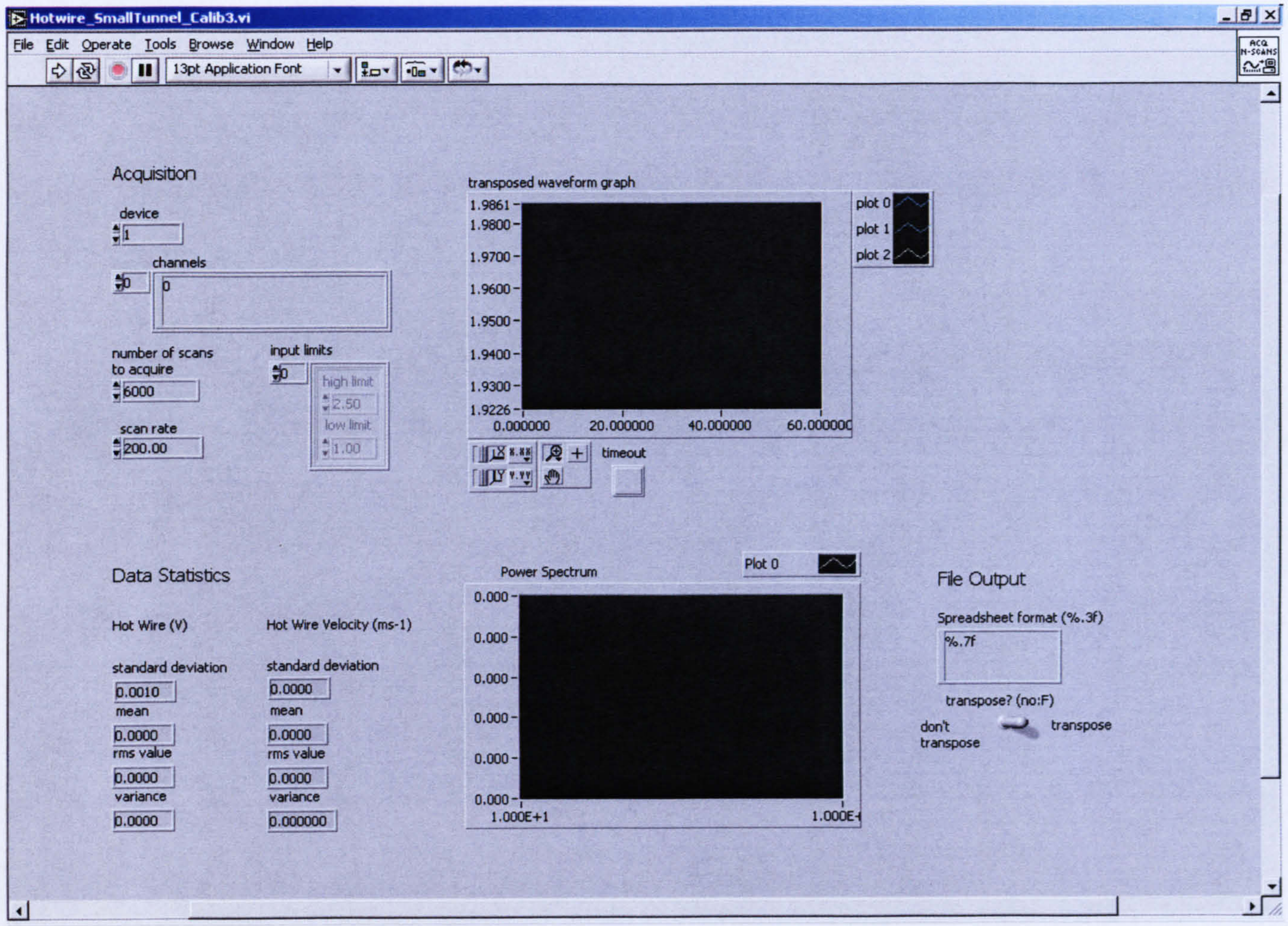

Interface to LabView virtual instrument for constant temperature anemometer data collection and transformation.

Figure 4.6

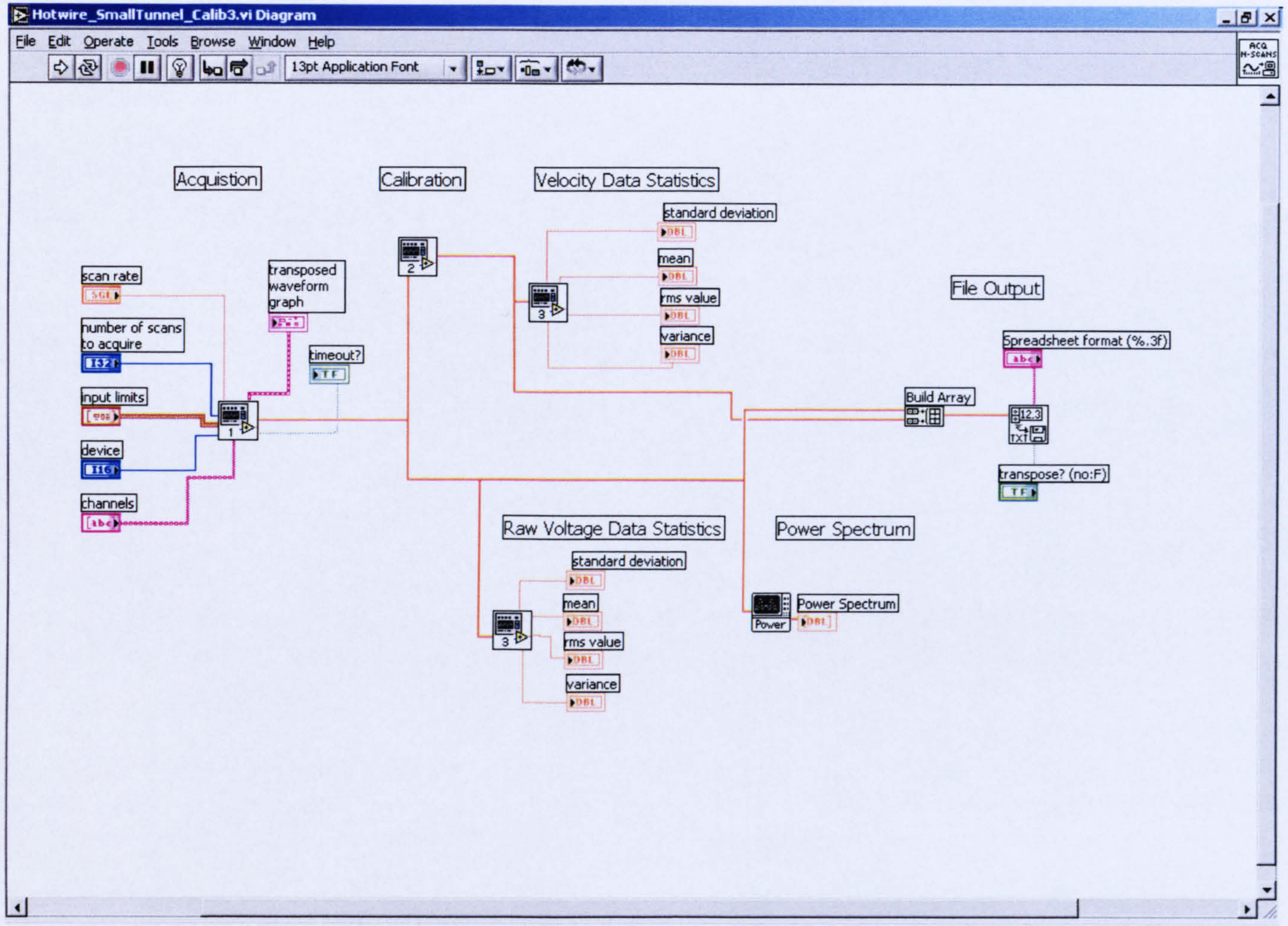

Diagram of LabView virtual instrument for constant temperature anemometer data collection and transformation. Boxes containing numbers 1, 2 and 3 represent sub-virtual instruments presented in figures below.

Figure 4.7

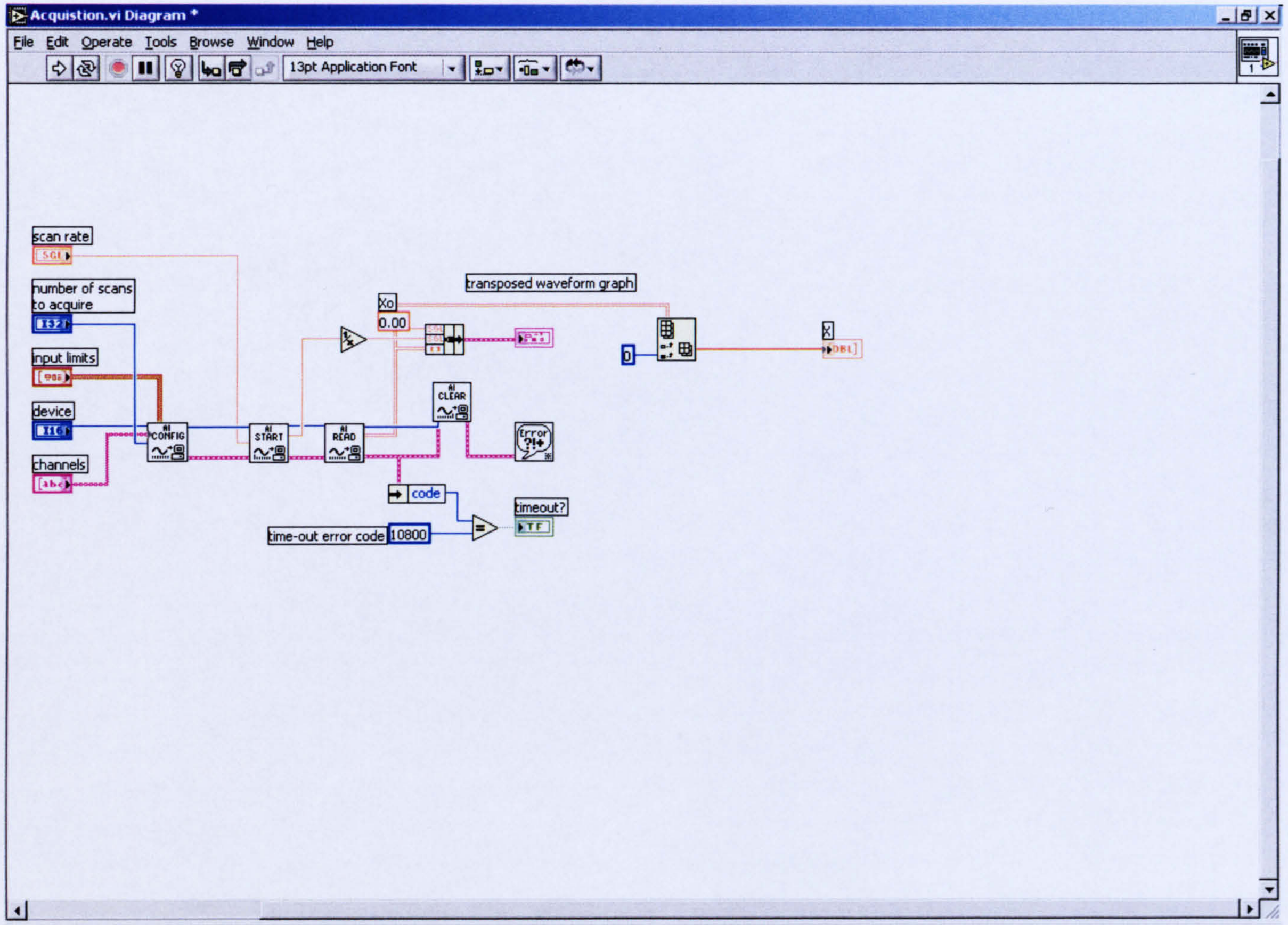

Diagram of LabView sub-virtual instrument 1, for data acquisition and graphing of raw data.

Figure 4.8

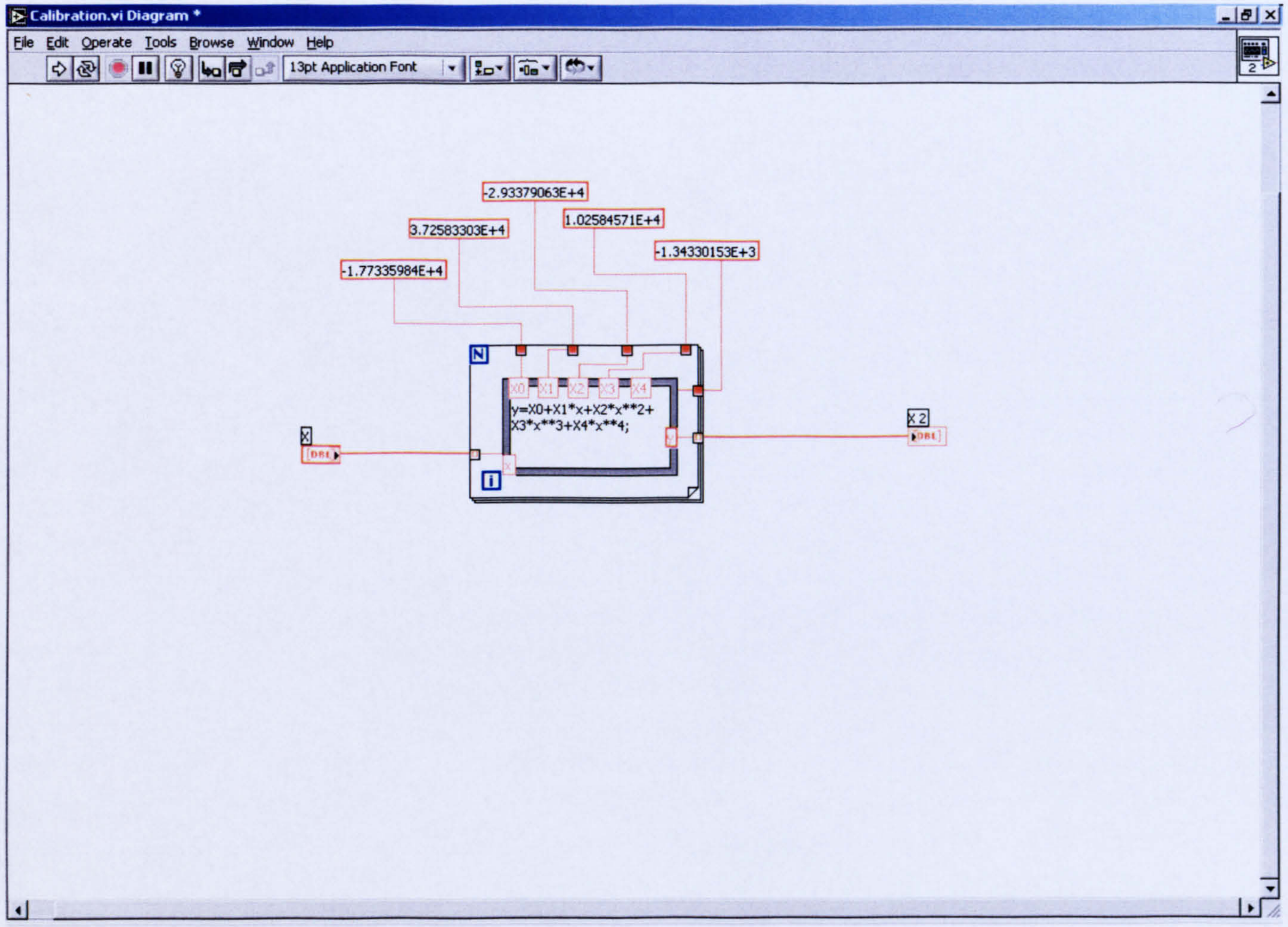

Diagram of LabView sub-virtual instrument 2, for transforming recorded voltages to velocities using a 4^{th} order polynomial. Note the large number of significant figures included for polynomial coefficents.

Figure 4.9

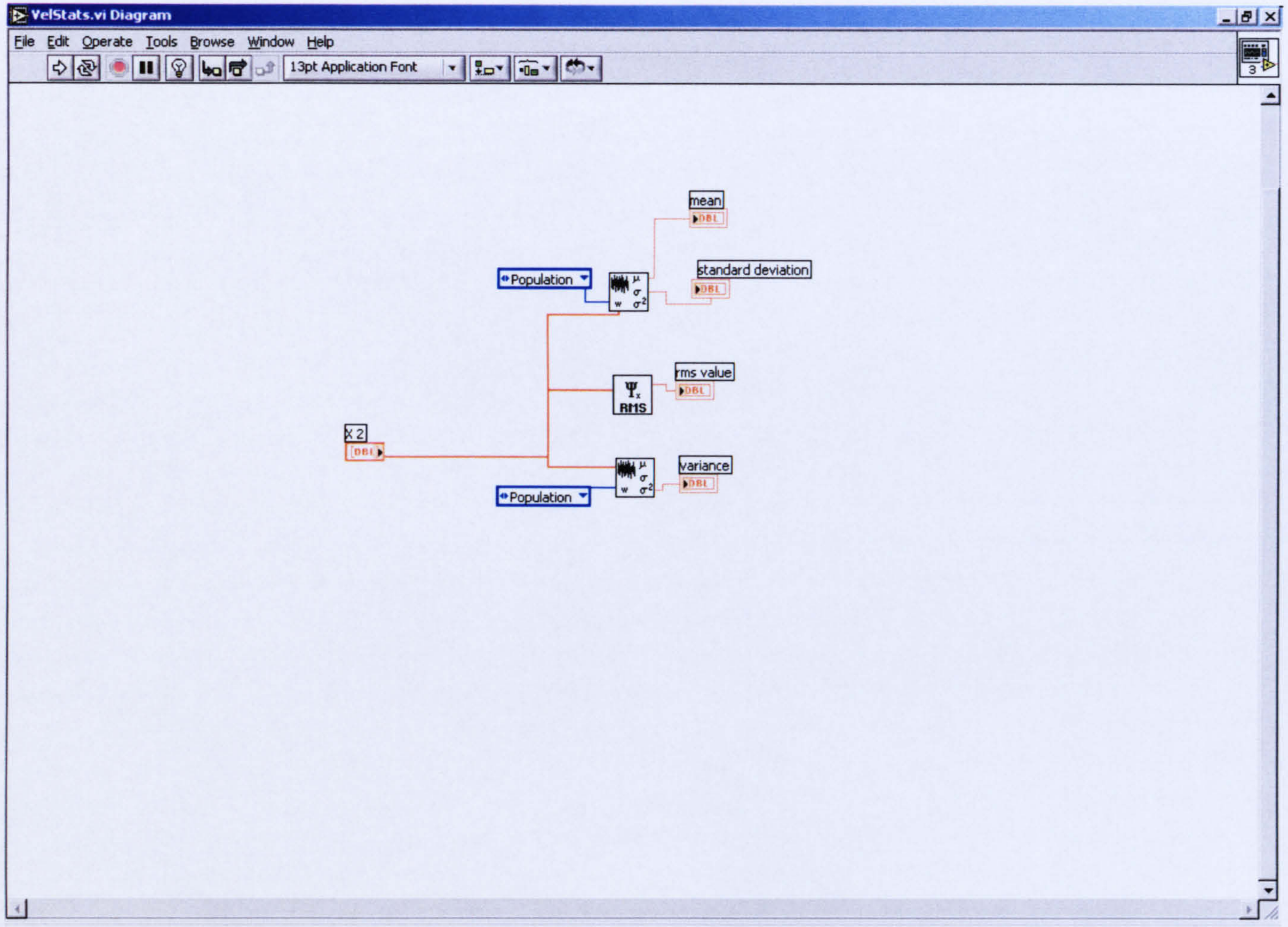

Diagram of LabView sub-virtual instrument 3, for calculating statistics of sampled data, both for raw voltages and calculated velocities.

Figure 4.10

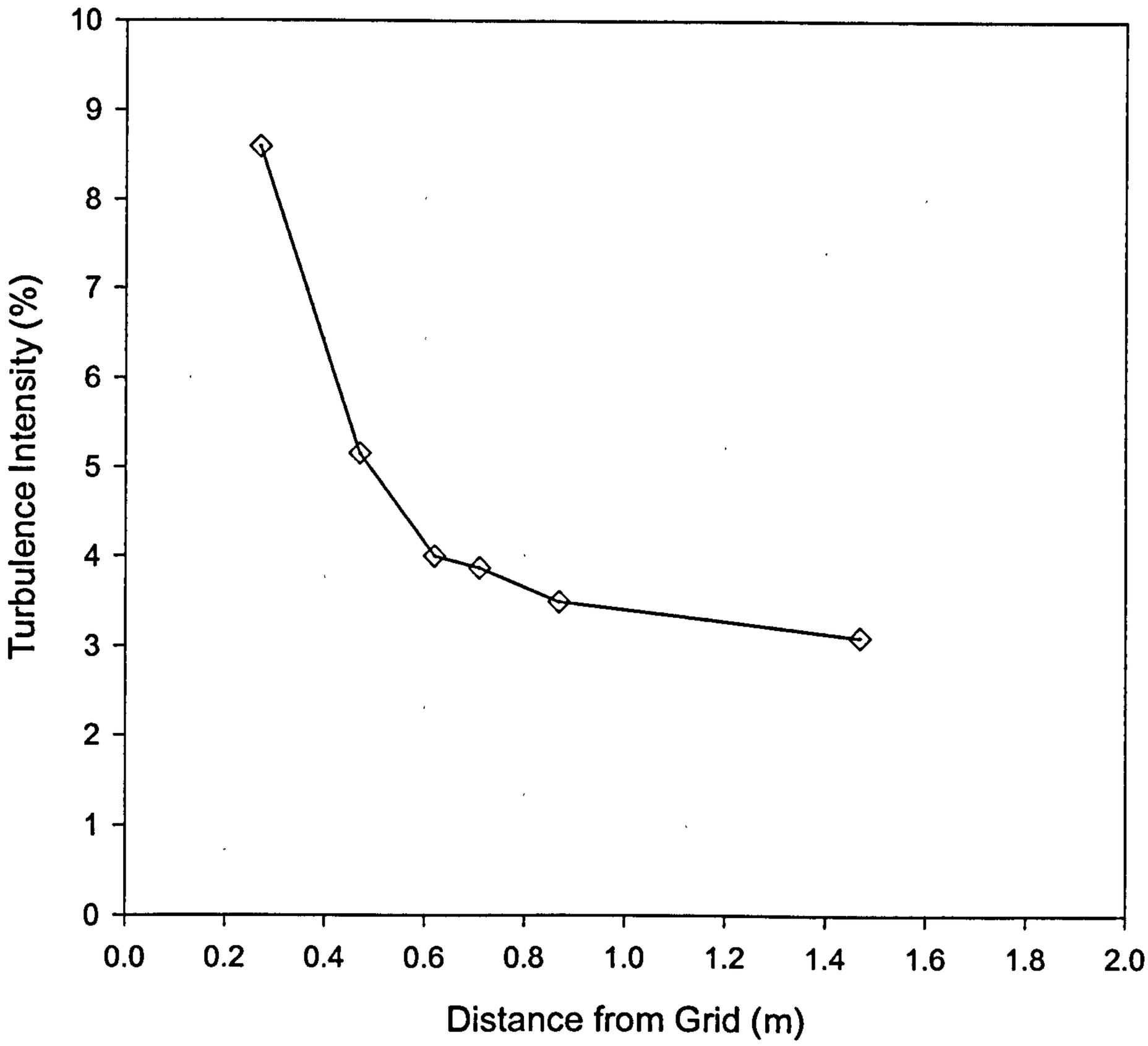

Graph of experimental streamwise turbulence intensity plotted against distance from grid.

Figure 4.11

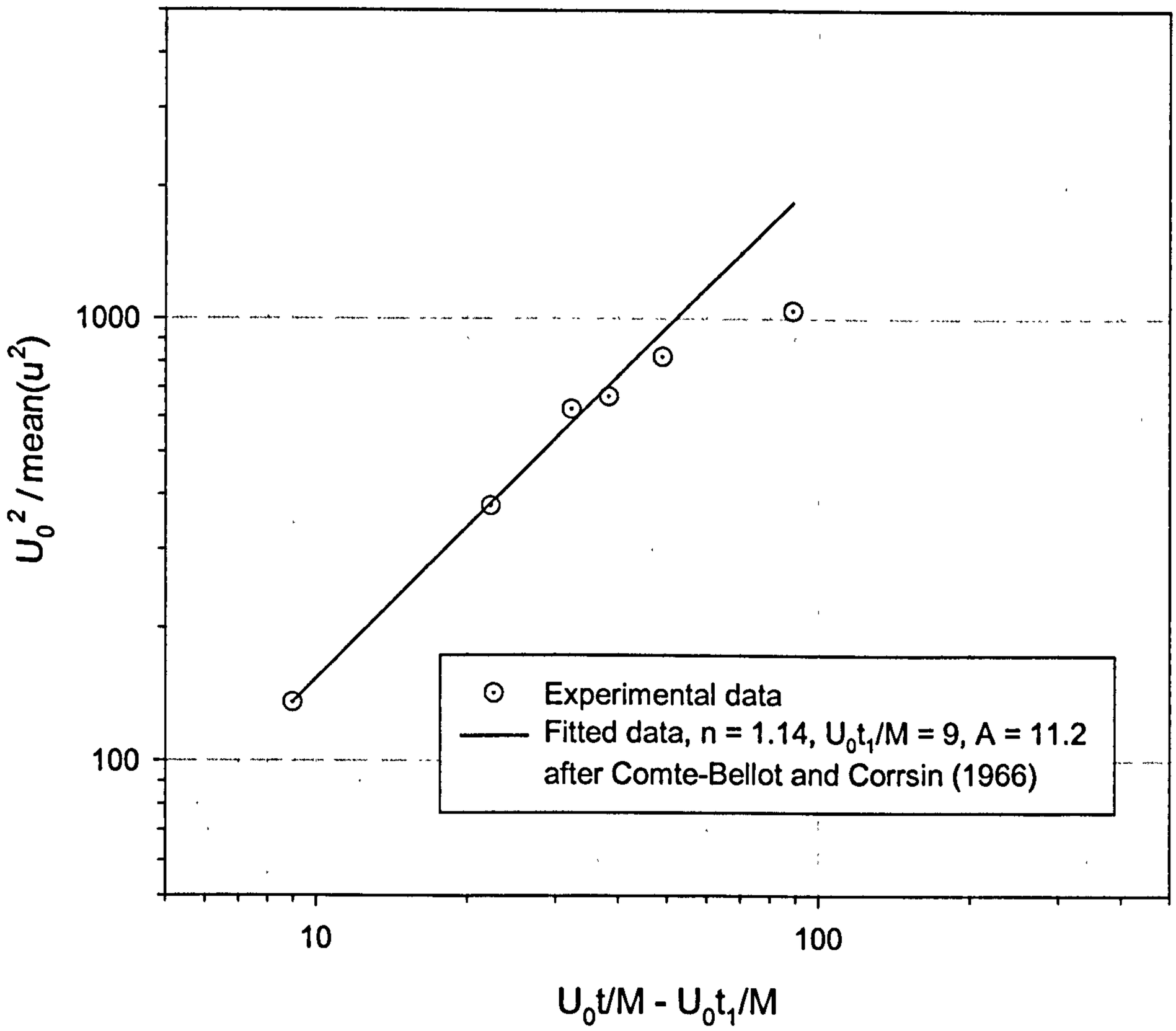

Ratio of the square of the mean velocity to the mean of the turbulent velocity squared, plotted against normalised downstream distance from grid. Experimental data show a larger degree of turbulence than predicted at larger downstream distances.

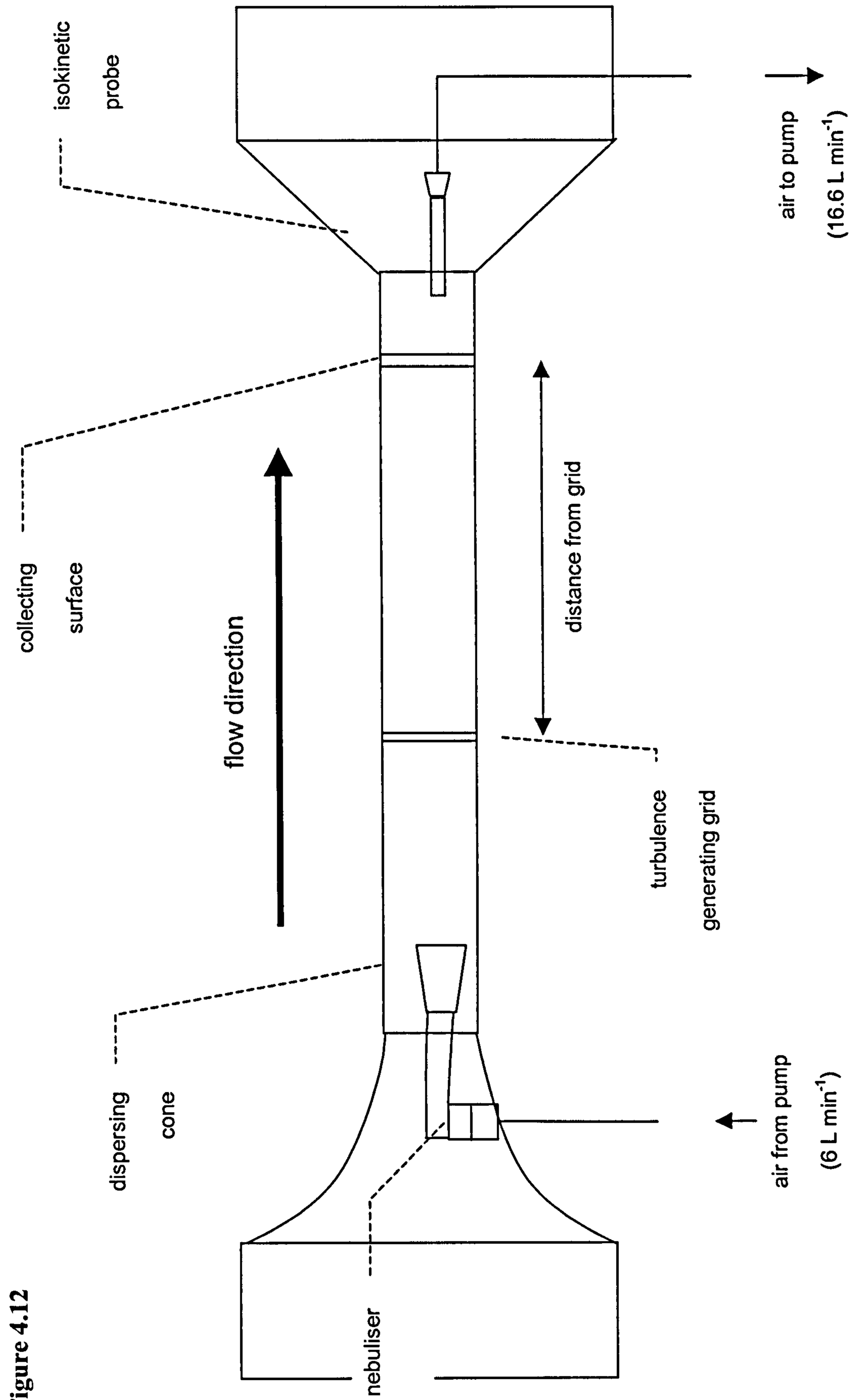

Figure 4.12 Diagram of wind tunnel arrangement, showing aerosol source and collecting surface.

Figure 4.13

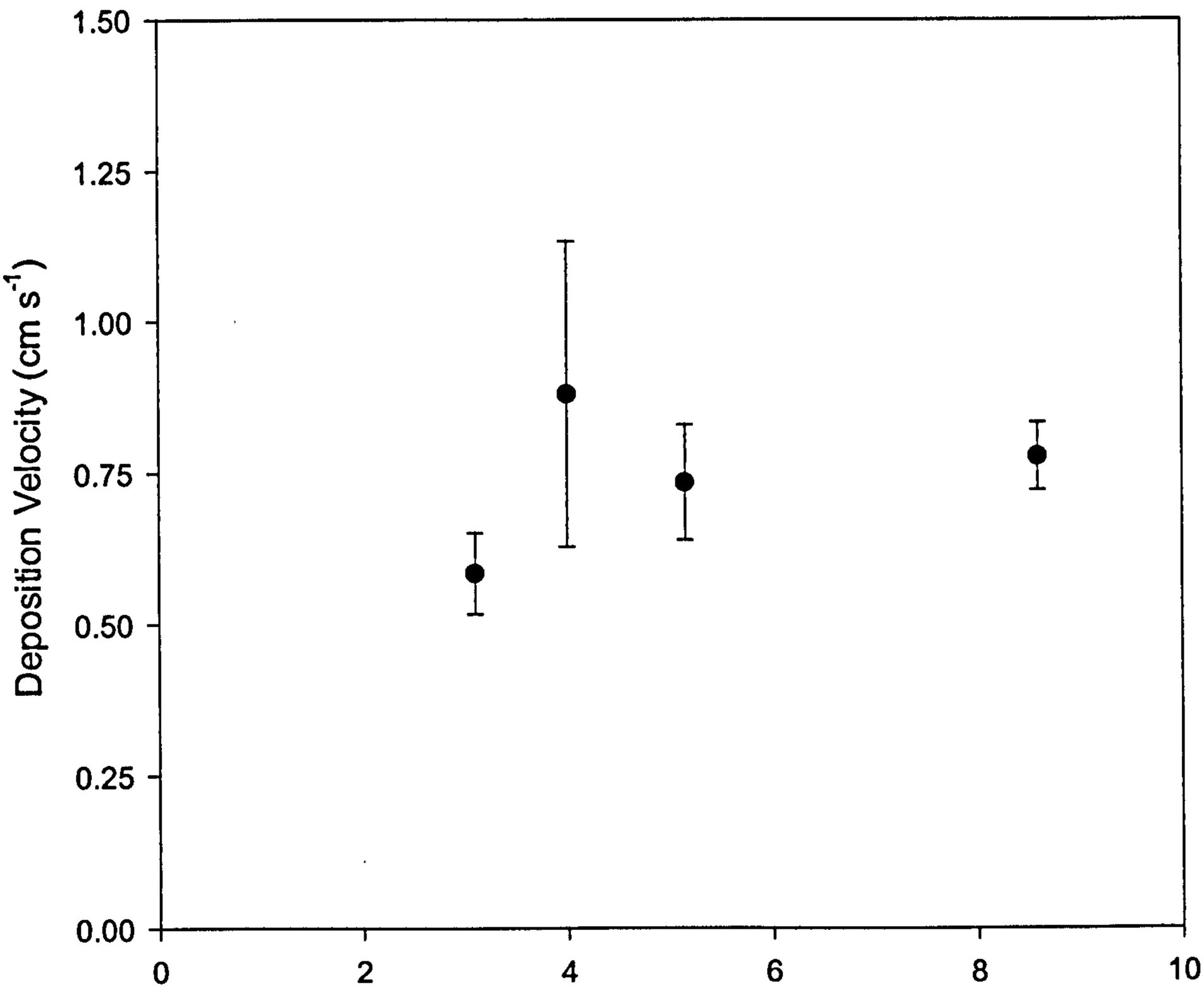

Variation of deposition velocity for a 20mm diameter cylinder. Points show average values for deposition velocity and error bars show range of values. Mean velocity 5 m s^{-1}.

Figure 4.14

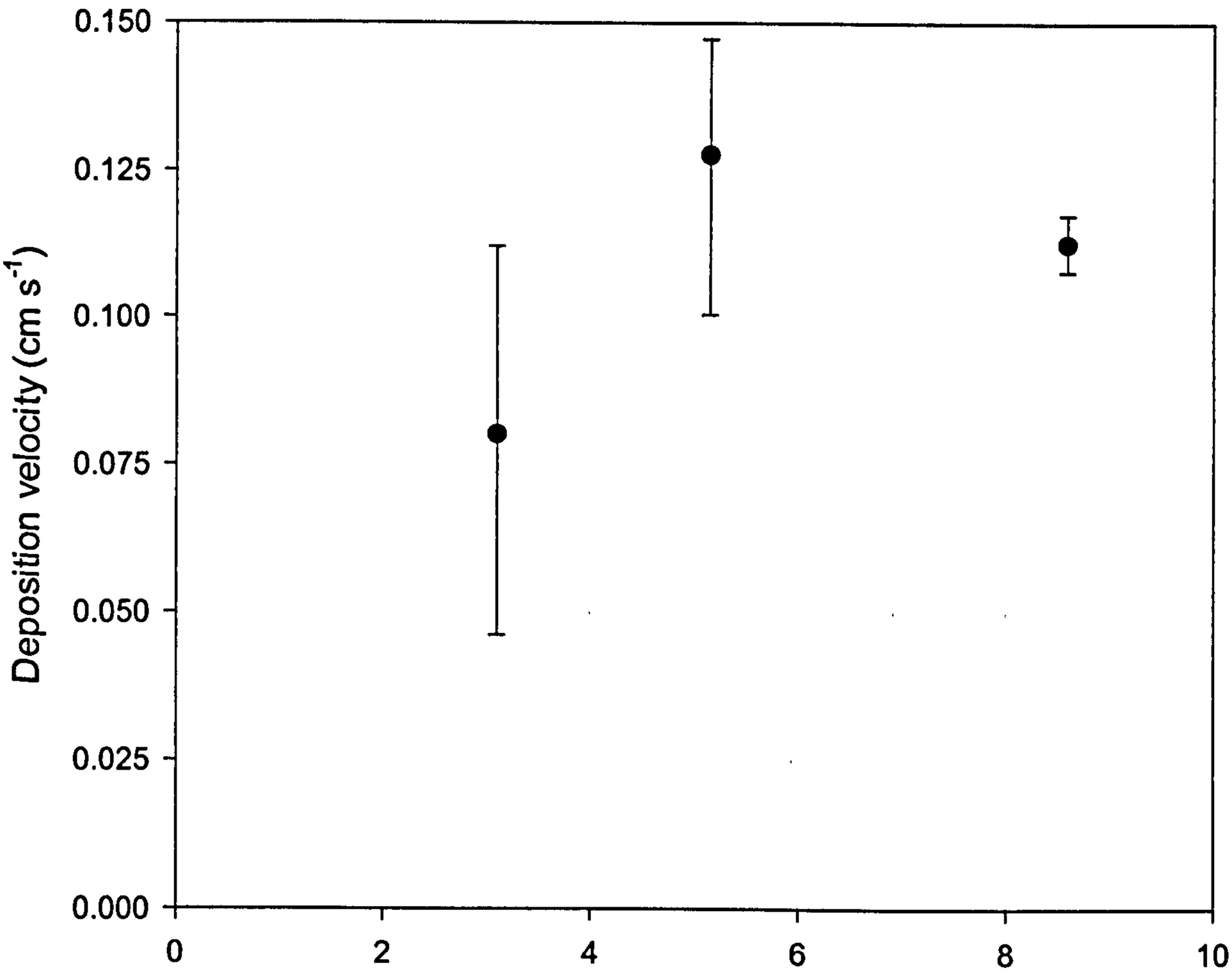

Variation of deposition velocity for a vertical plane. Points show average values for deposition velocity and error bars show range of values. Mean velocity 5 m s^{-1}.

Figure 5.1

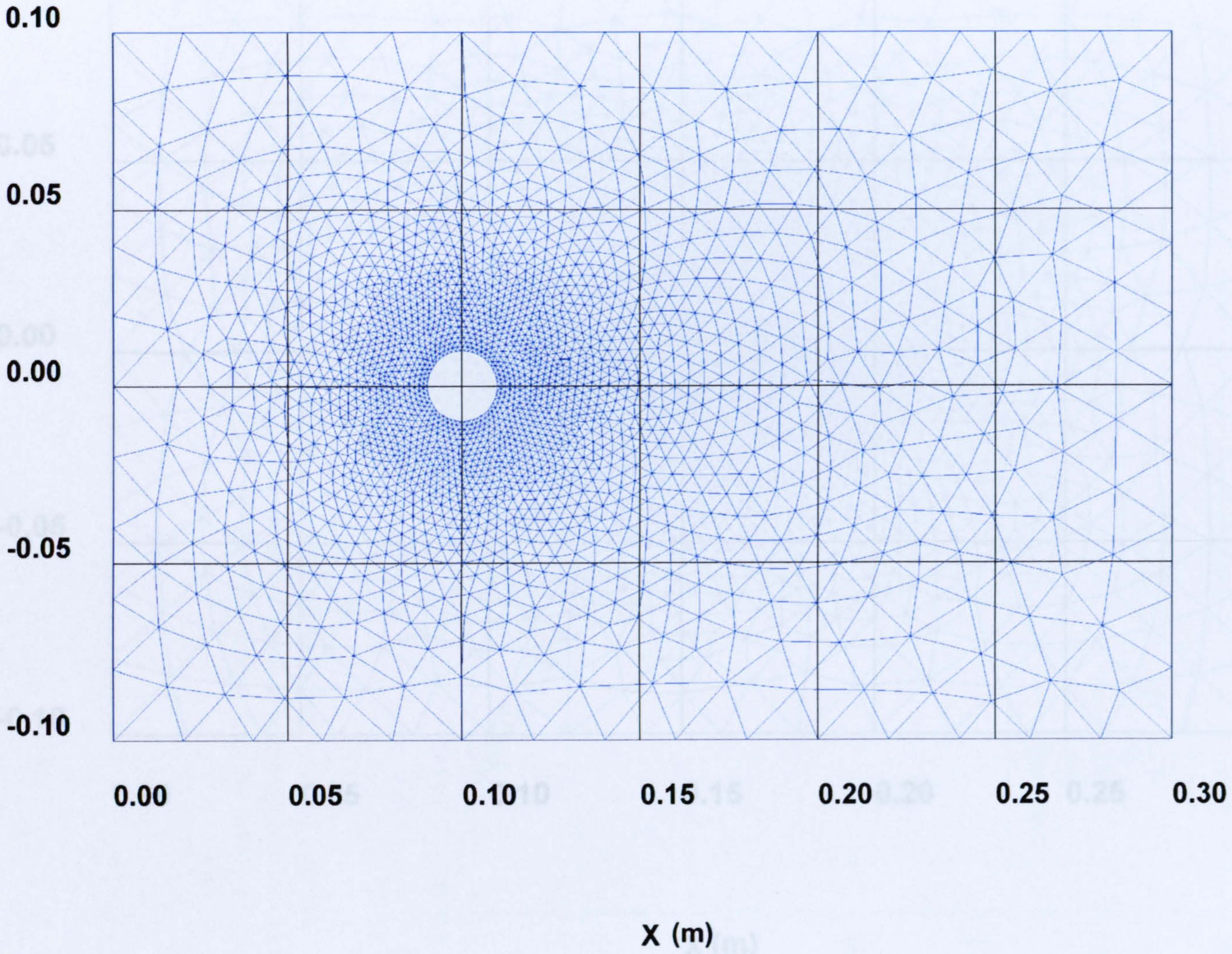

Mesh used for modelling flow around, and deposition to, a circular cylinder of 20mm diameter. Note flow direction is from left to right.

Figure 5.2

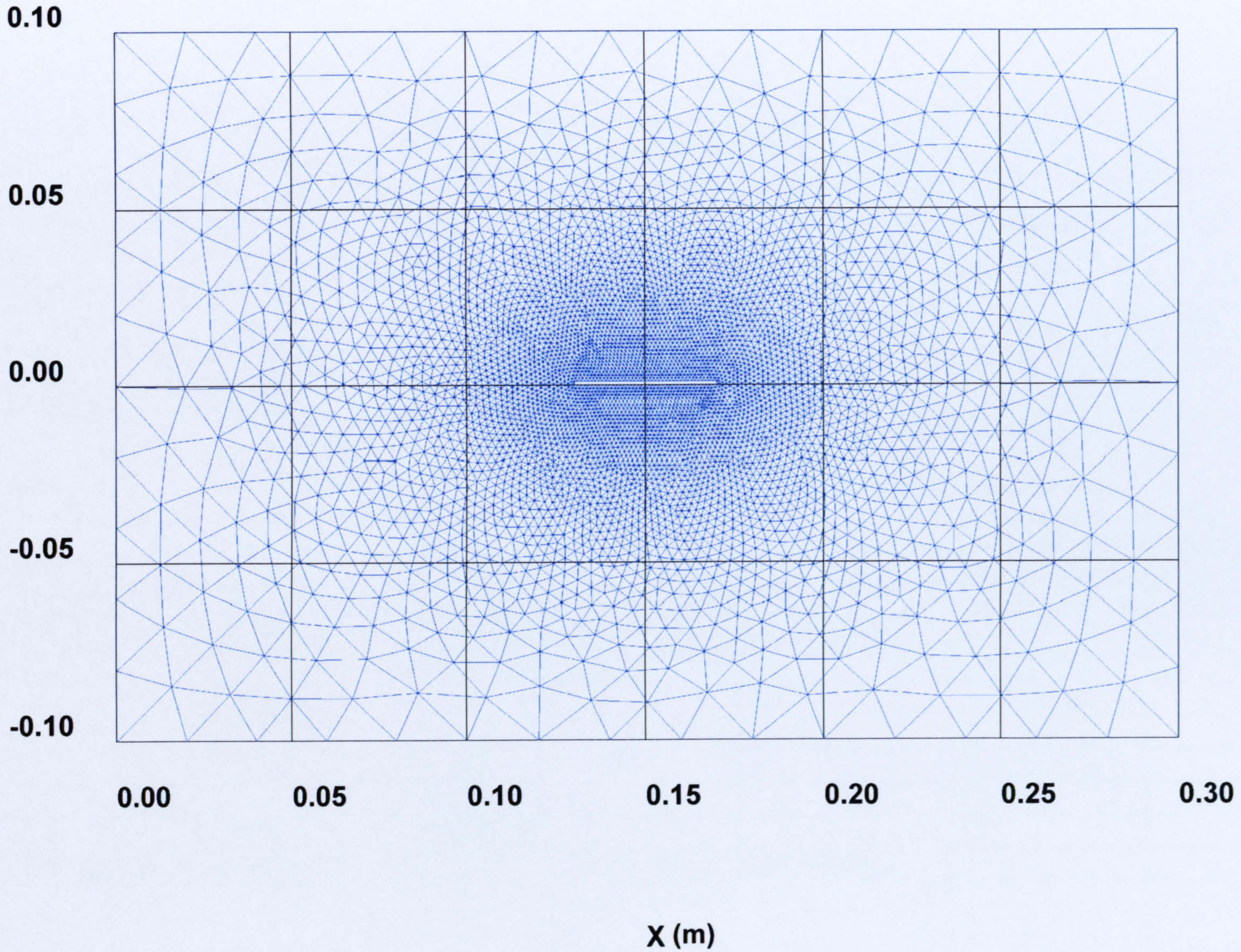

Mesh used for modelling flow around, and deposition to, a plane of length 40mm and width 1mm. Note flow direction is from left to right.

Figure 5.3

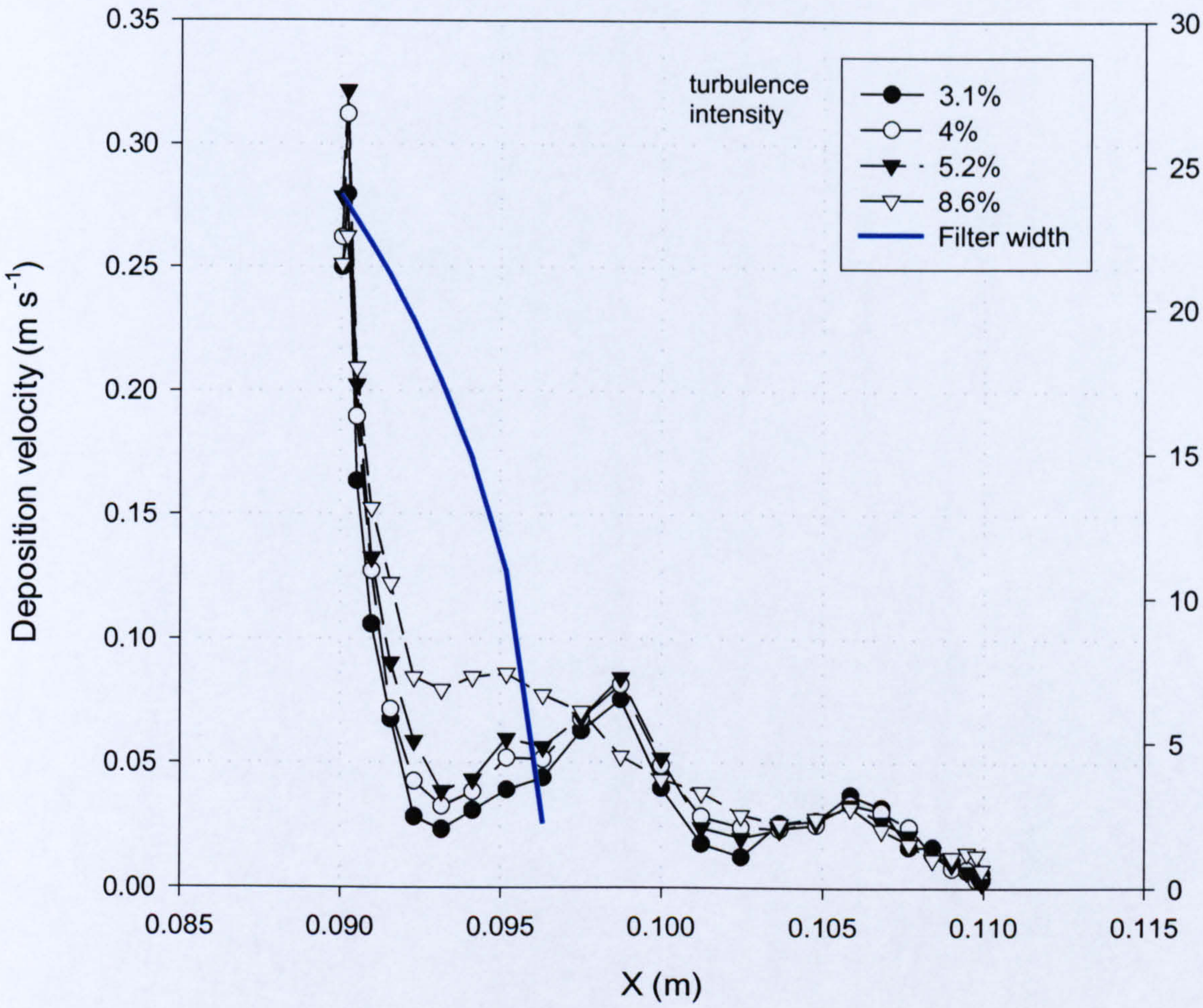

Graph showing deposition velocity to different parts of cylinder surface, plotted against downwind distance. Four plots for different values of turbulence intensity are included. The blue line shows the area covered by the filter in the experiment and the width of the filter. Cylinder centre is at X=0.1m.

Figure 5.4

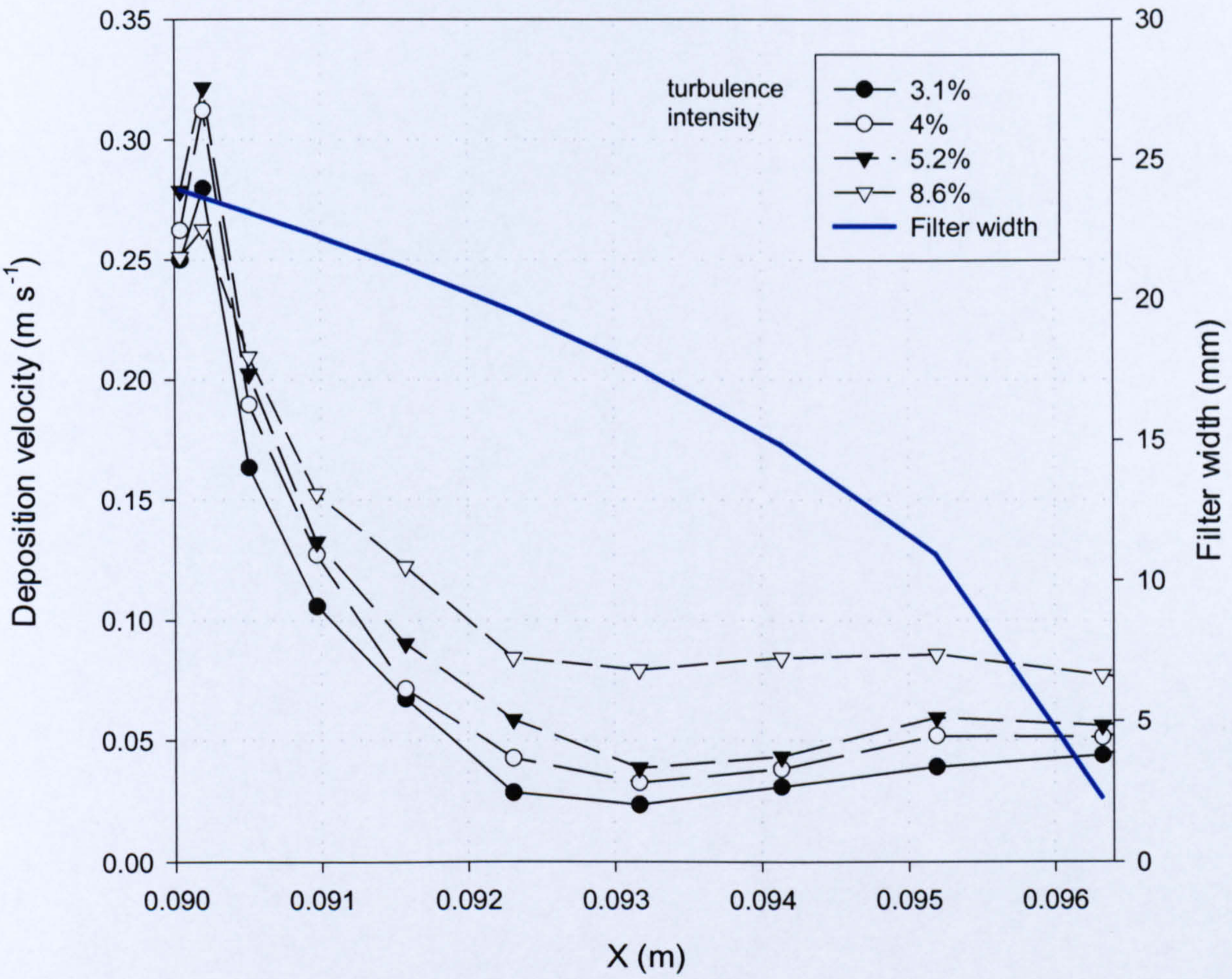

As Figure 5.3, but only showing area covered by filter. Note that at front face (X = 0.90 m) the most turbulent case (8.6% turbulence intensity) does not result in the highest deposition velocity. Cylinder centre is at X=0.1m.

Figure 5.5

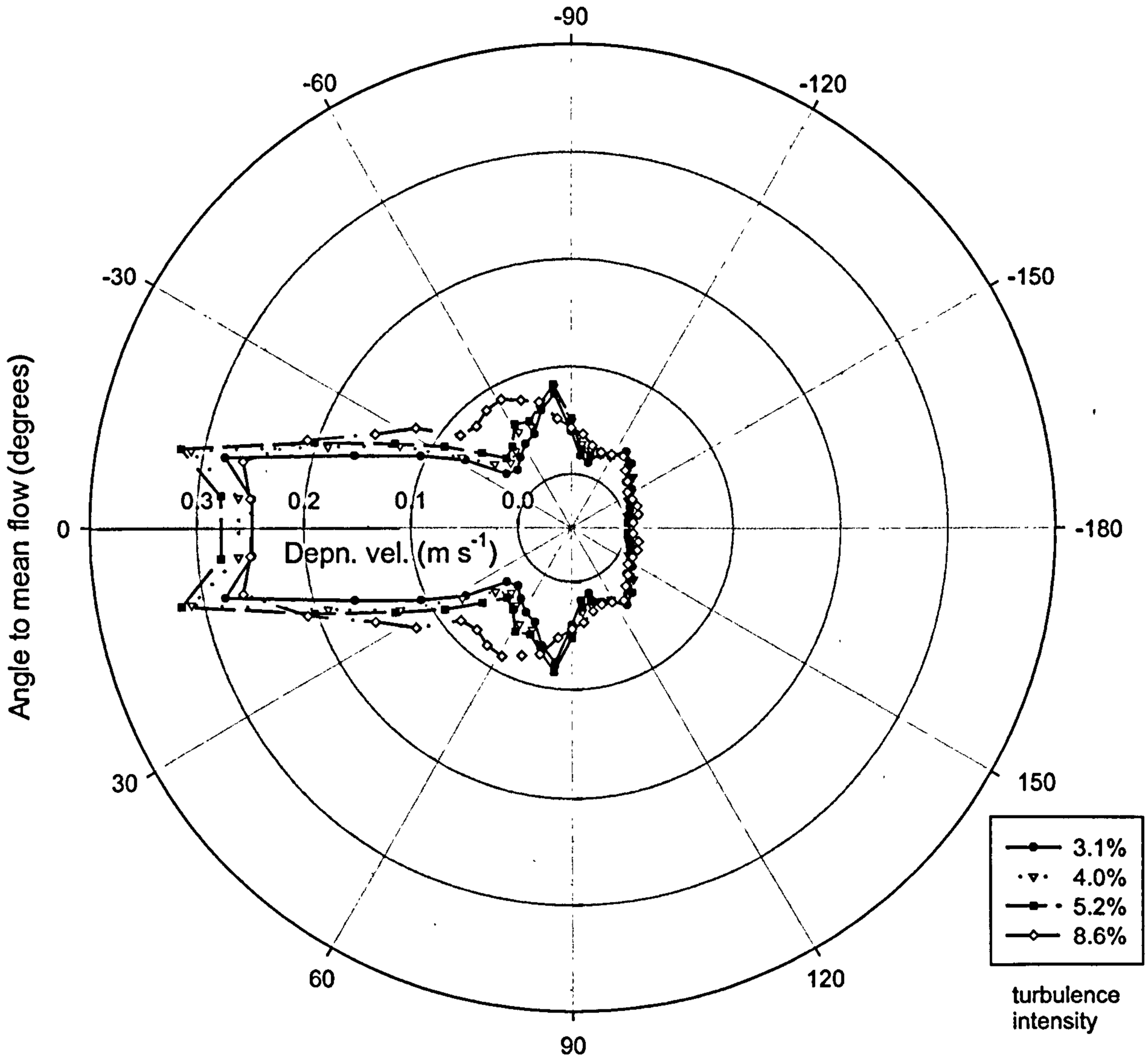

Deposition velocity to different parts of cylinder, polar plot. Flow from left to right. Four plots for different values of turbulence intensity are included. Note that the origin for the deposition velocity has been offset from the centre of the plot for clarity.

Figure 5.6

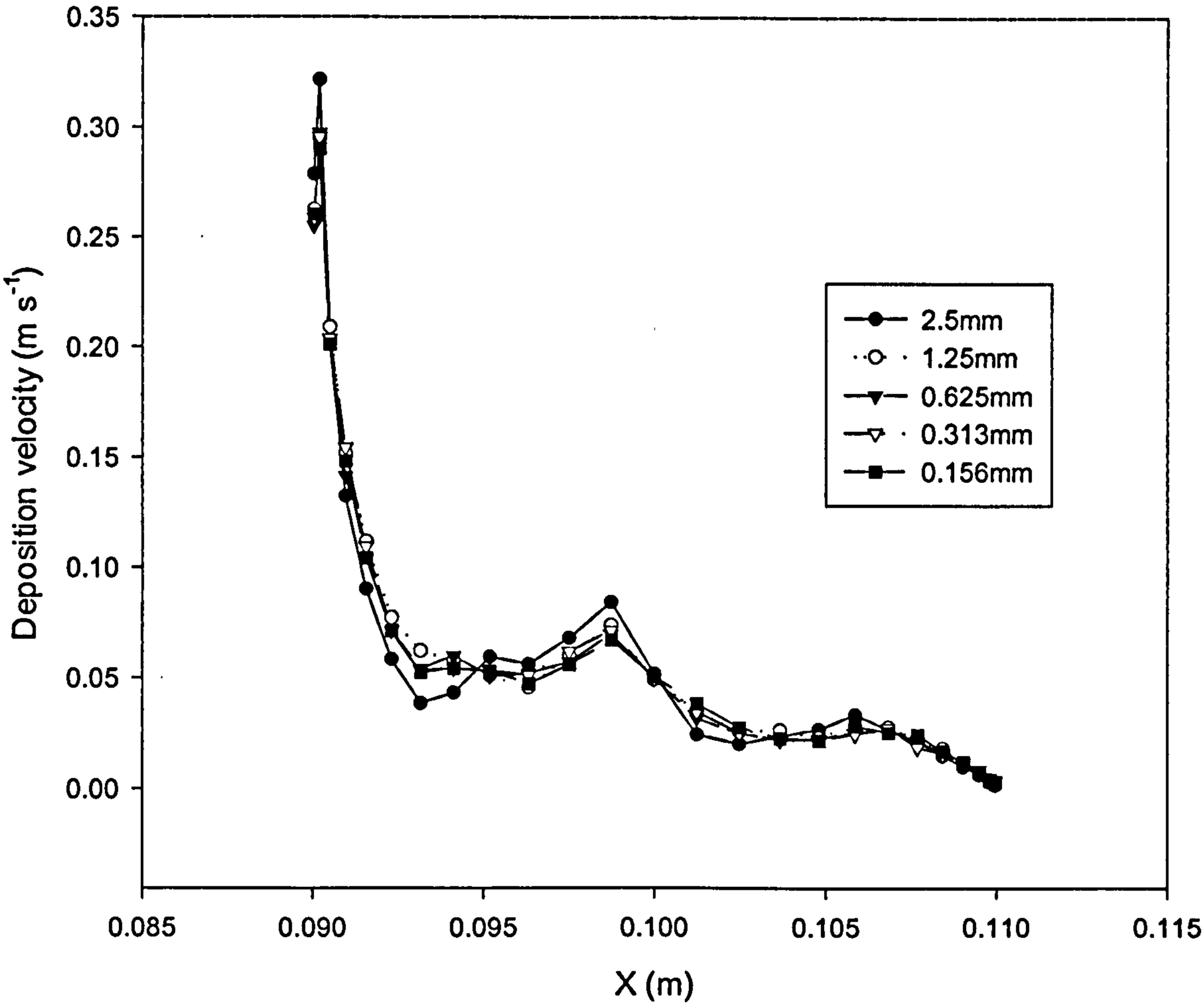

Variation of deposition velocity pattern with initial particle spacing. Particle spacings range from 2.5mm to 0.156mm.

Figure 5.7

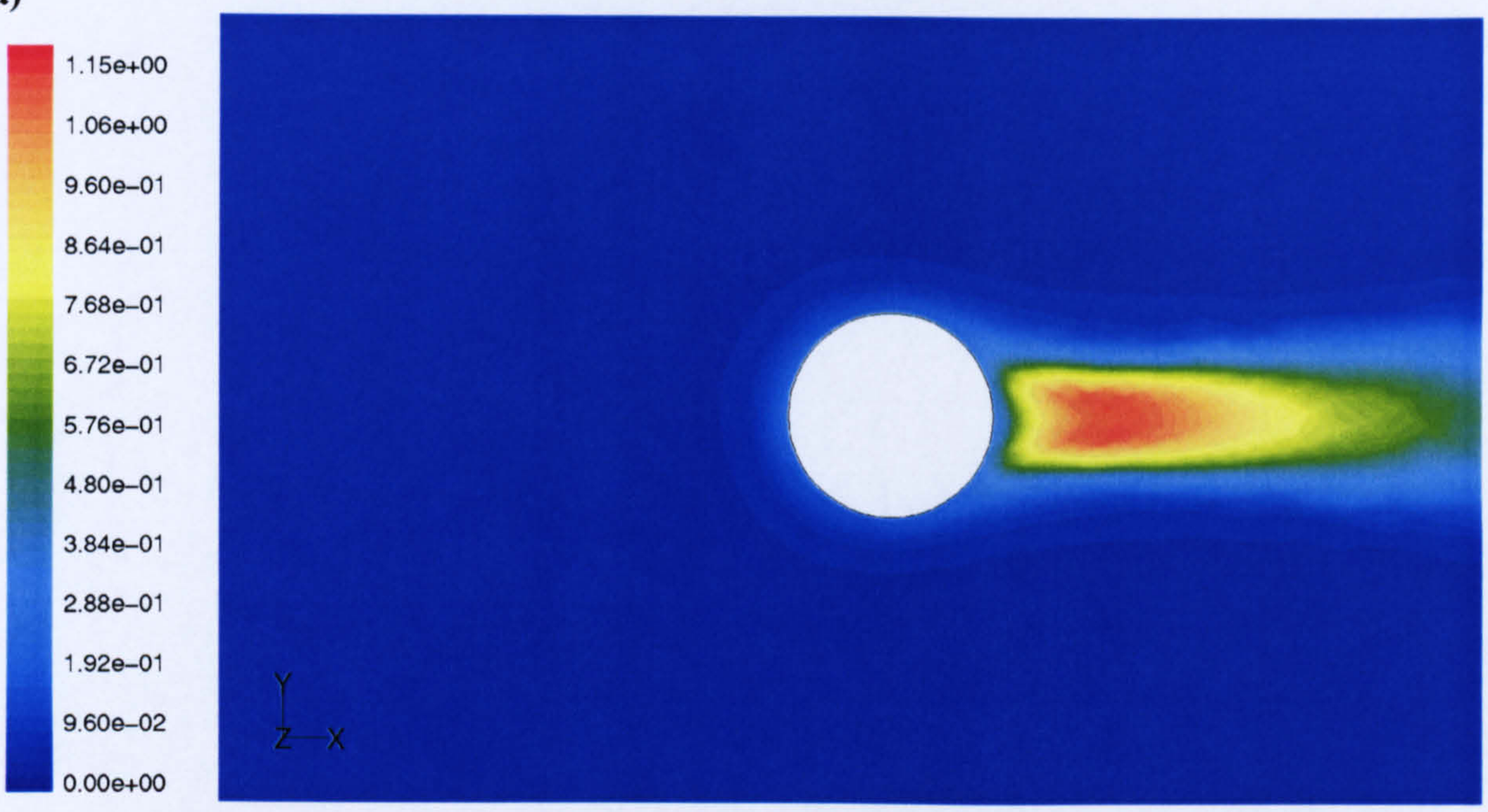

Contour plots of turbulent kinetic energy for 3.1% (a) and 8.6% (b) turbulent intensity at the inlet. Flow is from left to right. Units of turbulent kinetic energy are $m^2 s^{-2}$.

Figure 5.8

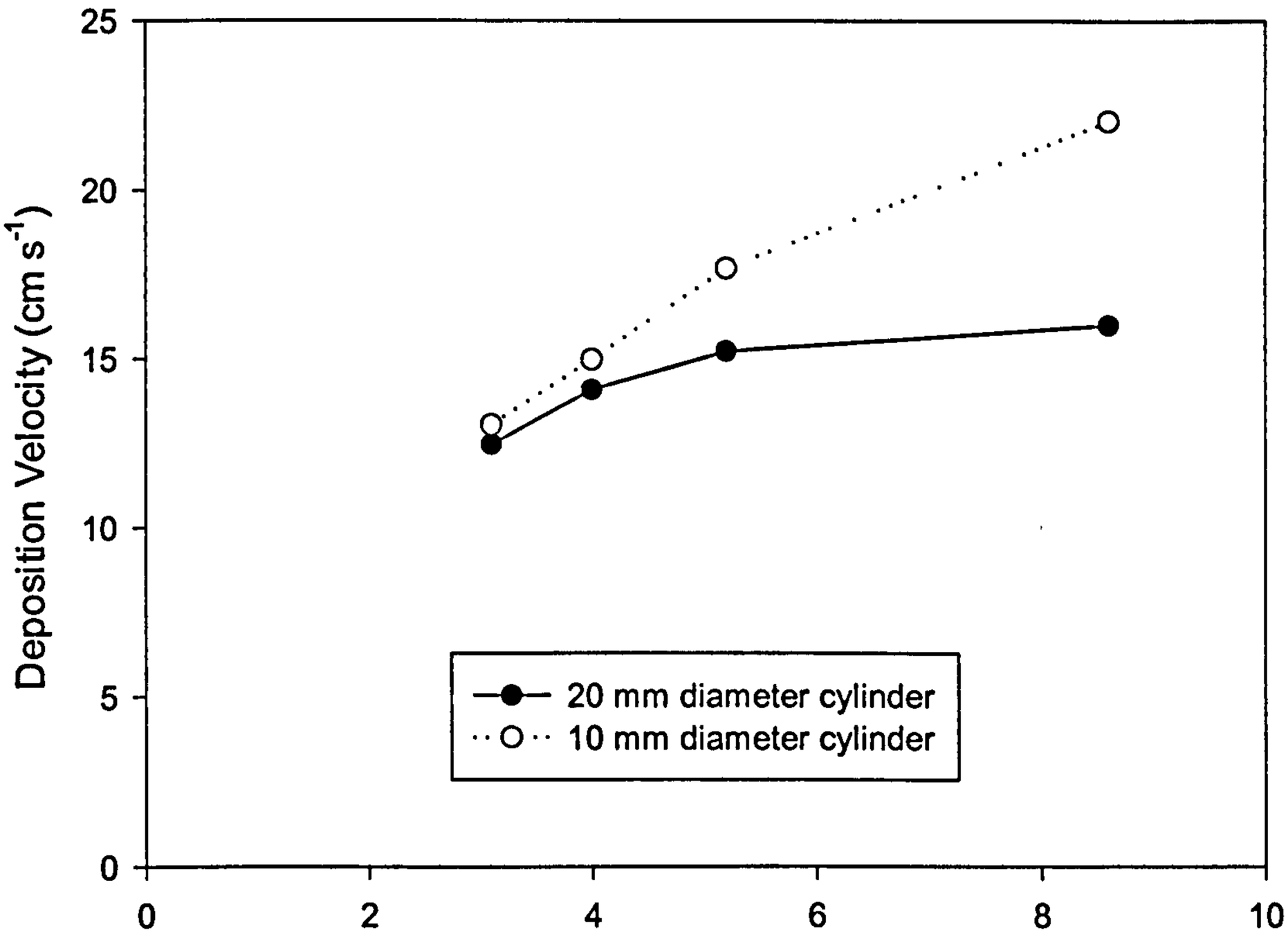

Comparison of calculated deposition velocities to a 20mm and a 10mm diameter cylinder for different turbulence intensities. Only deposition to filter area considered.

Figure 5.9

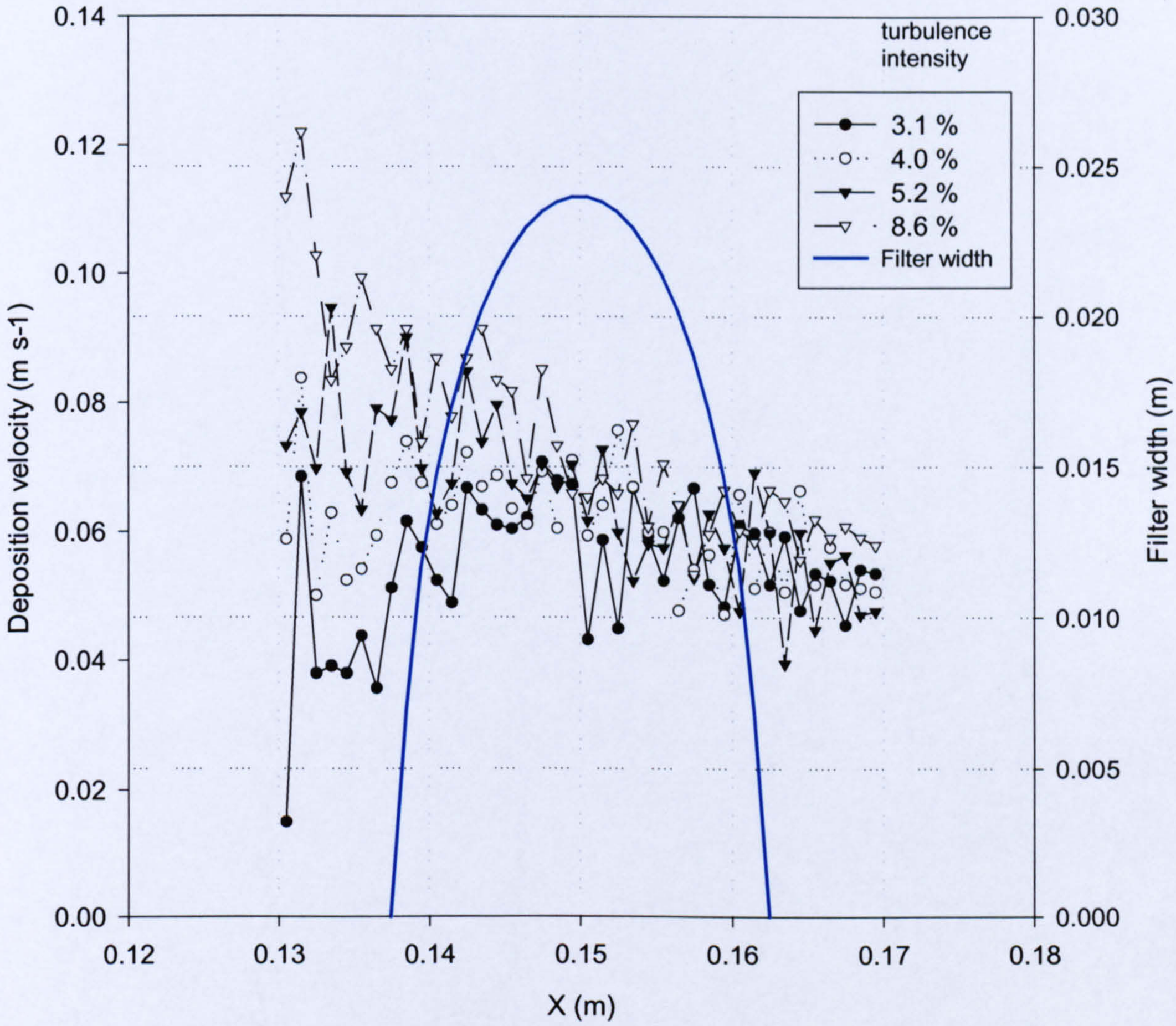

Graph showing deposition velocity to plane surface, plotted against downwind distance. Four plots for different values of turbulence intensity are included. Blue line shows area covered by filter in experiment and width of filter. Centre of plane at X=0.15m.

Figure 5.10

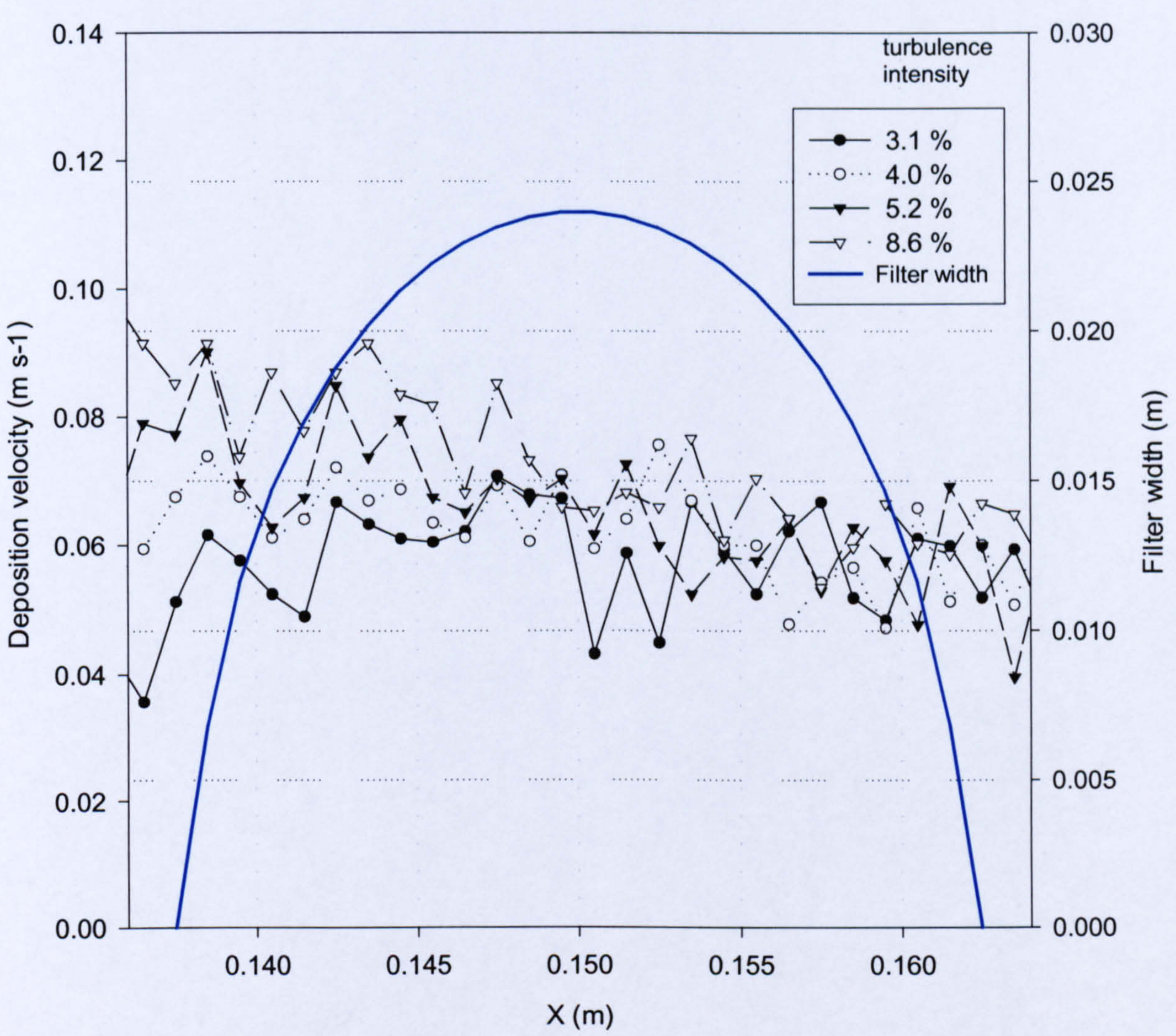

Graph showing deposition velocity to plane surface showing area of filter, plotted against downwind distance. Four plots for different values of turbulence intensity are included. Blue line shows area covered by filter in experiment and width of filter. Centre of plane at X=0.15m.

Figure 5.11

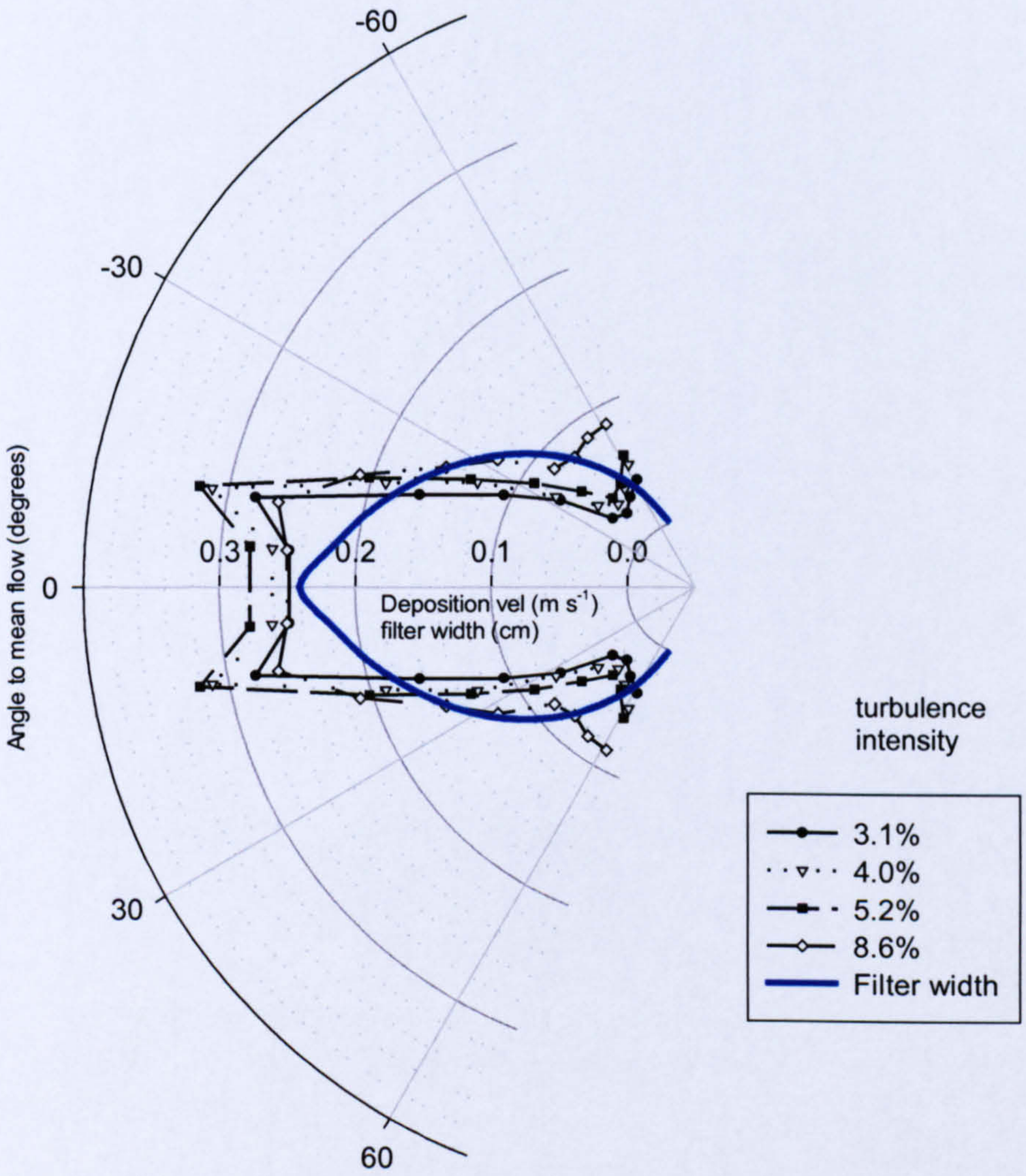

Deposition velocity to cylinder plotted against angle, polar plot. Four plots for different values of turbulence intensity are included. Showing only area covered by the filter and the filter width.

Figure 5.12

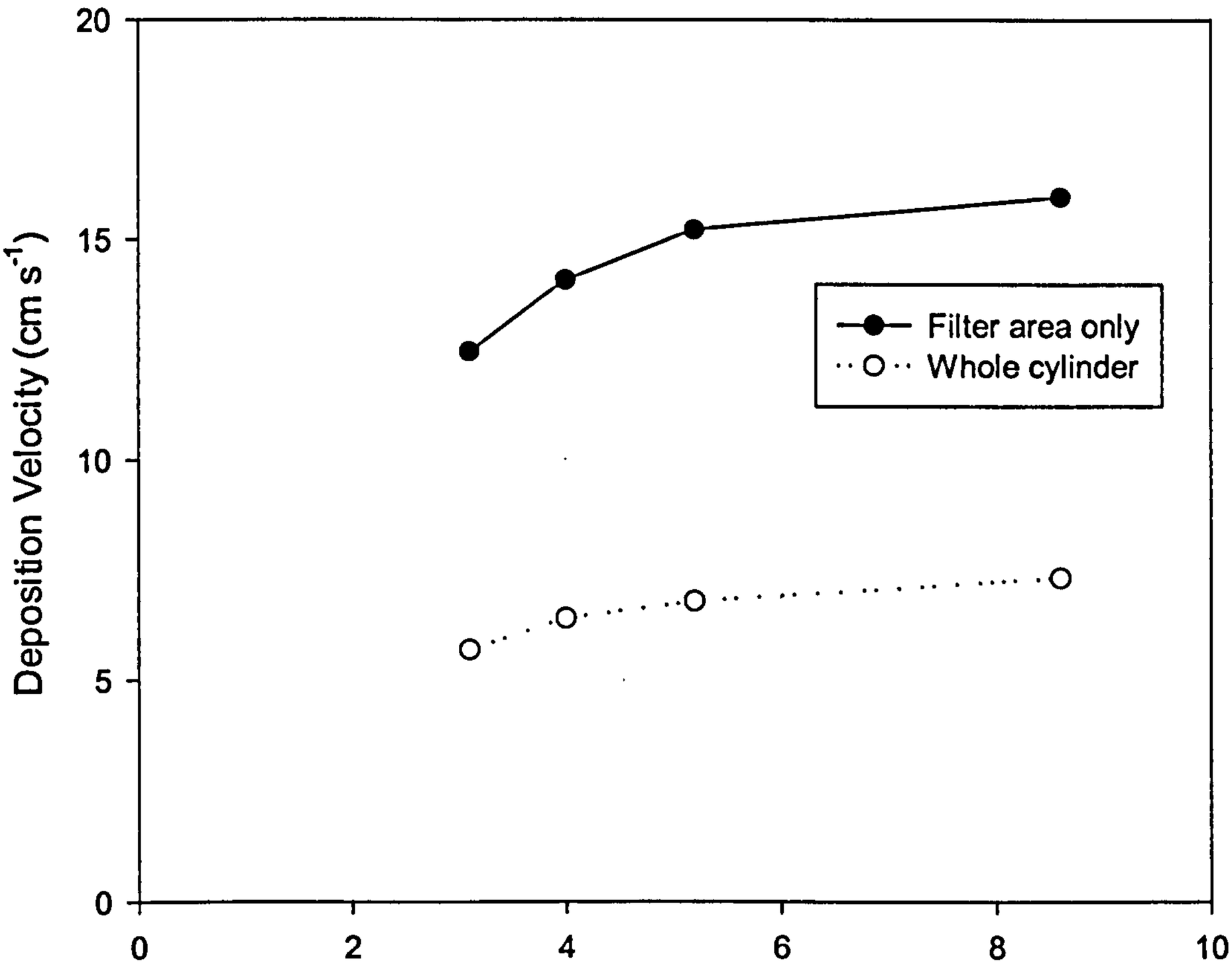

Comparison of calculated deposition velocities to the whole cylinder and to a circular filter on the upwind face.

Figure 5.13

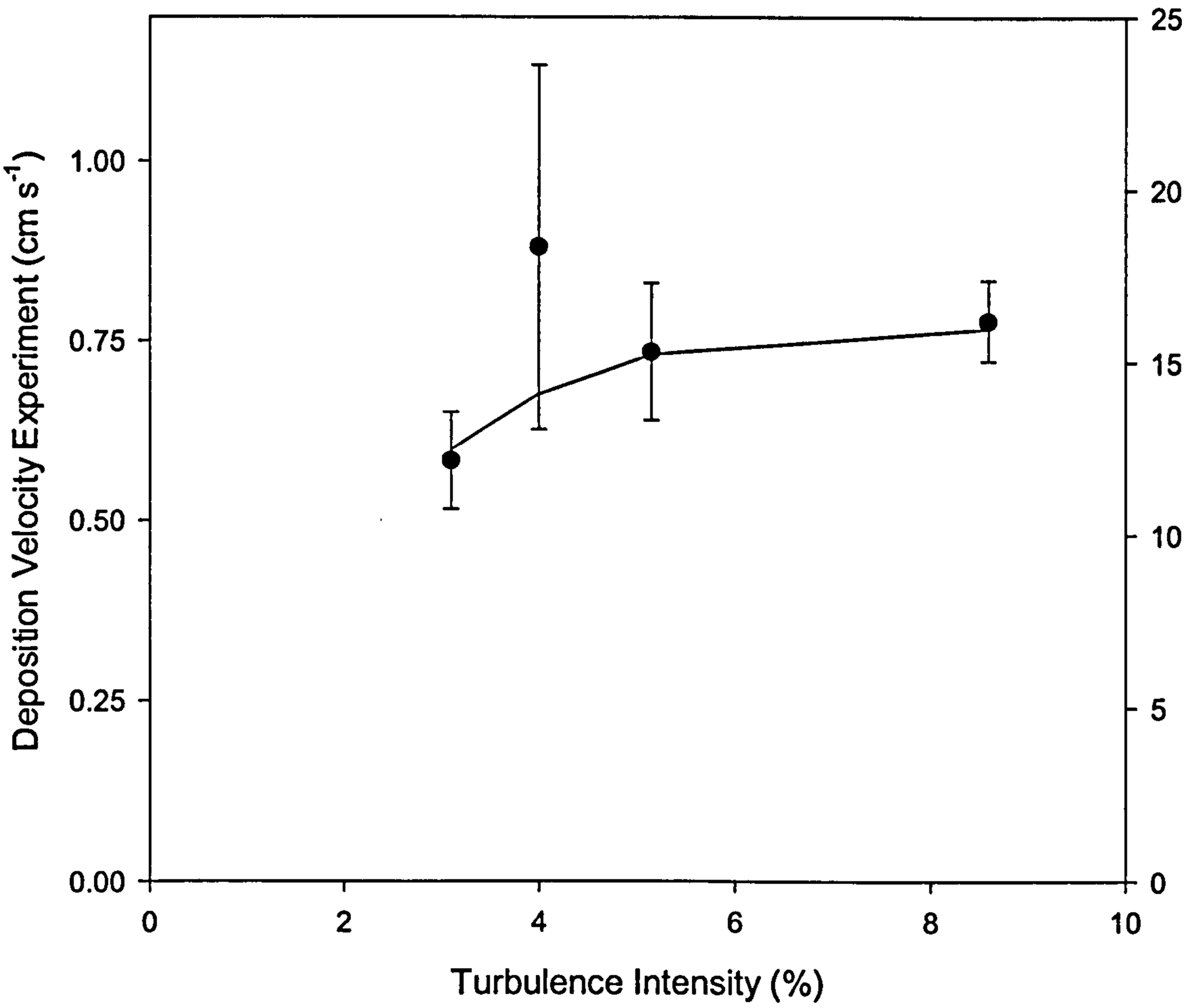

Graph showing comparison of CFD and experimentally determined deposition velocities to a 20mm cylinder. Note that CFD deposition velocities over-predict by a factor of approximately 20. CFD data is normalised by filter area to allow comparison.

Figure 5.14

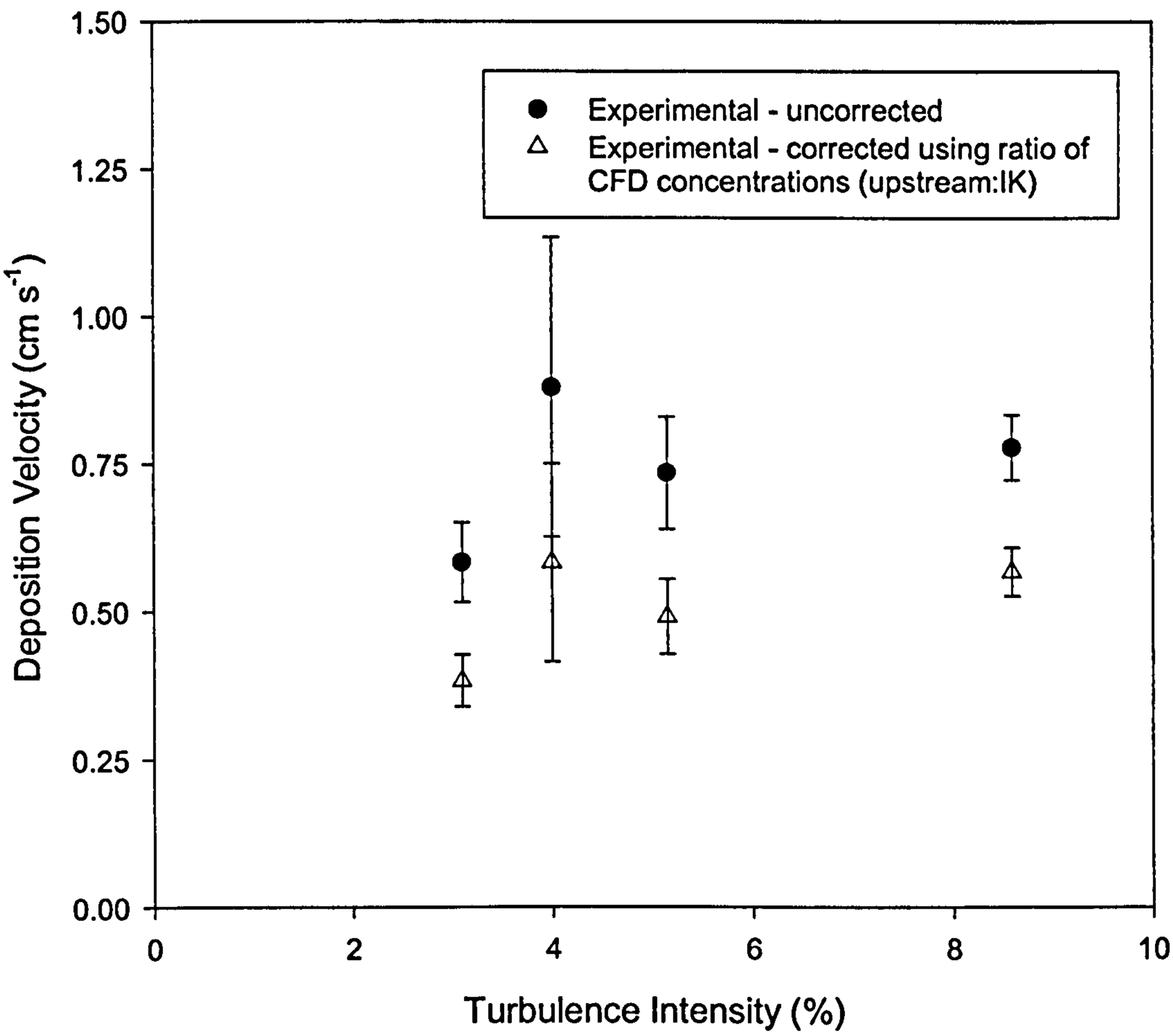

Graph showing experimentally determined deposition velocities to a 20mm cylinder, corrected using CFD calculated concentrations.

Figure 5.15

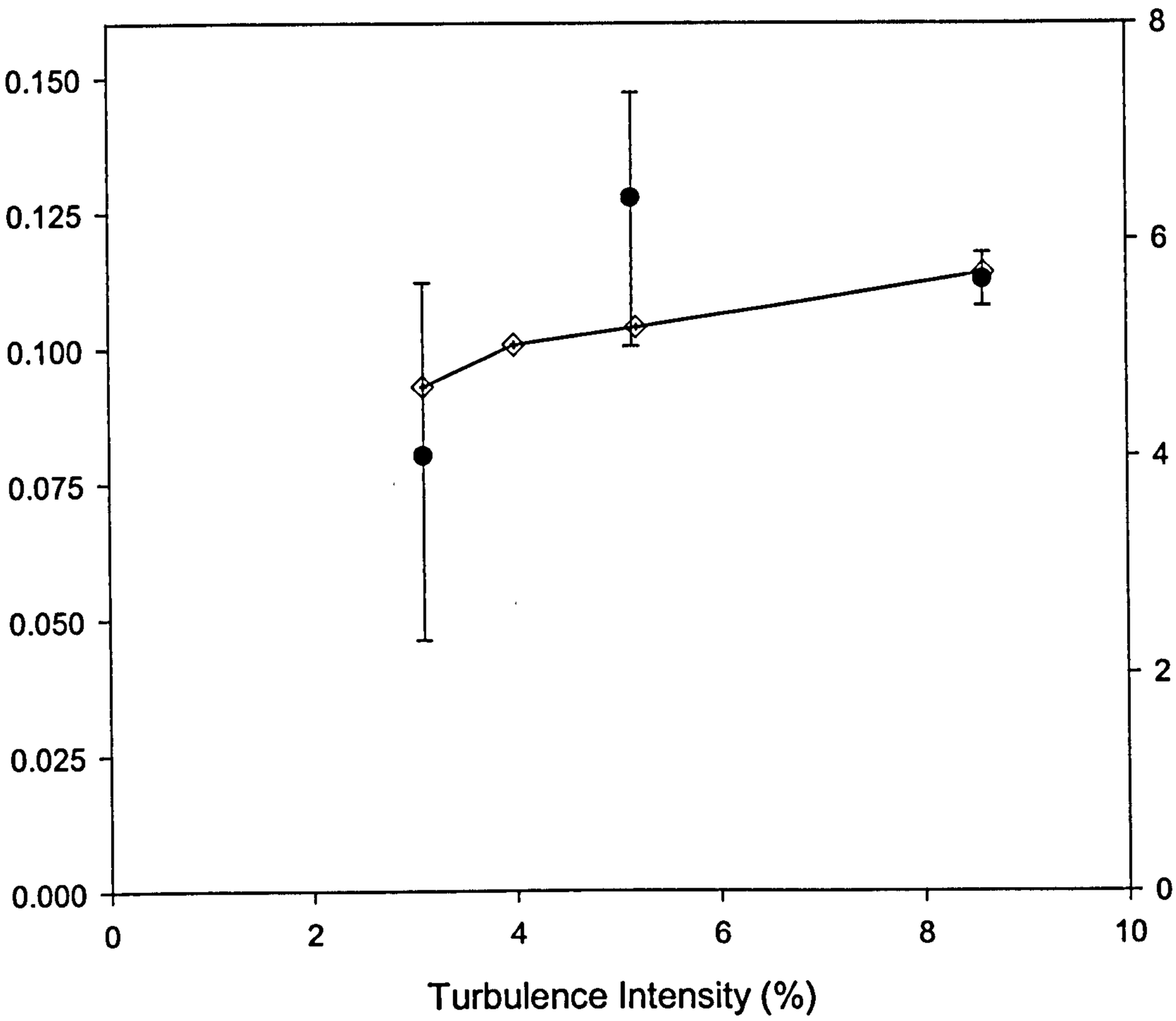

Graph showing comparison of CFD and experimentally determined deposition velocities to a 40mm vertical plane, parallel to the flow. Note that CFD deposition velocities over-predict by a factor of approximately 50. CFD data is normalised by filter area to allow comparison.

Figure 6.1

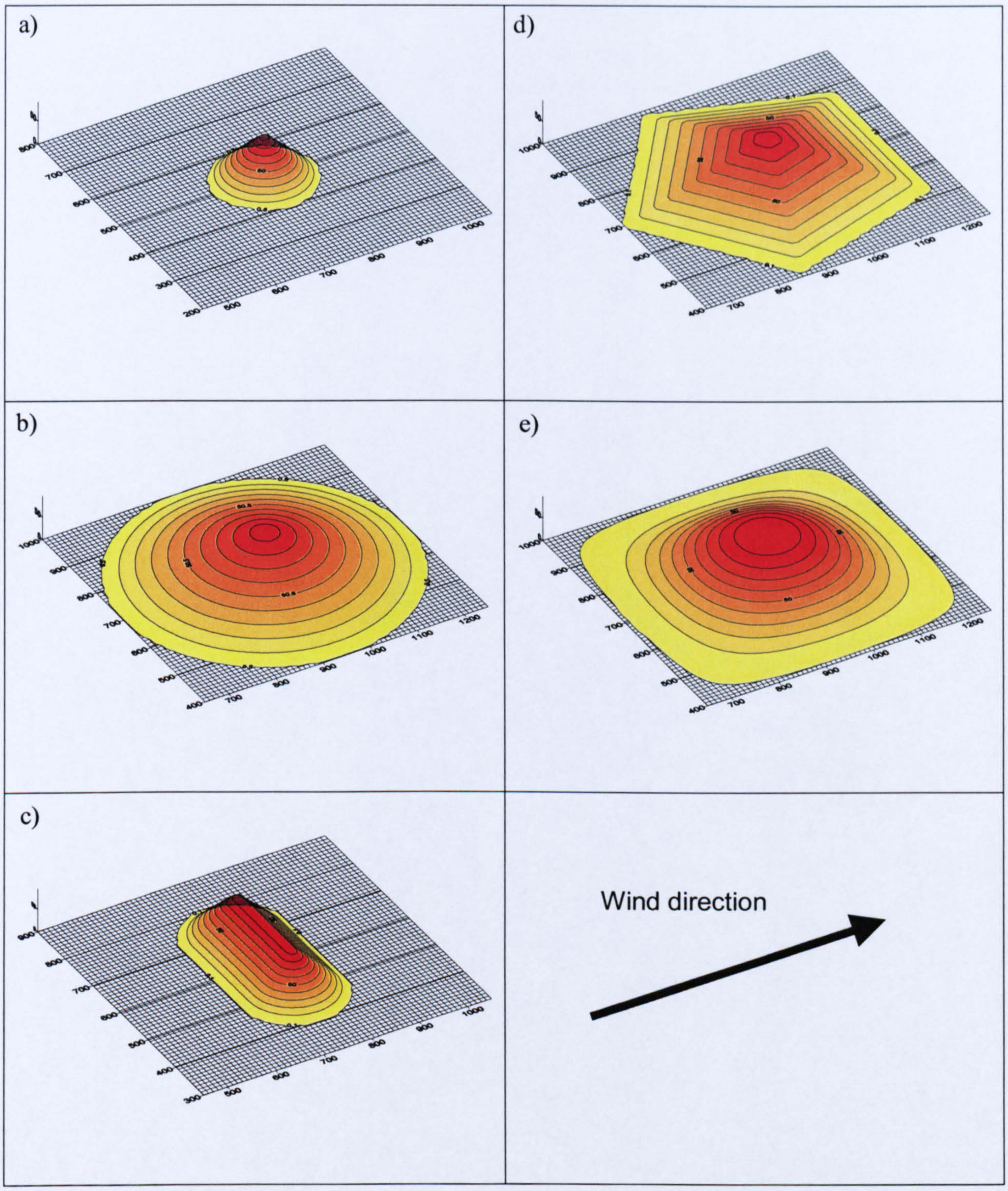

Visualisations of three-dimensional geometries studied. Contour plots of height overlaid on wireframe plots. Note that the maximum height in each case is 100m. a) cone 1 in 1, b) cone 1 in 3, c) elongated cone 1 in 1, d) 5-sided pyramid, and e) sinusoidal hill.

Figure 6.2

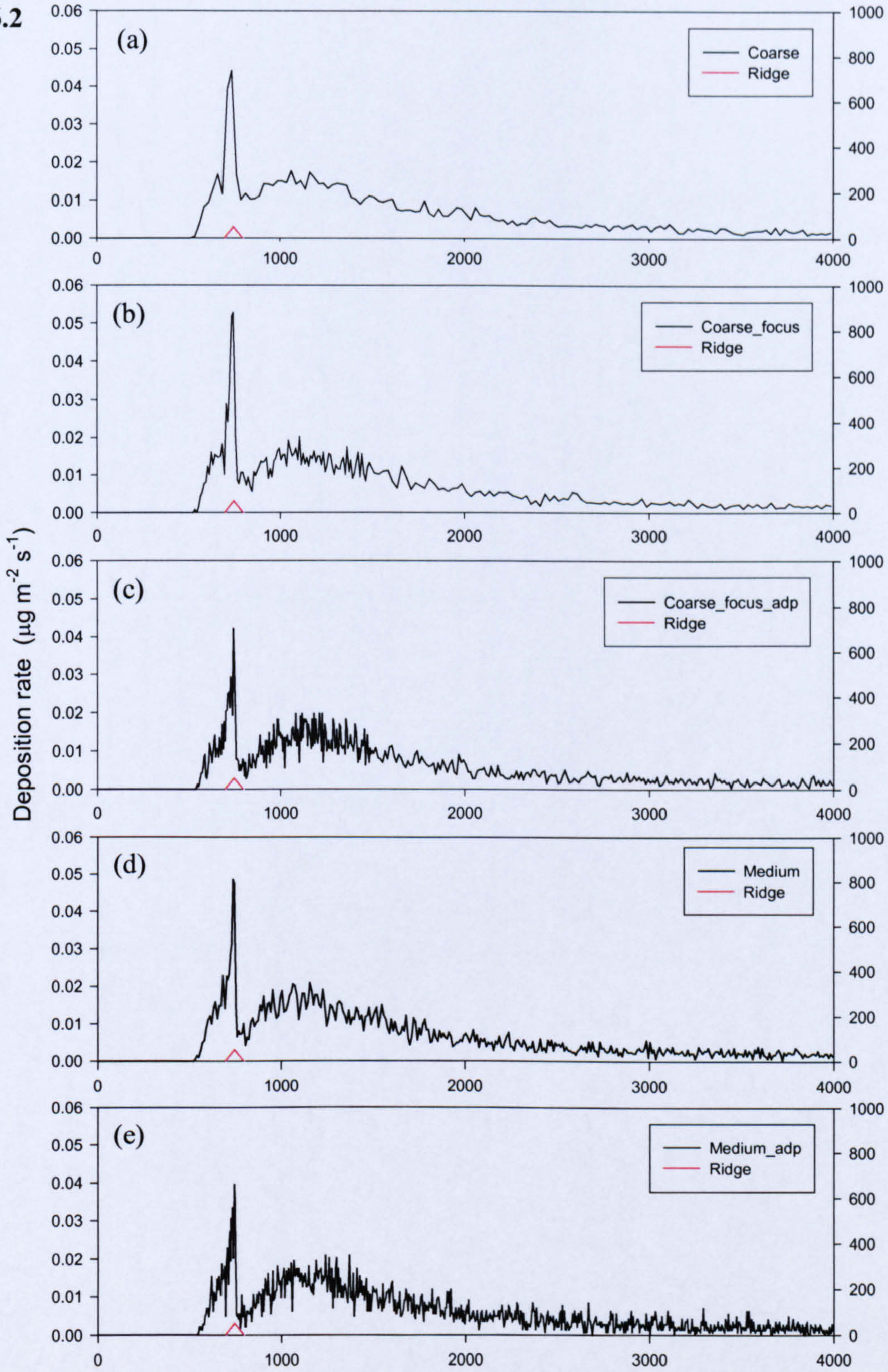

Graphs of predicted deposition rate using a variety of meshes. Note that the position of the ridge is indicated in red on each graph. Peak located at X=750m. Legend shows mesh density. X is downwind distance.

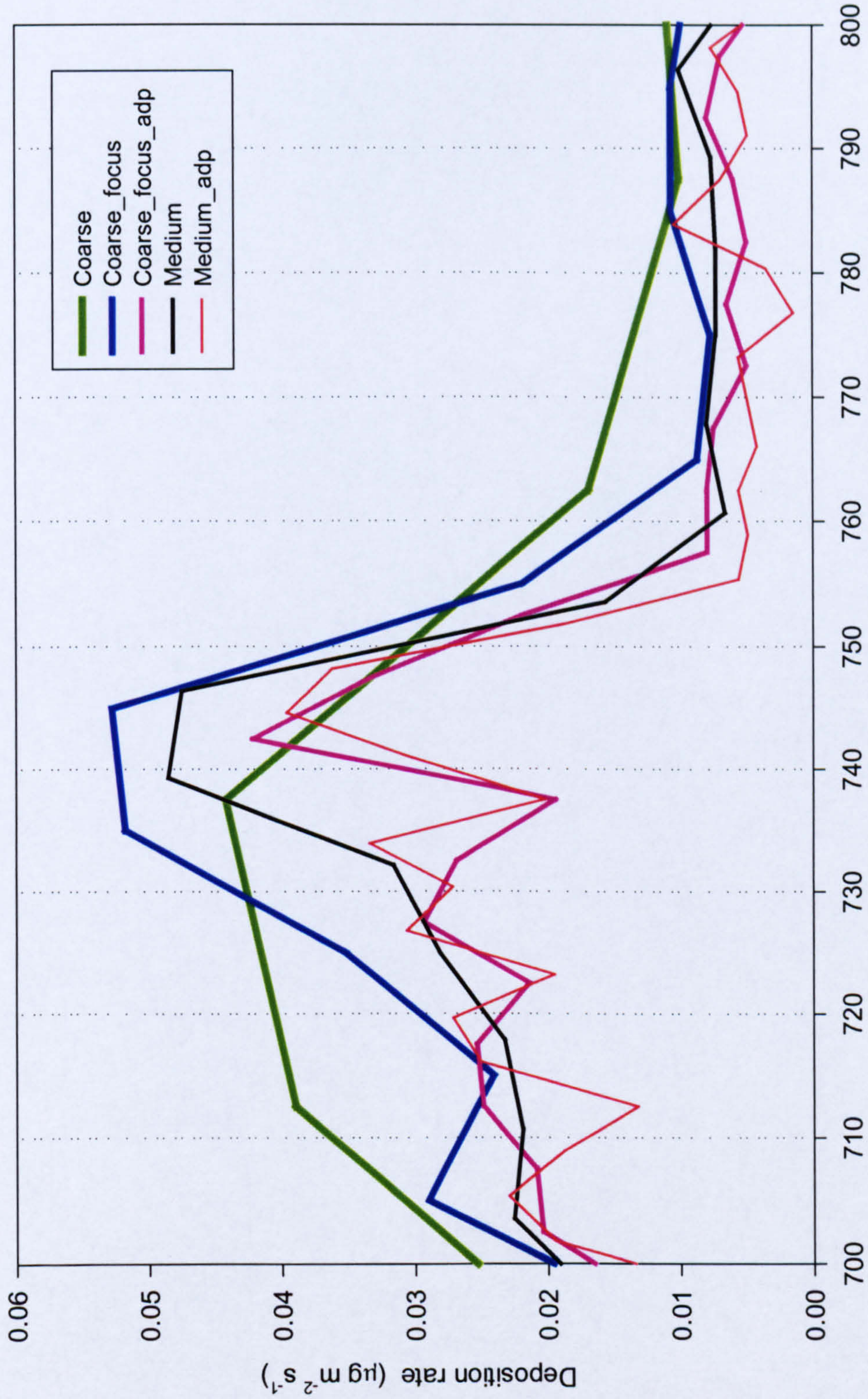

Figure 6.3

Graph of deposition rate for a variety of meshes. Overlaid and focused on area within 50m of peak (X=750m). Legend shows mesh density.

Figure 6.4

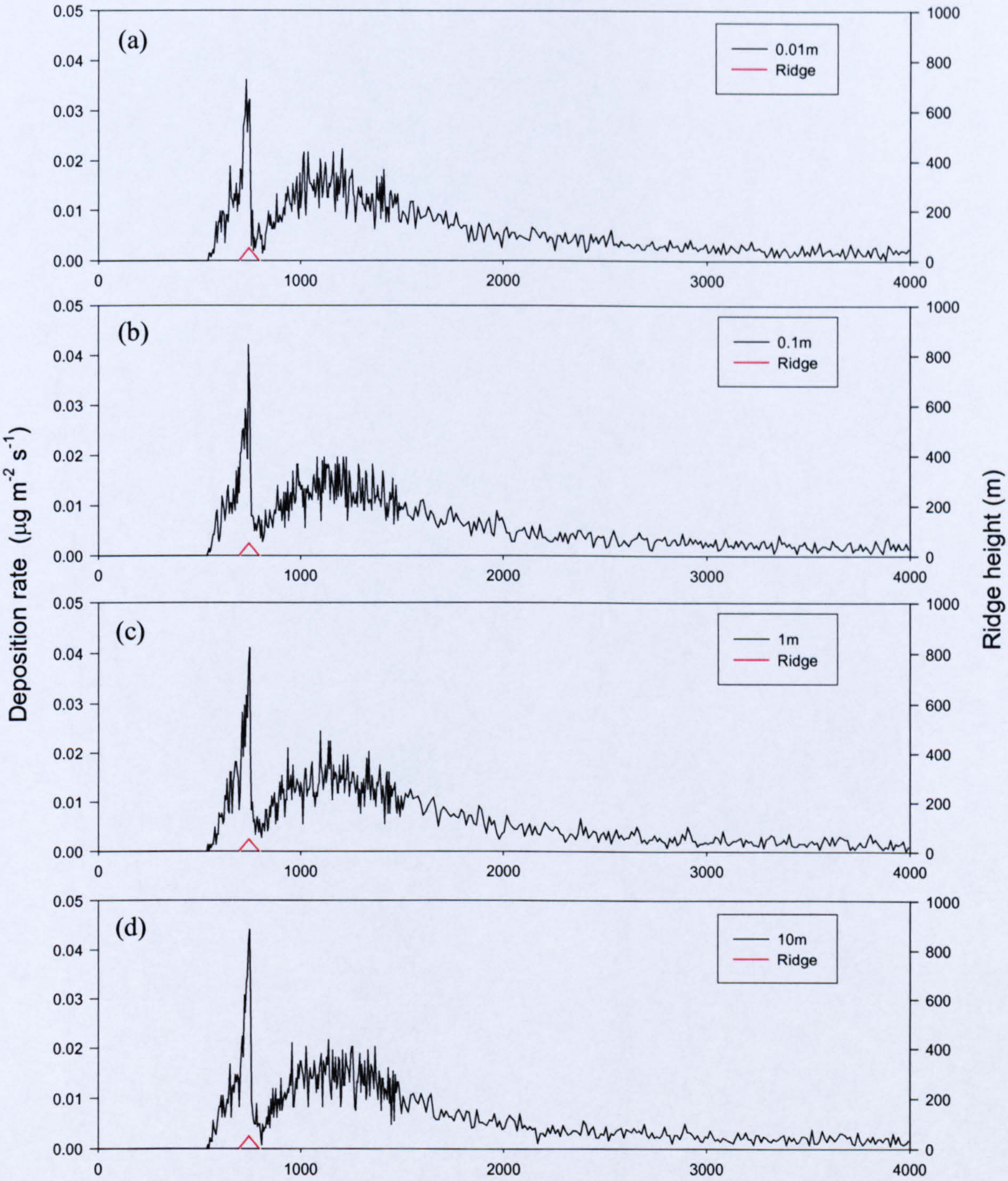

Graphs of predicted deposition rate for a range of particle trajectory step sizes. Legend shows maximum step size. Note that the position of the ridge is indicated in red on each graph. Peak located at X=750m.

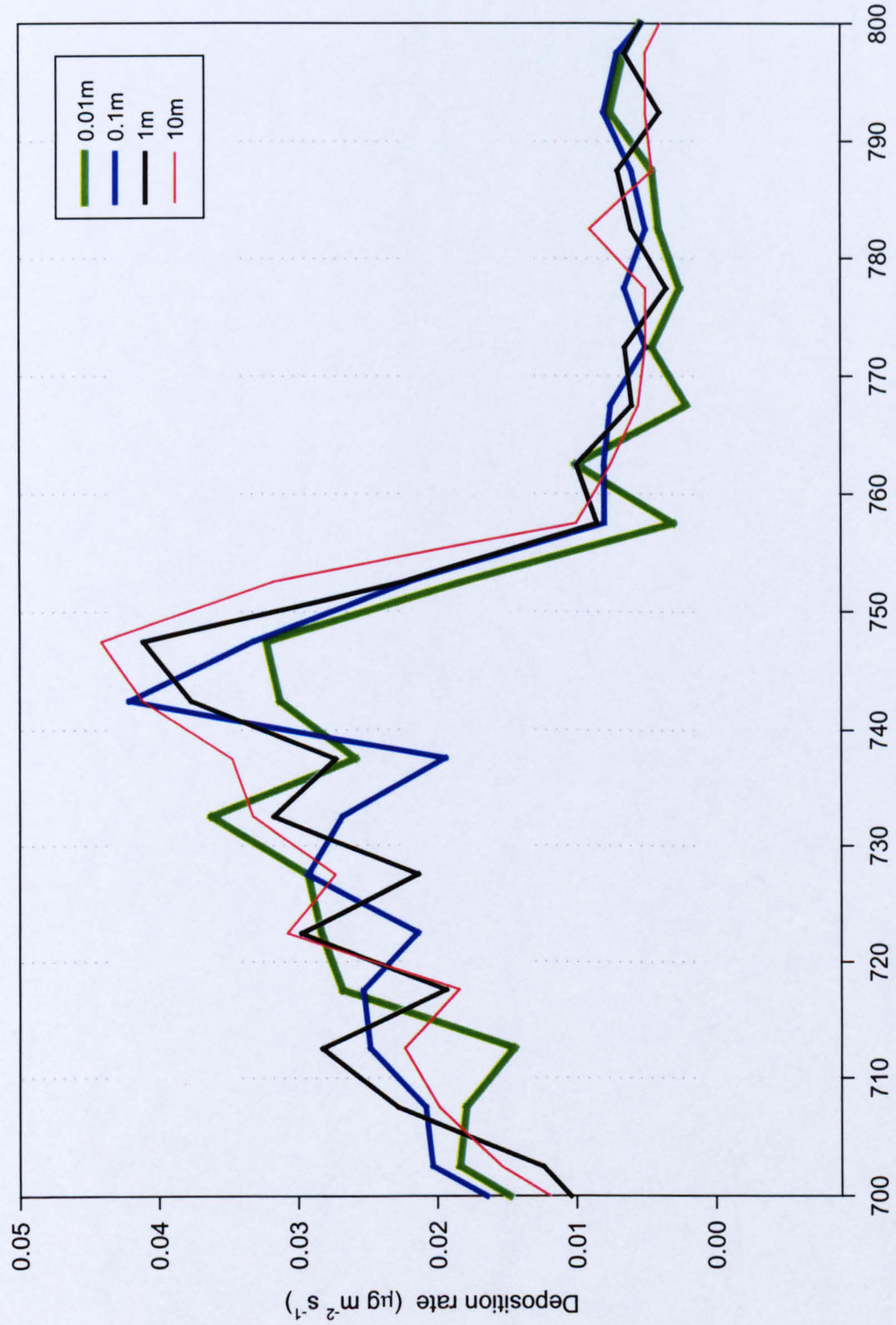

Figure 6.5 Graph of deposition rate for a range of particle trajectory step sizes. Legend shows maximum step size. Overlaid and focused on area within 50m of peak (X=750m, 10m).

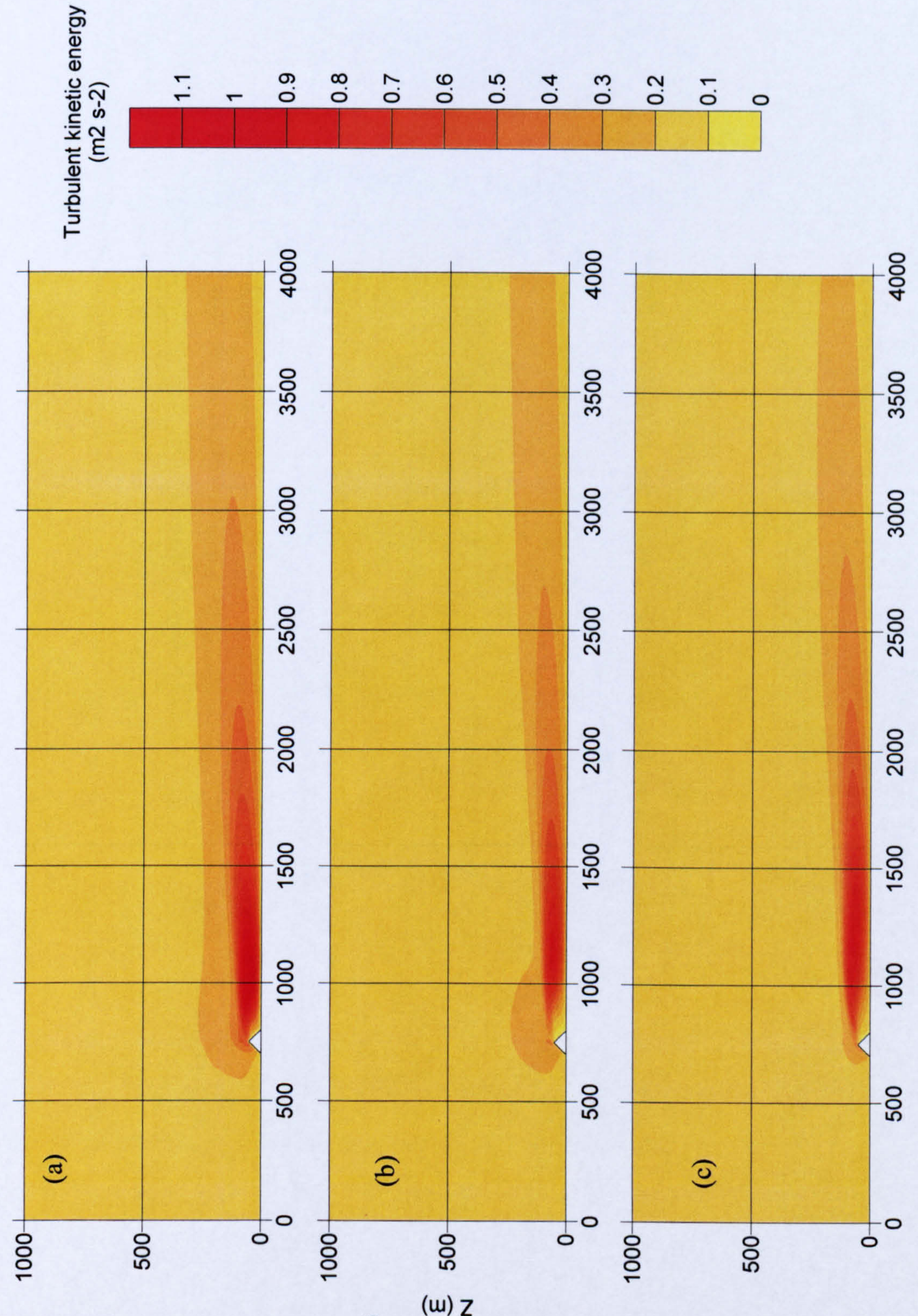

Figure 6.6 Contour plots of turbulent kinetic energy in flow over a triangular ridge, predicted using three different turbulence models.

a) STD k-eps

b) RNG k-eps

c) RSM

Figure 6.7

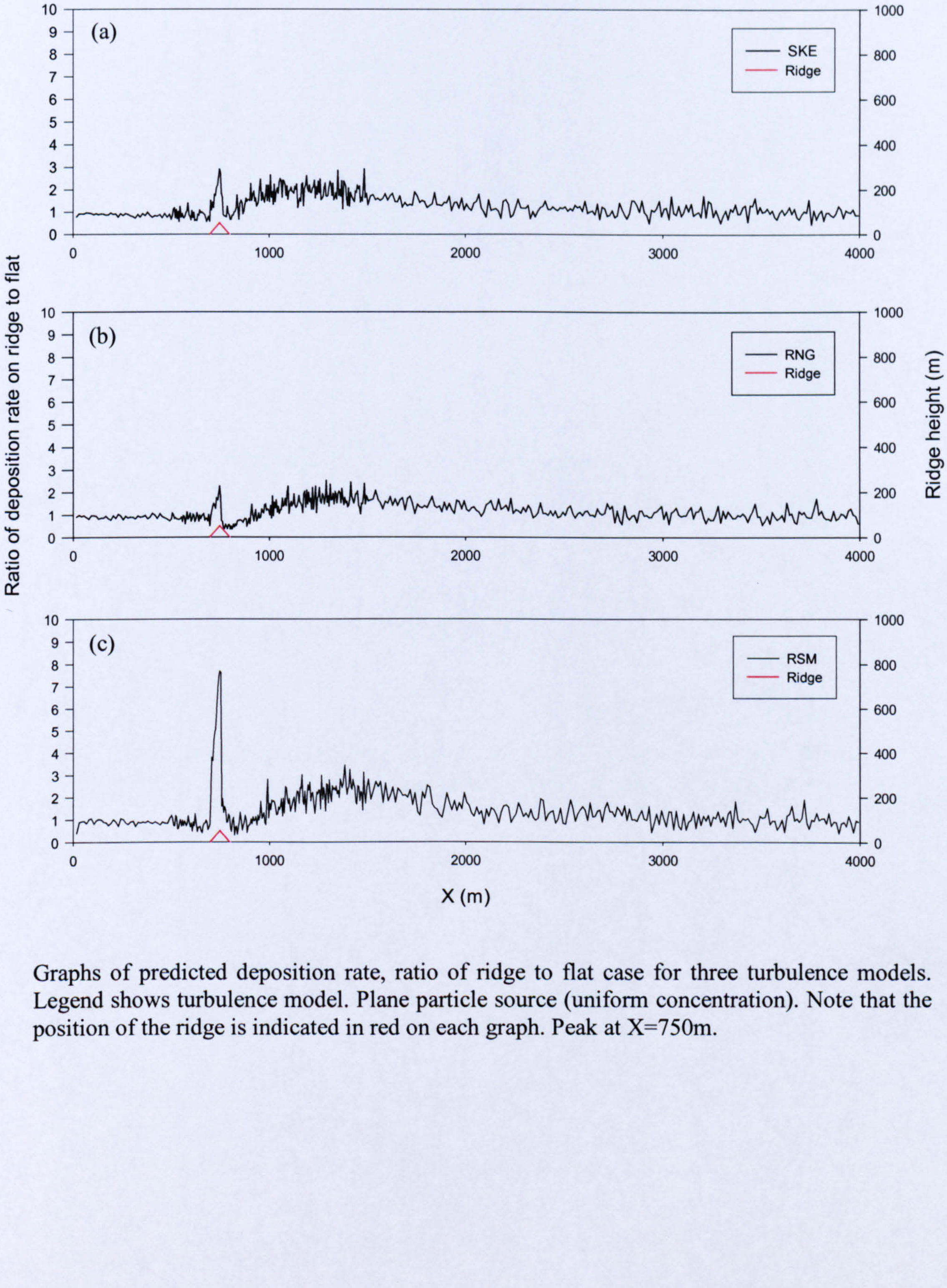

Graphs of predicted deposition rate, ratio of ridge to flat case for three turbulence models. Legend shows turbulence model. Plane particle source (uniform concentration). Note that the position of the ridge is indicated in red on each graph. Peak at X=750m.

Figure 6.8

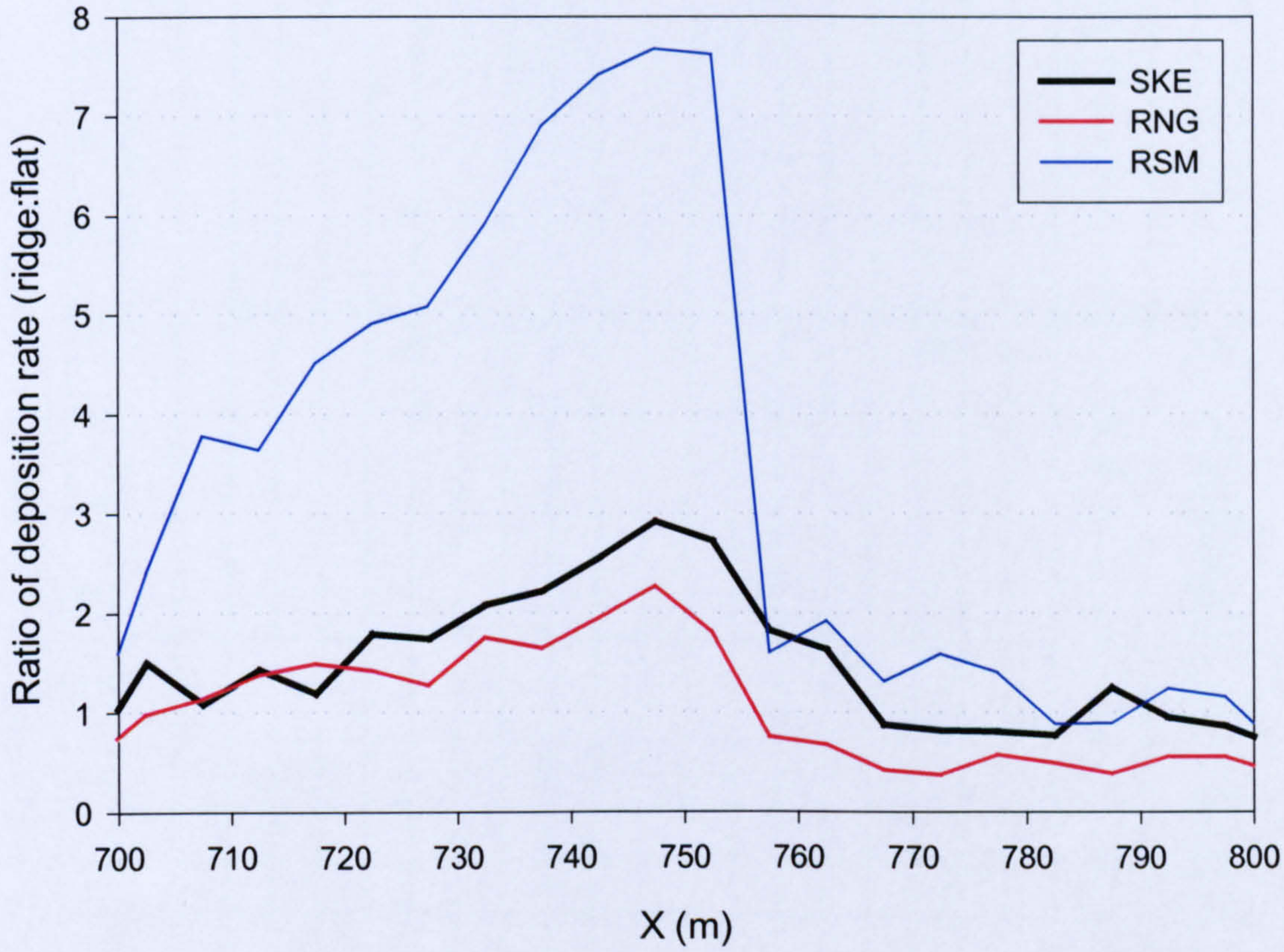

Graphs of predicted deposition rate, ratio of ridge to flat case for three turbulence models. Legend shows turbulence model. Area surrounding peak of ridge (X=750m). Graphs overlaid.

Figure 6.9

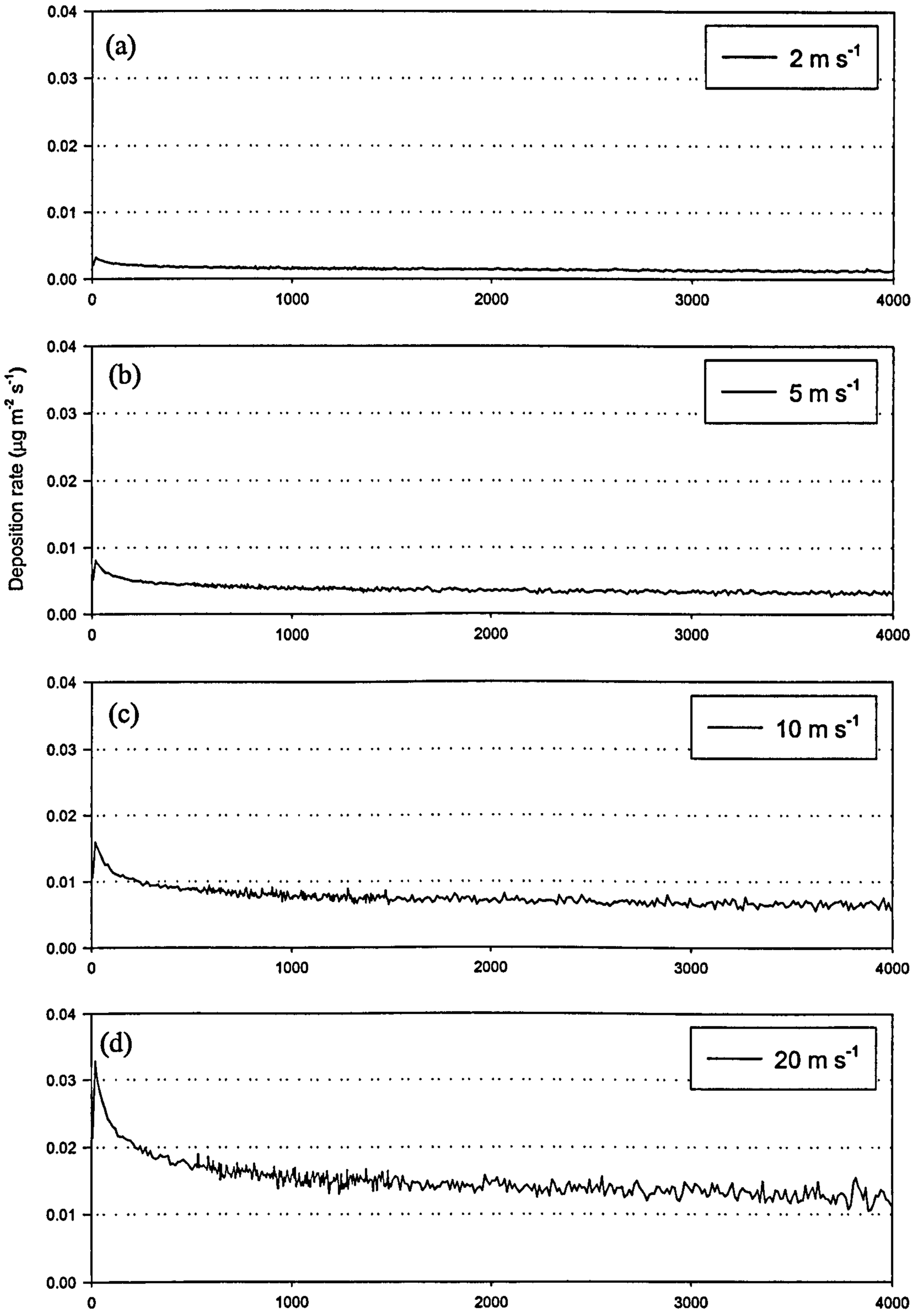

Deposition rates for flat case at four different wind speeds. Legend shows wind speed at 10m above the ground.

Figure 6.10

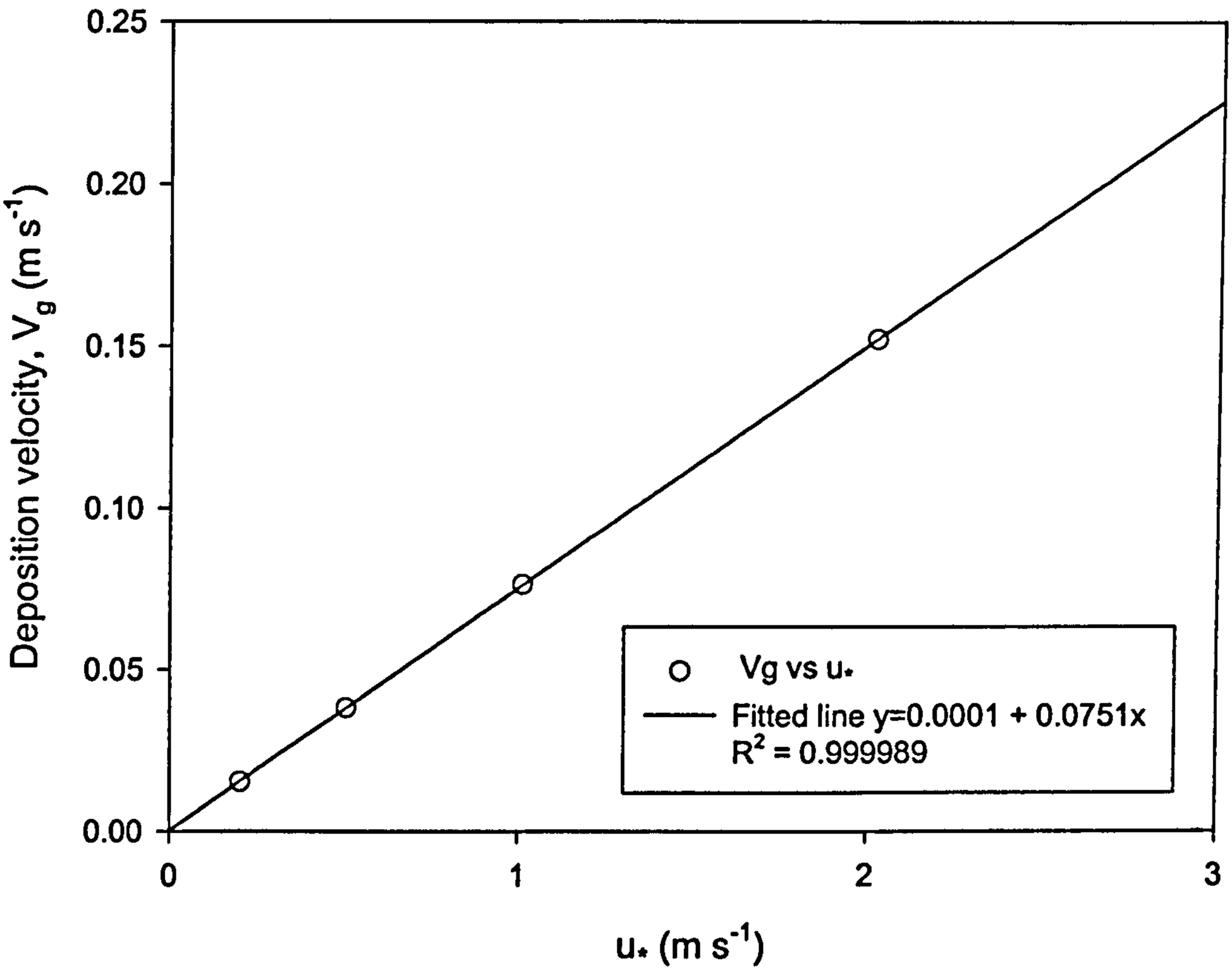

Graph of variation in average calculated deposition velocity (V_g) with friction velocity (u_*). Circles are CFD results, line is a fitted straight line with coefficients as shown on graph.

Figure 6.11

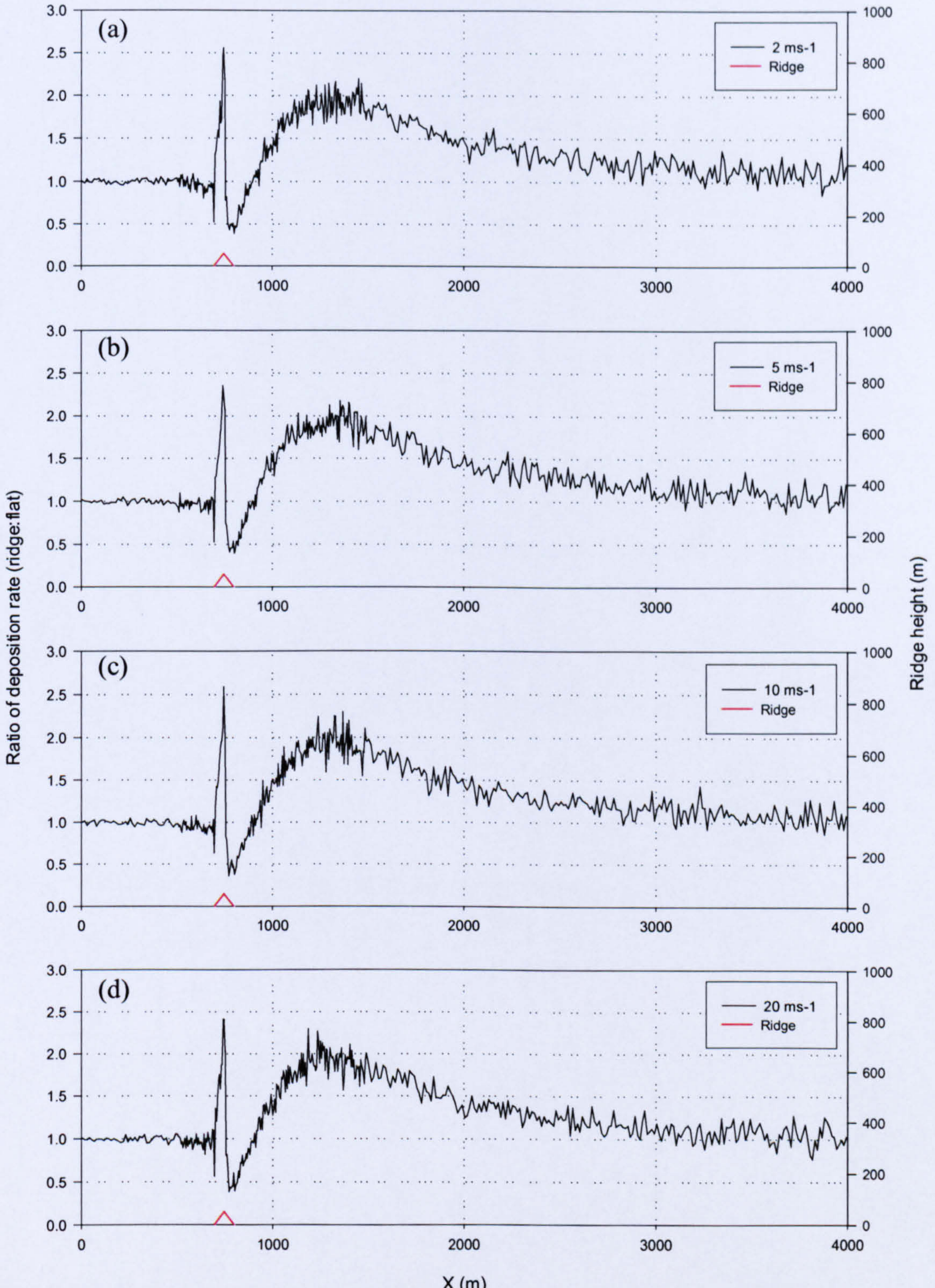

Graphs of ratio of deposition rate from ridge to flat case, for various wind speeds at 10m above the surface. Plane particle source (uniform concentration). Legend shows wind speed at 10m above surface. Note that the position of the ridge is indicated in red on each graph. Peak at X=750m.

Figure 6.12

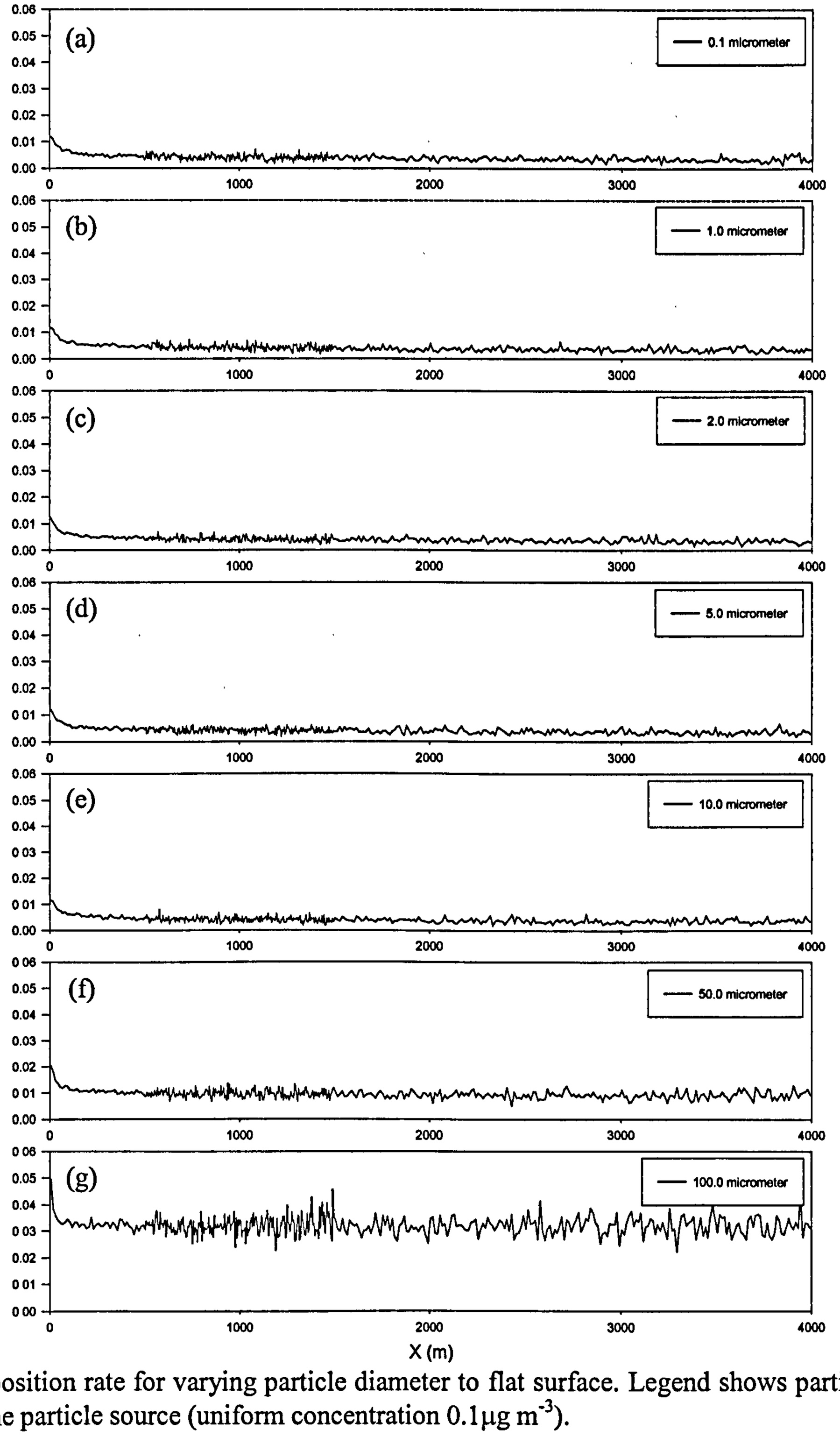

Graphs of deposition rate for varying particle diameter to flat surface. Legend shows particle diameter. Plane particle source (uniform concentration 0.1µg m^{-3}).

Figure 6.13

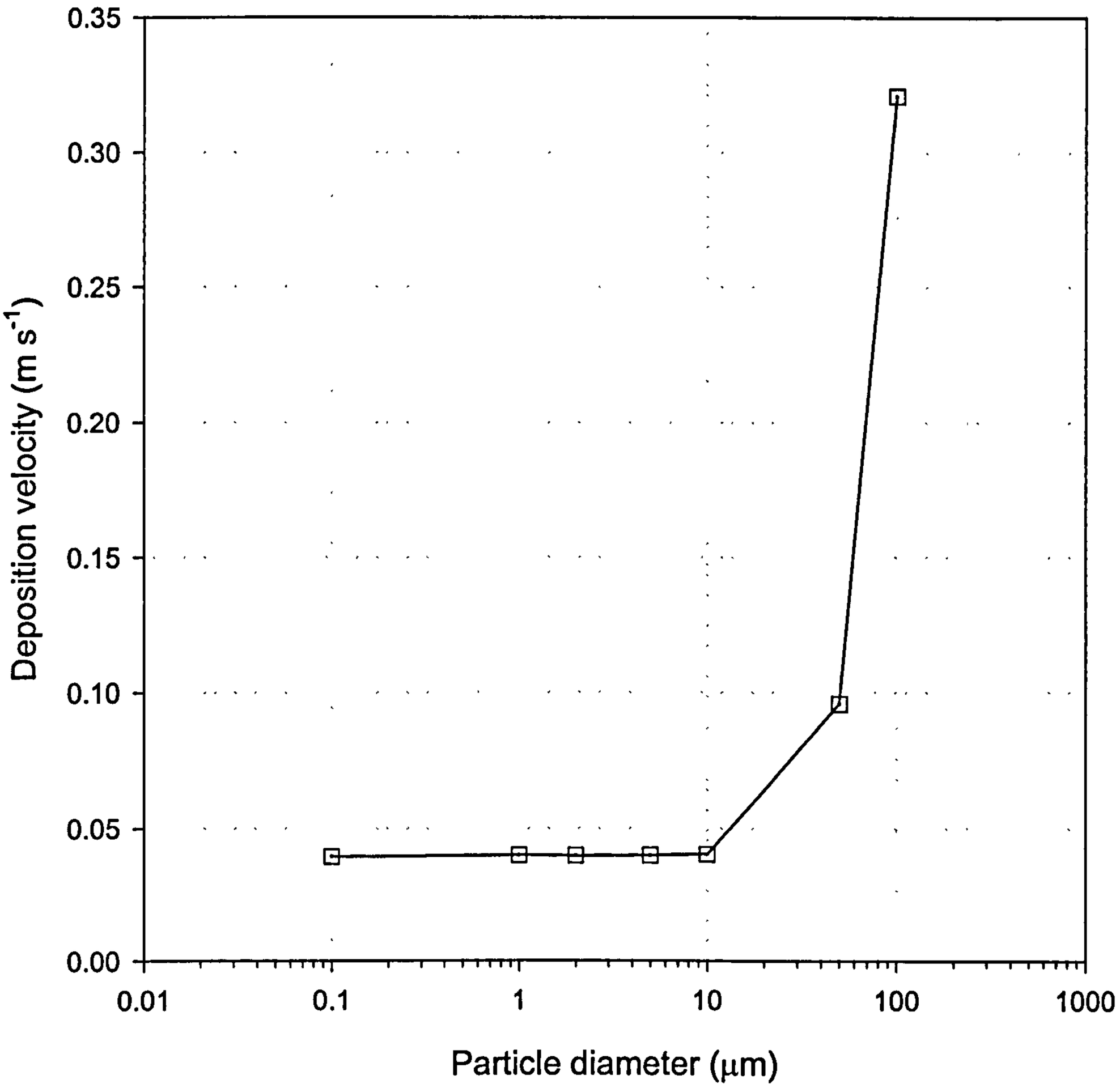

Graph showing average deposition velocity against particle diameter (diameter is shown on a log scale).

Figure 6.14

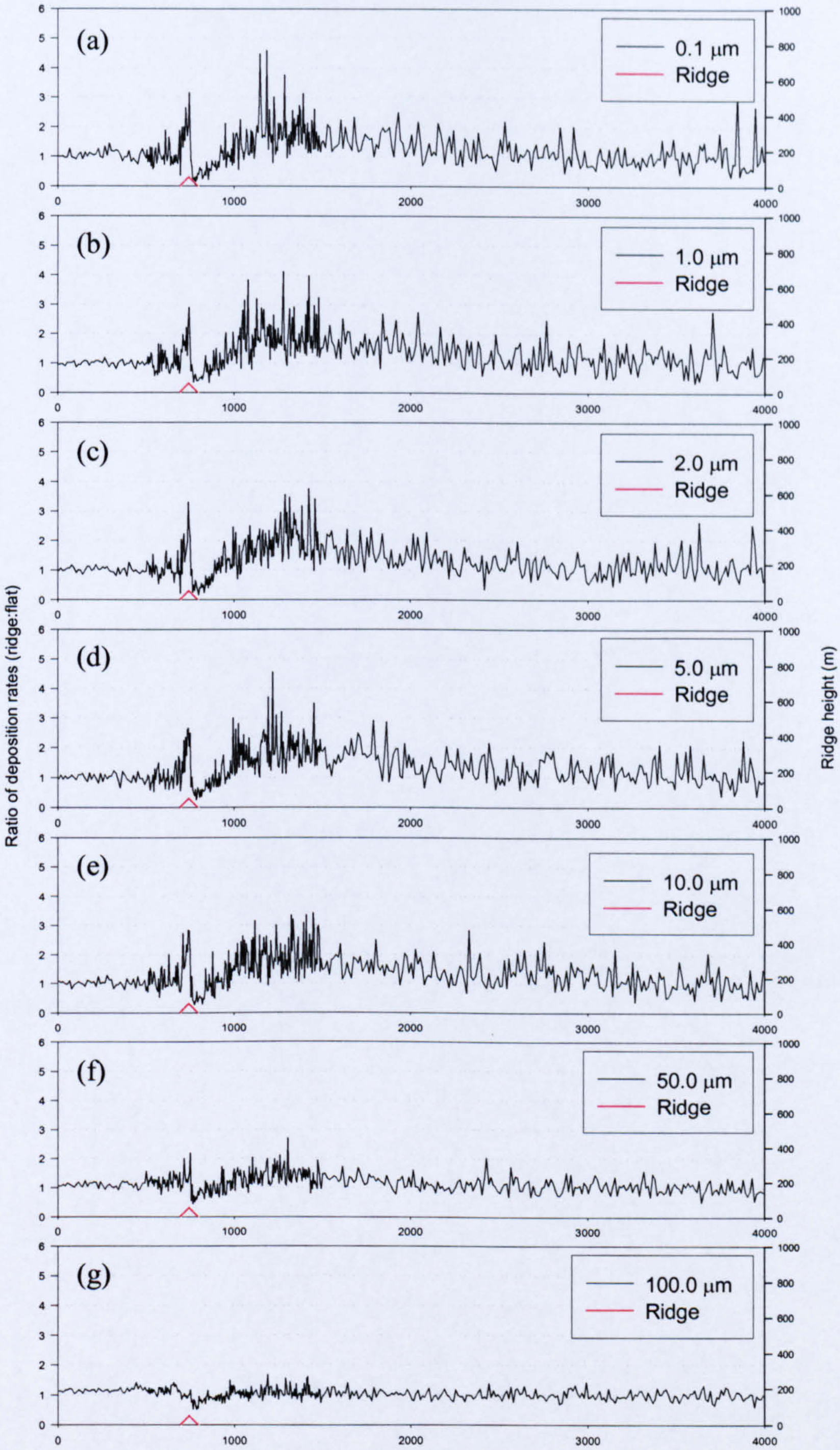

Ratio of deposition rate for ridge to flat case. Legend shows particle diameter. Plane particle source (uniform concentration). Note that the position of the ridge is indicated in red on each graph. Peak at X=750m.

Figure 6.15

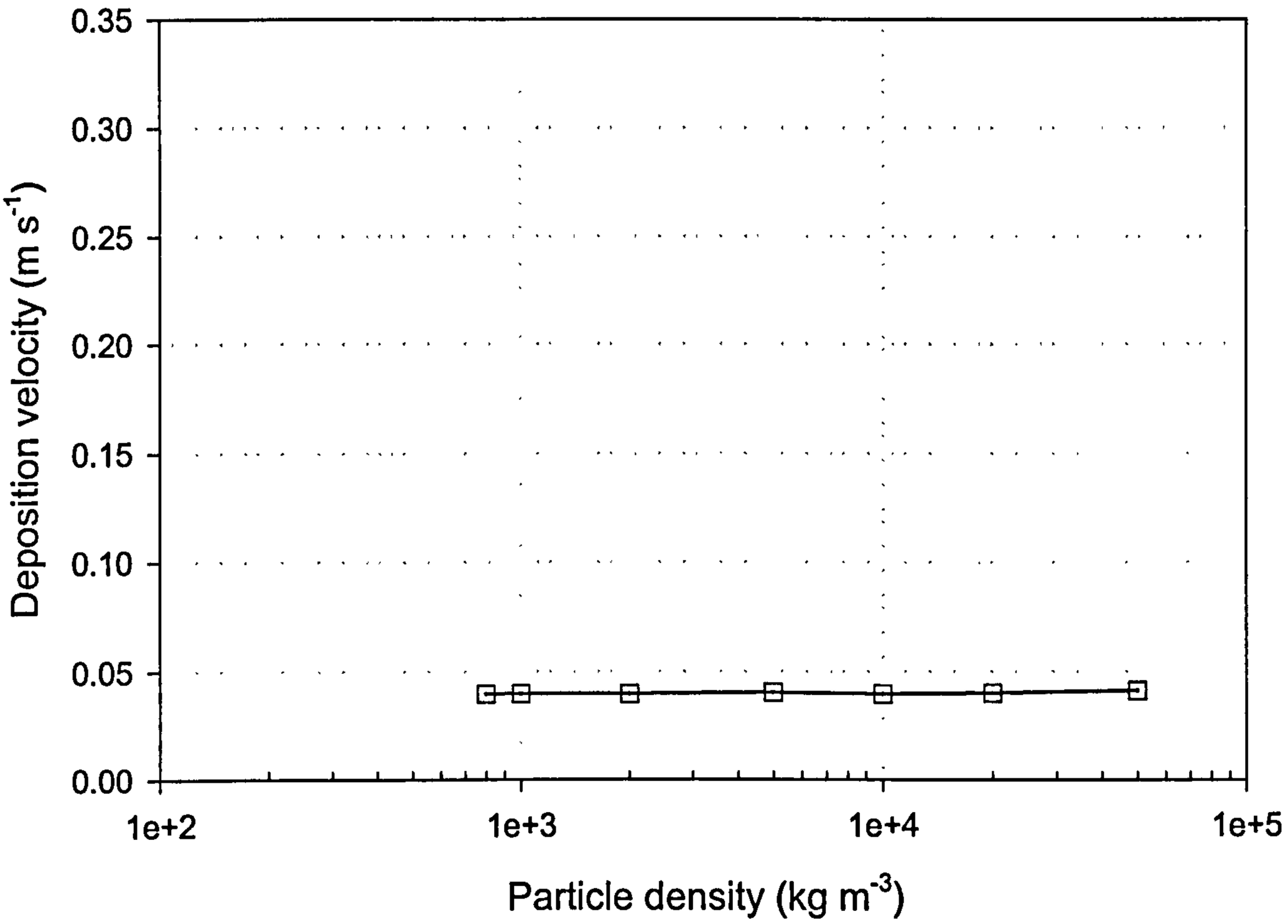

Graph showing average deposition velocity against particle density. Particle density plotted on a log scale. For ease of comparison the vertical scale is the same as Figure 6.13.

Figure 6.16

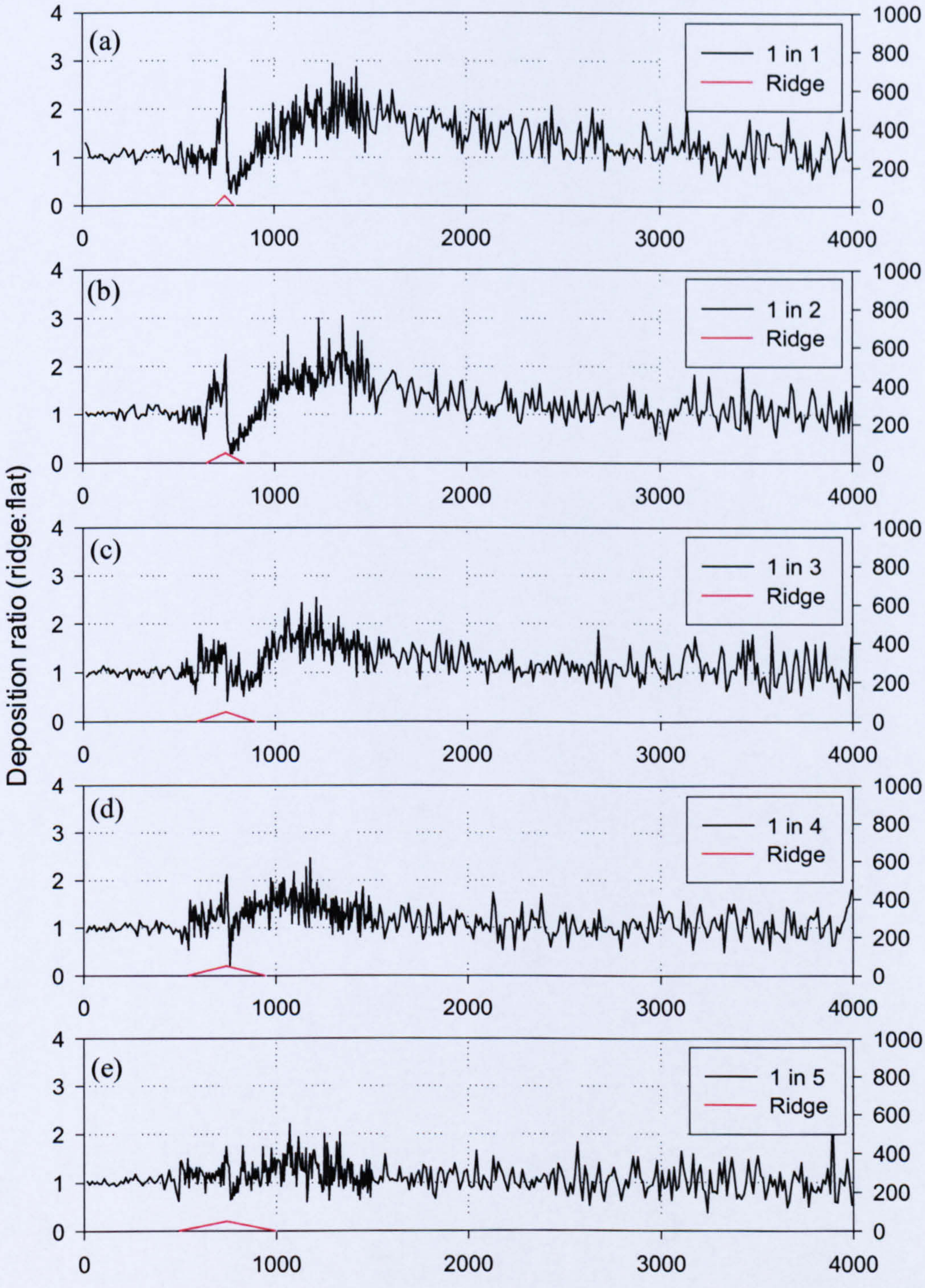

Ratio of deposition to flat case for five ridges of different slopes. Legend shows ridge slope. Plane particle source (uniform concentration). Note that the position of the ridge is indicated in red on each graph. Peak at X=750m.

Figure 6.17

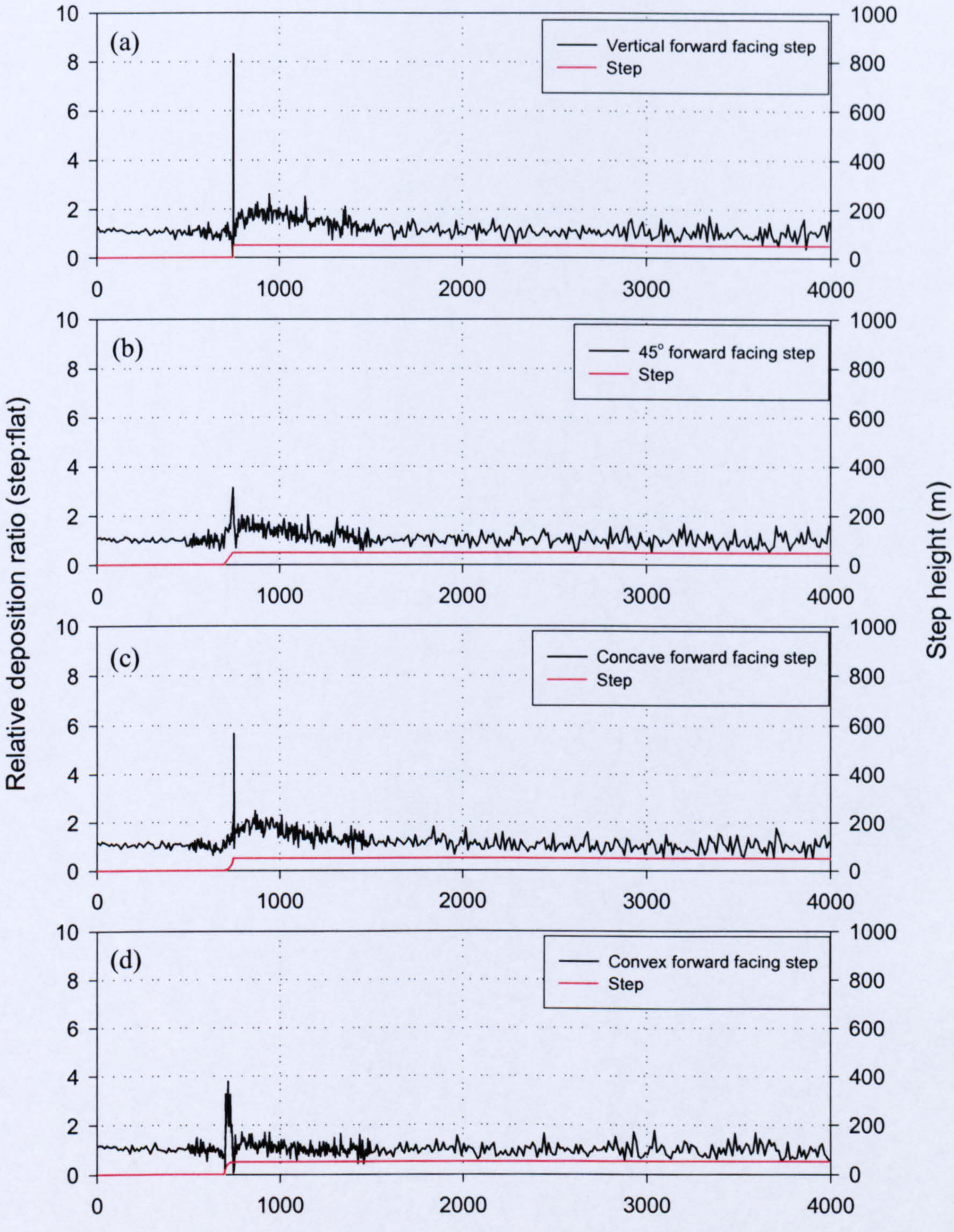

Graphs of relative deposition to four different forward facing steps. Legend shows step type. Plane particle source (uniform concentration). Note that the position of the step is indicated in red on each graph. Step is at X=700-750m depending on the geometry.

Figure 6.18

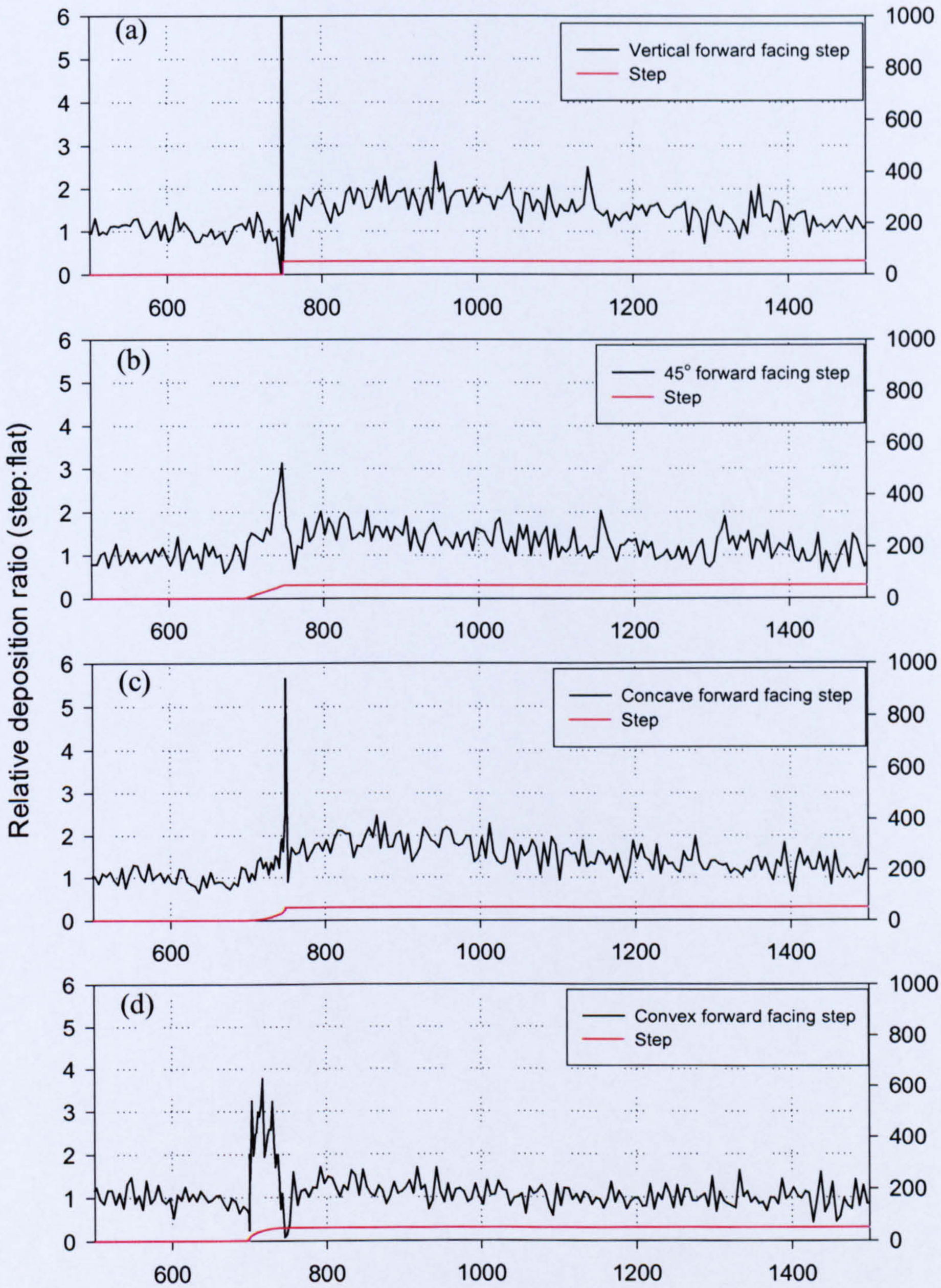

A selected portion of the graphs in Figure 6.17, focussing on the area round the step. Legend shows step type. Note that the top of the deposition curve for the vertical step is above the limit of the vertical axis in this figure.

Figure 6.19

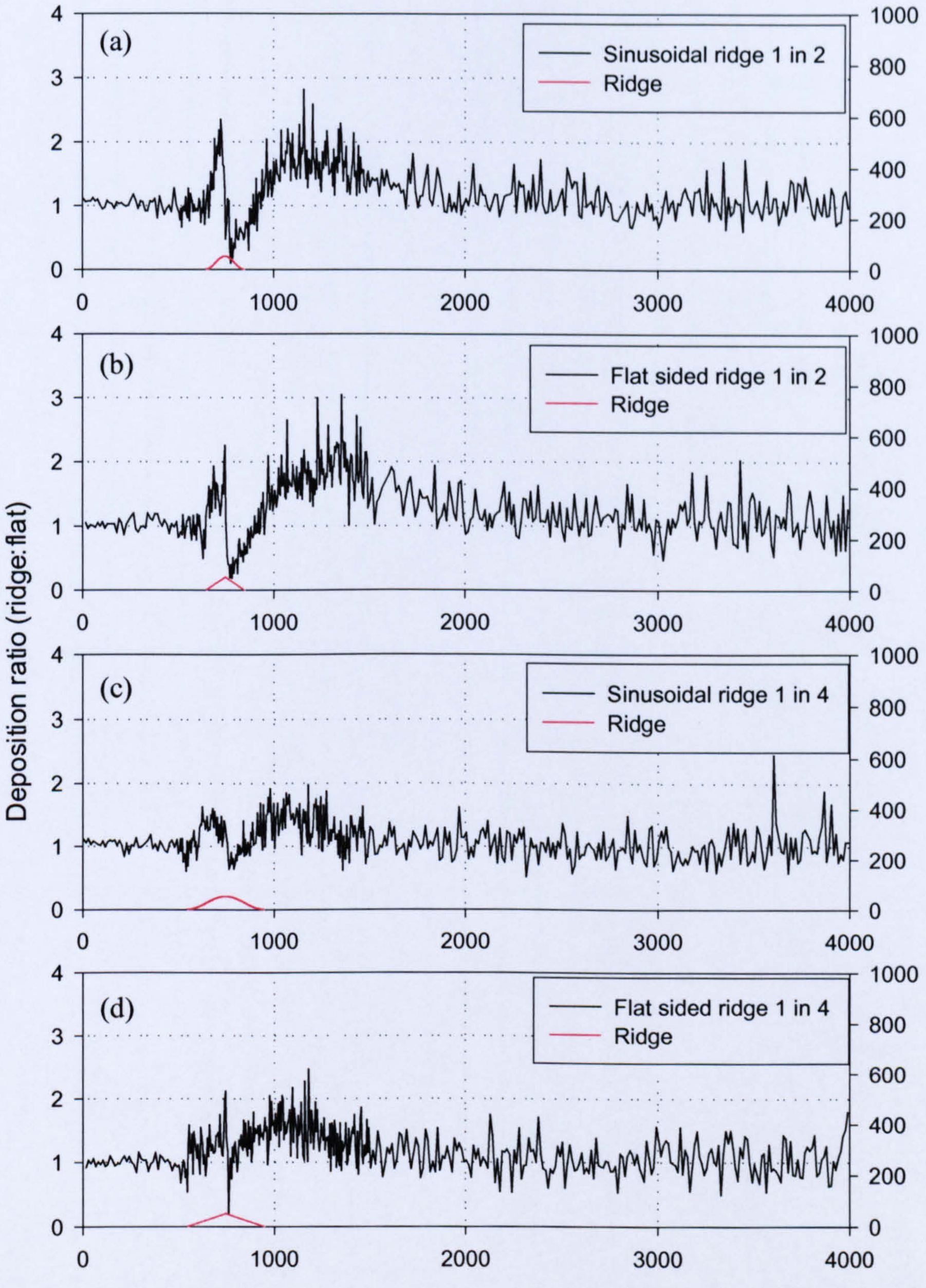

Graphs of relative deposition to sinusoidal cross-section ridges, presented with flat sided ridges for comparison. Plane particle source (uniform concentration). Legend shows ridge type and slope. Note that the position of the ridge is indicated in red on each graph. Peak at X=750m.

Figure 6.20

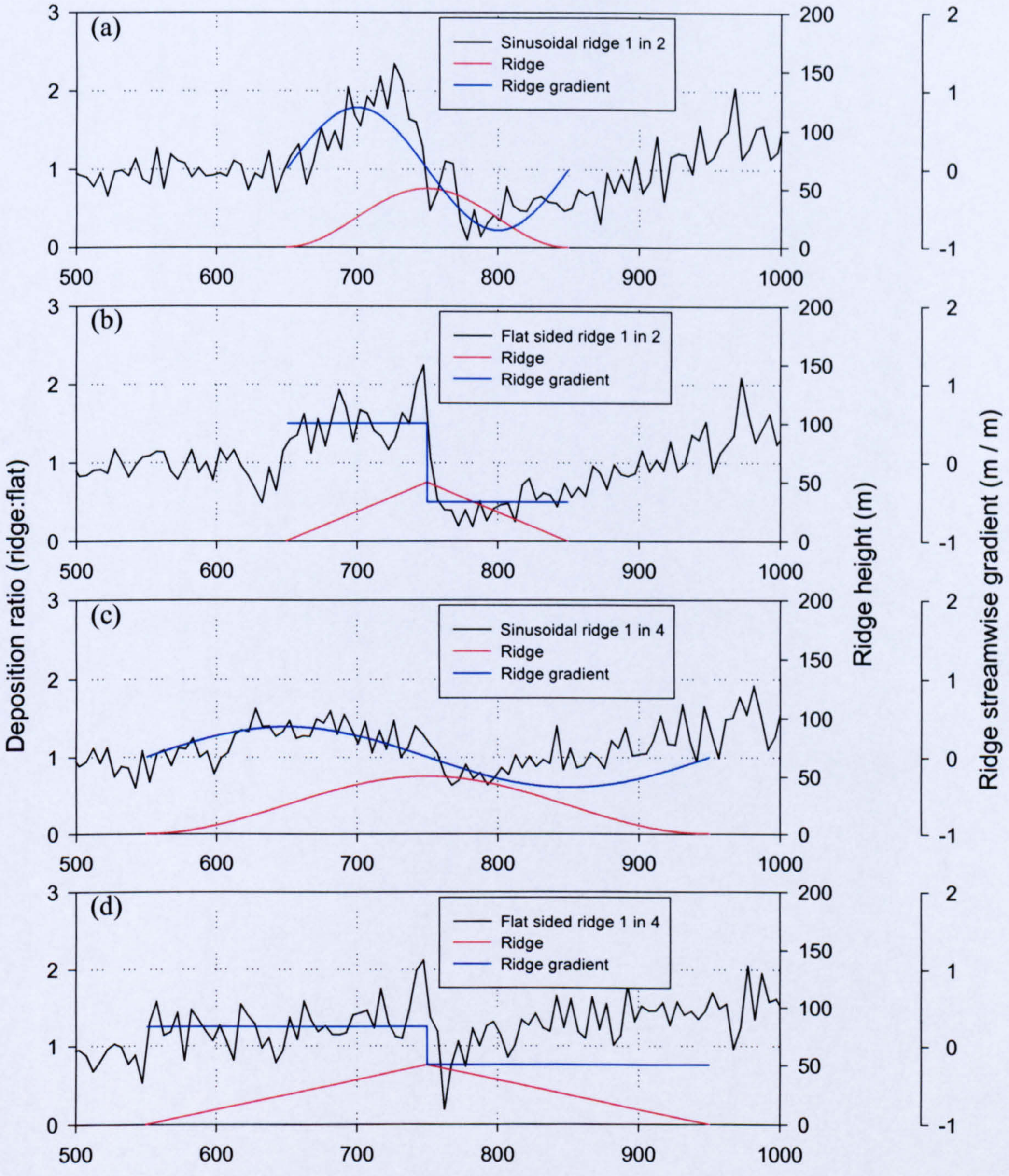

Graphs of relative deposition to sinusoidal cross-section ridges, presented with flat sided ridges for comparison. Plane particle source (uniform concentration). Legend shows ridge type and slope. Note that the position of the ridge is indicated in red on each graph. Streamwise gradient of ridges also included in blue.

Figure 6.21

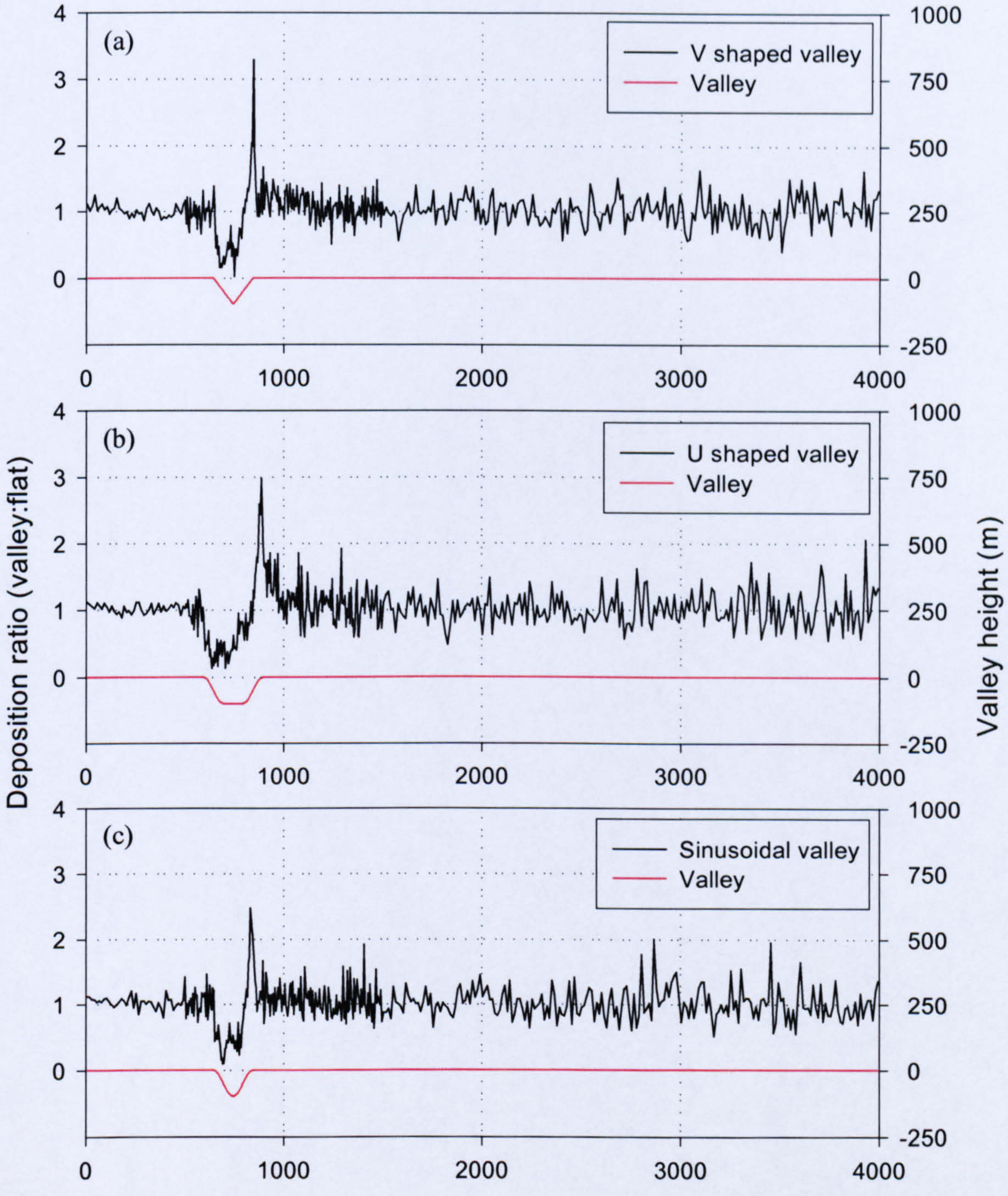

Graphs of relative deposition to three different valley geometries. Plane particle source (uniform concentration). Legend shows valley type. Note that the position of the valley is indicated in red on each graph.

Figure 6.22

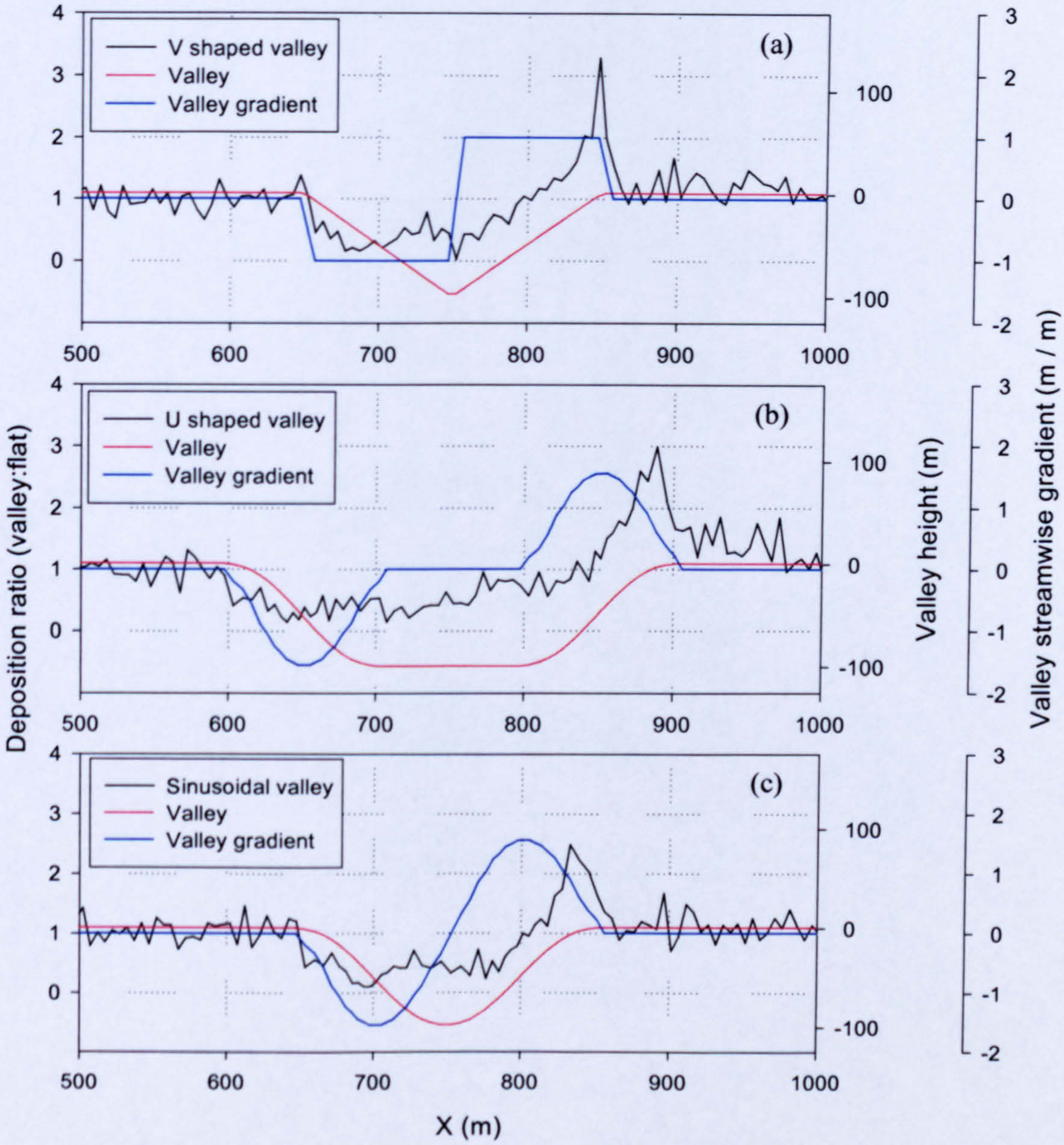

Graphs of relative deposition to three different valley geometries. Plane particle source (uniform concentration). Legend shows valley type. Note that the position of the valley is indicated in red on each graph. Streamwise gradient of valleys also included in blue.

Figure 6.23

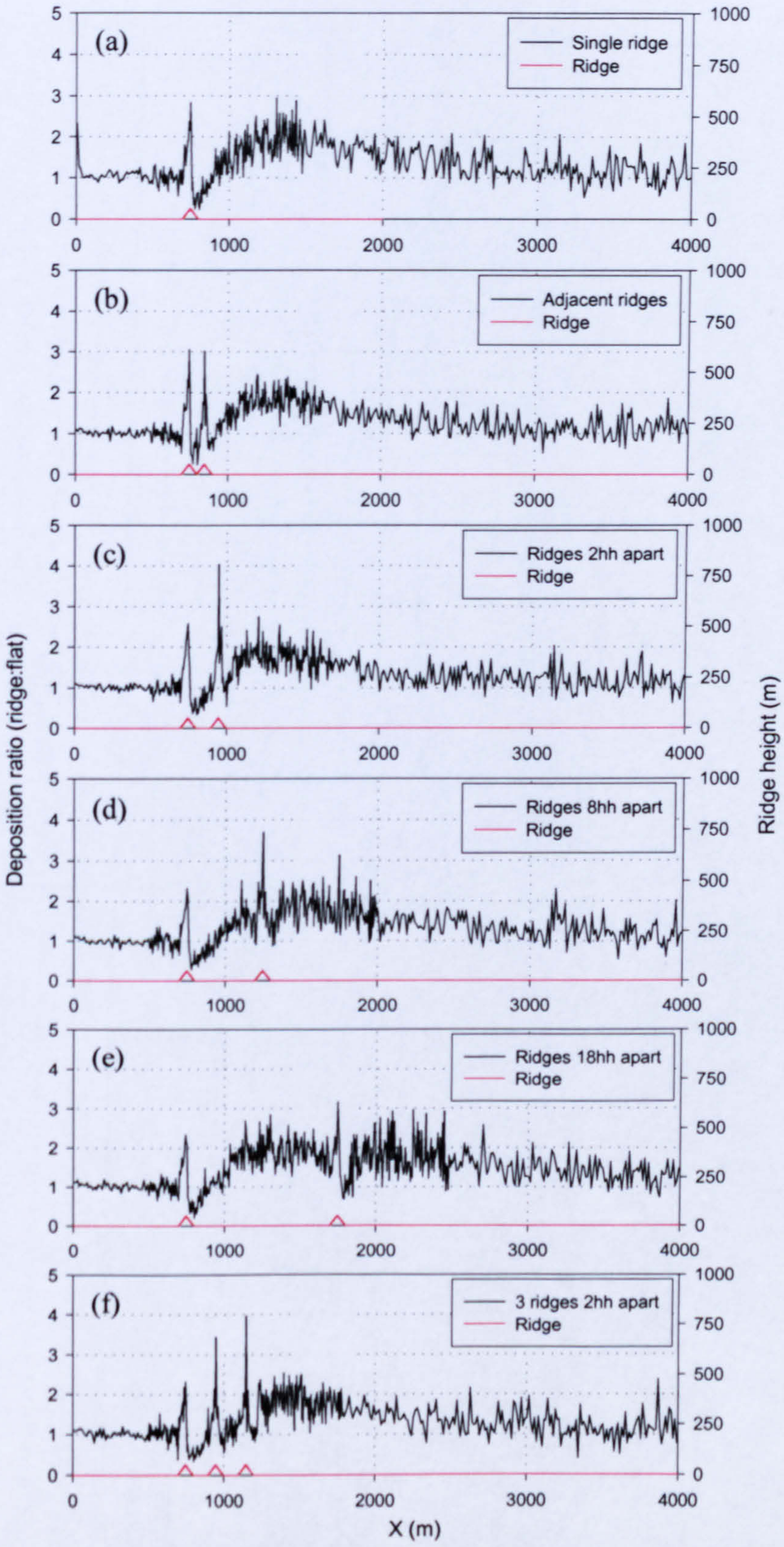

Graphs of relative deposition to multiple ridges, presented with single ridge for comparison. Plane particle source (uniform concentration). Legend shows ridge base separation. Note that the position of the ridges is indicated in red on each graph.

Figure 6.24

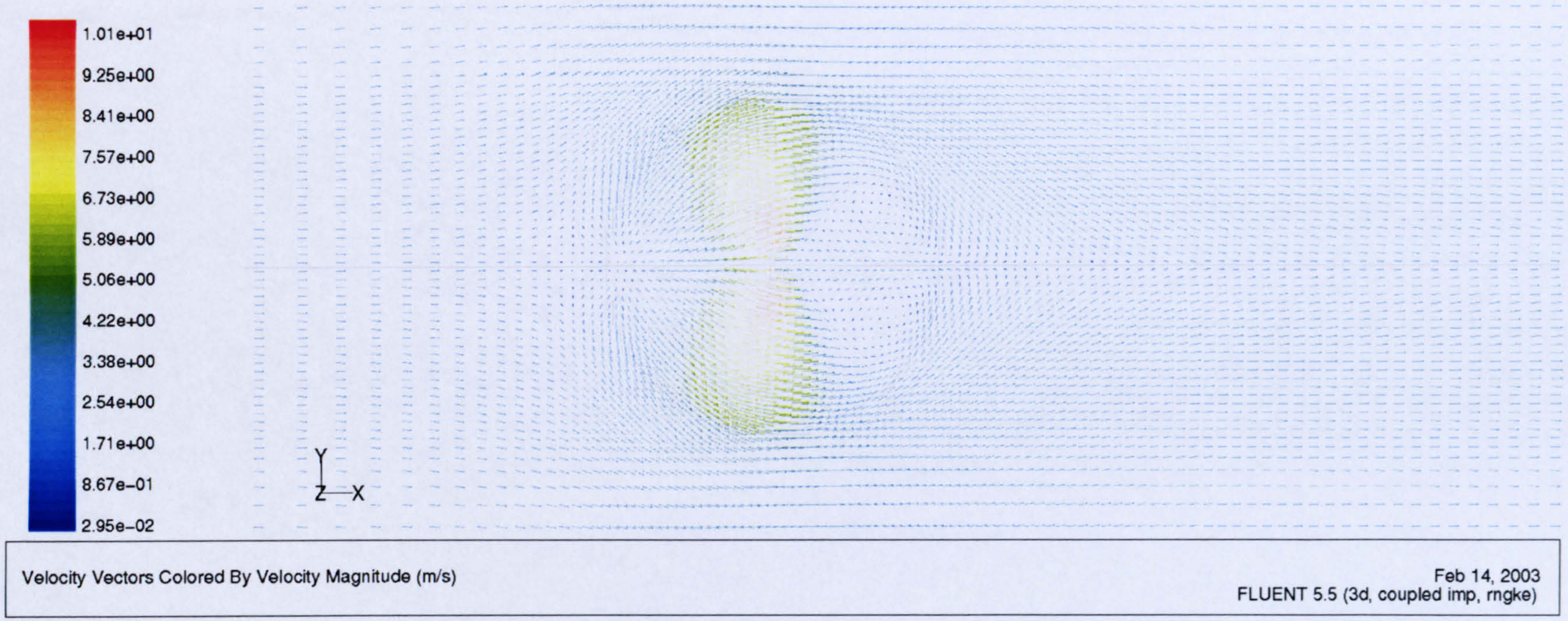

Plot of velocity vectors at 5m above the surface for a cone of slope 1 in 1. Size and colour of arrows indicate velocity magnitude. Legend shows velocity magnitude in m s^{-1}.

Figure 6.25

Plot of velocity vectors at 5m above the surface for a cone of slope 1 in 3. Size and colour of arrows indicate velocity magnitude. Legend shows velocity magnitude in m s^{-1}.

Figure 6.26

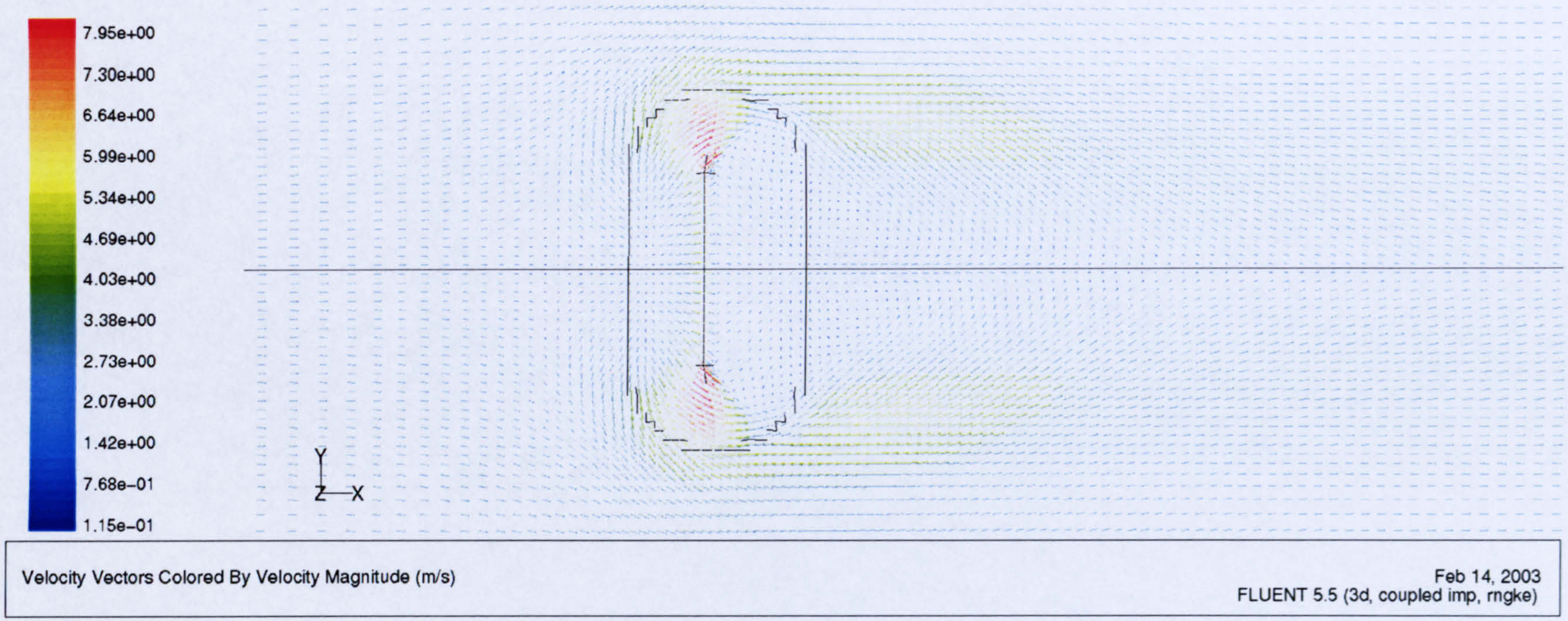

Plot of velocity vectors at 5m above the surface for an elongated cone of slope 1 in 1. Size and colour of arrows indicate velocity magnitude. Legend shows velocity magnitude in m s^{-1}.

Figure 6.27

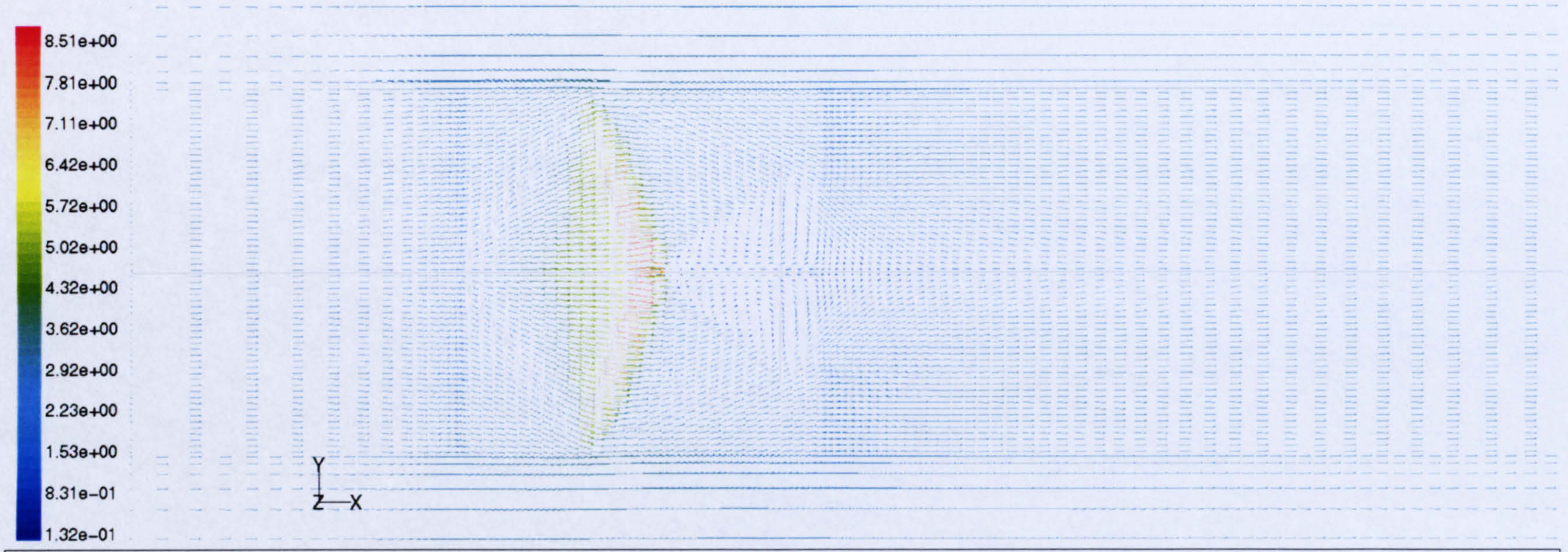

Plot of velocity vectors at 5m above the surface for a five-sided pyramid of slope 1 in 3. Size and colour of arrows indicate velocity magnitude. Legend shows velocity magnitude in m s^{-1}.

Figure 6.28

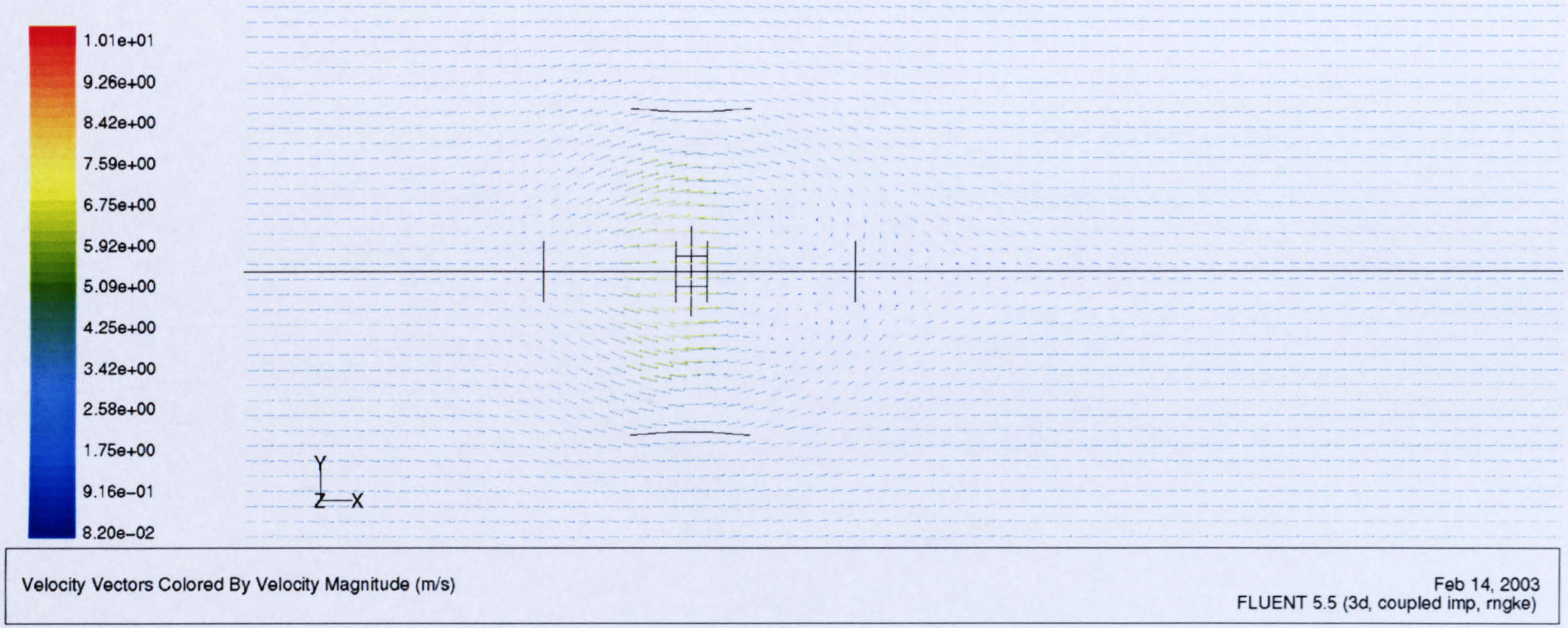

Plot of velocity vectors at 5m above the surface for a sinusoidal hill of average slope 1 in 2. Size and colour of arrows indicate velocity magnitude. Legend shows velocity magnitude in m s^{-1}.

Figure 6.29

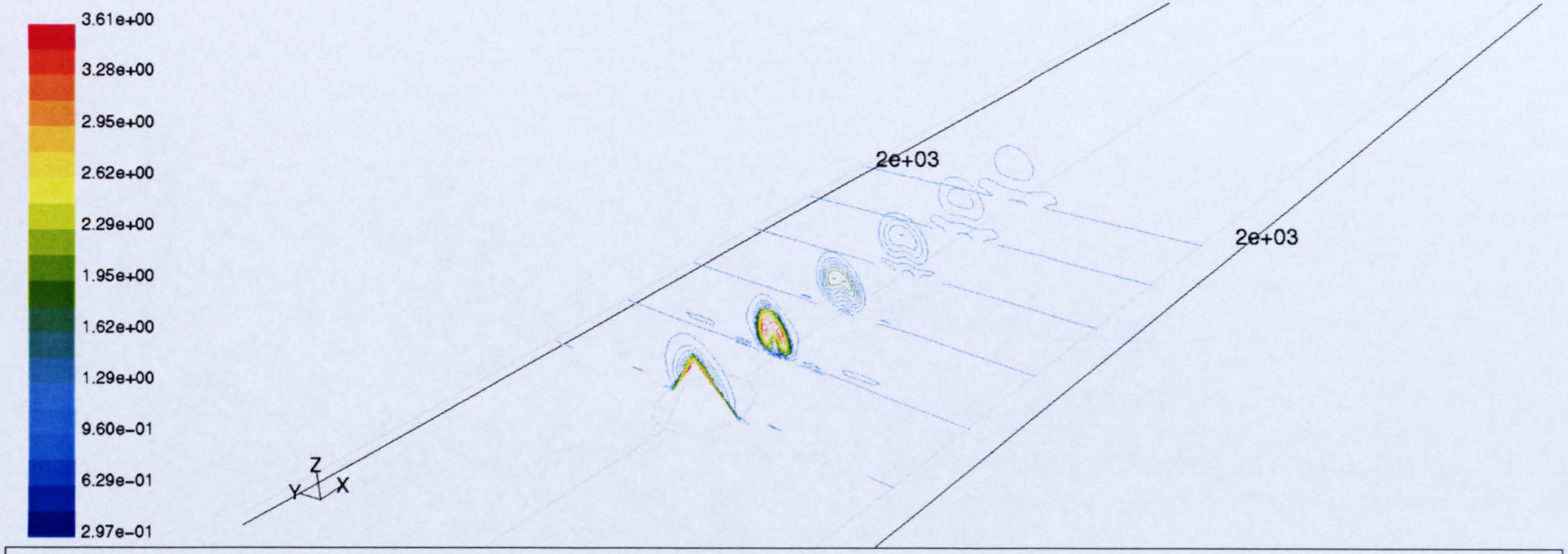

Plot of contours of turbulent kinetic energy in wake of cone of slope 1 in 1. Contours are plotted in vertical planes normal to the direction of the mean flow. Vertical planes are spaced at 200m apart, with the first plane coinciding with the hill peak. Legend shows turbulent kinetic energy in $m^2\ s^{-2}$.

Figure 6.30

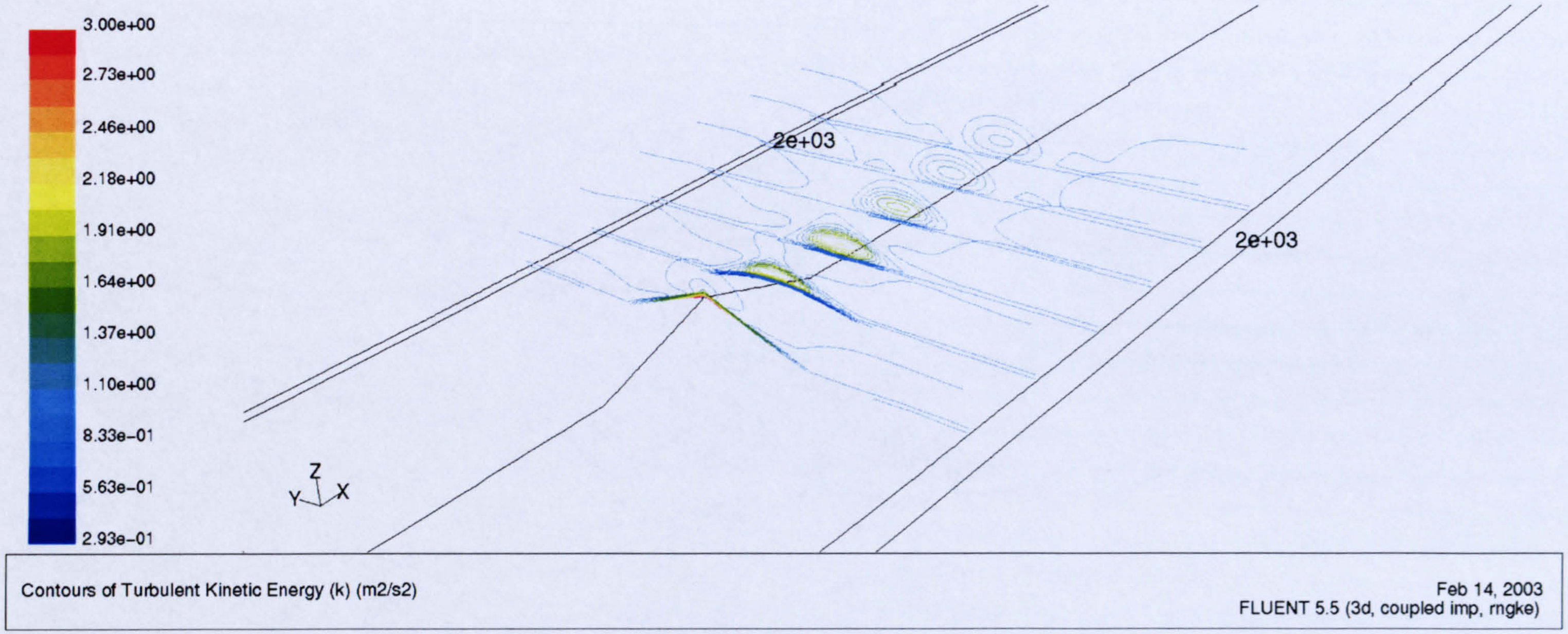

Plot of contours of turbulent kinetic energy in wake of cone of slope 1 in 3. Contours are plotted in vertical planes normal to the direction of the mean flow. Vertical planes are spaced at 200m apart, with the first plane coinciding with the hill peak. Legend shows turbulent kinetic energy in $m^2\ s^{-2}$.

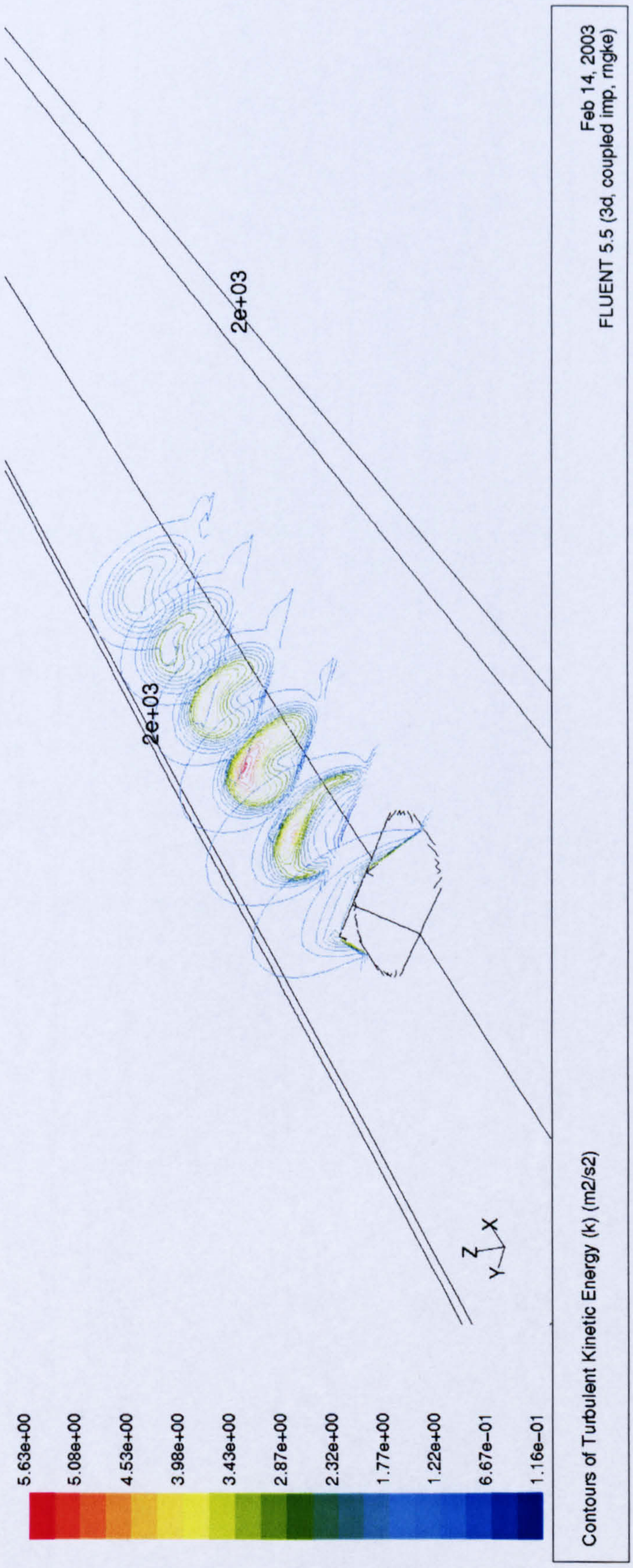

Figure 6.31

Plot of contours of turbulent kinetic energy in wake of an elongated cone of slope 1 in 1. Contours are plotted in vertical planes normal to the direction of the mean flow. Vertical planes are spaced at 200m apart, with the first plane coinciding with the hill peak. Legend shows turbulent kinetic energy in $m^2 s^{-2}$.

Figure 6.32

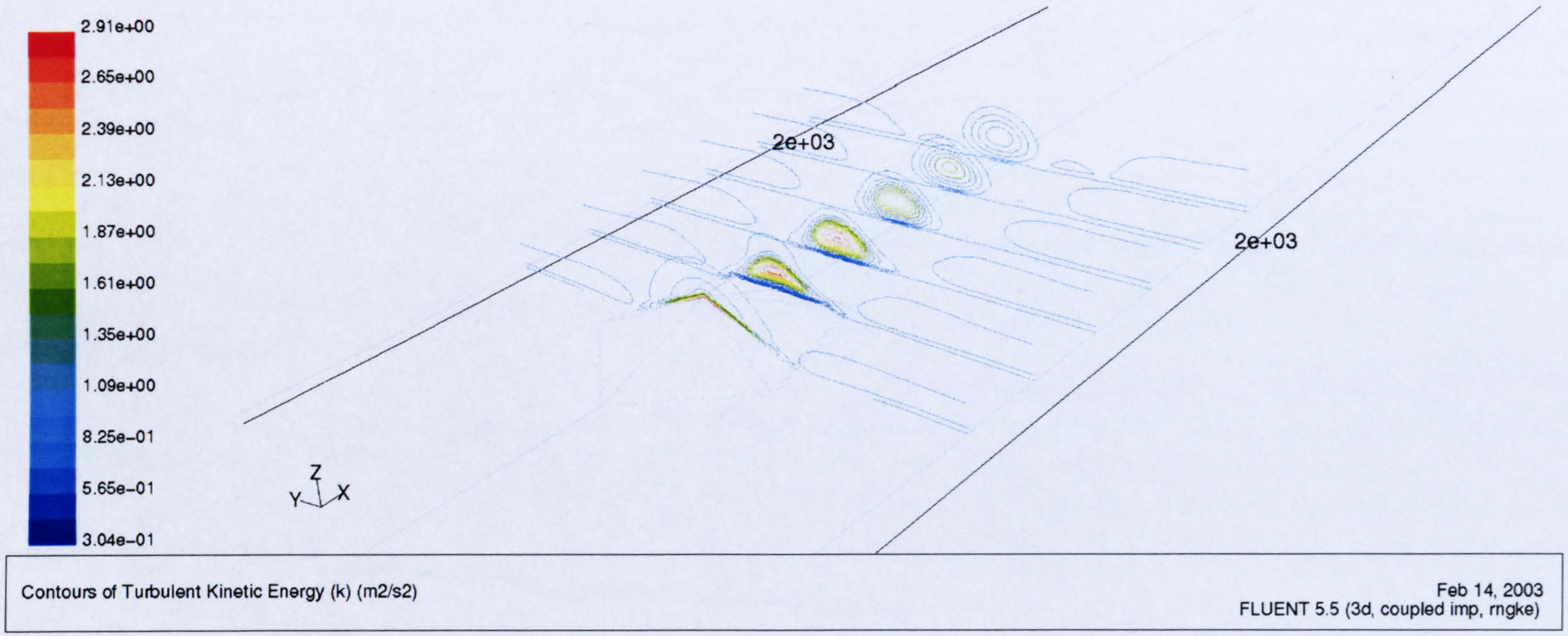

Plot of contours of turbulent kinetic energy in wake of a 5-sided pyramid of slope 1 in 3. Contours are plotted in vertical planes normal to the direction of the mean flow. Vertical planes are spaced at 200m apart, with the first plane coinciding with the hill peak. Legend shows turbulent kinetic energy in $m^2\ s^{-2}$.

Figure 6.33

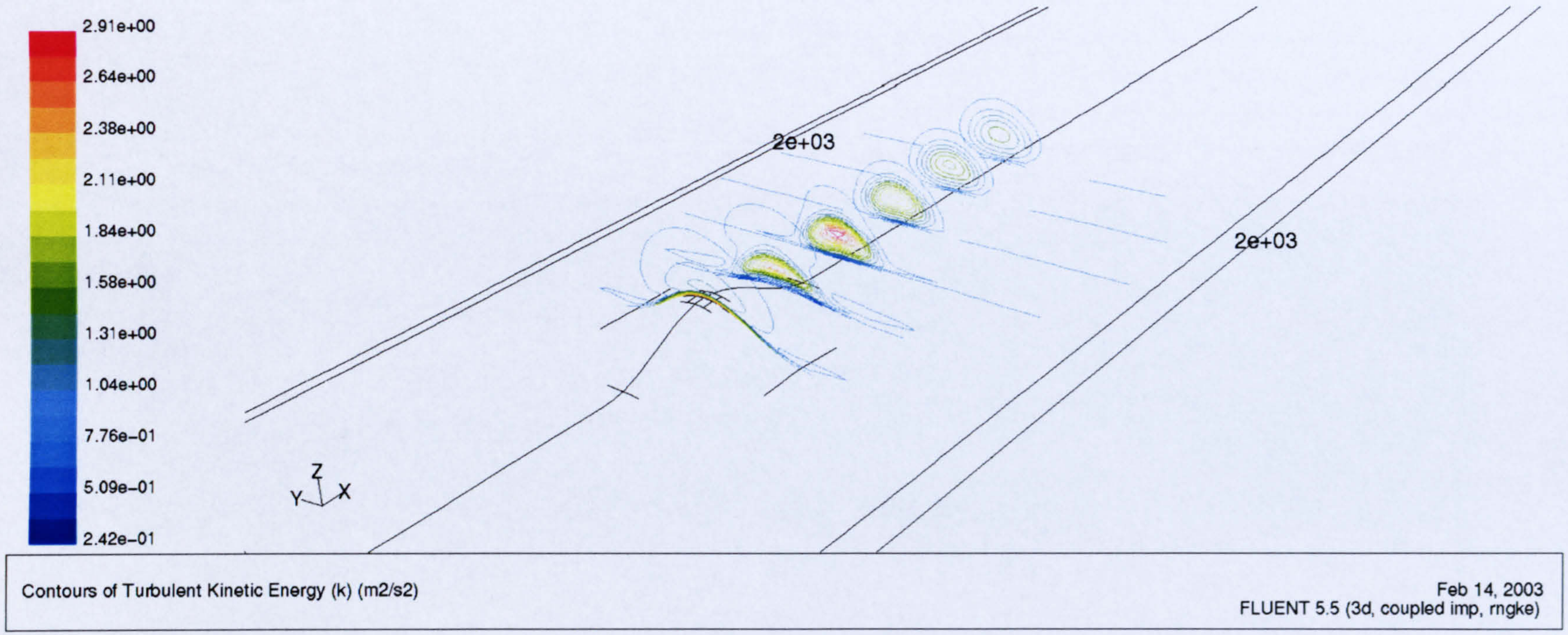

Plot of contours of turbulent kinetic energy in wake of a sinusoidal hill of average slope 1 in 2. Contours are plotted in vertical planes normal to the direction of the mean flow. Vertical planes are spaced at 200m apart, with the first plane coinciding with the hill peak. Legend shows turbulent kinetic energy in $m^2\ s^{-2}$.

Figure 6.34

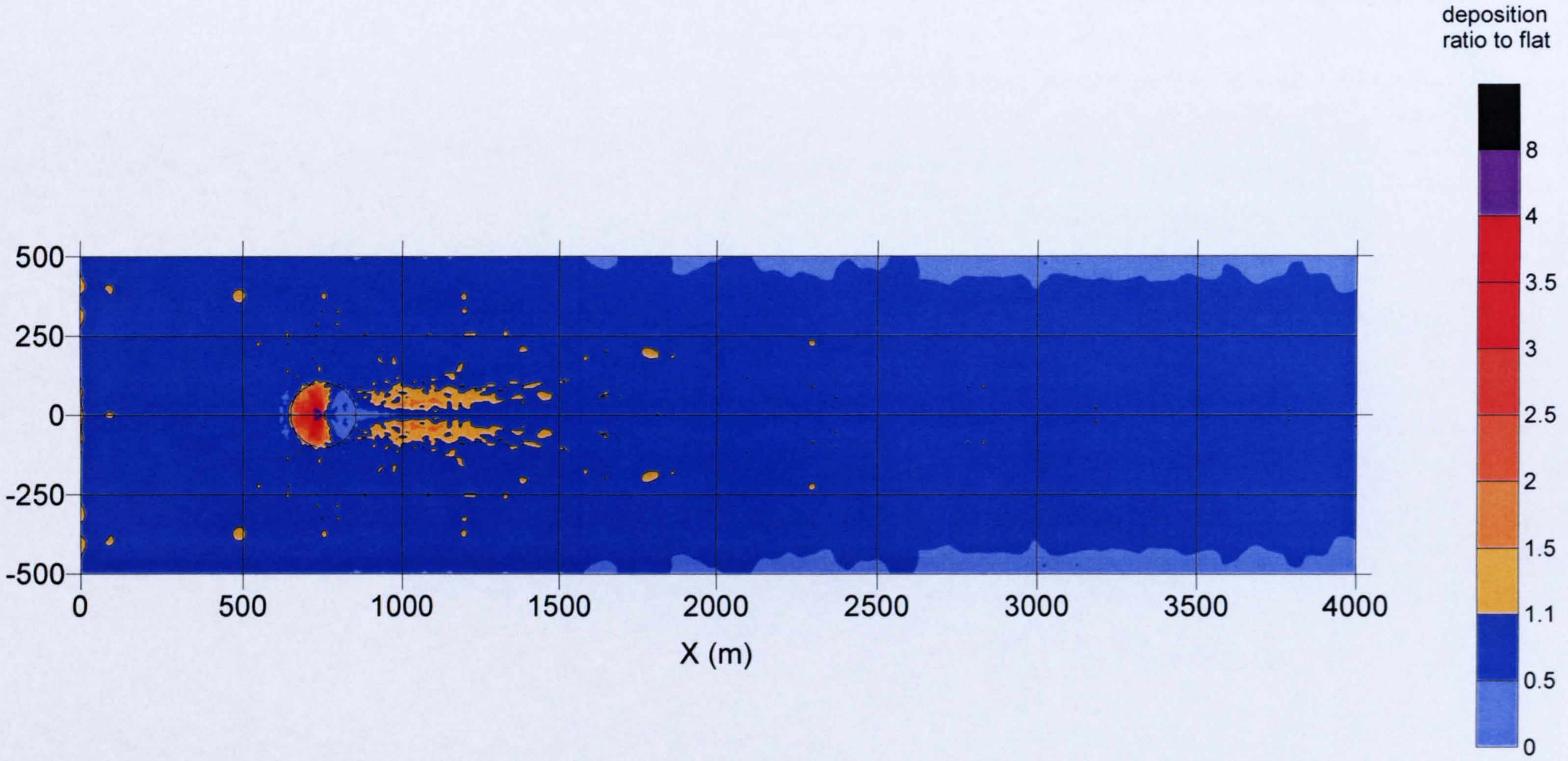

Plot of deposition rate to cone of slope 1 in 1, normalised to flat case. Orange and red areas inside the solid line are areas where the ratio is greater than 1.1. The blue areas outside of the solid line are below 1.1.

Figure 6.35

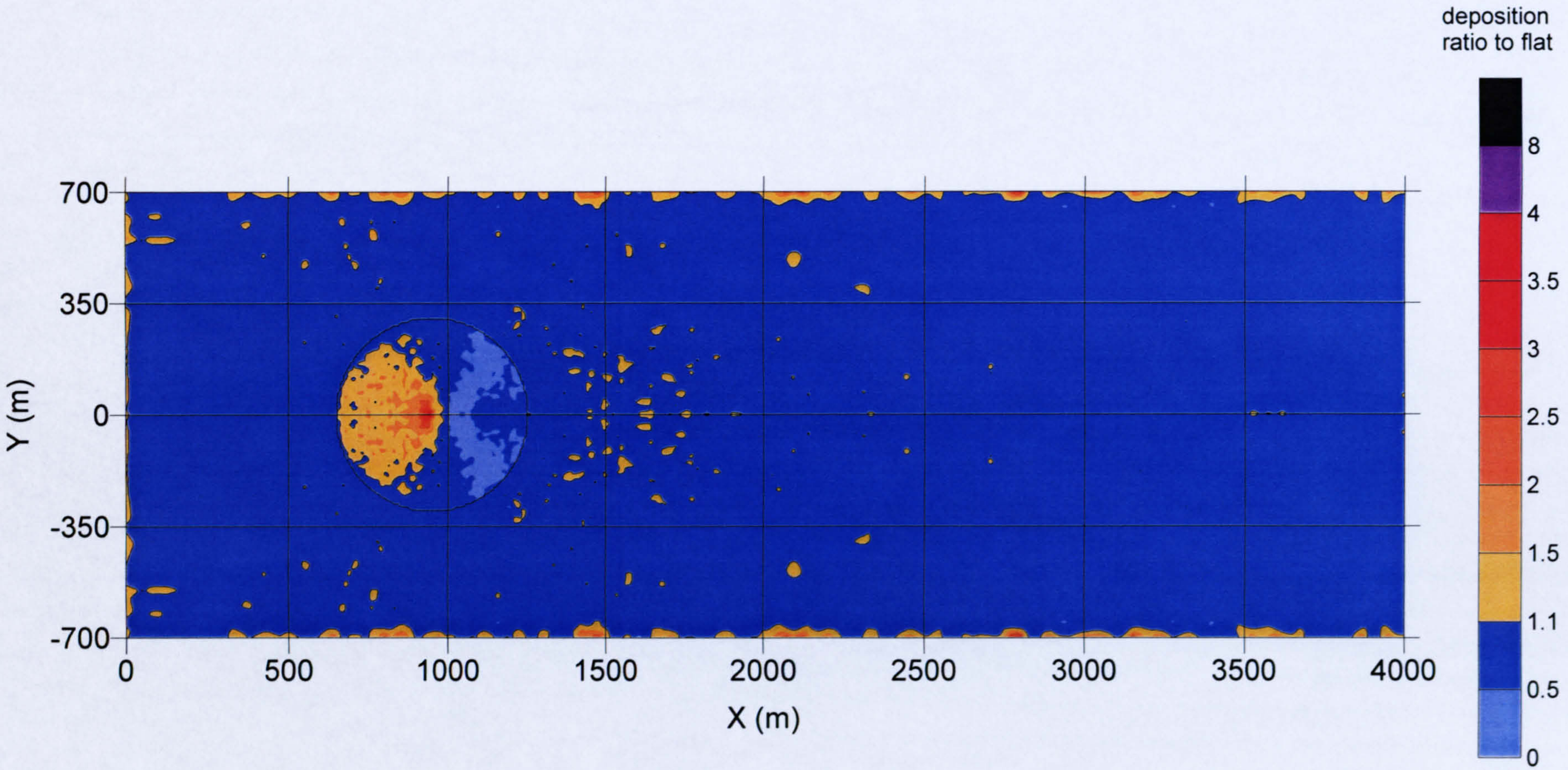

Plot of deposition rate to cone of slope 1 in 3, normalised to flat case. Orange and red areas inside the solid line are areas where the ratio is greater than 1.1. The blue areas outside of the solid line are below 1.1. Note that areas of enhanced deposition at the edges of the domain are artifacts of the interpolation and normalisation process.

Figure 6.36

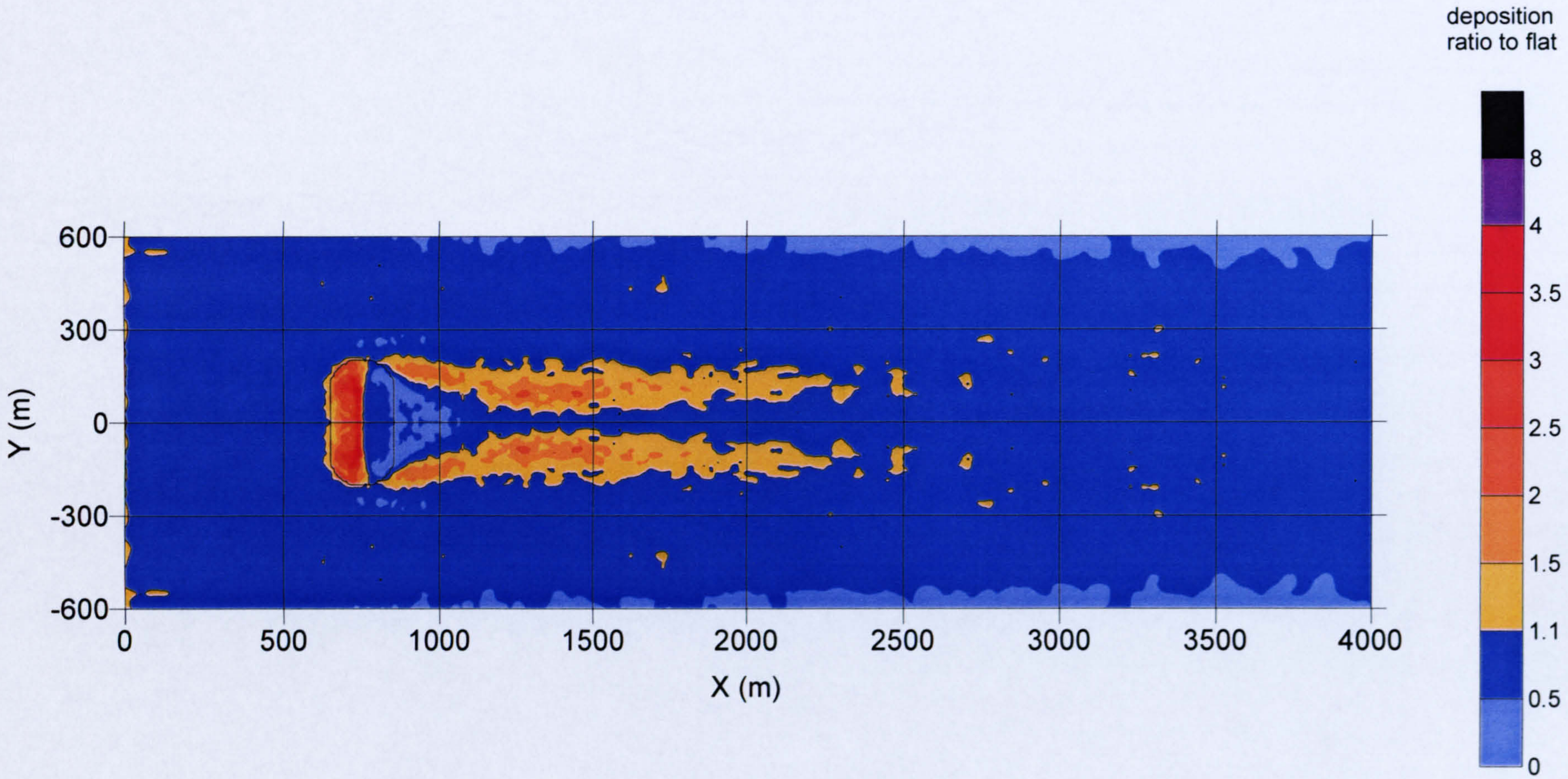

Plot of deposition rate to elongated cone of slope 1 in 1, normalised to flat case. Orange and red areas inside the solid line are areas where the ratio is greater than 1.1. The blue areas outside of the solid line are below 1.1.

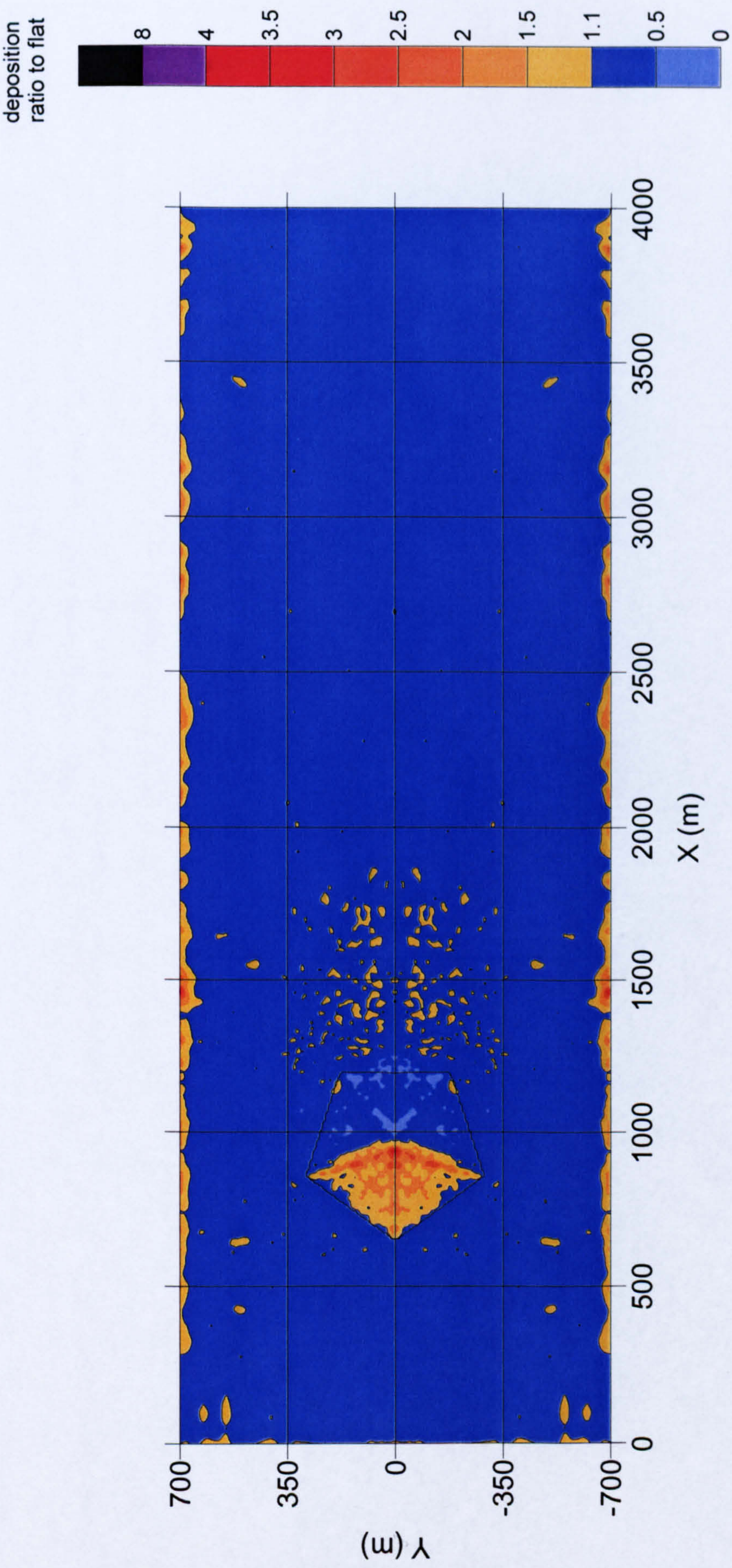

Figure 6.37

Plot of deposition rate to 5-sided pyramid of slope 1 in 3, normalised to flat case. Orange and red areas inside the solid line are areas where the ratio is greater than 1.1. Note that areas of enhanced deposition at the edges of the domain are artifacts of the interpolation and normalisation process.

Figure 6.38

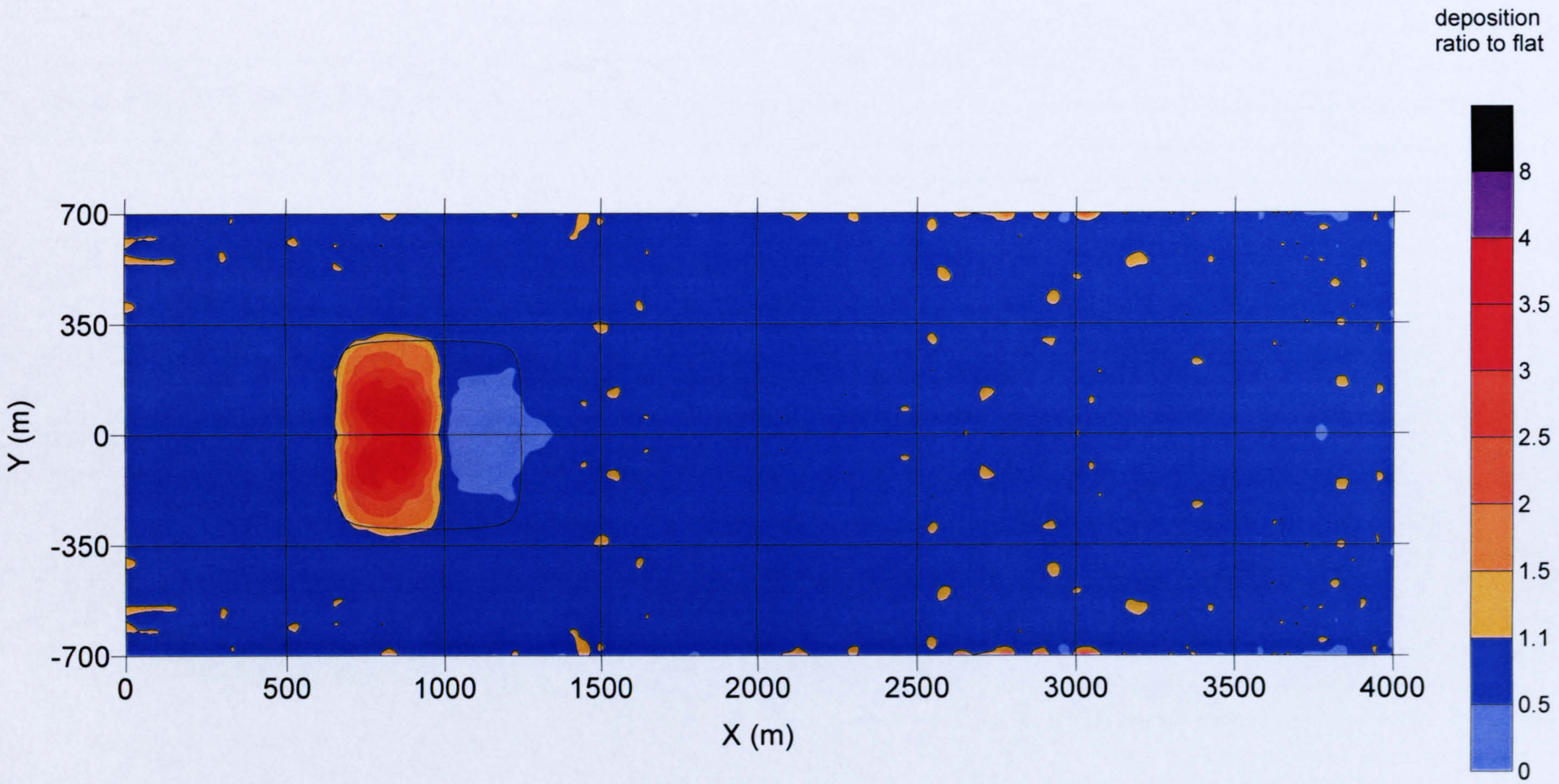

Plot of deposition rate for sinusoidal hill of slope 1 in 2, normalised to flat case. Orange and red areas inside the solid line are areas where the ratio is greater than 1.1. The blue areas outside of the solid line are below 1.1.

Figure 6.39

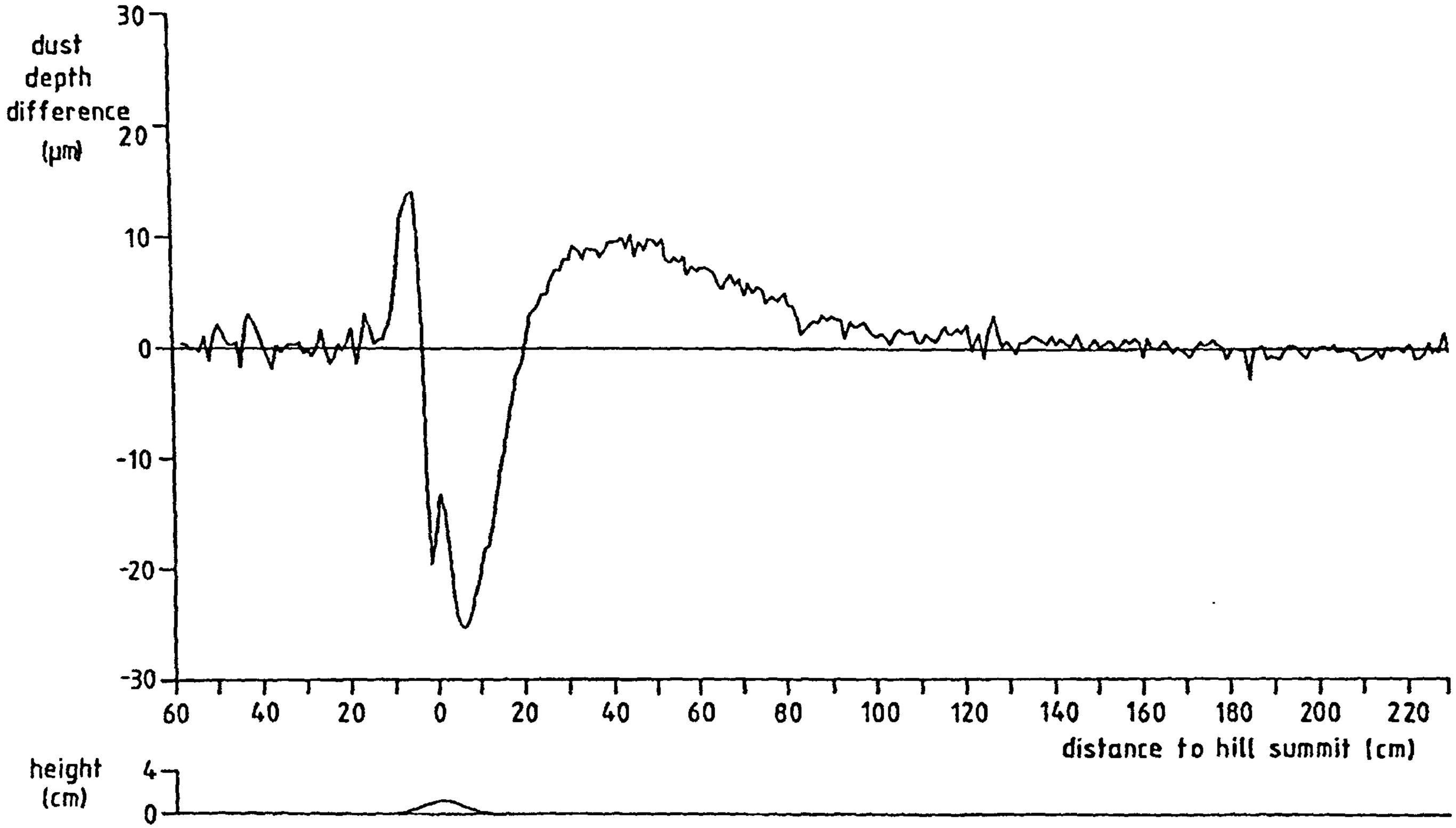

Plot of dust deposition to a curved symmetrical hill (ridge), reproduced from Offer and Goossens (1995). Note the similarity to Figure 6.19 (a). In this case dust deposition is plotted as difference from flat case rather than as ratio to the flat case.

Figure 6.40

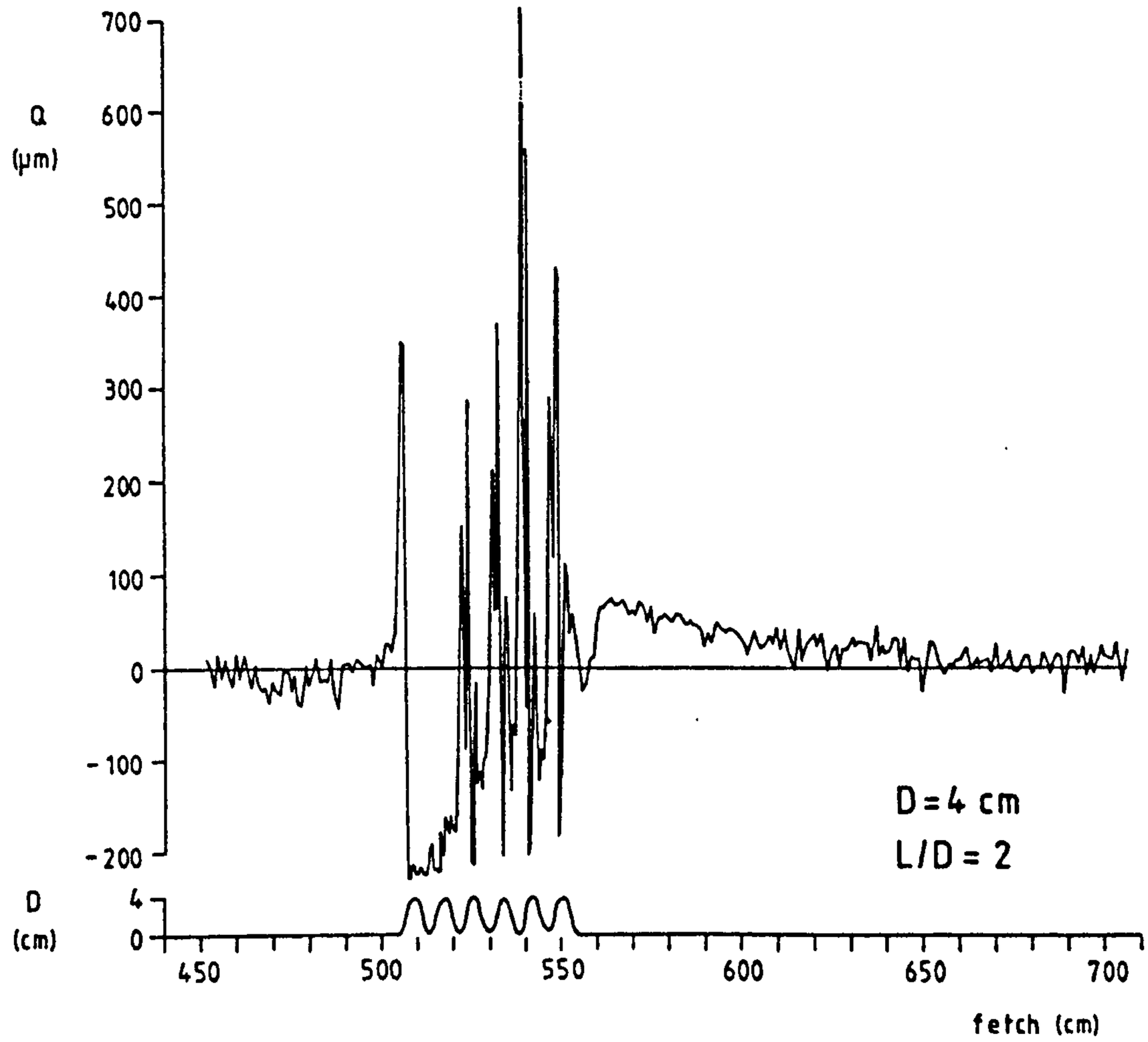

Plot of dust deposition height (Q) to a range of curved symmetrical hills (ridges), reproduced from Goossens, (1996). Note that the successive peaks increase in magnitude, and are similar to Figure 6.23 (f).

Figure 7.1

(a)

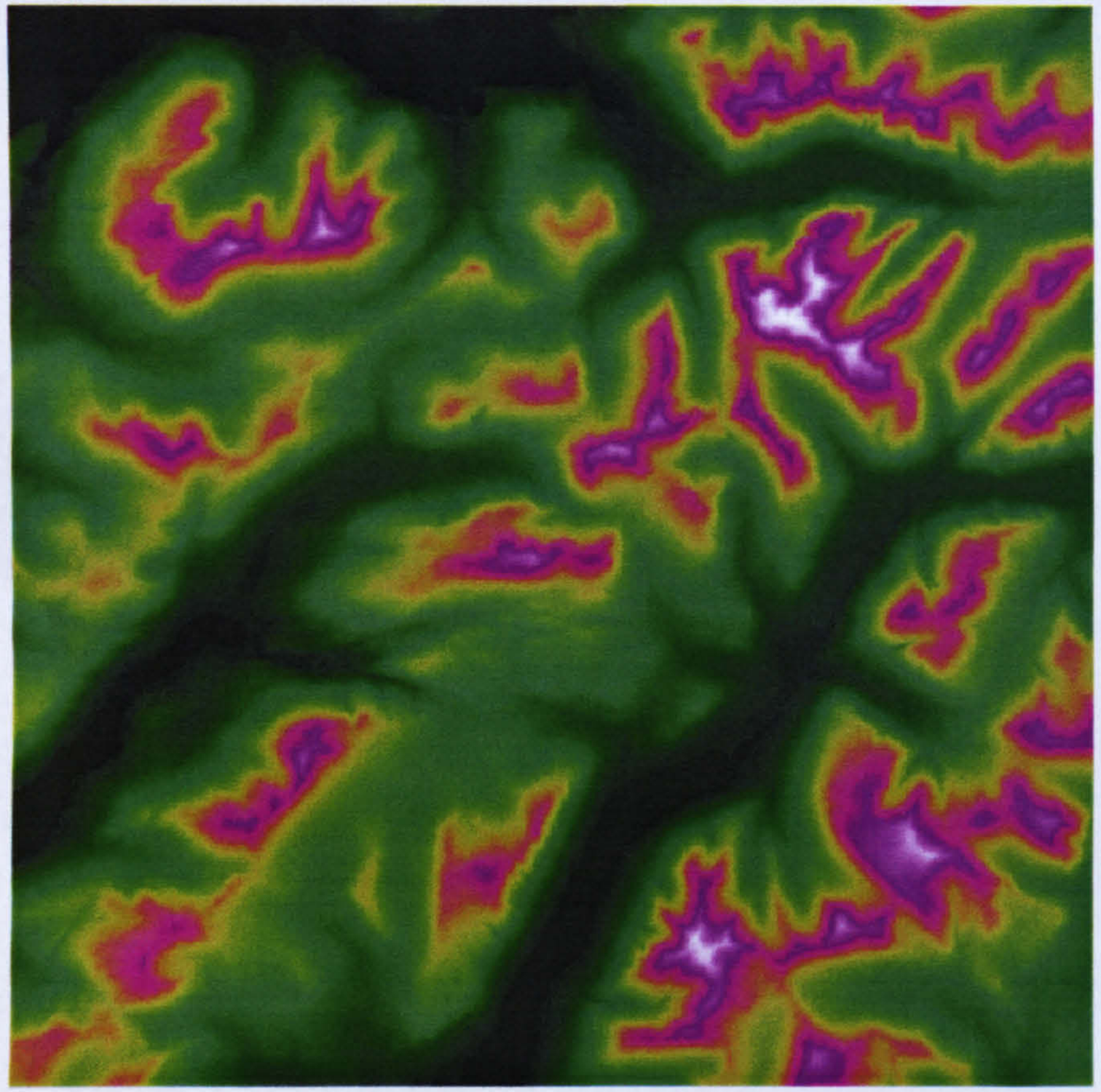

(b)

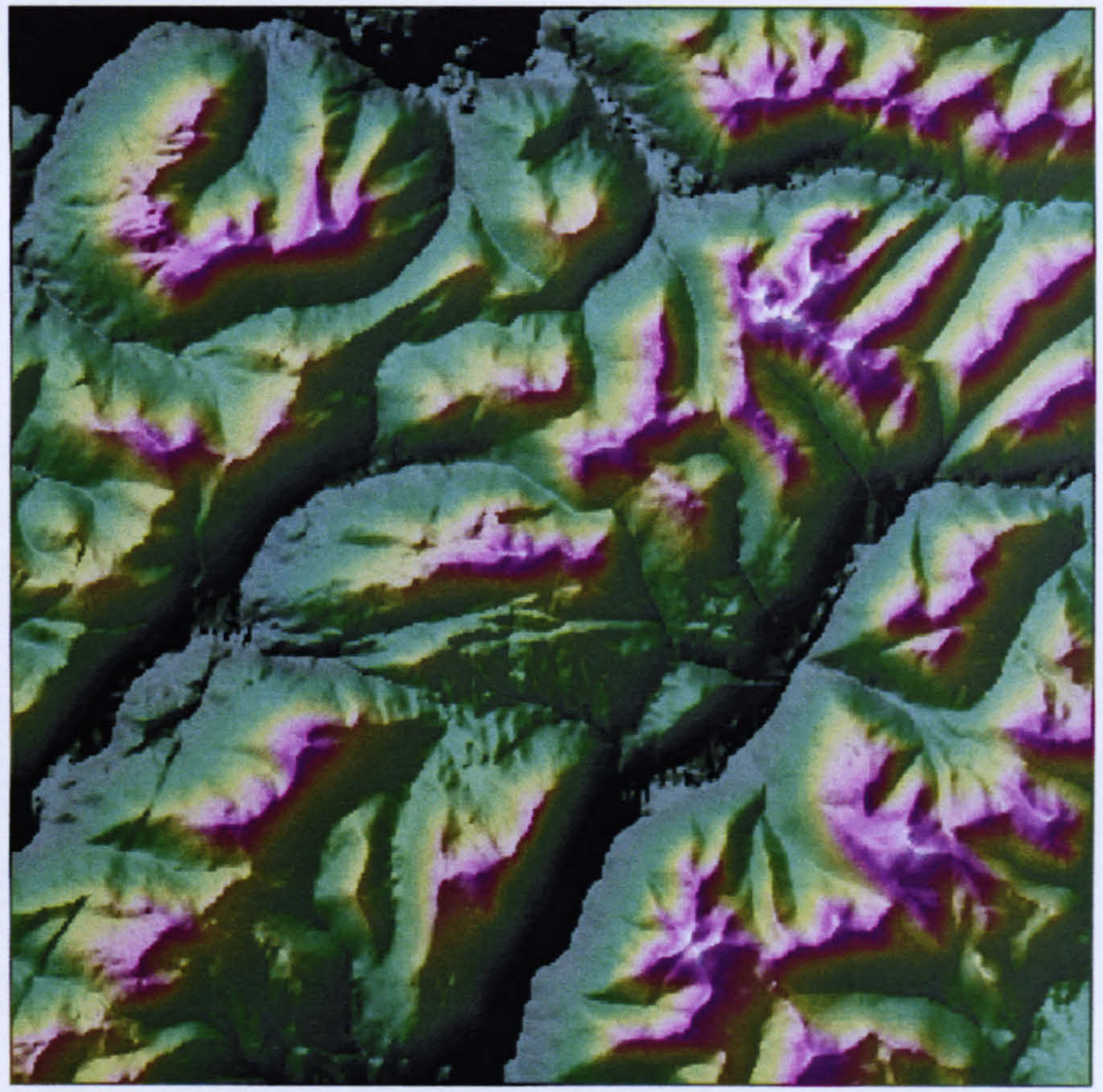

Example of DEM data for Glencoe area, Scotland, UK. In (a) colour represents elevation and in (b) this has been shaded to emphasise the relief. Each figure represents an area 20km x 20km. Produced with Landserf, using OS Landform Panorama data © Crown Copyright Ordnance Survey. An EDINA Digimap/JISC supplied service.

Figure 7.2

(a)

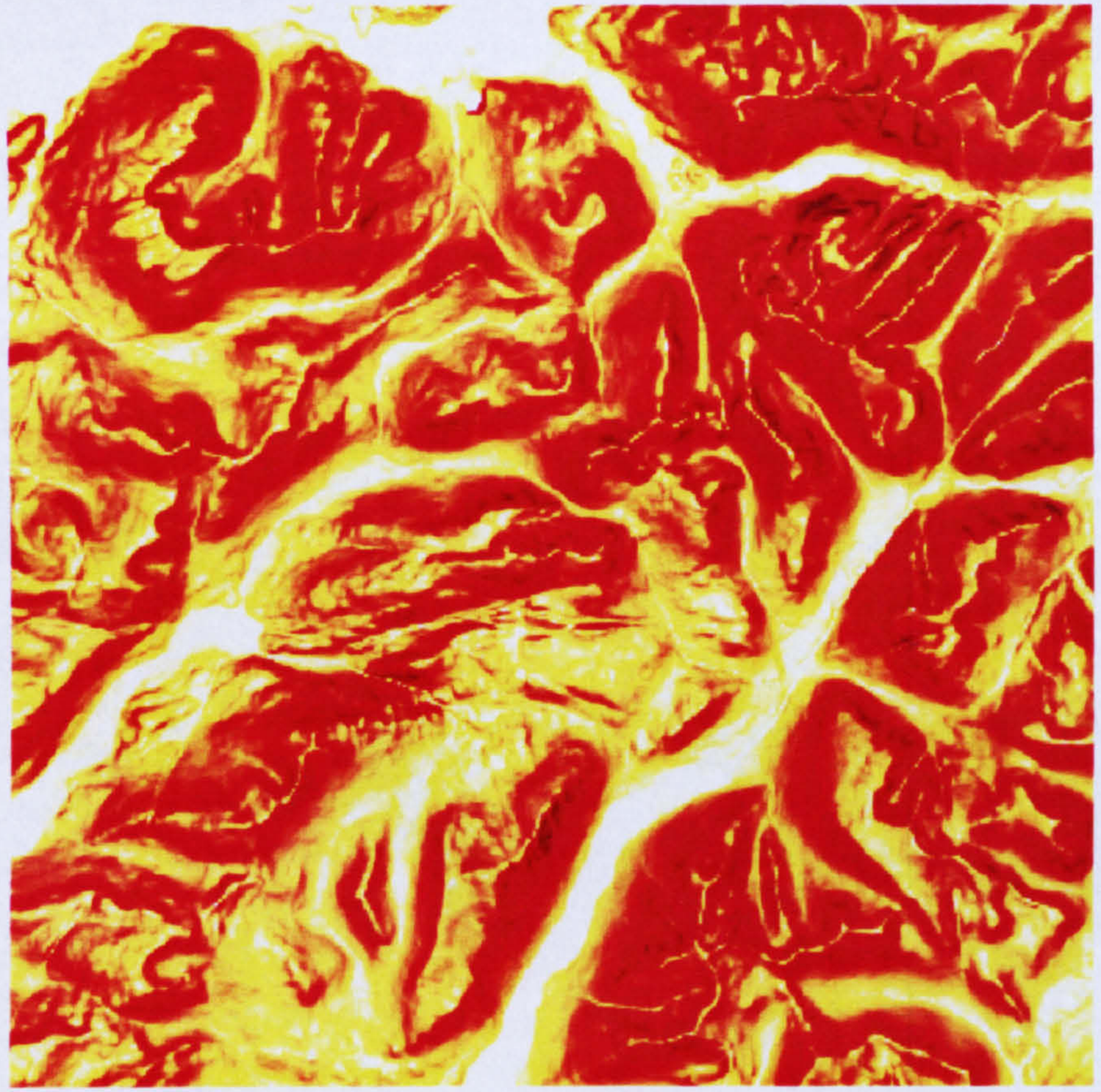

(b)

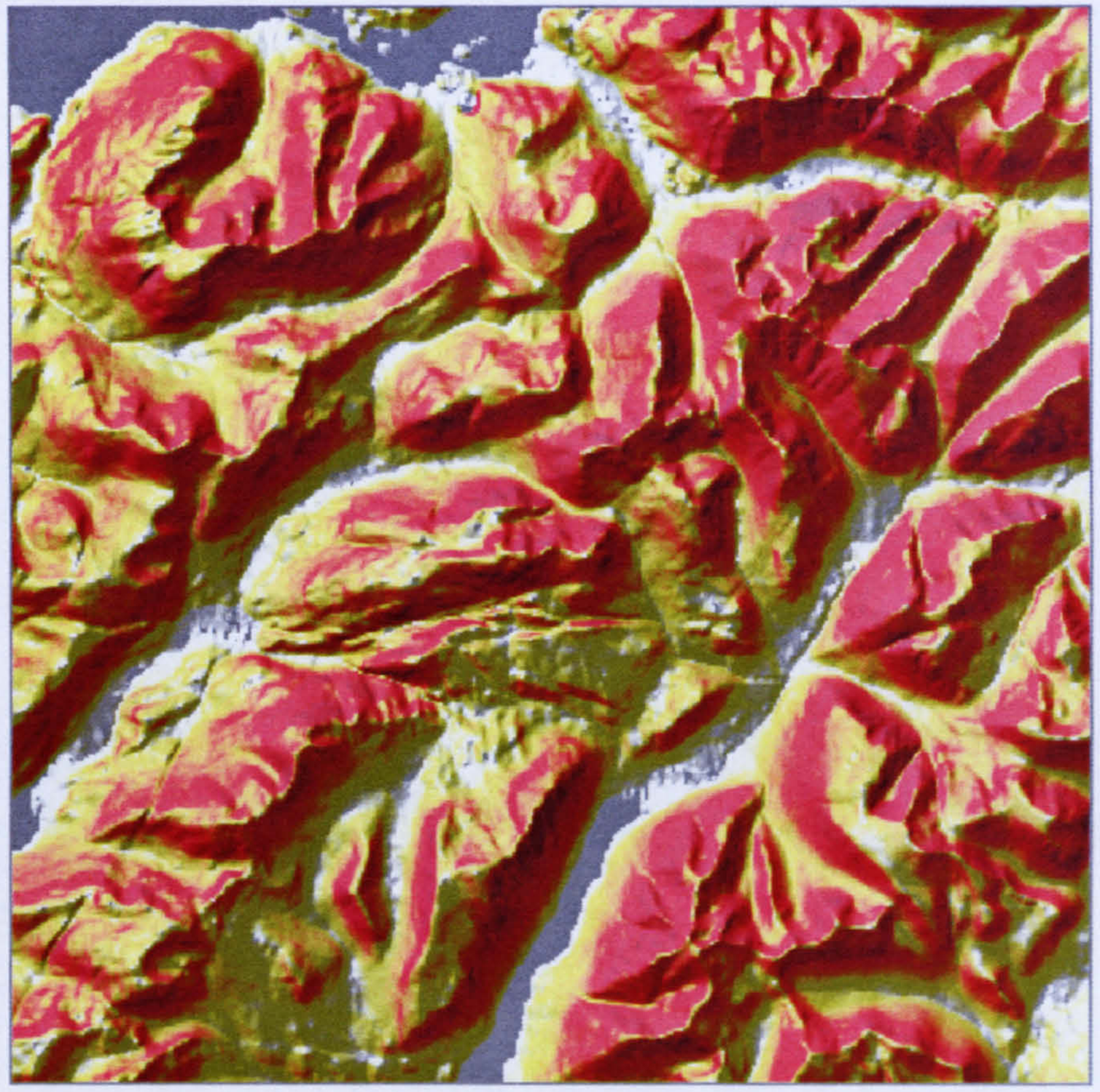

Slope calculated from DEM data in previous figure. Darker red indicates areas of greatest slope. (a) shows slope by colour. (b) shows slope by colour and shaded by elevation data so that slope can be compared with elevation. Produced with Landserf, using OS Landform Panorama data © Crown Copyright Ordnance Survey. An EDINA Digimap/JISC supplied service.

Figure 7.3

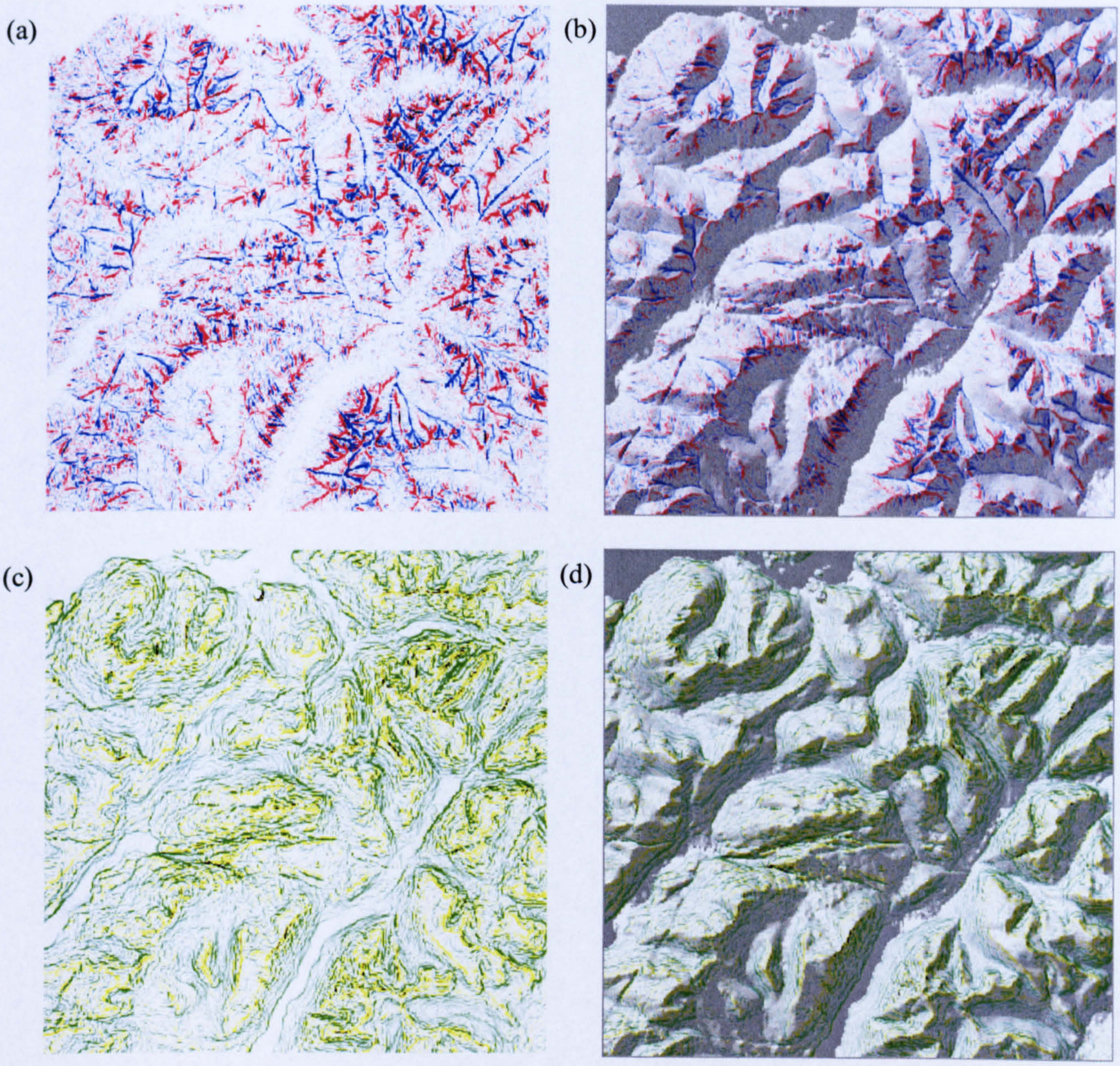

Figure shows cross-sectional curvature (a) and (b) and longitudinal curvature (c) and (d), derived from DEM elevation data. (a) and (c) show derived data only and (b) and (d) show derived data superimposed on relief. Produced with Landserf, using OS Landform Panorama data © Crown Copyright Ordnance Survey. An EDINA Digimap/JISC supplied service.

Figure 7.4

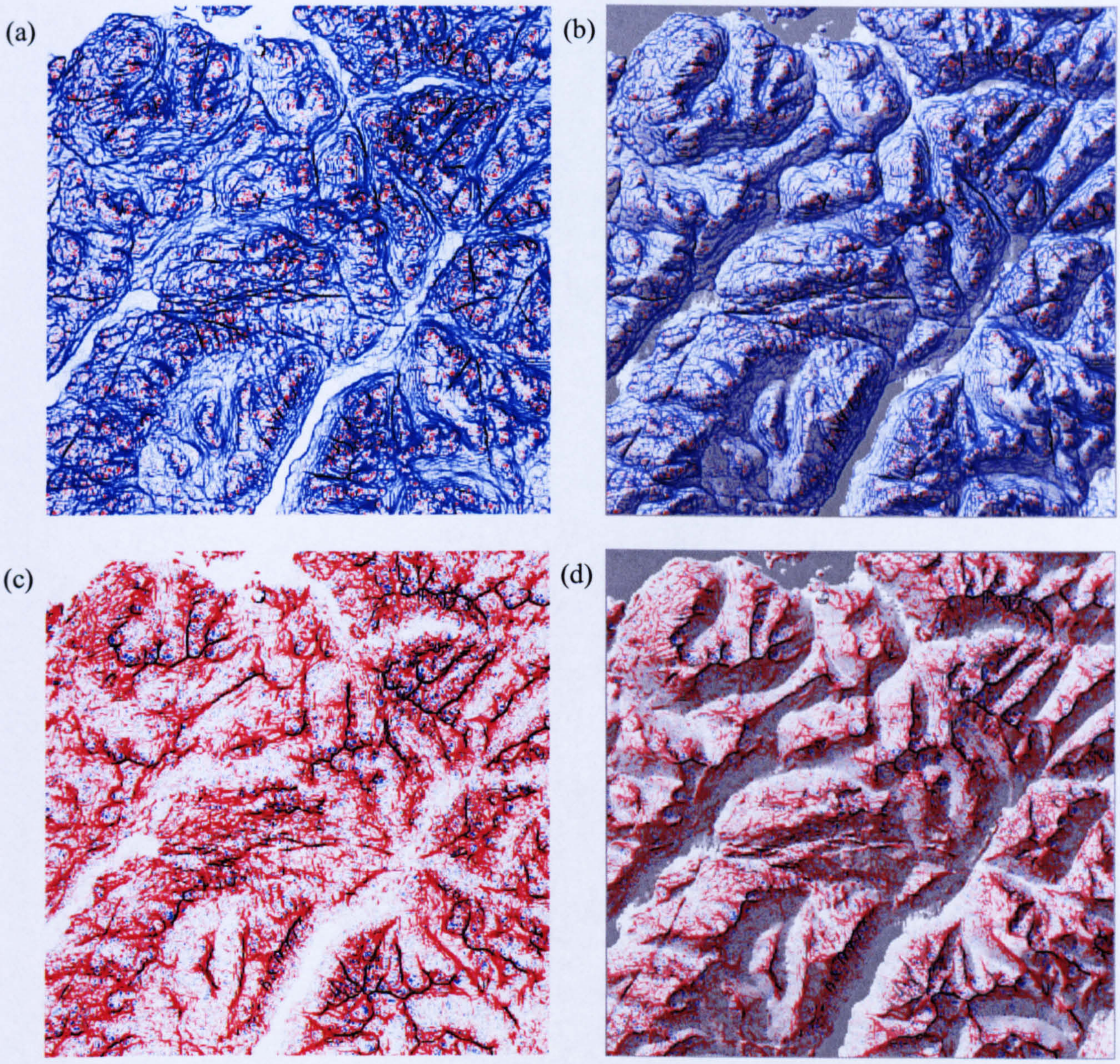

Figure shows minimum curvature (a) and (b) and maximum curvature (c) and (d), derived from DEM elevation data. (a) and (c) show derived data only and (b) and (d) show derived data superimposed on relief. Produced with Landserf, using OS Landform Panorama data © Crown Copyright Ordnance Survey. An EDINA Digimap/JISC supplied service.

Figure 7.5

(a)

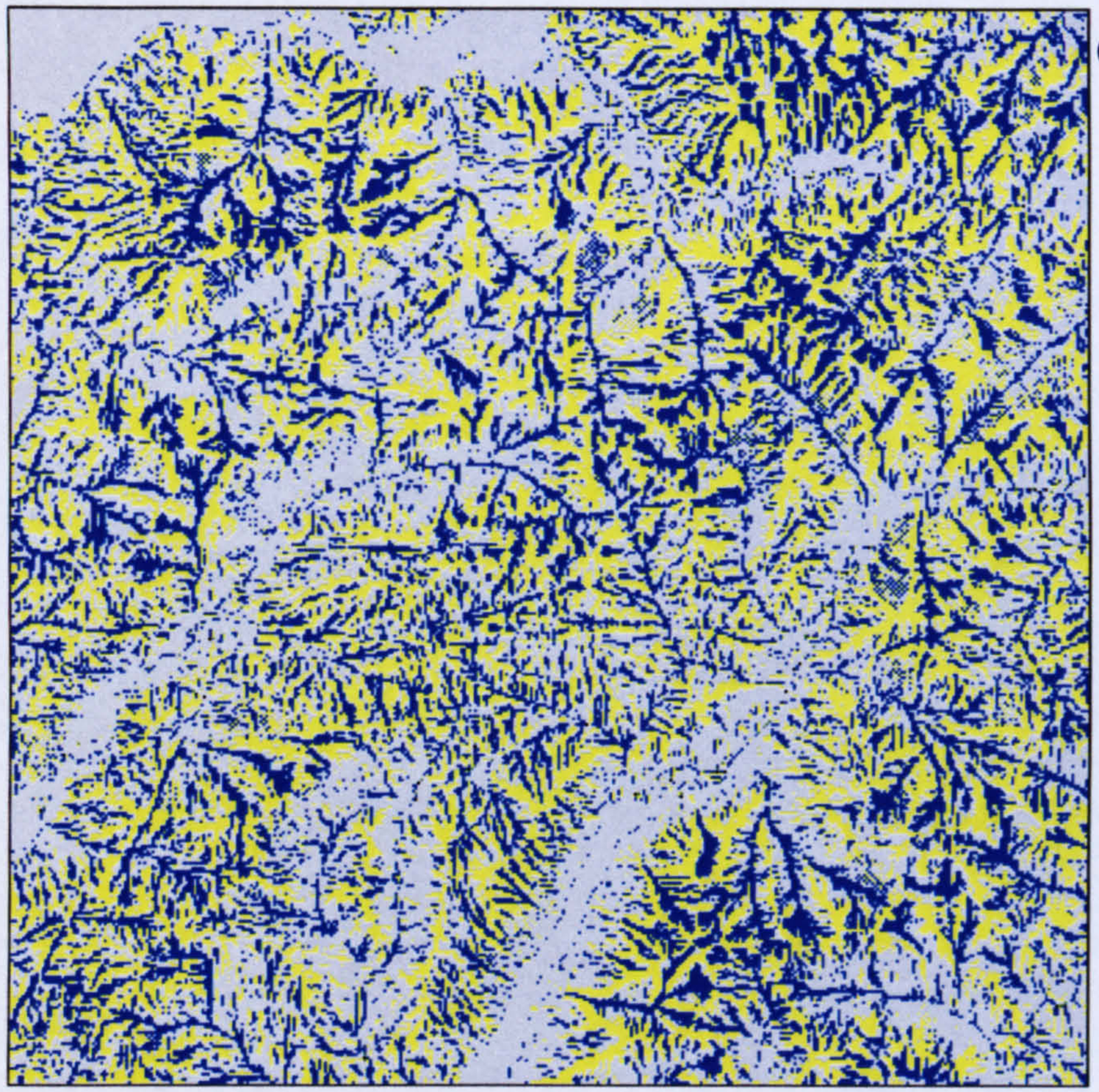

(b)

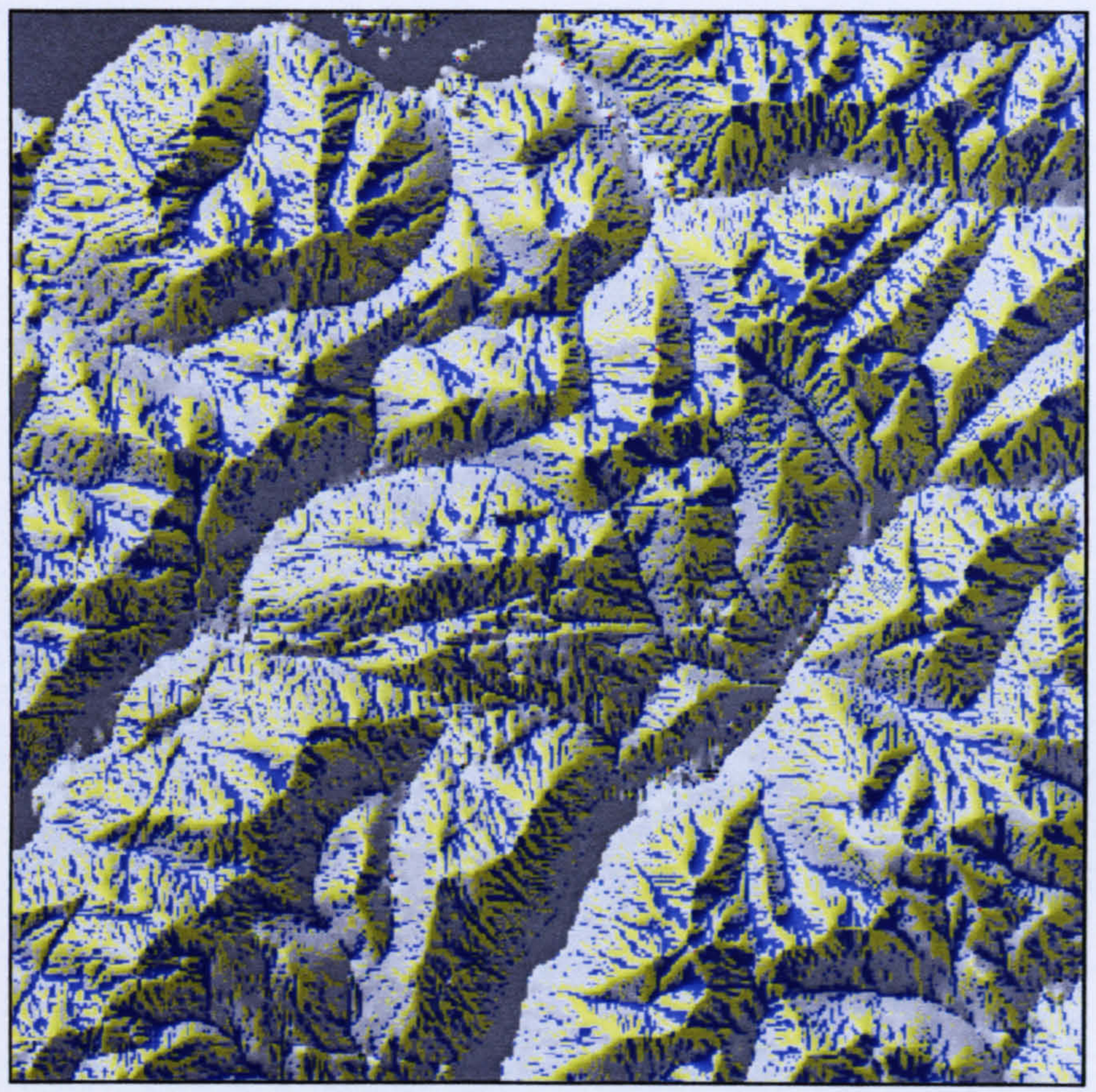

Figure shows extracted features from DEM elevation data. Colour coding as follows: red – peak, yellow – ridge, green – pass, blue – channel, black – pit. (a) shows derived data only and (b) shows derived data superimposed on relief. Produced with Landserf, using OS Landform Panorama data © Crown Copyright Ordnance Survey. An EDINA Digimap/JISC supplied service.

Figure 7.6

(a)

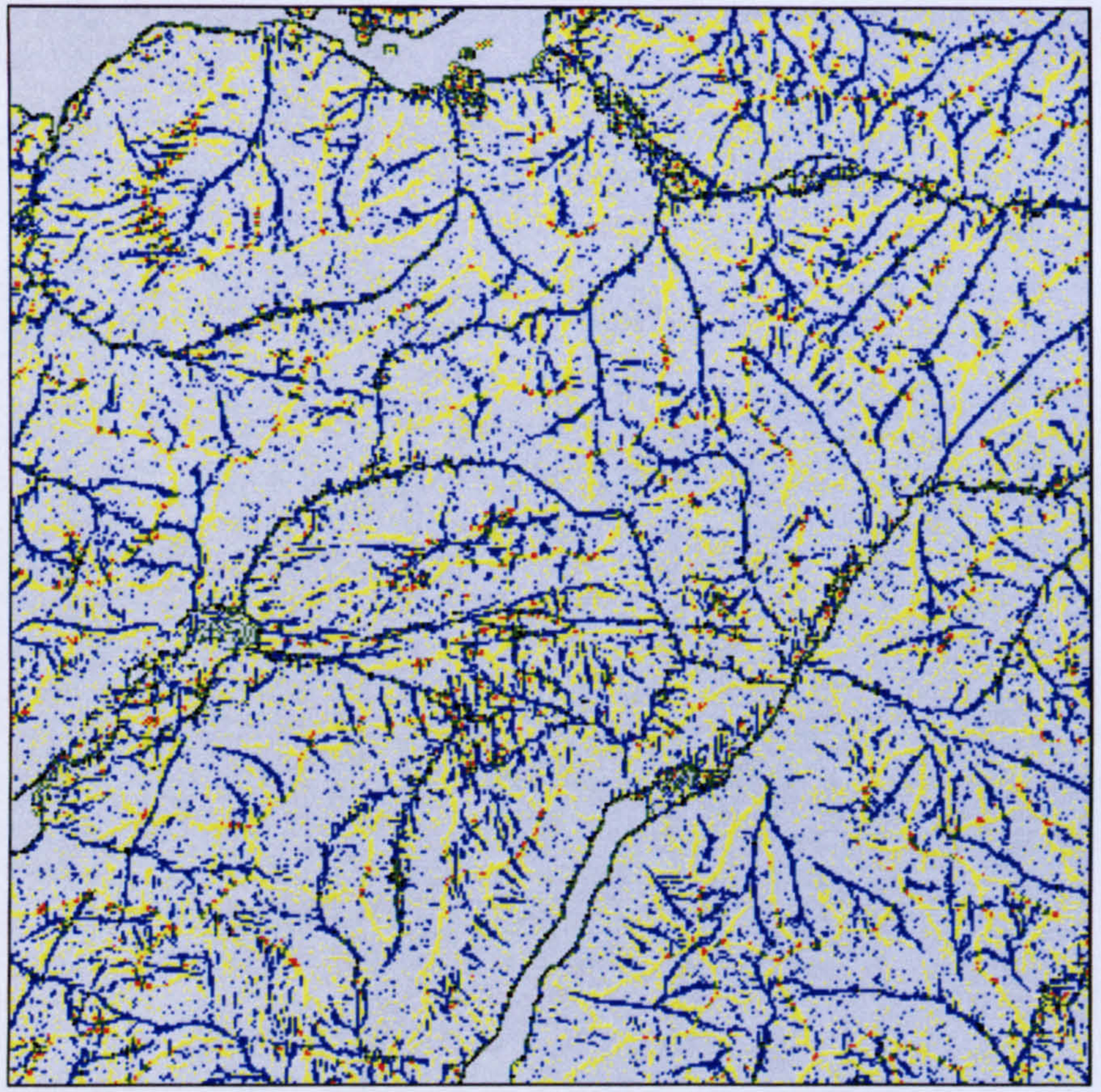

(b)

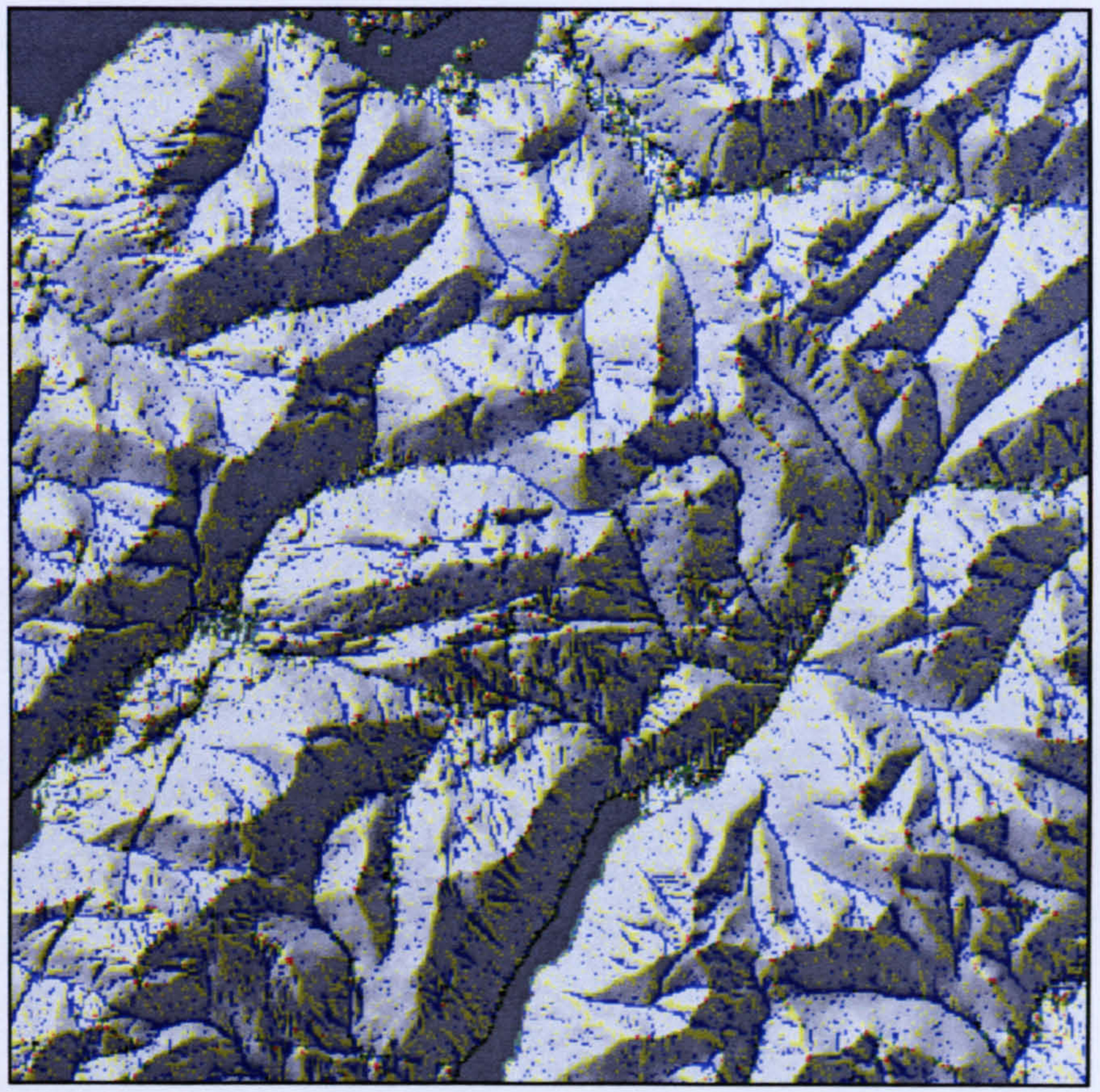

Figure shows extracted feature network from DEM elevation data. Colour coding as follows: red – peak, yellow – ridge, green – pass, blue – channel, black – pit. (a) shows derived data only and (b) shows derived data superimposed on relief. Produced with Landserf, using OS Landform Panorama data © Crown Copyright Ordnance Survey. An EDINA Digimap/JISC supplied service.

Figure 7.7

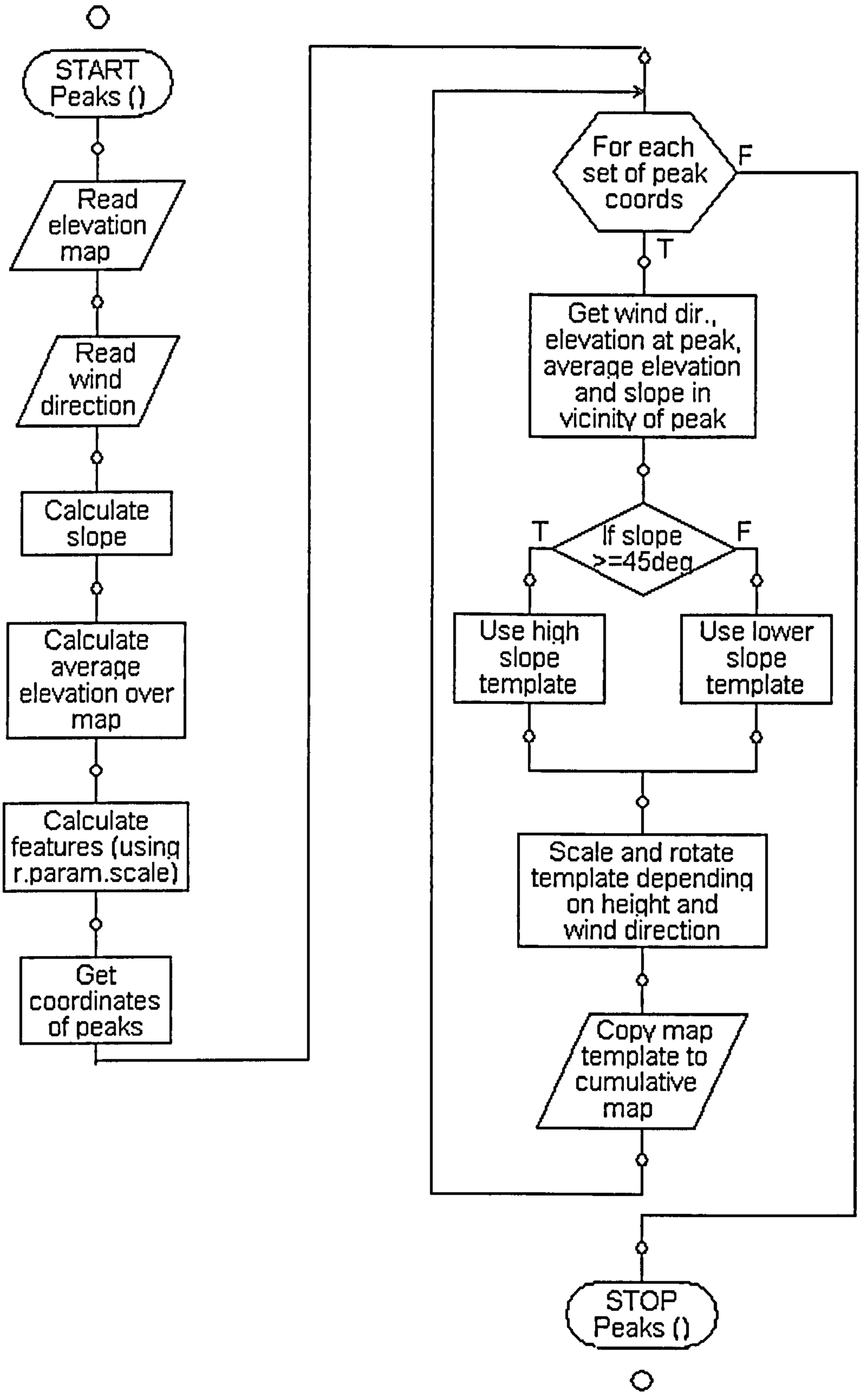

Flow chart showing the main steps in applying deposition rules to landscape peaks.

Figure 7.8

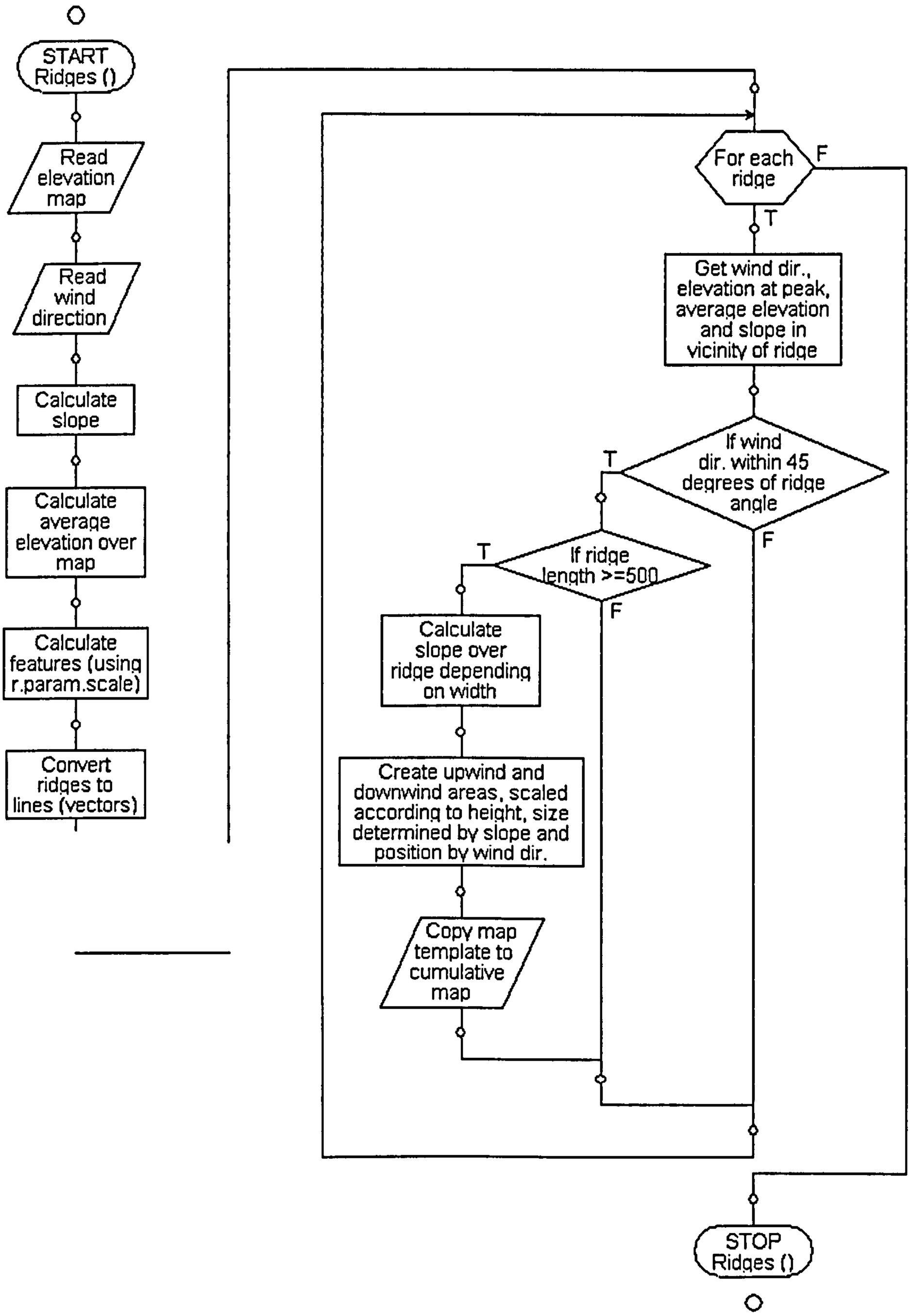

Flow chart showing the main steps in applying deposition rules to landscape ridges.

Figure 7.9

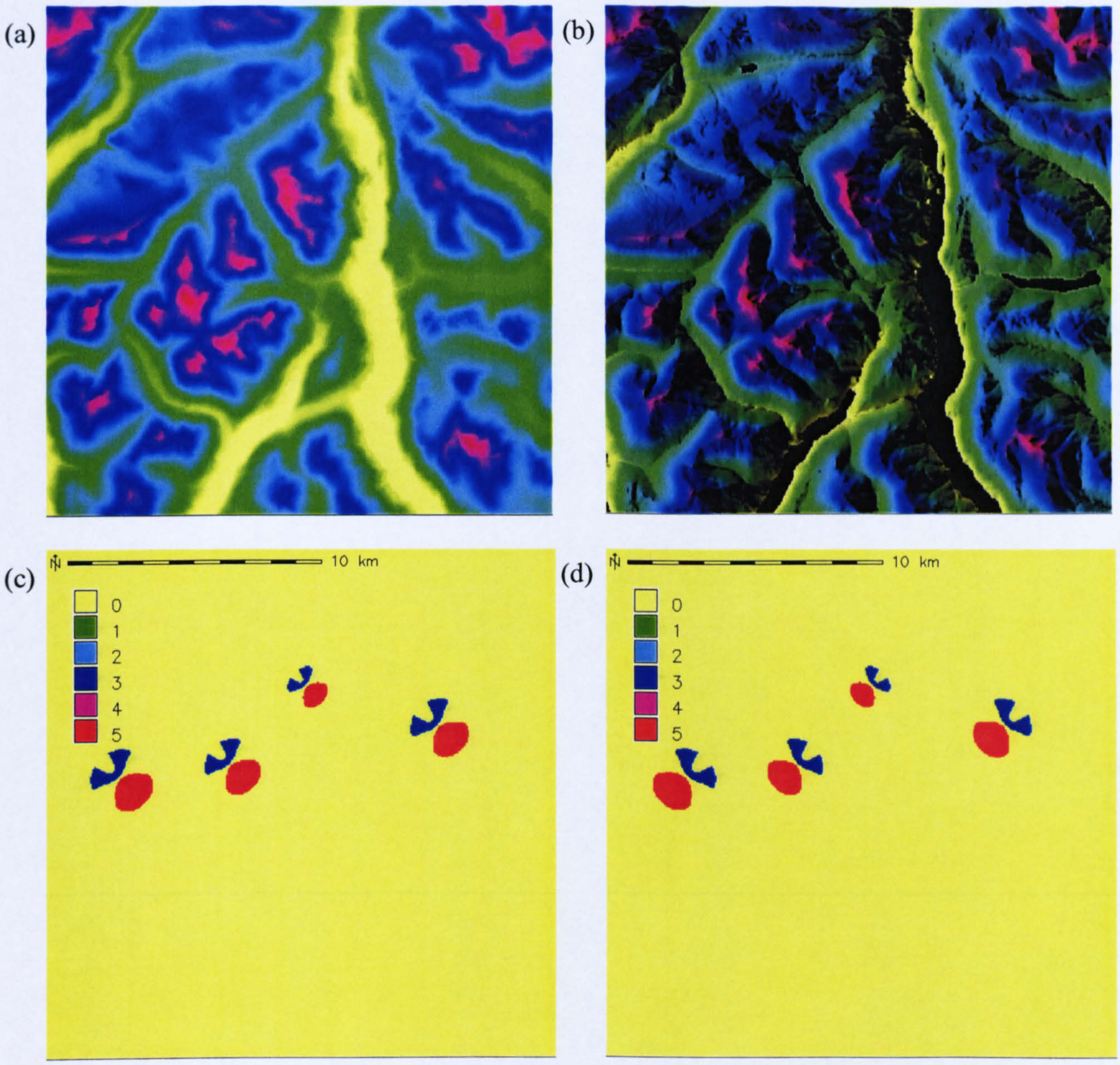

Example application of peak script. Elevation shown in maps (a) and (b), areas affected surrounding peaks for wind direction 135° in (c) and 225° in (d). In (c) and (d) red corresponds to increased deposition and blue to decreased deposition. Produced with Landserf (above) and GRASS GIS (below), using OS Landform Panorama data © Crown Copyright Ordnance Survey. An EDINA Digimap/JISC supplied service.

Figure 7.10

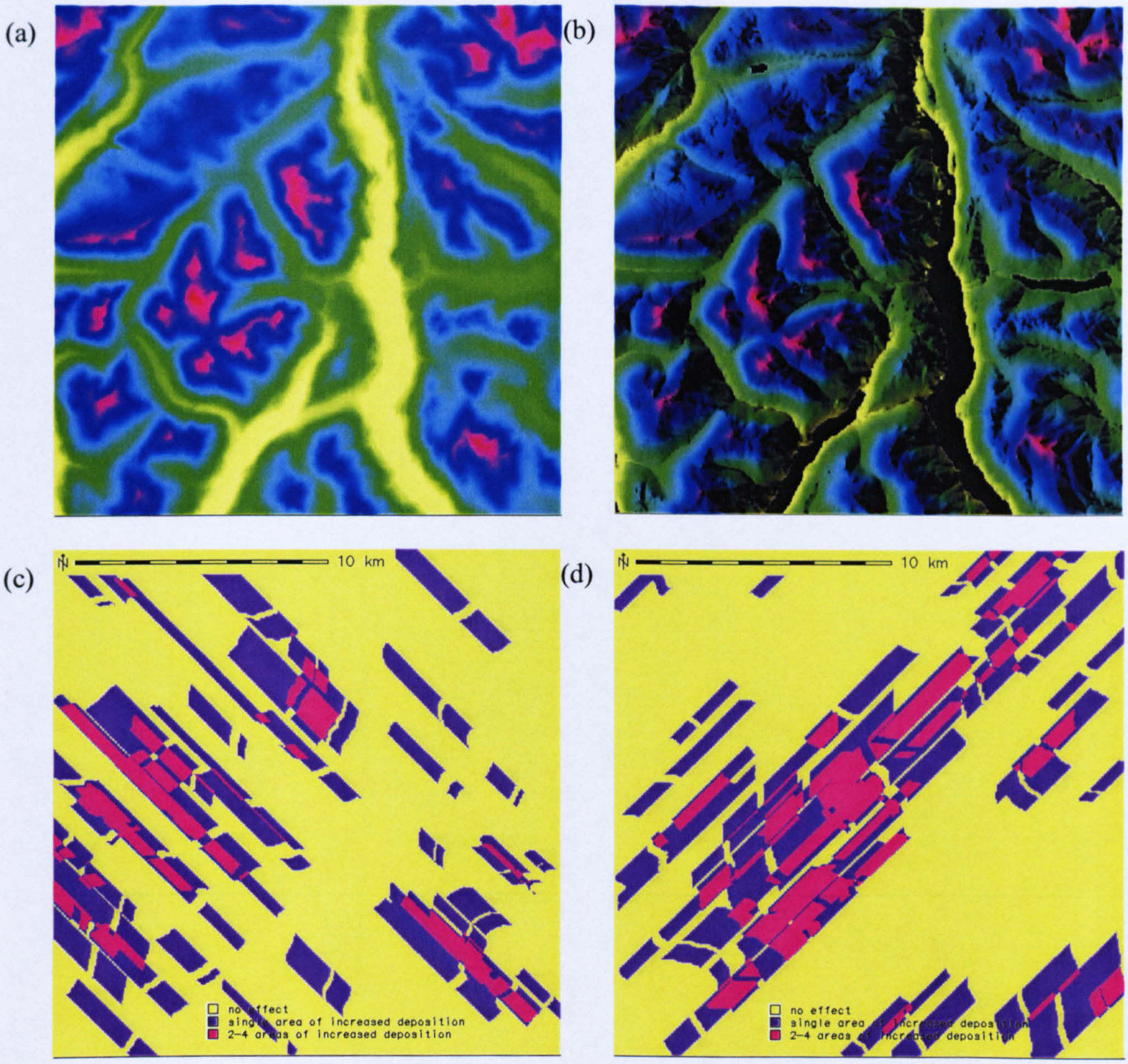

Example application of ridge script. Elevation shown in maps (a) and (b), areas affected surrounding ridges for wind direction 135° in (c) and 225° in (d). Produced with Landserf (above) and GRASS GIS (below), using OS Landform Panorama data © Crown Copyright Ordnance Survey. An EDINA Digimap/JISC supplied service.

Figure 7.11

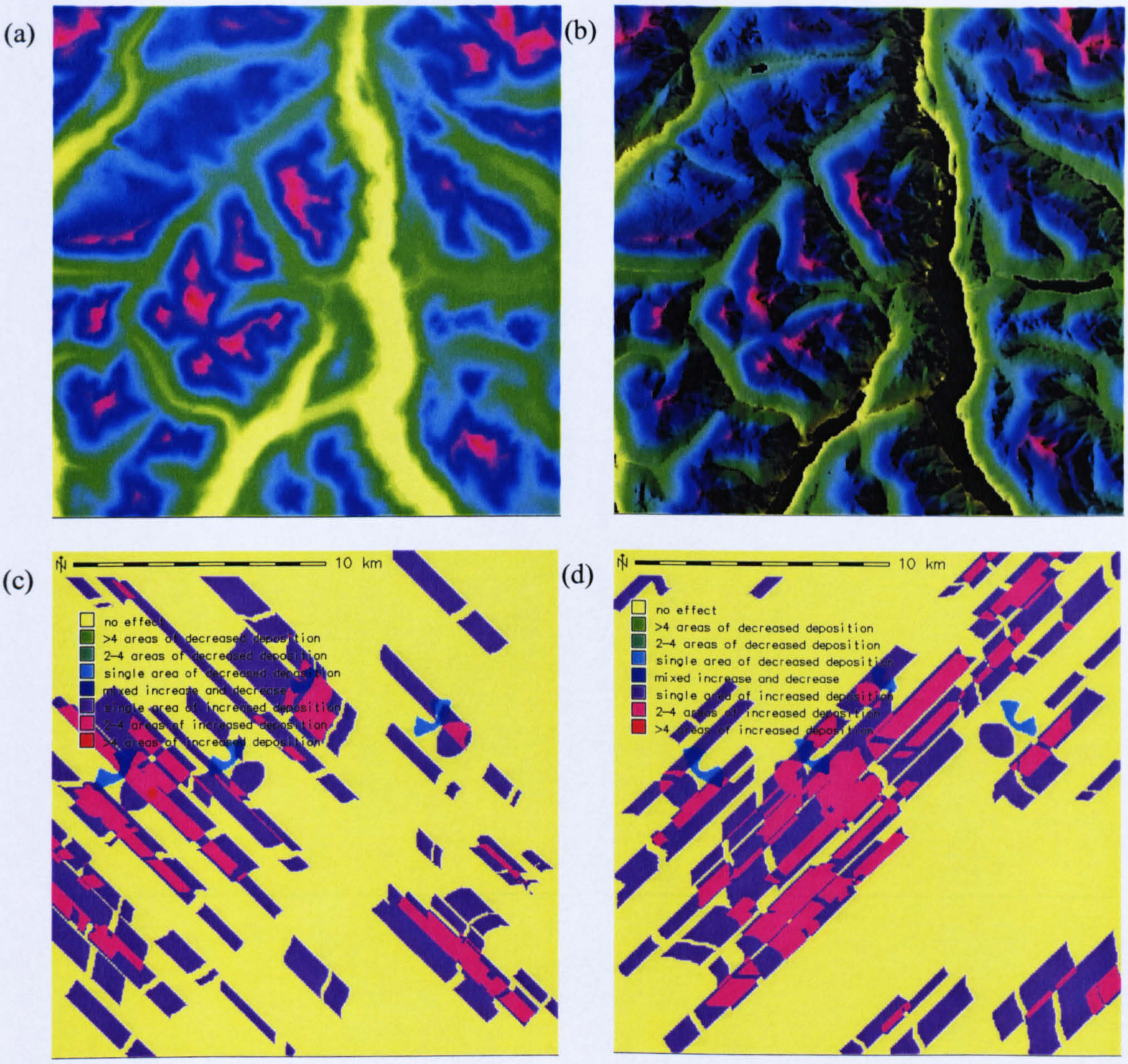

Example application of combine script. Elevation shown in maps (a) and (b), areas affected surrounding peaks and ridges for wind direction 135° in (c) and 225° in (d). Produced with Landserf (above) and GRASS GIS (below), using OS Landform Panorama data © Crown Copyright Ordnance Survey. An EDINA Digimap/JISC supplied service.

Figure 7.12

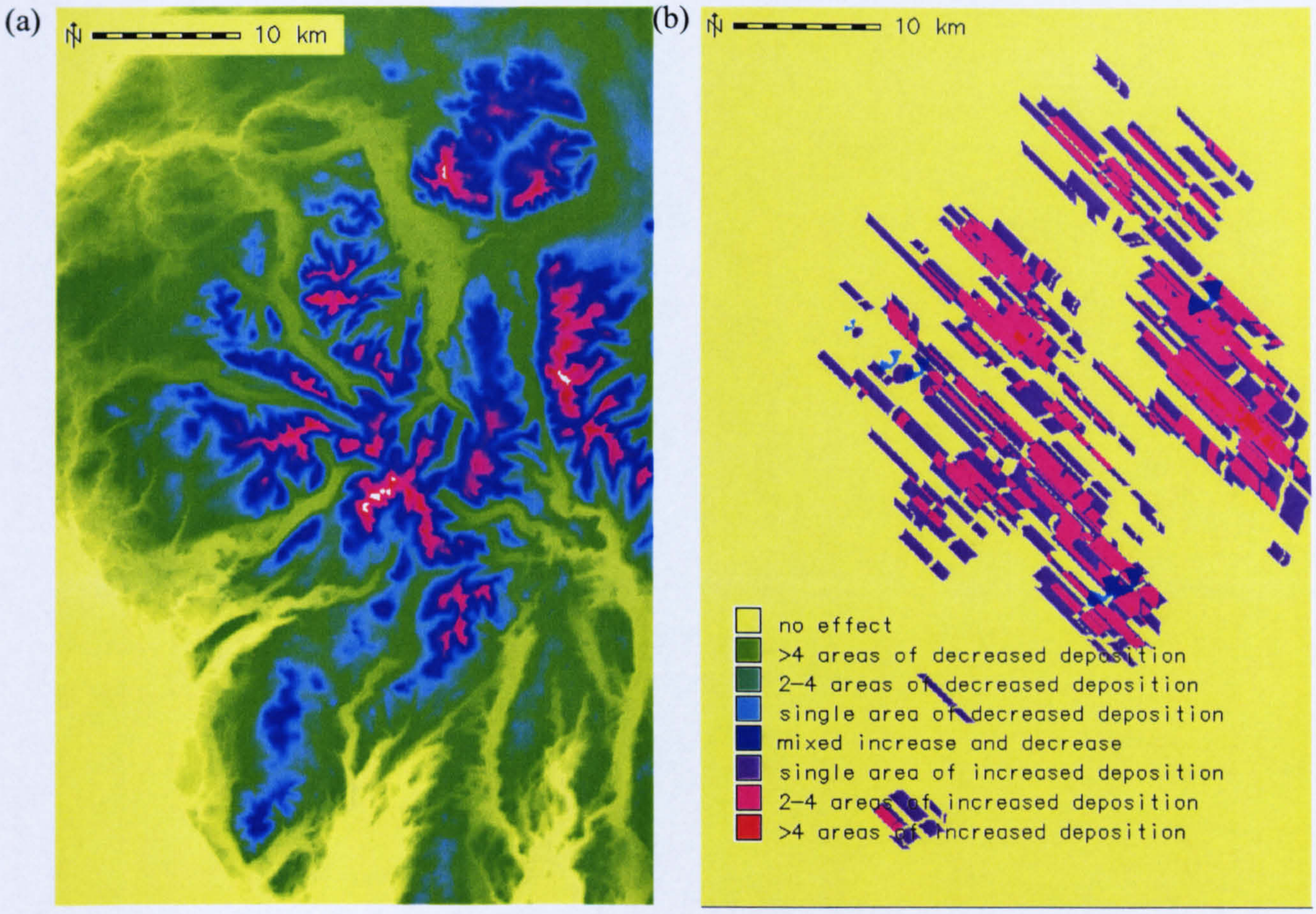

Results from combined script applied to Lake District, assuming a wind direction of 135°. (a) shows elevation and (b) the results of the script showing affected areas. Produced with GRASS GIS, using OS Landform Panorama data © Crown Copyright Ordnance Survey. An EDINA Digimap/JISC supplied service.

Figure 7.13

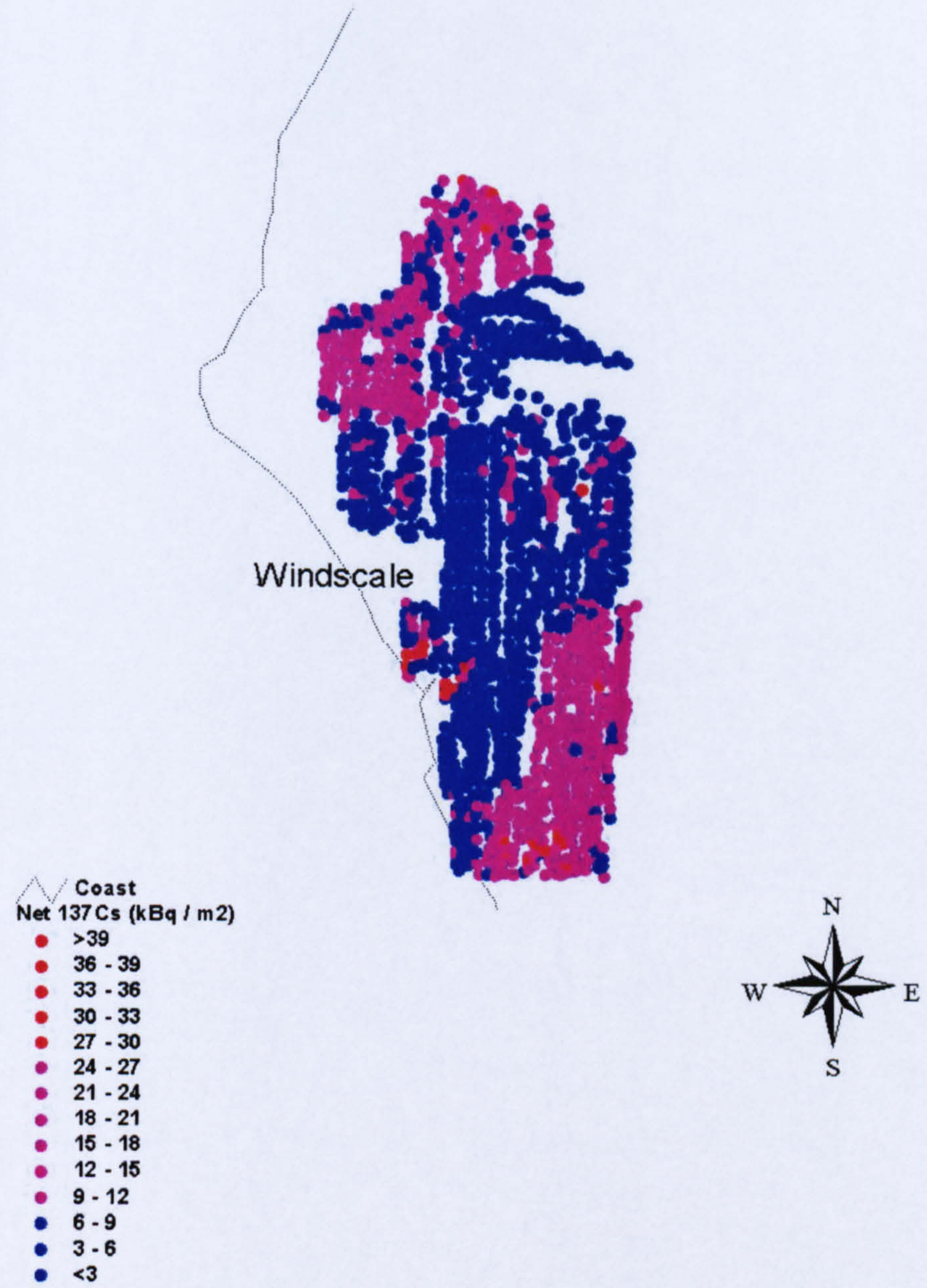

Net caesium-137 deposition from Windscale release, reproduced from Argyraki *et al.* (1999). Legend shows colour coded deposition density.

Figure 7.14

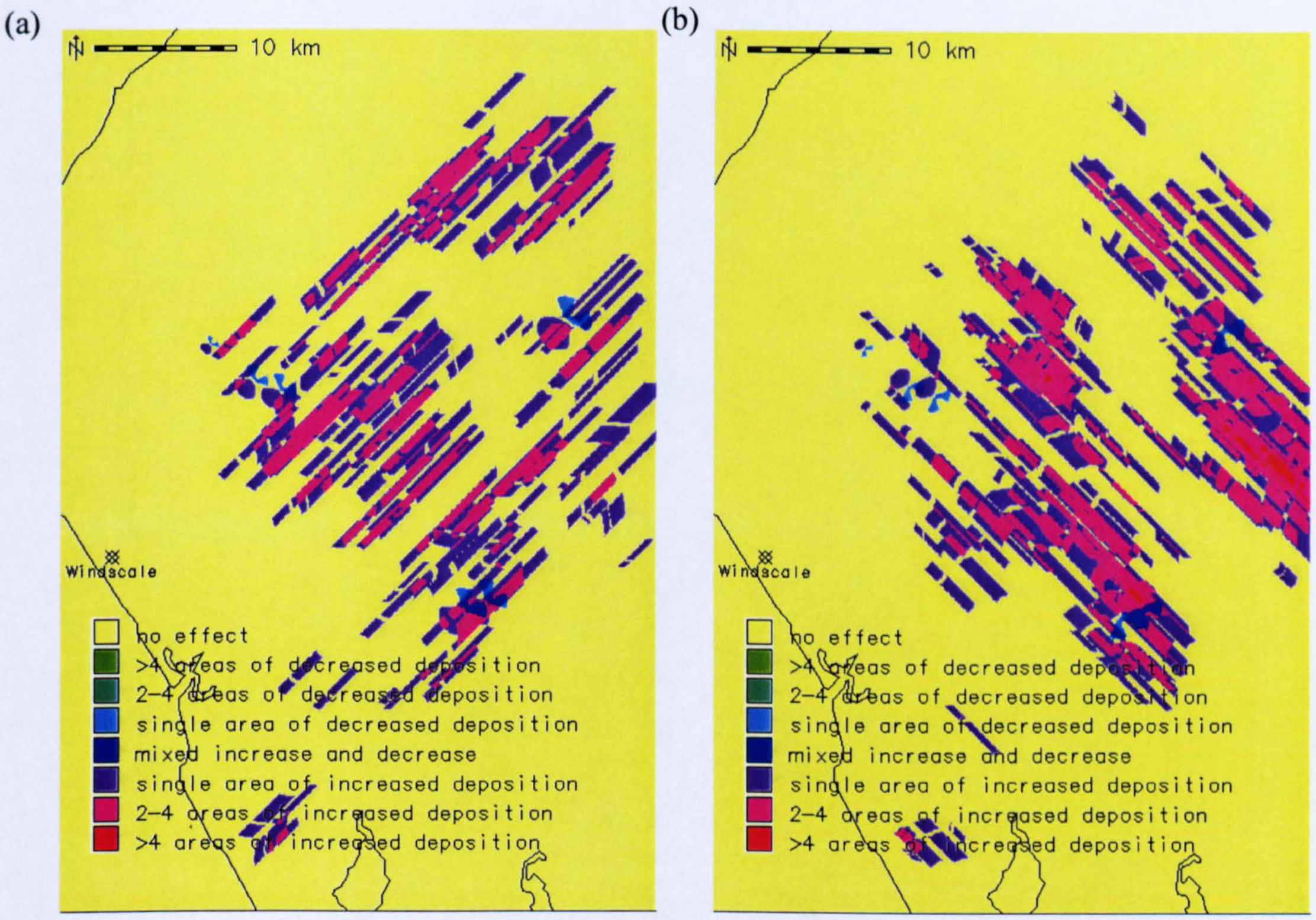

Results from script applied to case study of Windscale release, for (a) 225° and (b) 315° wind direction. Produced with GRASS GIS, using OS Landform Panorama data © Crown Copyright Ordnance Survey. An EDINA Digimap/JISC supplied service.

Figure 7.15

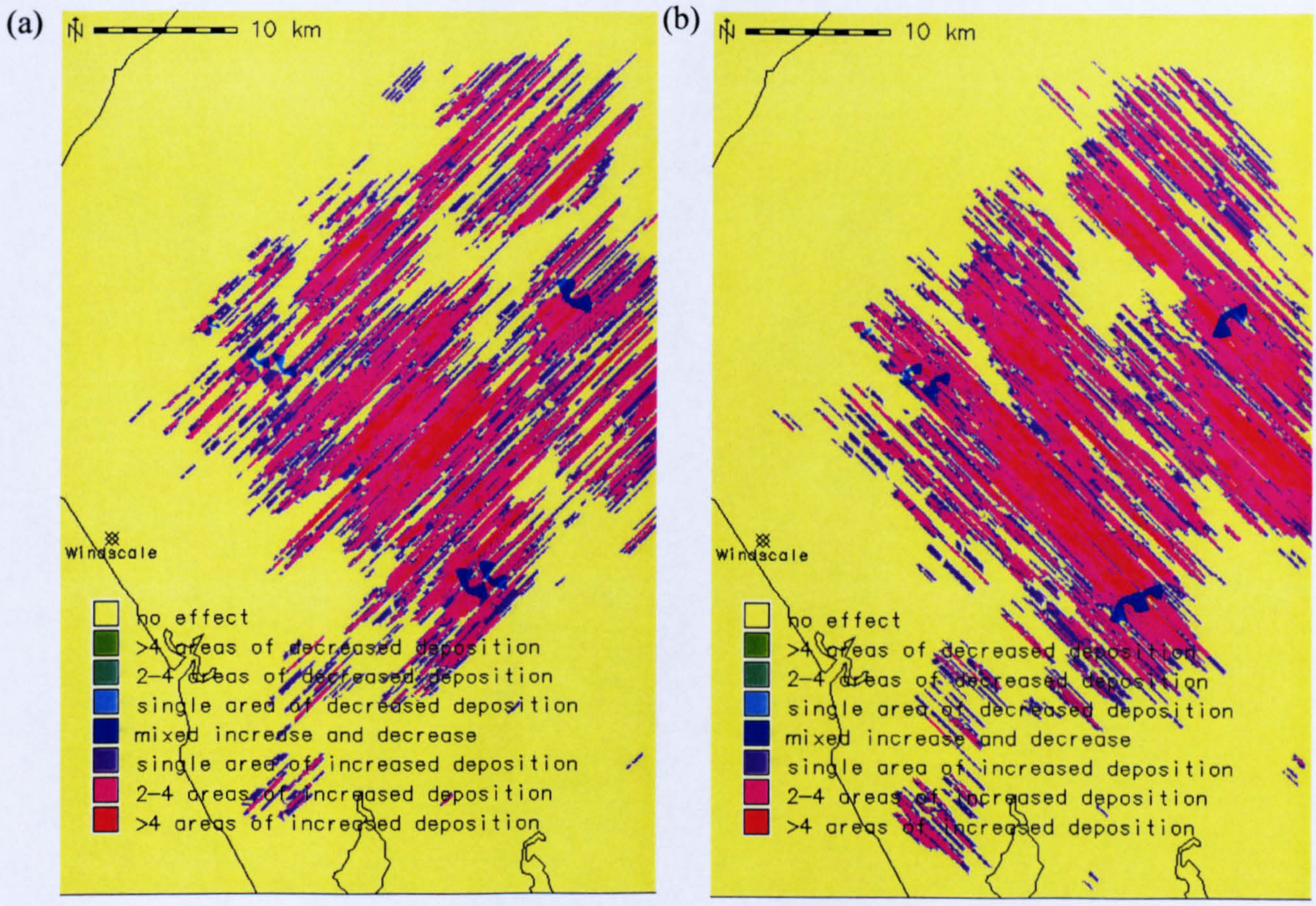

Results from script, with shorter ridge length threshold, applied to case study of Windscale release, for (a) 225° and (b) 315° wind direction. Produced with GRASS GIS, using OS Landform Panorama data © Crown Copyright Ordnance Survey. An EDINA Digimap/JISC supplied service.

(a)

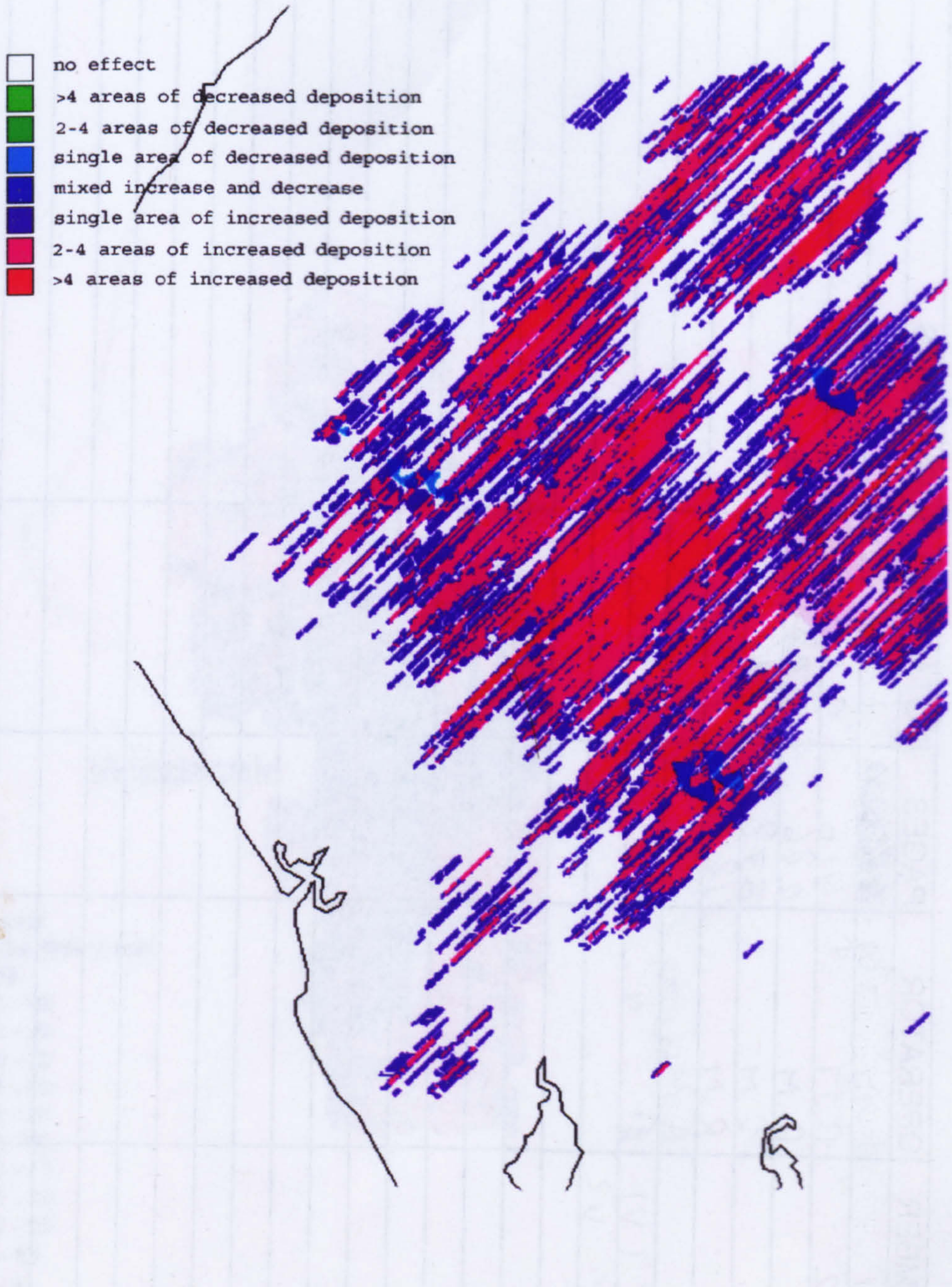
no effect
>4 areas of decreased deposition
2-4 areas of decreased deposition
single area of decreased deposition
mixed increase and decrease
single area of increased deposition
2-4 areas of increased deposition
>4 areas of increased deposition

Figure 7.16

(b)

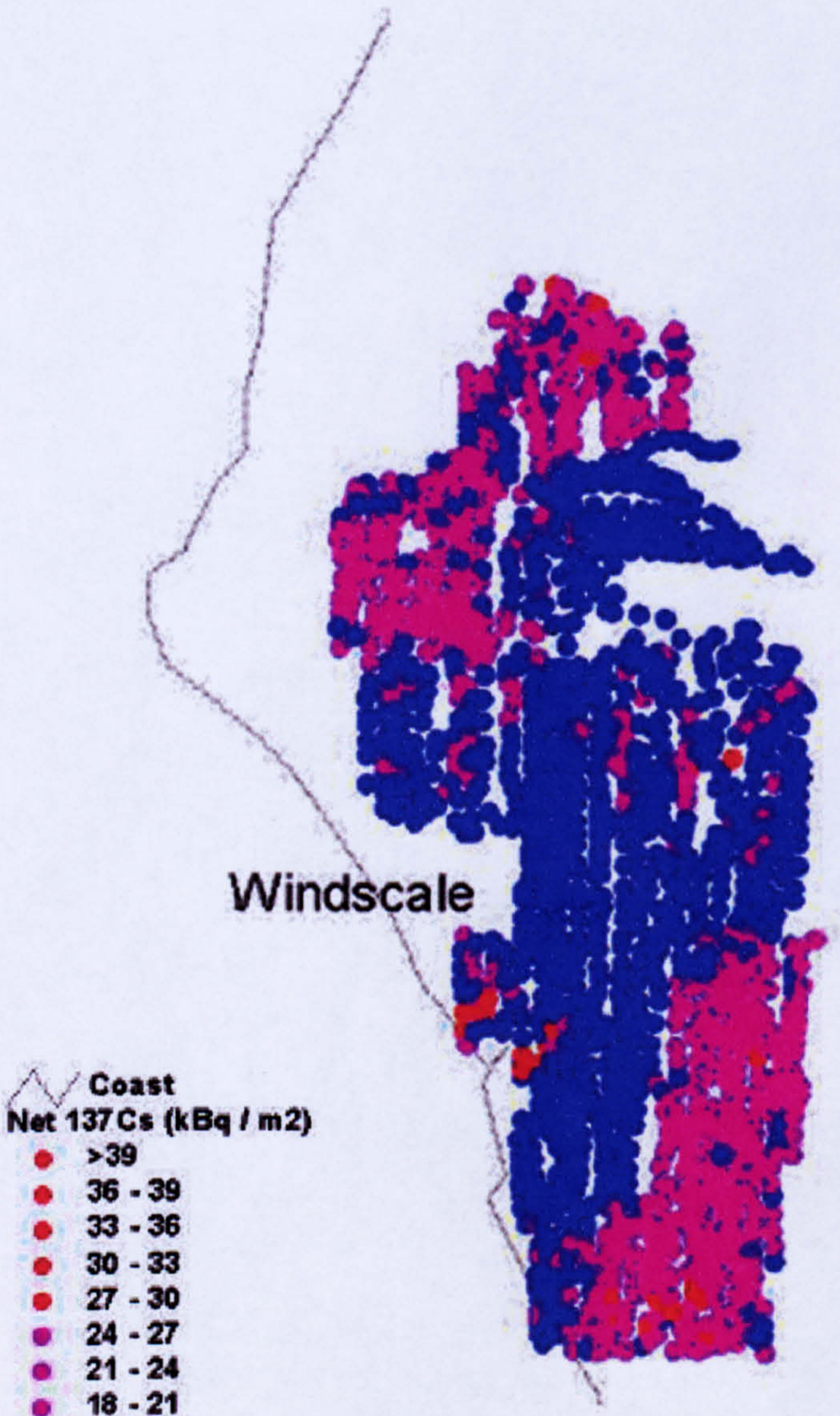

Comparison of net caesium-137 deposition and deposition likelihood map for wind direction 225°. Note dark blue colour on (a) corresponds to increased deposition, whereas on (b) this indicates low levels of deposition. Caesium data reproduced from Argyraki *et al.* (1999).

Figure 7.16

(a) (b)

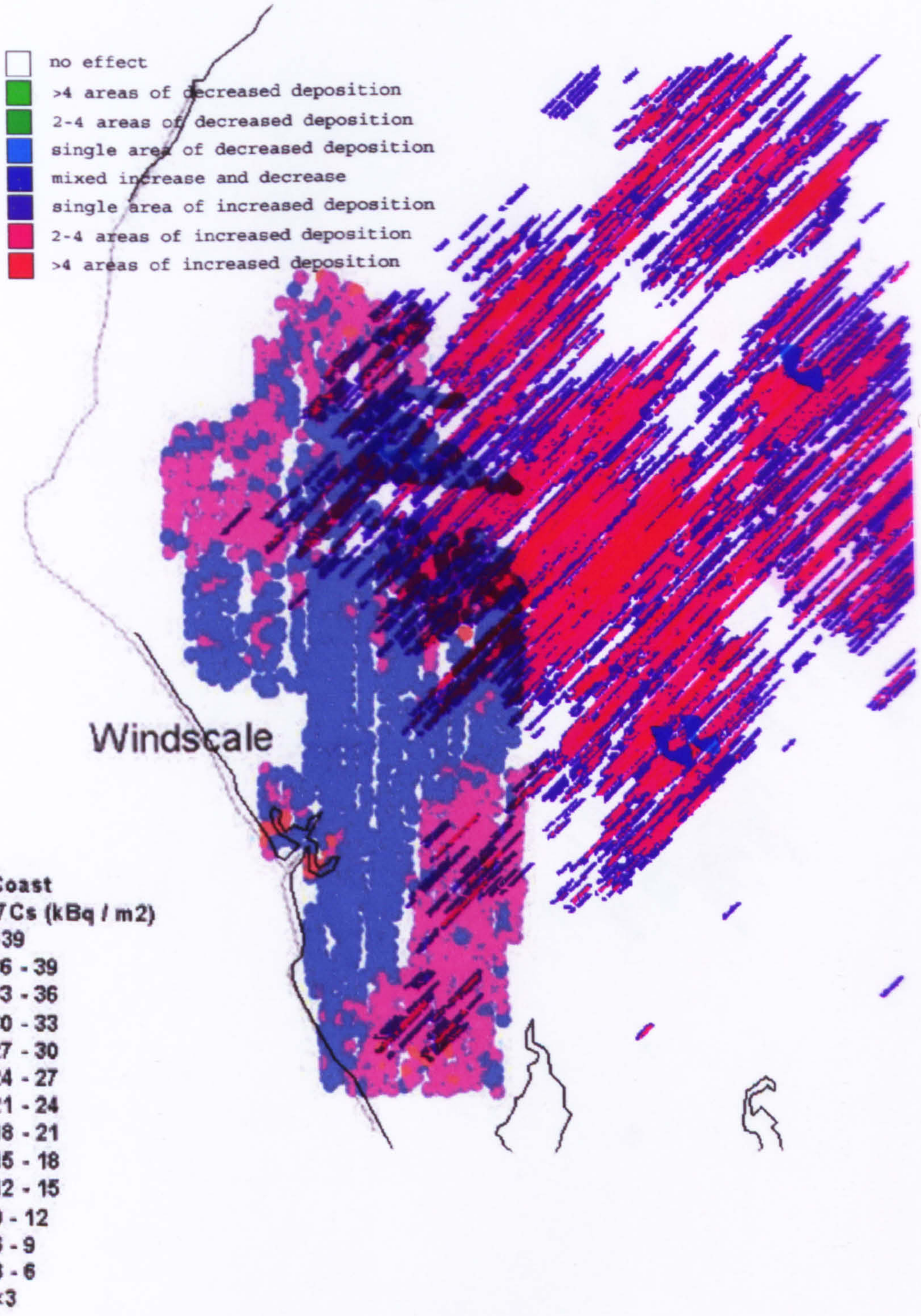

Comparison of net caesium-137 deposition and deposition likelihood map for wind direction 225°. Note dark blue colour on (a) corresponds to increased deposition, whereas on (b) this indicates low levels of deposition. Caesium data reproduced from Argyraki *et al.* (1999).

(a)

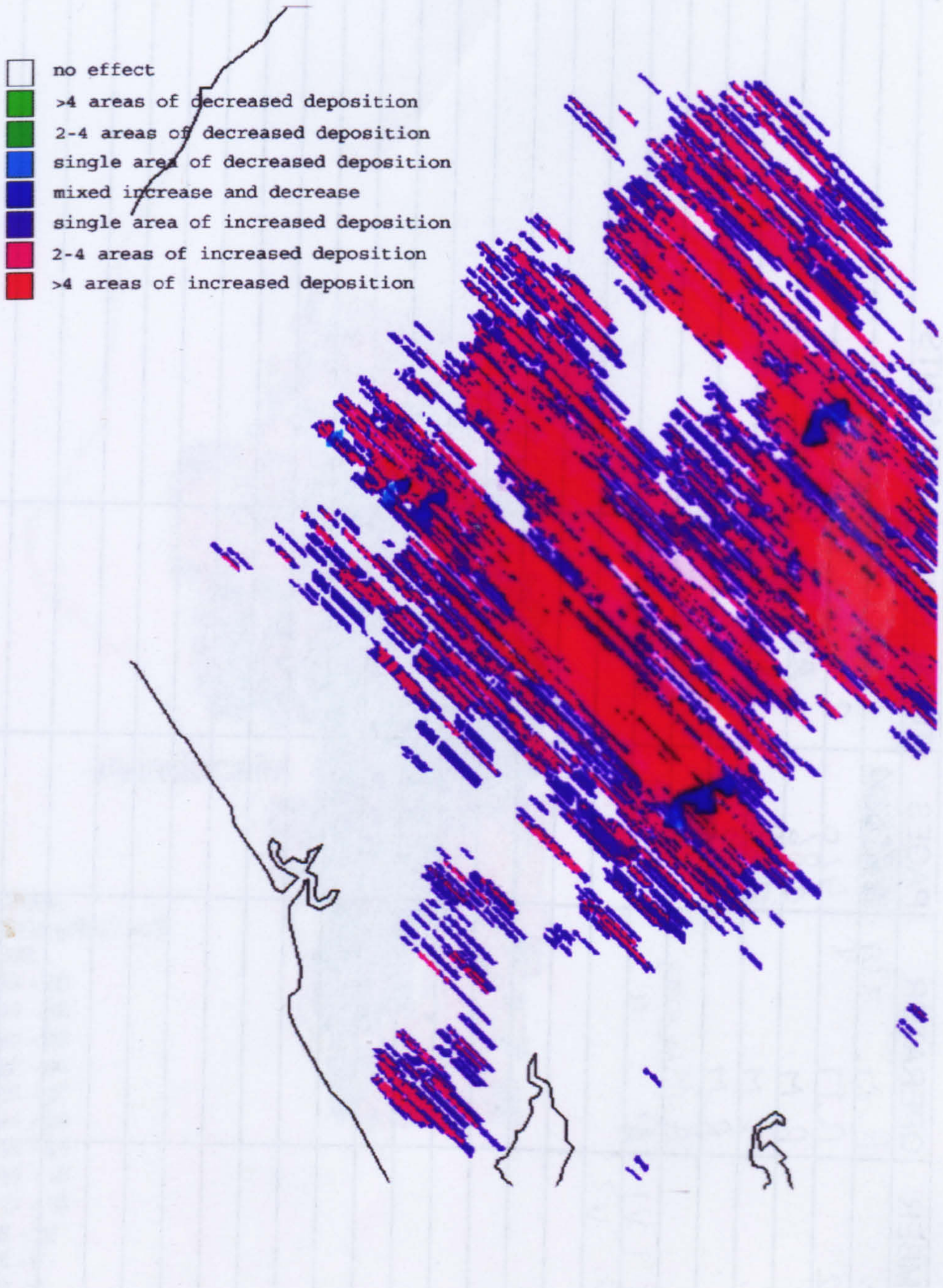
no effect
>4 areas of decreased deposition
2-4 areas of decreased deposition
single area of decreased deposition
mixed increase and decrease
single area of increased deposition
2-4 areas of increased deposition
>4 areas of increased deposition

Figure 7.17

(b)

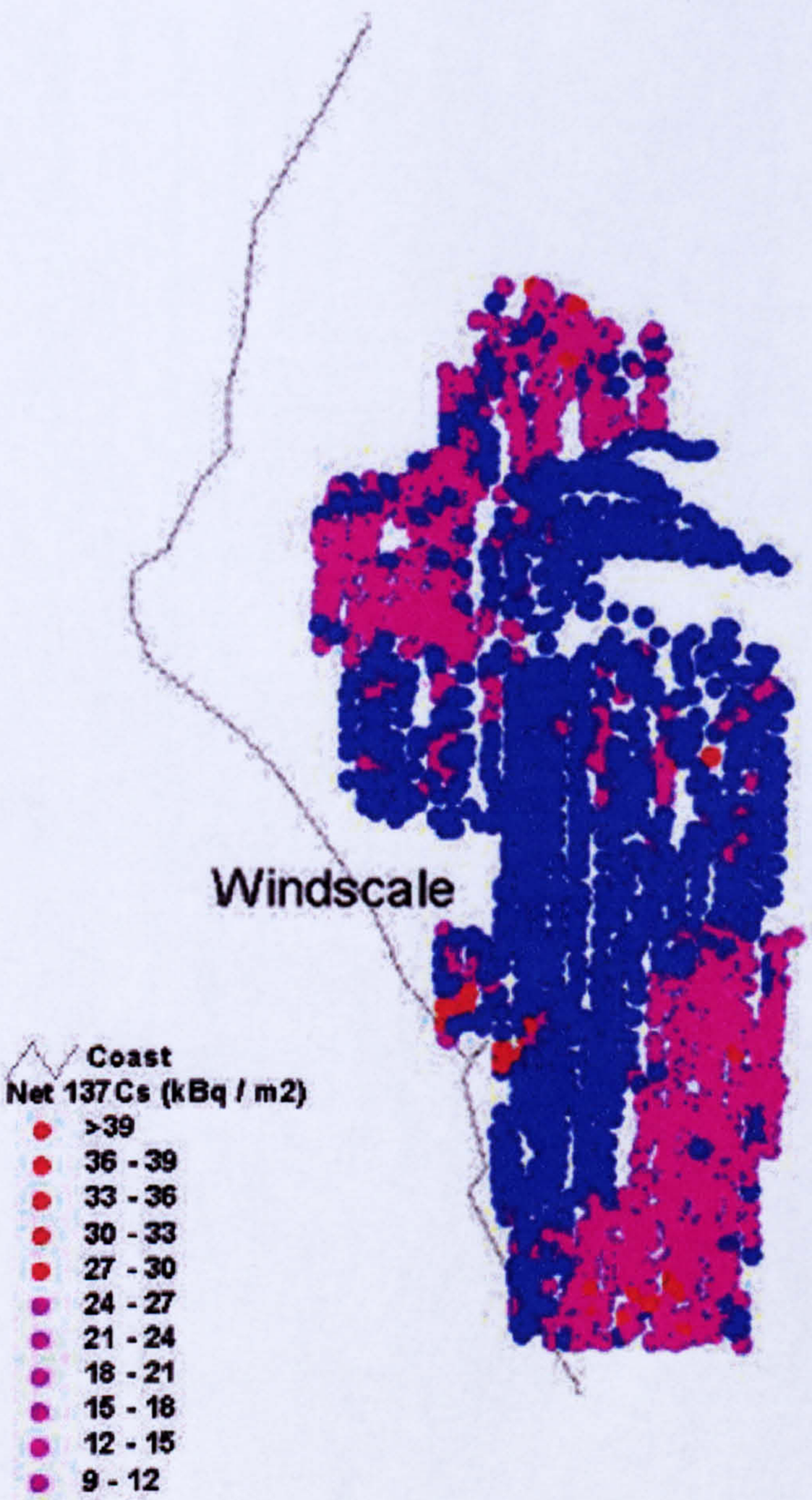

Comparison of net caesium-137 deposition and deposition likelihood map for wind direction 315°. Note dark blue colour on (a) corresponds to increased deposition, whereas on (b) this indicates low levels of deposition. Caesium data reproduced from Argyraki *et al.* (1999).

Figure 7.17

(a) **(b)**

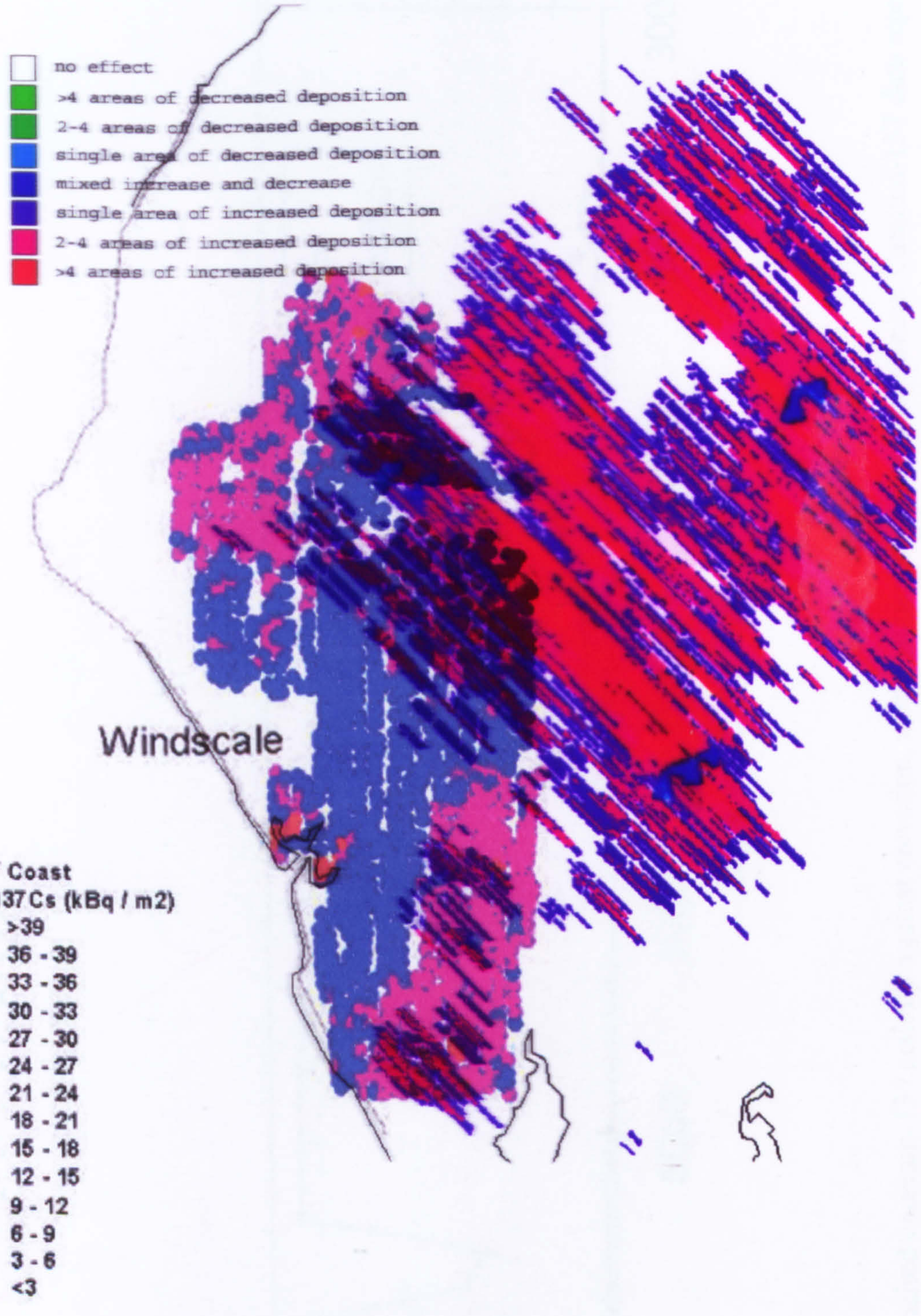

Comparison of net caesium-137 deposition and deposition likelihood map for wind direction 315°. Note dark blue colour on (a) corresponds to increased deposition, whereas on (b) this indicates low levels of deposition. Caesium data reproduced from Argyraki *et al.* (1999).

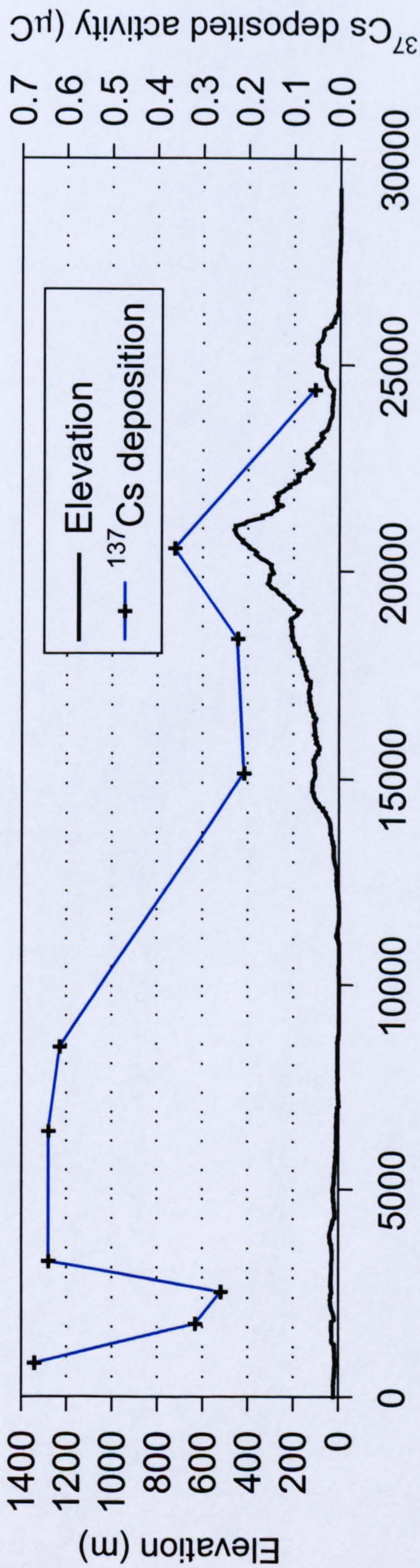

Figure 7.18

Comparison of deposited caesium-137 activity against elevation, along plume centreline from release. Caesium-137 data reproduced from Chamberlain (1959).

TABLES

Table 2.1

Geometry 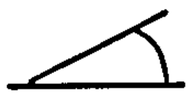	***Model***			***Full-scale***			***Location of peak***		***Gradient***
	H(m)	*L(m)*	*W(m)*	*H(m)*	*L(m)*	*W(m)*	*DS (m)*	*AS (m)*	*θ*
Ridge 1in1	0.1	0.2	2.50	100	200	2500	1.1	-	45°
Ridge 1in3	0.1	0.6	2.50	100	600	2500	1.1	-	18.43°
Cone	0.2	0.4	0.4	200	400	400	1.5	1.25	45°
Flat	0	0	0	0	0	0	-	-	0°

Model geometry dimensions at model-scale (1:1000) and full-scale. The table shows the height, streamwise length and across stream width of the model at model- and full-scale. The positions of the peak downstream (DS) from the end of the roughness elements and laterally from the wind tunnel wall (AS) are given, along with the slope of the models.

Table 2.2

$\overline{u'^2}$ ($m^2\ s^{-2}$)	$\overline{u'w'}$ ($m^2\ s^{-2}$)	$\overline{w'^2}$ ($m^2\ s^{-2}$)	u_* ($m\ s^{-1}$)
0.18	-0.039	0.14	0.20

Turbulent velocity components, average of values measured at z=0.05 for flat case. Friction velocity, u_*, calculated as $\sqrt{-\overline{u'w'}}$ is also included.

Table 3.1

Geometry	*Measurement height above surface (m)*	*Reattachment or reversal lengths (hill heights)*	
		Wind tunnel	*CFD*
Ridge 1in1	0.00	N.D.	11.3
	0.05	9.0	8.1
Ridge 1in3	0.00	N.D.	7.0
	0.02	5.0	5.9
	0.05	3.5 slight reversal	no reversal, min. velocity at 3.1
Cone	0.00	N.D.	1.6
	0.02	1.4	1.6
	0.05	1.4	1.7

Comparison of reattachment and reversal lengths between wind tunnel and CFD. The table shows the distance downwind from the peak of the reattachment point or reversal point. Note that for the ridge of slope 1 in 3 the wind tunnel measurements indicated a minor recirculation with a velocity of $-0.02 ms^{-1}$. The CFD result at this height showed no recirculation, but the position of minimum velocity is given. N.D. = no data.

Table 3.2

Source	*Details*	*Reattachment lengths (hill heights)*
Arya and Shipman (1981)	Experiment	13.0
Mouzakis and Bergeles (1991)	k-ε (modified)	10.0
Jung (1994)	Modified constants	12.0
Kim and Patel (2000)	k-ε (model)	9.8
	k-ω (model)	11.5
	PDM model	9.8
	RNG model	13.5
	Modified constants	16.5
Present study	Wind tunnel (z=0.05m)	9.0
	RNG	11.3

Comparison of experimental and model data for reattachment lengths behind a triangular ridge. Reproduced from Kim and Patel (2000). Note that the wind tunnel value from the present study was the reversal point measured at 0.05m above the surface. Scaling this by the ratio of reattachment/reversal lengths from the CFD would yield a value of 12.6 hill heights.

Table 6.1

Parameter investigated	*Geometry*	*Code*	*Values*
Mesh density	Flat sided ridge	fsrmd	coarse → medium adapted
Particle trajectory step	Flat sided ridge	fsrsd	0.01 – 10m
Turbulence model	Flat	flattm	std. k-eps, RNG k-eps, RSM
Turbulence model	Flat sided ridge	fsrtm	std. k-eps, RNG k-eps, RSM
Wind speed	Flat	flatws	2, 5, 10, 20 m s^{-1} at z=10m
Wind speed	Flat sided ridge	fsrws	2, 5, 10, 20 m s^{-1} at z=10m
Slope	Flat sided ridge	fsrs	1 in 1 → 1 in 5
Shape	Forward facing step	ffst	vertical, 45o, concave, convex
Shape	Sinusoidal hill	sh	average slope of 1 in 2, 1 in 4
Shape	Valley	v	V- , U- and sinusoidal-shaped
Peak separation	Multiple ridge	mr	various 2 ridge, and one 3 ridge case
Particle diameter	Flat	flatpd	0.1 – 100 μm
Particle diameter	Flat sided ridge	fsrpd	0.1 – 100 μm
Particle density	Flat	flatprho	800 – 50,000 kg m^{-3}
Particle density	Flat sided ridge	fsrprho	800 – 50,000 kg m^{-3}

Overview of two-dimensional cases investigated. Including CFD parameters, landscape geometries and particle properties.

Table 6.2

Case	*Vertical spacing*	*Horizontal spacing before adaption*	*Minimum vertical Spacing (m)*	*Minimum horizontal spacing (m)*	*Adapted*	*No of cells*
coarse	40 steps * 1.1 g.p.	25m	2.26	25	no	6400
coarse_focus	40 steps * 1.1 g.p.	25m (10m 500>x>1500)	2.26	10	no	8800
coarse_focus_adp	40 steps * 1.1 g.p. (doubled y<200)	25m (10m 500>x>1500)	1.13	5	yes (0<x<4000,0<y<200)	24610
medium	40 steps * 1.1 g.p.	10m	2.26	10	no	16000
medium_adp	40 steps * 1.1 g.p (doubled y<200)	10m	1.13	5	yes (0<x<4000,0<y<200)	44758

Details of meshes used for two-dimensional mesh dependency study (fsrmd). Note, vertical spacing defined as 40 intervals, increasing in size by a geometric progression (g.p.) with a factor of 1.1 (for the adapted cases this resolution is doubled).

Table 6.3

Case	*Slope*	*Degrees*	*Upwind edge (m)*	*Peak (m)*	*Downwind edge (m)*
fsrs11	1 in 1	45.0	700,0	750,50	800,0
fsrs12	1 in 2	26.6	650,0	750,50	850,0
fsrs13	1 in 3	18.4	600,0	750,50	900,0
fsrs14	1 in 4	14.0	550,0	750,50	950,0
fsrs15	1 in 5	11.3	500,0	750,50	1000,0

Dimensions of ridges of varying slope. Note that the location of the ridge peak does not change between cases, only the extent of the base. Positions are given relative to the start of the domain.

Table 6.4

Case	*Vertical spacing*	*Horizontal spacing before adaption*	*Minimum vertical Spacing (m)*	*Minimum horizontal spacing (m)*	*Adapted*	*No of cells*
coarse_focus	30 steps * 1.1 g.p.	25m (10m 500>x>1500, 250>y>500)	6.08	10	no	134160
coarse_focus_adp	30 steps * 1.1 g.p. (doubled z<200)	25m (10m 500>x>1500, 250>y>500)	3.04	5	yes (600<x<1200, 350<y<500, 0<z<200)	211076
medium_focus	30 steps * 1.1 g.p.	50m (5m 500>x>1500, 250>y>500)	6.08	5	no	207360

Details of meshes used for three-dimensional mesh dependency study. Note, vertical spacing defined as 30 intervals, increasing in size by a geometric progression (g.p.) with a factor of 1.1 (for the adapted cases this resolution is doubled).

Table 6.5

Case	*Description*	*Slope*	*Base dimensions*	
			Downwind (m)	*Crosswind (m)*
cone11	steep sided cone	1 in 1	200	200
cone13	shallower sided cone	1 in 3	600	600
elong200cone11	steep sided cone elongated in crosswind direction	1 in 1	200	400
pyramid	5-sided pyramid	1 in 3	~550	~600
sinehill	sinusoidal hill	1 in 2 (average)	400	400

Details of the geometry of the three-dimensional cases studied. Base dimensions are lengths rather than positions.

Table 7.1

Parameter investigated	***Effect on deposition***
Wind speed	Deposition velocity appears to rise linearly with a rise in velocity for a uniform concentration. For the range of speeds investigated there appears to be no change in the increase relative to the flat case for different wind speeds, either in quantity or location of deposition change.
Particle diameter	Little dependence on particle diameter below 10μm, above this value deposition velocity increases and pattern changes. Although CFD results did not show increase for small particle size this would be expected from theory as Brownian motion becomes more significant. This effect though should not be spatially dependent.
Particle density	Little change expected for the range of expected densities.

Summary of effects of a number of parameters on particle deposition

Table 7.2

Geometry	*Parameter investigated*	*Effect on deposition*
Ridge	Location relative to peak	Deposition varied depending on the area considered. Deposition increased to the windward face. There was a reduction to the leeward face and a further increase in the wake.
	Slope	An increase in slope causes a number of effects: a sharpening of the upwind deposition peak, an increase in the maximum amount of increase, a more prominent region of reduced deposition in the lee and a movement of the downwind deposition peak further from the ridge.
	Shape of ridge	There were only subtle differences between a sinusoidal and flat sided ridge for the same average gradient.
Forward facing step		A peak of deposition was seen at the step, with the exact location and size dependent on the geometry of step. An increase was seen in the wake.
Valley		There is a decrease in the valley and an increase on the leeward edge. The shape of the valley has little impact.
Multiple ridges		If the ridges are closer than 2 ridge heights apart then the peak depositions can be superimposed and the wake effect remains the same as a single ridge. If they are further apart than 8 ridge heights then the peak and the wake can both be superimposed.

Summary of effects of the geometry of two-dimensional landscapes on particle deposition.

Table 7.3

Geometry	*Effect on deposition*
1 in 1 cone	Increase on windward face and in two regions in the wake. Decrease on leeward face.
1 in 3 cone	A smaller increase on the windward face compared to the 1 in 1 cone. No significant increase in wake. Decrease on leeward face.
Elongated 1 in 1 hill	Similar to 1 in 1 cone but the area of reduced deposition is further from the hill at the centre.
1 in 3 slope pyramid	Similar to cone of same slope but with more deposition in the wake.
1 in 2 smoothly sloped hill	Similar to 1 in 3 slope cone but no wake deposition (no sharp edges).

Summary of effects of the geometry of three-dimensional landscapes on particle deposition.

Table 7.4

Ridge slope	*Area of upwind increase (hill heights from peak)*	*Area of downwind increase (hill heights from peak)*	*Lower threshold gradient (degrees)*
1 in 1	-1 -> 0	3 -> 40	35.8
1 in 2	-2 -> 0	3.5 -> 25	22.5
1 in 3	-3 ->0	3.5 -> 22	16.2
1 in 4	-4 -> 0	1 -> 15	12.7
1 in 5	-5 -> 0	1 -> 12	1 *

Summary of affected areas (>1.1 deposition ratio) resulting from ridges of different slopes. * Note lower cut-off value was not result of CFD study, rather it is an arbitrary value from landscape feature extraction algorithm.

Table 7.5

Band	*Meaning*
0	No effect
1	2-4 areas of decreased deposition
2	2-4 areas of decreased deposition
3	1 area of decreased deposition
4	Mixed increase and decrease
5	1 area of increased deposition
6	2-4 areas of increased deposition
7	2-4 areas of increased deposition

Banding of deposition effects.

APPENDIX 1 – PUBLISHED WORK

Wind and Structures, Vol. 5, No. 2~4 (2002) 177-192

A 6 m cube in an atmospheric boundary layer flow Part 2. Computational solutions

P. J. Richards† and A. D. Quinn‡

Environment Group, Silsoe Research Institute, Wrest Park, Silsoe, Bedfordshire, MK45 4HS, U.K.

S. Parker‡†

Division of Environmental Health & Risk Management, University of Birmingham, Edgbaston, Birmingham B15 2TT, U.K.

Abstract. Computation solutions for the flow around a cube, which were generated as part of the Computational Wind Engineering 2000 Conference Competition, are compared with full-scale measurements. The three solutions shown all use the RANS approach to predict mean flow fields. The major differences appear to be related to the use of the standard k-ε, the MMK k-ε and the RNG k-ε turbulence models. The inlet conditions chosen by the three modellers illustrate one of the dilemmas faced in computational wind engineering. While all modeller matched the inlet velocity profile to the full-scale profile, only one of the modellers chose to match the full-scale turbulence data. This approach led to a boundary layer that was not in equilibrium. The approach taken by the other modeller was to specify lower inlet turbulent kinetic energy level, which are more consistent with the turbulence models chosen and lead to a homogeneous boundary layer. For the 0° case, wind normal to one face of the cube, it is shown that the RNG solution is closest to the full-scale data. This result appears to be associated with the RNG solution showing the correct flow separation and reattachment on the roof. The other solutions show either excessive separation (MMK) or no separation at all (K-E). For the 45° case the three solutions are fairly similar. None of them correctly predicting the high suctions along the windward edges of the roof. In general the velocity components are more accurately predicted than the pressures. However in all cases the turbulence levels are poorly matched, with all of the solutions failing to match the high turbulence levels measured around the edges of separated flows. Although all of the computational solutions have deficiencies, the variability of results is shown to be similar to that which has been obtained with a similar comparative wind tunnel study. This suggests that the computational solutions are only slightly less reliable than the wind tunnel.

Key words: computational wind engineering; cube; turbulence modelling.

1. Introduction

At the initial stage of organising CWE2000 there was discussion on the standing of computational methods applied to problems in wind engineering. To assess progress a test case was proposed with boundary conditions closely defined. Solutions were sought from the computational wind engineering

† Visiting Scientist from the University of Auckland, New Zealand
‡ Research Scientist
‡† Research Student

ELSEVIER

Atmospheric Environment 38 (2004) 3867–3878

ATMOSPHERIC ENVIRONMENT

www.elsevier.com/locate/atmosenv

A computational and wind tunnel study of particle dry deposition in complex topography

S.T. Parker, R.P. Kinnersley*,[1]

Division of Environmental Health and Risk Management, School of Geography, Earth and Environmental Sciences, University of Birmingham, Edgbaston, Birmingham B15 2TT, UK

Received 1 August 2003; received in revised form 1 March 2004; accepted 10 March 2004

Abstract

An understanding of the likely pattern of dry deposition of small particles over a landscape is a key prerequisite to designing strategies for sampling ground contamination following routine or accidental releases to atmosphere. Wind tunnel and computational fluid dynamics studies of flow and particle deposition over landscape features have been carried out. The presence of elevated landscape features showed a strong effect on the pattern of deposition relative to a flat landscape case. A relatively small area of increased deposition occurred on the upwind face, with a larger area of decreased deposition in the wake. The slope of the landscapes affected the magnitude of the effect and the size of the affected region in the wake. The pattern of deposition for a three-dimensional landscape was complex. Good quantitative agreement was seen between the CFD predicted deposition and the wind tunnel results for the two-dimensional cases and reasonable qualitative agreement for the three-dimensional case, suggesting that CFD studies might be an appropriate tool to systematically explore the influence of complex topography on particle deposition.

Keywords: Aerosol; CFD; Complex terrain; Hills; Turbulence

1. Introduction

Deposition of particulate material from the atmosphere to the ground is a significant transfer pathway for many environmental pollutants. It provides an entry point for contaminants into the food chain, and is one of the factors that govern the rate at which clouds of contaminant become depleted. An understanding of this pathway is important in protecting the population from the adverse effects of airborne contaminants. Of particular concern is the fate of radioactive or toxic chemical aerosols released over a short period, for example, as a result of an accident at a nuclear installation. Effective emergency management following such a release, including the direction of survey teams and delimiting of restricted land use areas, requires an understanding of the spatial distribution of subsequent deposits of contaminant.

Currently, quantification of deposition relies upon deposition velocities that are strictly applicable only to uniform roughness, and do not account for local variations in topography and land cover. Such variations give rise to changes in local wind velocity and turbulence levels that can significantly influence particle deposition rates. The use of such simplifications during emergency exercises has led to operatives deploying finite surveying resources in a less-than-optimal way, and in some cases missing "hot-spots" of contamination (Argyraki et al., 1999).

*Corresponding author.
E-mail [redacted]

1352-2310/$ - see front matter © 2004 Elsevier Ltd. All rights reserved.
doi:10.1016/j.atmosenv.2004.03.046

APPENDIX 2 - GIS SCRIPTS

Script 1: Peaks

```
#!/usr/bin/perl

#Define constants
$em=pdel;#elevation map
$pi=3.1415927;
$wd=225; #wind direction

`g.region raster=$em`;
`r.mapcalc "$em.peak.effect=0"`;
#Calculate slope of input elevation map
#uncomment next section if ridges.pl not run already
#`r.slope.aspect elevation=$em slope=$em.slope`;
#`r.mapcalc "$em.coverage=1"` ;
#`r.average base=$em.coverage cover=$em output=$em.av`;
#`d.erase`;
#`r.mapcalc "winddir=$wd"`;
#`r.param.scale in=$em  out=$em.feat s_tol=1 c_tol=0.001 size=11 param=feature exp=0`;

#put peaks only into a separate file
`r.mapcalc "$em.peaks=if(($em.feat==6),1,null())"` ;

#convert peak raster file to sites file
`r.to.sites input=$em.peaks output=$em.s.peaks`;

#Get site coordinates and put into an array
$n=1;
@peakcoords=`s.out.ascii -a -d -i sites=$em.s.peaks`;

foreach (@peakcoords) {

    @coords=split;
    $x=$coords[0];
    $y=$coords[1];

#Get elevation at peak and average elevation value for map ($em.av)
    print "$n\tX: $x, Y: $y\n";
```

```
    $elev_out=`r.what input=$em,$em.av,winddir east_north=$x,$y`;
    @elevs=split /\|/, $elev_out;
    $elevation=$elevs[3];
    $average=$elevs[4];
    $winddir=$elevs[5];
    chomp($winddir);
    $wdrad=($winddir+90)*$pi/180;
    print "$elevation $average $winddir $wdrad\n";
    $X=$elevation-$average;
    $XB=$X*cos($wdrad);
    $YB=-$X*sin($wdrad);
    $XC=$X*sin($wdrad);
    $YC=$X*cos($wdrad);
    $XD=$X*sin($wdrad)+$X*cos($wdrad);
    $YD=-$X*sin($wdrad)+$X*cos($wdrad);
    printf "X:%.1f %.1f %.1f Y:%.1f %.1f %.1f\n",$XB,$XC,$XD,$YB,$YC,$YD;

#Calculate transformation points using elevation
    $x_os_b=$x+$XB;
    $y_os_b=$y+$YB;
    $x_os_c=$x+$XC;
    $y_os_c=$y+$YC;
    $x_os_d=$x+$XD;
    $y_os_d=$y+$YD;

#Open points file for transformation of vector area
    open (OUT,">points");
    print OUT "0 0 $x $y\n";
    print OUT "0 100 $x_os_c $y_os_c\n";
    print OUT "100 0 $x_os_b $y_os_b\n";
    print OUT "100 100 $x_os_d $y_os_d\n";
    close OUT;

#Calculate average slope in vicinity (2*height) of peak
#Note, an alternative approach would be to use the multiple
#window size calculations of slope used in ridges.pl
#offset by 50,50 to allow for null value at circle centre

    $xx=$x+50;
```

```
    $yy=$y+50;
    `r.circle output=circle coordinate=$xx,$yy`;
    $radius=$X;
    `r.mapcalc "newmap=if(circle<$radius,1,null())"`;
    `r.average base=newmap cover=$em.slope output=temp.avsl`;
#    print"r.what input=temp.avsl east_north=$x,$y\n";


    $slope_out=`r.what input=temp.avsl east_north=$x,$y`;
    @slopes=split /\|/, $slope_out;
    $slope=$slopes[3];
#    print"@slopes";

    print"slope = $slope\n";

#Transform affected area template to location of peak and rebuild vector file
    if($slope>=45){
      `v.transform input=peak11a output=temp.aa2 pointsfile=points`;}
    else{
      `v.transform input=peak13 output=temp.aa2 pointsfile=points`;}
`v.support option=build map=temp.aa2`;

#convert to raster and add to $em.ridge.effect

`v.to.rast input=temp.aa2 output=pk.rast.temp`;
`r.support -r map=rd.rast.temp`;
`r.mapcalc "$em.pe.temp=if(isnull(pk.rast.temp),0,pk.rast.temp)"`;
`r.mapcalc "$em.pe.temp2=if(($em.pe.temp==20),($em.peak.effect+1.0),$em.peak.effect)"`;
`r.mapcalc "$em.pe.temp3=if(($em.pe.temp==10),($em.pe.temp2+0.0001),$em.pe.temp2)"`;
`g.rename -o rast=$em.pe.temp3,$em.peak.effect`;
```

```
#Put resulting vector into a combined file, rebuild and rename back to original name

    `v.patch input=temp.aa2,peaks.total output=peaks.totaltemp`;
    `v.support option=build map=peaks.totaltemp`;
    `g.rename -o vect=peaks.totaltemp,peaks.total`;
    $n++;
}

    `r.support -r map=$em.peak.effect`;
```

Script 2: Ridges

```
#!/usr/bin/perl

#Define constants
$pi=3.1415927;

#Inputs to be changed on each run
$wd=225; #Wind direction, clockwise from grid North. Direction wind blows from.
$em=pdel; #Elevation map raster name
`g.region raster=$em`;
`r.slope.aspect elevation=$em slope=$em.slope`;
`r.mapcalc "$em.coverage=1"` ;

`r.average base=$em.coverage cover=$em output=$em.av`;
`d.erase`;
`d.rast map=$em`;

#Create raster of wind direction
`r.mapcalc "winddir=$wd"`;
`r.mapcalc "$em.ridge.effect=0"`;

#Extend region in direction of wind angle, by distance $extend
$extend=10000;
$wdrad=($wd-180)*$pi/180;
$n="";
$e="";
$s="";
$w="";
$ns=$extend*cos($wdrad);
$ns=int($ns/50)*50; #round to nearest 50
$ew=$extend*sin($wdrad);
$ew=int($ew/50)*50; #round to nearest 50

if ($ns>0){
    $n="n=n+$ns";}
elsif($ns<0){
#    $sadj=-$ns;
```

```
    $s="s=s$ns";}
if ($ew>0){
    $e="e=e+$ew";}
elsif($ew<0){
#    $wadj=-$ew;
    $w="w=w$ew";}

print "g.region $n $e $s $w\n";
`g.region $n $e $s $w`;

#Remove temporary files used before beginning
`g.remove vect=totalv,totaltempv`;

#Extract features from elevation map
#`r.param.scale in=$em  out=$em.feat s_tol=1 c_tol=0.001 size=11 param=feature exp=0`;
`d.erase`; # clear display
`d.rast map=$em.feat`; # display extracted features

#Extract slope from elevation map at different scales
#window size = 3
#`r.param.scale in=$em  out=$em.sl3 size=3 param=slope exp=0`;
#window size = 5
#`r.param.scale in=$em  out=$em.sl5 size=5 param=slope exp=0`;
#window size = 9
#`r.param.scale in=$em  out=$em.sl9 size=9 param=slope exp=0`;
#window size = 13
#`r.param.scale in=$em  out=$em.sl13 size=13 param=slope exp=0`;
#window size = 17
#`r.param.scale in=$em  out=$em.sl17 size=17 param=slope exp=0`;

#Rut ridges only into a separate file
`r.mapcalc "$em.ridges=if(($em.feat==5),1,null())"` ;
#Thin them so that they can be converted to vectors more accurately
`r.thin input=$em.ridges output=$em.ridges.thin`;

`d.erase`; #clear display
`d.rast map=$em.ridges`; #display ridges (unthinned)

#Convert thinned raster ridges to vectors and build
```

```
`r.line input=$em.ridges.thin output=$em.v.ridges type=line`;
`v.support -s map=$em.v.ridges option=build`;
#Remove excess lines twice to allow for lines joining other lines
#maxlength may need adjustment
`v.rm.dangles input=$em.v.ridges output=$em.v.ridges.nd1 maxlength=500`;
`v.support -s map=$em.v.ridges.nd1 option=build`;
`v.rm.dangles input=$em.v.ridges.nd1 output=$em.v.ridges.nd maxlength=500`;
`v.support -s map=$em.v.ridges.nd option=build`;

#Output vector file of ridge coordinates to text file
`v.out.ascii input=$em.v.ridges.nd output=ridgetext`;

#Read in text file containing ridges and process each ridge in turn
open(RIDGE, "<PERMANENT/dig_ascii/ridgetext");
$line=0;
$segindex=0;
$segments=0;
while (<RIDGE>) {
    chomp;
if ($_=~/^L/){
  @seg_line=split;
  $segments=@seg_line[1];
  if ($line!=0){
  #Query wind angle at start of ridge
  $wind_out=`r.what input=winddir east_north=$x[1],$y[1]`;
  @wind=split /\|/, $wind_out;
  $winddir=$wind[3];
  $wdrad=($winddir-180)*$pi/180;

  #Calculate angle between ridge and wind (note atan2 avoids div. by zero errors)
  $ridgeangrad=atan2(($y[$segindex]-$y[1]),($x[$segindex]-$x[1]));
  $ridgeangle=(180/$pi)*$ridgeangrad;
  $anglediff=abs($winddir-$ridgeangle);

    #calculate ridge length, if > 500 then include
  #also if wind angle within 45 degrees
  #printf "X0: %.0f\t%.0f\t Y: %.0f\t%.0f\t\n",$x[$segindex],$x[1],$y[$segindex],$y[1];
  $rl=sqrt((($x[$segindex]-$x[1])**2)+(($y[$segindex]-$y[1])**2));
```

```
      printf "Wind: %.0f\tRidge: %.0f\tDiff.: %0.f\tLength: %0.f\n",$winddir,$ridgeangle,($anglediff-90),$rl;
      if (($rl>=500) && ($anglediff>=45)&&($anglediff<=135)){

            #fetch elevation and slope data for ridge
          $elevation=0;
          $slope=0;
          $sl3=0;
          $sl5=0;
          $sl9=0;
          $sl13=0;
          $sl17=0;


          for($i=1;$i<=$segindex;$i++){
            $tempridgedata=`r.what          input=$em,$em.slope,$em.sl3,$em.sl5,$em.sl9,$em.sl13,$em.sl17,$em.av
east_north=$x[$i],$y[$i]`;
            @ridgedata=split /\|/, $tempridgedata;
            $elevation+=$ridgedata[3];
            $slope+=$ridgedata[4];
            $sl3+=$ridgedata[5];
            $sl5+=$ridgedata[6];
            $sl9+=$ridgedata[7];
            $sl13+=$ridgedata[8];
            $sl17+=$ridgedata[9];
            $elevav=$ridgedata[10];
          }

          #calculate average values for ridge
          $elevation=$elevation/$segindex;
          $slope=$slope/$segindex;
          $sl3=$sl3/$segindex;
          $sl5=$sl5/$segindex;
          $sl9=$sl9/$segindex;
          $sl13=$sl13/$segindex;
          $sl17=$sl17/$segindex;

          #calculate ridgeheight
          $rh=$elevation-$elevav;
          printf "%.0f %0.f %0.3f %.3f %.3f %.3f %.3f    %.3f %0.f\n",
```

```
$elevation,$rh,$slope,$sl3,$sl5,$sl9,$sl13,$sl17, $elevav;
          #if ridge height and slope above thresholds then output affected areas

          if(($rh>50)&&($sl5>8)){
            #determine which slope value to use
            $rsla=$sl5*$pi/180;#calc. rough slope angle
            $base=$rh*(cos($rsla)/sin($rsla));#calc. rough base length

            if($base<=200){
                $slopeuse=$sl3;}
            elsif(($base>200)&&($base<=350)){
                $slopeuse=$sl5;}
            elsif(($base>350)&&($base<=550)){
                $slopeuse=$sl9;}
            elsif(($base>550)&&($base<=750)){
                $slopeuse=$sl13;}
            else{
                $slopeuse=$sl19;}

#assign offsets depending on slope
if($slopeuse<=12.67){
    @offsets=(-5,1,12);}
elsif(($slopeuse>12.67)&&($slopeuse<=16.24)){
    @offsets=(-4,1,15);}
elsif(($slopeuse>16.24)&&($slopeuse<=22.50)){
    @offsets=(-3,3.5,22);}
elsif(($slopeuse>22.50)&&($slopeuse<=35.78)){
    @offsets=(-2,3.5,25);}
elsif($slopeuse>35.78){
    @offsets=(-1,3,40);}

#write vector ascii file for selected ridges
`cp header PERMANENT/dig_ascii/lines.$line`;
open (LINE, ">>PERMANENT/dig_ascii/lines.$line");
$nodes=2*$segindex+1;

    #write upwind area of ridge (windward face)
print LINE "A $nodes\n";
```

```
for($i=1;$i<=$segindex;$i++){   #NOTE SYNTAX!
    print LINE " $y[$i] $x[$i]\n"; #write coordinates of ridge
}

for($i=$segindex;$i>=1;$i--){
    $x1=$x[$i]+$rh*$offsets[0]*sin($wdrad); #write coordinates of offset value
    $y1=$y[$i]+$rh*$offsets[0]*cos($wdrad);
    print LINE " $y1 $x1\n";
}
print LINE " $y[1] $x[1]\n";


#write downwind area of ridge (wake region)
print LINE "A $nodes\n";
for($i=1;$i<=$segindex;$i++){   #NOTE SYNTAX!
    $x1=$x[$i]+$rh*$offsets[1]*sin($wdrad); #write coordinates of offset value
    $y1=$y[$i]+$rh*$offsets[1]*cos($wdrad);
   print LINE " $y1 $x1\n"; #write coordinates of ridge
}

for($i=$segindex;$i>=1;$i--){
    $x1=$x[$i]+$rh*$offsets[2]*sin($wdrad); #write coordinates of offset value
    $y1=$y[$i]+$rh*$offsets[2]*cos($wdrad);
    print LINE " $y1 $x1\n";
}
$x1=$x[1]+$rh*$offsets[1]*sin($wdrad); #finish loop
$y1=$y[1]+$rh*$offsets[1]*cos($wdrad);
print LINE " $y1 $x1\n";

close (LINE);

#read in ascii file and add to totalv map
`v.in.ascii input=lines.$line output=lines.$line.v`;
`v.support option=build map=lines.$line.v`;

#convert to raster and add to $em.ridge.effect
`v.alabel map=lines.$line.v value=1 label=increase`;
`v.support map=lines.$line.v`;
`v.to.rast              input=lines.$line.v output=rd.rast.temp`;
```

```
            #`r.support map=rd.rast.temp`;
            `r.mapcalc
"$em.re.temp=if(isnull(rd.rast.temp),$em.ridge.effect,($em.ridge.effect+rd.rast.temp))"`;
            `g.rename -o rast=$em.re.temp,$em.ridge.effect`;


            `v.patch input=lines.$line.v,totalv output=totaltempv`;
            `v.support option=build map=totaltempv`;
            `g.rename -o vect=totaltempv,totalv`;
            `g.remove vect=lines.$line.v`;
      }

      }
    }
      $line++;
      $segindex=0;
    }
    elsif ($_=~/^\s/){ #put coordinates in a storage array
      $segindex++;
#     print "$_";
      @segcoords=split;
      $x[$segindex]=$segcoords[1];
      $y[$segindex]=$segcoords[0];
#     print "@segcoords $y[$segindex] $segindex segments:$segments\n";
    }
}
#print last line
close (RIDGE);

`r.support -r map=$em.ridge.effect`;
```

Script 3: Combining outputs

```
#!/usr/bin/perl

#Script to combine output from peaks and ridge effect scripts
$em=pdel;

`g.region raster=$em.ridge.effect`;
`r.mapcalc "pkrd.effect.1=$em.peak.effect+$em.ridge.effect"`;
`r.mapcalc "pkrd.effect.2=float(pkrd.effect.1%1)"`;

`r.mapcalc "pkrd.effect.3=if((pkrd.effect.1>1)&&(pkrd.effect.2>0.00001),0.1,pkrd.effect.1)"`;

`r.recode input=pkrd.effect.3 output=$em.pkrd.effect << EOF
0:0:0:0
0.00041:0.0999:1:1
0.00019:0.000409:2:2
0.00009:0.00011:3:3
0.09:0.11:4:4
1:1:5:5
2:4:6:6
4.1:999:7:7
EOF`;

`r.reclass input=$em.pkrd.effect output=$em.pkrd.effect2 << EOF
0 = 0   no effect
1 = 1   > 4 decrease areas
2 = 2   2-4 decrease areas
3 = 3   1 decrease area
4 = 4   mixed
5 = 5   1 increase area
6 = 6   2-4 increase areas
7 = 7   > 4 increase areas
end
EOF
`;

`r.support -r map=$em.pkrd.effect2`;
```

LIST OF REFERENCES

Ahmadi, G., Li, A. (2000) Computer simulation of particle transport and deposition near a small isolated building. *Journal of Wind Engineering and Industrial Aerodynamics* **84,** (1) 23-46.

Argyraki, A., Kinnersley, R. P., Ramsey, M. H. (1999) Optimising emergency sampling strategy following a release of radioactive material into the environment. MAFF Research Contract No. RP 0249.

Arya, S., Shipman, M. (1981) An experimental investigation of flow and diffusion in the disturbed boundary layer over a ridge - I. Mean flow and turbulence structure. *Atmospheric Environment* **15,** 1173-1184.

Baker, C. J., Wood, C. J., Gawthorpe, R. G. (1985) Strong winds in complicated hilly terrain - field measurements and wind-tunnel study. *Journal of Wind Engineering and Industrial Aerodynamics* **18,** 1-26.

Batchelor, G. K. (1967) *An Introduction to Fluid Dynamics*. Cambridge University Press, Cambridge.

Belcher, S. E., Hunt, J. C. R. (1998) Turbulent flow over hills and waves. *Annual Review of Fluid Mechanics* **30,** 507-538.

Biryukov, S. (1998) An experimental study of the dry deposition mechanism for airborne dust. *Journal of Aerosol Science* **29,** (1-2) 129-139.

Bradbury, L. J. S., Castro, I. P. (1971) A pulsed-wire technique for velocity measurements in highly turbulent flows. *Journal of Fluid Mechanics* **49,** (4) 657-691.

Carpenter, P., Locke, N. (1999) Investigation of wind speeds over multiple two-dimensional hills. *Journal of Wind Engineering and Industrial Aerodynamics* **83,** (1-3) 109-120.

Castro, I. P., Apsley, D. D. (1997) Flow and dispersion over topography: a comparison between numerical and laboratory data for two-dimensional flows. *Atmospheric Environment* **31,** (6) 839-850.

Castro, I. P., Snyder, W. H. (1982) A wind-tunnel study of dispersion from sources downwind of 3-dimensional hills. *Atmospheric Environment* **16,** (8) 1869-1887.

Castro, I. P., Snyder, W. H., Lawson, R. E. (1988) Wind direction effects on dispersion from sources downwind of steep hills. *Atmospheric Environment* **22,** (10) 2229-2238.

Cermak, J. E. (1984) Physical modelling of flow and dispersion over complex terrain. *Boundary-Layer Meteorology* **30,** 261-292.

Chamberlain, A. C. (1959) Deposition of iodine-131 in Northern England in October 1957. *Quarterly Journal of the Royal Meteorological Society* **85,** 350-361.

Chamberlain, A. C. (1984) Transport of gases and particulates to surafces with widely spaced roughness elements. *Boundary-Layer Meteorology* **29,** 343-360.

Chatzipanagiotidis, A., Olivari, D. (1996) Pollutant dispersal downstream of a hill in different wind conditions. *Journal of Wind Engineering and Industrial Aerodynamics* **64,** 233-248.

Cionco, R. M. (1989) AMADEUS: A dispersion study over moderately complex terrain. *6th Joint Conference on Applications of Air Pollution Meteorology, Anaheim, CA, Jan 30 - Feb 3.*

Comte-Bellot, G., Corrsin, S. (1966) The use of a contraction to improve the isotropy of grid-generated turbulence. *Journal of Fluid Mechanics* **25,** (4) 657-682.

Counihan, J. (1975) Adiabatic atmospheric boundary layers: A review and analysis of data from the period 1880-1972. *Atmospheric Environment* **9,** 871-905.

Cowan, I. R., Castro, I. P., Robins, A. G. (1997) Numerical considerations for simulations of flow and dispersion around buildings. *Journal of Wind Engineering and Industrial Aerodynamics* **67-8,** 535-545.

Crabtree, J. (1959) The travel and diffusion of the radioactive material emitted during the Windscale accident. *Quarterly Journal of the Royal Meteorological Society* **85,** 362-370.

Dai, W. P., Davidson, C. I., Etyemezian, V., Zufall, M. (2001) Wind tunnel studies of particle transport and deposition in turbulent boundary flows. *Aerosol Science and Technology* **35,** (5) 887-898.

Davidson, C. I., Wu, Y.-L. (1990). Dry deposition of particles and vapors. In: *Acidic Precipitation*. S. E. Lindberg, A. L. Page and S. A. Norton. Springer-Verlag, New York 103-216.

Department of Environment (1987) *Handling Geographic Information*. HMSO, London.

Draaijers, G. P. J., Ivens, W. P. M. F., Bleuten, W. (1988) Atmospheric deposition in forest edges measured by monitoring canopy throughfall. *Water Air and Soil Pollution* **42,** (1-2) 129-136.

ERCOFTAC (2000) *The ERCOFTAC Best Practice Guidelines for Industrial Computational Fluid Dynamics, European Research Community on Flow, Turbulence and Combustion, Special Interest Group on "Quality and Trust in CFD" Best Practice Guidelines Version 1.0* Internet resource http://imhefwww.epfl.ch/lmf/ERCOFTAC/SIGs/BPG.html, Accessed: 18th July.

Farell, C., Iyengar, A. K. S. (1999) Experiments on the wind tunnel simulation of atmospheric boundary layers. *Journal of Wind Engineering and Industrial Aerodynamics* **79,** (1-2) 11 - 35.

Finnigan, J. J., Raupach, M. R., Bradley, E. F., Aldis, G. K. (1990) A wind tunnel study of turbulent flow over a two-dimesional ridge. *Boundary-Layer Meteorology* **50,** 277 - 317.

Fluent (1999a). 9.2.4 The Spalart-Allmaras model. In: *Fluent 5 User's Guide*. Fluent Inc.

Fluent (1999b). 9.4.1 The standard k-epsilon model. In: *Fluent 5 User's Guide*. Fluent Inc.

Fluent (1999c). 9.8.1 Near-wall mesh guidelines for wall functions. In: *Fluent 5 User's Guide*. Fluent Inc.

Fluent (1999d). 14.1 Overview of discrete phase modeling. In: *Fluent 5 User's Guide*. Fluent Inc.

Fluent (1999e). 17.15.1 Monitoring residuals. In: *Fluent 5 User's Guide*. Fluent Inc.

Giostra, U., Tampieri, F., Trombetti, F. (1989) On the onset of separation in turbulent boundary-layer flow over two-dimensional humps of various size. *Nuovo Cimento Della Societa Italiana Di Fisica C-Geophysics and Space Physics* **12,** (5) 649-661.

Gittings, B. (2003) *Digital Elevation Data Catalogue* Internet resource http://www.geo.ed.ac.uk/home/ded.html, Accessed: 6th August 2003.

Goharrizi, A. S. (1998) Prediction of particle deposition from a turbulent stream around a surface mounted ribbon. *Aerosol Science and Technology* **29,** (141-151).

Goossens, D. (1988a) The effect of surface curvature on the deposition of loess: a physical model. *Catena* **15,** 179-194.

Goossens, D. (1988b) Sedimentation characteristics of natural dust in the wake of symmetrical hills. *Zeitschrift fur Geomorphologie* **32,** (4) 499-502.

Goossens, D. (1995) Comparisons of day-time and night-time dust accumulation in desert region. *Journal of Arid Environments* **31,** 253 - 281.

Goossens, D. (1996) Wind tunnel experiments of aeolian dust deposition along ranges of hills. *Earth Surface Processes and Landforms* **21,** 205-216.

Goossens, D., Offer, Z. I. (1990) A wind tunnel simulation and field verification of desert dust deposition (Avdat Experimental Station, Negev Desert). *Sedimentology* **37,** 7 - 22.

GRASS GIS (2003) *GRASS GIS homepage* Internet resource http://grass.itc.it/index.html, Accessed: 21 September 2003.

Greeley, R., Iversen, J. D., Pollack, J. B., Udovich, N., White, B. (1974) Wind tunnel studies of Martian aeolian processes. *Proceedings of the Royal Society of London Series A-Mathematical Physical and Engineering Sciences* **341,** 331-360.

Hall, D. J., Kukadia, V., Walker, S., Marsland, G. W. (1998) Deposition of large particle from warehouse fire plumes - a small-scale wind tunnel model study. *Journal of Hazardous Materials* **59,** 13-29.

Hanna, S. R., Hansen, O. R., Dharmavaram, S. (2004) FLACS CFD air quality model perfomrance evaluation with Kit Fox, MUST, Prairie Grass. and EMU observations. *Atmospheric Environment* **38,** 4675-4687.

Hasselrot, B., Grennfelt, P. (1987) Deposition of air-pollutants in a wind-exposed forest edge. *Water Air and Soil Pollution* **34,** (2) 135-143.

Hill, J. H. (1994) *Atmospheric modelling of the Amersham International Cardiff site,* MSc. Thesis. Centre for Environmental Technology, Imperial College of Science, Technology and Medicine, University of London.

Hinds, W. C. (1999) *Aerosol Technology: properties, behaviour and measurement of airborne particles*. John Wiley & Sons, Inc., New York.

Holden, J. J., Derbyshire, S. H., Belcher, S. E. (2000) Tethered balloon observations of the nocturnal stable boundary layer in a valley. *Boundary-Layer Meteorology* **97,** (1) 1-24.

Irwin, H. P. A. H. (1981) The design of spires for wind simulation. *Journal of Wind Engineering and Industrial Aerodynamics* **7,** 361-366.

Jacobson, M. Z. (1999) *Fundamentals of Atmospheric Modelling*. Cambridge University Press, Cambridge.

Jung, S. J. (1994) Application of the E-e turbulence numerical model to a flow and dispersion around a triangular ridge (I). *Journal of Korea Air Pollution Research Association* **10,** 116-123.

Kestin, J., Maeder, P. F., Sogin, H. H. (1961) The influence of turbulence on the transfer of heat to cylinders near the stagnation point. *Zeitschrift für angewandte Mathematik und Physik* **12,** (115-132).

Kim, H. G., Lee, C. M., Lim, H. C., Kyong, N. H. (1997) An experimental and numerical study on the flow over two-dimensional hills. *Journal of Wind Engineering and Industrial Aerodynamics* **66,** 17-33.

Kim, H. G., Patel, V. C. (2000) Test of turbulence models for wind flow over terrain with separation and recirculation. *Boundary-Layer Meteorology* **94,** (1) 5-21.

Kim, H. G., Patel, V. C., Lee, M. L. (2000) Numerical simulation of wind flow over hilly terrain. *Journal of Wind Engineering and Industrial Aerodynamics* **87,** 45-60.

Kim, S. E., Boysan, F. (1999) Application of CFD to environmental flows. *Journal of Wind Engineering and Industrial Aerodynamics* **81,** 145-158.

Kind, R. J. (1986) Snowdrifting: a review of modelling methods. *Cold Regions Science and Technology* **12,** 217-228.

Lai, A. C. K., Nazaroff, W. W. (2000) Modeling indoor particle deposition from turbulent flow onto smooth surfaces. *Journal of Aerosol Science* 31, (4) 463-476.

Launder, B. E., Spalding, D. B. (1974) The numerical computation of turbulent flows. *Computer Methods in Applied Mechanics and Engineering* **3,** 269-289.

Mason, P. J. (1996). Boundary layer flow over hills. In: *Modelling of Atmospheric Flow Fields*. D. P. Lalas and C. F. Ratto. World Scientific Publishing Co Pte Ltd, Singapore.

Maurizi, A. (2000) Numerical simulation of turbulent flows over 2-D valleys using three versions of the kappa-epsilon closure model. *Journal of Wind Engineering and Industrial Aerodynamics* **85,** (1) 59-73.

May, K. R., Clifford, R. (1967) Deposition of the impaction of aerosol particles on cylinders, spheres, ribbons and discs. *Ann. Occup. Hyg.* **10,** 83-95.

Meroney, R. N., Leitl, B. M., Rafailidis, S., Schatzmann, M. (1999) Wind-tunnel and numerical modeling of flow and dispersion about several building shapes. *Journal of Wind Engineering and Industrial Aerodynamics* **81,** (1-3) 333-345.

Mouzakis, F. N., Bergeles, G. C. (1991) Numerical prediction of turbulent flow over a two-dimensional ridge. *International Journal For Numerical Methods in Fluids* **12,** 287-296.

Neff, D. E., Meroney, R. N. (1998) Wind-tunnel modeling of hill and vegetation influence on wind power availability. *Journal of Wind Engineering and Industrial Aerodynamics* **74-76,** 335-343.

Nicholson, K. W. (1988) The dry deposition of small particles: a review of experimental measurements. *Atmospheric Environment* **22,** (12) 2653-2666.

Offer, Z. Y., Goossens, D. (1995) Wind tunnel experiments and field measurements of aeolian dust deposition on conical hills. *Geomorphology* **14,** 43 - 56.

Okabayashi, K., Ide, Y., Kitabayashi, K., Okamoto, S., Kobayashi, K. (1996) Effects of wind directional fluctuations on gas diffusion over a model terrain. *Atmospheric Environment* **30,** (16) 2871 - 2880.

Oke, T. R. (1987) *Boundary Layer Climates*. Routledge, London.

Parker, S. T., Kinnersley, R. P. (2004) A computational and wind tunnel study of particle dry deposition in complex topography. *Atmospheric Environment*, **38**, 3867-3878.

Pielke, R. A., Cotton, W. R., Walko, R. L., Tremback, C. J., Lyons, W. A., Grasso, L. D., Nicholls, M. E., Moran, M. D., Wesley, D. A., Lee, T. J., Copeland, J. H. (1992) A comprehensive meteorological modeling system - RAMS. *Meteorology and Atmospheric Physics* **49,** (1-4) 69-91.

Reynolds, A. M. (1999) A Lagrangian stochastic model for heavy particle deposition. *Journal of Colloid and Interface Science*.

Richards, P. J., Hoxey, R. P. (1993) Appropriate boundary conditions for computational wind engineering models using the k-epsilon turbulence model. *Journal of Wind Engineering and Industrial Aerodynamics* **46&47,** 145-153.

Richards, P. J., Quinn, A. D., Parker, S. (2002) A 6m cube in an atmospheric boundary layer flow. Part 2. Computational solutions. *Wind and Structures* **5,** 177-192.

Richards, P. J., Wanigaratne, B. S. (1993) A comparison of computer and wind-tunnel models of turbulence around the Silsoe structures building. *Journal of Wind Engineering and Industrial Aerodynamics* **46&47,** 439-447.

Ruijgrok, W., Davidson, C. I., Nicholson, K. W. (1995) Dry deposition of particles. *Tellus* **47B,** 587 - 601.

Sagrado, A. P. G., van Beeck, J., Rambaud, P., Olivari, D. (2002) Numerical and experimental modelling of pollutant dispersion in a street canyon. *Journal of Wind Engineering and Industrial Aerodynamics* **90,** 321-339.

Schack, C. J., Pratsinis, S. E., Friedlander, S. K. (1985) A general correlation for deposition of suspended particles from turbulent gases to completely rough surfaces. *Atmospheric Environment* **19,** (6) 953-960.

Schatzmann, M., 1999. Wind tunnel modelling of fog droplet deposition on cylindrical obstacles. *Journal of Wind Engineering and Industrial Aerodynamics* **83**, 371-380.

Schlichting, H. (1968) *Boundary-Layer Theory*. McGraw-Hill, New York.

Schmidt, E., Wenner, K. (1941) Warmeabgabe uber den umfang eines angelblasenen geheitzen zylinders. *Forschg. Ing.-Wes.* **12,** 65-73.

Sehmel, G. A. (1980) Particle and gas dry deposition: a review. *Atmospheric Environment* 14, 983-1011.

Sehmel, G. A., Hodgson, W. H. (1980) A model for predicting dry deposition of particles and gases to environmental surfaces. *The American Institute of Chemical Engineers, Symposium Series* **76,** (196) 218-230.

Shams, M., Ahmadi, G., Rahimzadeh, H. (2000) A sublayer model for deposition of nano- and micro-particles in turbulent flows. *Chemical Engineering Science* **55,** 6097-6107.

Slinn, W. G. N. (1978) Parameterizations for resuspension and for wet and dry deposition of particles and gases for use in radiation dose calculations. *Nuclear Safety* **19,** (2) 205-219.

Smith, L. M., Woodruff, S. L. (1998) Renormalization-Group analysis of turbulence. *Annual Review of Fluid Mechanics* **30,** 275-310.

Snyder, W. H. (1972) Similarity criteria for the application of fluid models to the study of air pollution meteorology. *Boundary-Layer Meteorology* **3,** 113-134.

Stull, R. B. (1988) *An Introduction to Boundary Layer Meteorology*. Kluwer Academic Publishers, Dordrecht.

Sutton, O. G. (1949) *Atmospheric Turbulence*. Methuen.

Takahashi, T., Ohtsu, T., Yassin, M. F., Kato, S., Murakami, S. (2002) Turbulence characteristics of wind over a hill with a rough surface. *Journal of Wind Engineering and Industrial Aerodynamics* **90,** (12-15) 1697-1706.

Tampieri, F. (1987) Separation features of boundary-layer flow over valleys. *Boundary-Layer Meteorology* **40,** (3) 295-307.

Taylor, P. A., Mason, P. J., Bradley, E. F. (1987) Boundary-layer flow over low hills. *Boundary-Layer Meteorology* **39,** (1-2) 107-132.

Taylor, P. A., Teunissen, H. W. (1987) The Askervein Hill project - overview and background data. *Boundary-Layer Meteorology* **39,** (1-2) 15-39.

Tennekes, H., Lumley, J. L. (1972) *A First Course in Turbulence*. The MIT Press, Cambridge, Massachusetts.

Trombetti, F., Busuoli, M., Tampieri, F., 1995. A diagnostic study of turbulence features in wind tunnel flow over simple topographic shapes. *Il Nuovo Cimento* **18,** (4) 441 - 456.

Unterweger, M. P., Hoppes, D. D., Schima, F. J. (1992) New and revised half-life measurements results. *Nuclear Instruments and Methods in Physics Research* **A312,** 349-352.

van Haarlem, B., Boersma, B. J., Nieuwstadt, T. M. (1998) Direct numerical simulation of particle deposition onto a free-slip and no-slip surface. *Physics of Fluids* **10,** (10) 2608-2620.

Versteeg, H. K., Malalasekera, W. (1995) *An Introduction to Computational Fluid Dynamics*. Longman, Harlow.

Vosper, S. B., Castro, I. P., Snyder, W. H., Mobbs, S. D. (1999) Experimental studies of strongly stratified flow past three-dimensional orography. *Journal of Fluid Mechanics* **390,** 223-249.

Warner, F., Harrison, R. M., Eds. (1993) *Radioecology After Chernobyl: Biogeochemical Pathways of Artificial Radionuclides - SCOPE 50.* (Scientific Committee on Problems of the Environment (SCOPE)), John Wiley & Sons Ltd, Chichester.

Wood, J. (1996) *The Geomorphological Characterisation of Digital Elevation Models*, Ph.D. thesis. Department of Geography, University of Leicester.

Wood, N. (1995) The onset of separation in neutral, turbulent flow over hills. *Boundary-Layer Meteorology* **76,** 137-164.

Xu, Z. G., Walklate, P. J., Rigby, S. G., Richardson, G. M. (1998) Stochastic modelling of turbulent spray dispersion in the near-field of orchard sprayers. *Journal of Wind Engineering and Industrial Aerodynamics* **74-76,** 295-304.

Xuan, J., Robins, A. (1994) The effects of turbulence and complex terrain on dust emissions and depositions from coal stockpiles. *Atmospheric Enviornment* **28,** (11) 1951-1960.

Zhang, H., Ahmadi, G. (2000) Aerosol particle transport and deposition in vertical and horizontal turbulent duct flows. *Journal of Fluid Mechanics* **406,** 55-80.

Zhang, L., Gong, S., Padro, J., Barrie, L. (2001) A size-segregated dry deposition scheme for an atmospheric aerosol module. *Atmospheric Environment* **35,** 549-560.

Zufall, M. J., Davidson, C. I. (1998). Dry Deposition of Particles. In: *Atmospheric Particles*. R. M. Harrison and R. E. van Grieken. John Wiley & Sons, Chichester.

Zufall, M. J., Dai, W., Davidson, C. I., Etyemezian, V. (1999a) Dry deposition of particles to wave surfaces: I. Mathematical modeling. *Atmospheric Environment* **33,** (26) 4273-4281.

Zufall, M. J., Dai, W., Davidson, C. I. (1999b) Dry deposition of particles to wave surfaces: II. Wind tunnel experiments. *Atmospheric Environment* **33,** (26) 4283-4290.